**Transactions of the ASME, Journal of Heat Transfer** (ISSN 0022-1481) is published monthly by The American Society of Mechanical Engineers, Three Park Avenue, New York, NY 10016. Periodicals postage paid at New York, NY and additional mailing offices. POSTMASTER: Send address changes to Transactions of the ASME, Journal of Heat Transfer, c/o THE AMERICAN SOCIETY OF MECHANICAL ENGINEERS, 22 Law Drive, Box 2300, Fairfield, NJ 07007-2300. **CHANGES OF ADDRESS** must be received at Society headquarters seven weeks before they are to be effective. Please send old label and new address.


# Journal of Heat Transfer

**Published Monthly by ASME**

**VOLUME 130 • NUMBER 2 • FEBRUARY 2008(pp.021401-027007)**

## RESEARCH PAPERS



## TECHNICAL BRIEFS



**(Contents continued on inside back cover)**

This journal is printed on acid-free paper, which exceeds the ANSI Z39.48-1992 specification for permanence of paper and library materials. ♾™
♻ 85% recycled content, including 10% post-consumer fibers.

## DISCUSSIONS



## ERRATA



The ASME Journal of Heat Transfer is abstracted and indexed in the following:

*Applied Science and Technology Index, Chemical Abstracts, Chemical Engineering and Biotechnology Abstracts (Electronic equivalent of Process and Chemical Engineering), Civil Engineering Abstracts, Compendex (The electronic equivalent of Engineering Index), Corrosion Abstracts, Current Contents, E & P Health, Safety, and Environment, Ei EncompassLit, Engineered Materials Abstracts, Engineering Index, Enviroline (The electronic equivalent of Environment Abstracts), Environment Abstracts, Environmental Engineering Abstracts, Environmental Science and Pollution Management, Fluidex, Fuel and Energy Abstracts, Index to Scientific Reviews, INSPEC, International Building Services Abstracts, Mechanical & Transportation Engineering Abstracts, Mechanical Engineering Abstracts, METADEX (The electronic equivalent of Metals Abstracts and Alloys Index), Petroleum Abstracts, Process and Chemical Engineering, Referativnyi Zhurnal, Science Citation Index, SciSearch (The electronic equivalent of Science Citation Index), Theoretical Chemical Engineering*

# Exergy Analysis of Data Center Thermal Management Systems

**Amip J. Shah**[1]
e-mail: amipshah@engineeralum.berkeley.edu

**Van P. Carey**
e-mail: vcarey@me.berkeley.edu

Department of Mechanical Engineering,
University of California,
Berkeley, CA 94720-1740

**Cullen E. Bash**
e-mail: cullen.bash@hp.com

**Chandrakant D. Patel**
e-mail: chandrakant.patel@hp.com

Hewlett Packard Laboratories,
1501 Page Mill Road,
M/S 1183,
Palo Alto, CA 94304-1126

*The modeling of recirculation patterns in air-cooled data centers is of interest to ensure adequate thermal management of computer racks at increased heat densities. Most metrics that describe recirculation are based exclusively on temperature inside the data center, and therefore fail to provide adequate information regarding the energy efficiency of the thermal infrastructure. This paper addresses this limitation through an exergy analysis of the data center thermal management system. The approach recognizes that the mixing of hot and cold streams in the data center airspace is an irreversible process and must therefore lead to a loss of exergy. Experimental validation in a test data center confirms that such an exergy-based characterization in the cold aisle reflects the same recirculation trends as suggested by traditional temperature-based metrics. Further, by extending the exergy-based model to include irreversibilities from other components of the thermal architecture, it becomes possible to quantify the amount of available energy supplied to the cooling system that is being utilized for thermal management purposes. The energy efficiency of the entire data center cooling system can then be collapsed into the single metric of net exergy loss. When evaluated against a ground state of the external ambience, this metric enables an estimate of how much of the energy emitted into the environment could potentially be harnessed in the form of useful work. Thus, this paper successfully demonstrates that the proposed exergy-based approach can provide a foundation upon which the data center cooling system can be simultaneously evaluated for thermal manageability and energy efficiency.* [DOI: 10.1115/1.2787024]

*Keywords: exergy, second-law analysis, data center, thermal management, electronics cooling, energy efficiency*

## Background

Recent trends of miniaturization in electronic devices and increased levels of integration on computer chips have enabled the extensive compaction of equipment in data centers. Consequently, power density loads and corresponding heat dissipation in data centers have multiplied over the past few years, leading to significant cooling challenges and costs. For example, as discussed by Patel et al. [1], the core building block of a typical state-of-the-art data center can be considered to consist of a hundred 10 kW racks, air handlers and other thermal management devices in the racks, as well as a supporting infrastructure of switchgear, generators, uninterruptible power supplies (UPSs) and associated batteries/flywheel, power distribution units (PDUs), chillers, hydronics, cooling towers, etc. Such a core would require approximately 1 MW for the compute hardware core, 100 kW for air movers and other thermal management devices in the racks, and up to an additional 1 MW for the cooling resources used to remove the heat from the racks [1,2]. In addition to the environmental burden imposed by such energy use, the data center cooling infrastructures also impose a significant economic burden. Using standard grid rates, Patel and Shah [3] have estimated the annual cost of running the above core at $2 million in recurring power delivery, plus an additional $1.2 million each year in preventive maintenance and amortization expenses. Considering that next-generation data centers may consist of numerous such cores, the performance of data center thermal management systems is of interest for purposes of environmental energy conservation and potential economic savings.

Figure 1 shows a schematic of a typical raised-floor air-cooled data center. As with all compute equipment, the electrical power supplied to the racks gets dissipated to the surrounding environment in the form of heat. To cool the data center, cold air is supplied from a computer room air-conditioning (CRAC) unit. The best practice is to divide the physical airspace of the data center into cold and hot aisles, so that cold air enters the room from the CRAC, gets heated up in the rack, and then is removed from the room in the hot aisle [4,5]. Such a layout is represented in Fig. 1, where a raised floor design is used to pressurize an underfloor plenum that delivers flow to the room via perforated tiles in the cold aisle. It should be noted that some equipment manufacturers supply cold air from the top and/or sides of the equipment and exhaust it from the top (or bottom) [6–8], but the vast majority of data center cooling systems consist of a raised floor as described above. The rack exhaust from the hot aisle is removed from the computing environment either via a room return or ceiling return mechanism. The warm air is then returned to the CRAC unit, where it is refrigerated by a chilled water stream or other thermal work input before being resupplied to the data center environment at a desired supply temperature.

Such a data center architecture provides no direct control to prevent the mixing of cold and warm airstreams. Previous researchers have suggested localized control of recirculation through blanking panels [9], refrigerant-assisted spot cooling [10], or use of liquid heat exchangers on rack doors [11], but these solutions are far from commonplace. As a result, the typical data center continues to reflect several inefficiencies in the cooling infrastructure. For example, after the cold supply from the CRAC unit has passed through an equipment rack and picked up the dissipated heat, the warm stream may then return to a neighboring rack and subsequently nullify the effect of cooling from vent tiles.

[1]Now at Hewlett Packard Laboratories, 1501 Page Mill Road, M/S 1183, Palo Alto, California 94304-1126.

Contributed by the Heat Transfer Division of ASME for publication in the JOURNAL OF HEAT TRANSFER. Manuscript received July 10, 2006; final manuscript received May 25, 2007; published online February 4, 2008. Review conducted by Yogendra Joshi. Parts of paper presented at the 2003 ASME International Mechanical Engineering Congress (IMECE2003), Washington, DC, November 15–21, 2003.

  

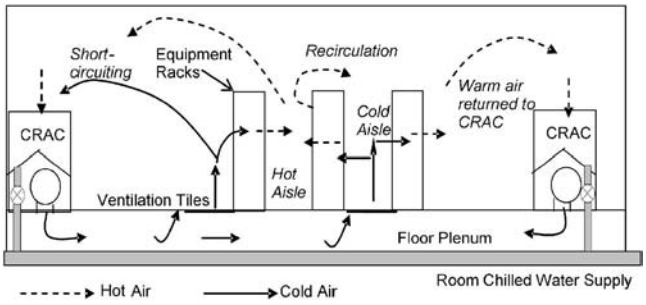


**Fig. 1 Typical thermal architecture in a raised-floor data center. Best practice dictates dividing the room into hot aisles and cold aisles on either side of a row of racks.**

This phenomenon, known as recirculation, is very common in the internal areas of the data center where the equipment density is high. If the warm air is recirculated to the rack inlet without any abatement, the intake of warm air to the chip-scale package could result in equipment failure. To avoid such an increase in inlet temperatures to the computer rack units, data center operators often enable additional cooling capacity by minimizing the CRAC supply temperature and increasing the CRAC flow rate. However, as shown in Fig. 1, if the vent tiles are poorly configured, then this increase in flow rate in turn may lead to short circuiting (direct passage of cold air from vent tiles to system return), and the significant amount of energy spent in the CRAC units—meant for cooling of racks—is essentially wasted.

Thus, potential cost and energy savings could be realized if recirculation concerns are resolved during the design or management of data center thermal architecture. As a result, much recent research has focused on studying airflow patterns in data centers. Early studies, such as those by Kang et al. [12], Patel et al. [13], and Schmidt [14], were based on computational fluid dynamics (CFD) models of the data center airspace. Subsequent studies have explored in greater depth the impact of CRAC handling on data center airflow. For example, VanGilder and Lee [15] and Schmidt et al. [16] have explored flow-management techniques via control of subplenum configurations and vent tile layout. Karki et al. [17,18] have performed various CFD simulations to characterize the relationship between airflow and data center physical characteristics, while VanGilder and Schmidt [19] and Radmehr et al. [20] have characterized the flow through vent tiles in raised floor data centers via computational modeling [19] and experimental measurement [20] for different CRAC settings. The supply air distribution resulting from a single CRAC unit was numerically modeled by Rambo and Joshi [21], who also presented computational models of subrack thermal responses to various CRAC responses.

In addition to the above studies, which focus almost exclusively on the fluidic aspects of recirculation, several researchers have also explored the impact of other parameters on data center thermal management. For example, Patel et al. [2] and Sharma et al. [22] have studied the impacts of asymmetry in data center rack layout on inlet air temperature specifications, while Bhopte et al. [23] and Schmidt and Iyengar [24] have investigated and attempted to optimize the data center layout for various design parameters, such as plenum height, ceiling height, and row length on rack inlet temperatures. Similarly, the impact of rack parameters, such as location, loading, and local fan flow rates on the resulting rack inlet temperatures, have been parametrically assessed by Schmidt and Cruz [25–28]. For nonraised floor data center cooling configurations (such as room-supply/ceiling-return or ceiling-supply/ceiling-return, etc.), variations in the rack inlet air temperature have been modeled by Shrivastava et al. [7] and Iyengar et al. [8], who found significantly different patterns of recirculation for different data center architectures. The physics behind inefficiencies, such as recirculation and short circuiting, have been examined in greater detail by Bash et al. [29], who in conjunction with Sharma et al. [30,31] proposed the development of high-level control policies to enable real-time feedback and control of data center thermal architecture. To enable such policies, the following nondimensional parameters were proposed based on rack inlet and exhaust temperature [29,30]:

$$\mathrm{SHI} = \frac{\delta Q}{Q + \delta Q} = \frac{\text{Enthalpy rise in cold aisle due to infiltration of warm air}}{\text{Total enthalpy rise at rack exhaust}} \tag{1}$$

$$\mathrm{RHI} = \frac{Q}{Q + \delta Q} = \frac{\text{Total enthalpy rise in data center airspace}}{\text{Total enthalpy rise at rack exhaust}} \tag{2}$$

where SHI is the supply heat index and RHI is the return heat index of the data center. Note that the sum of SHI and RHI is always unity, and both parameters are scaled to vary between 0 and 1. Ideally, a case of no recirculation corresponds to SHI=0, which will simultaneously lead to a value of RHI=1.

Numerical simulations by Sharma et al. [30] have demonstrated that larger amounts of recirculation do indeed lead to higher SHI values. The effects of geometric layout, rack height, and row length can all be captured indirectly in the changing values of SHI. These metrics can be useful for real-time feedback regarding data center airspace behavior, particularly because the normalized nondimensional nature enables scalability across the rack, row, and room levels.

While the high-level estimates of mixing provided by the SHI are useful for purposes of cooling control and thermal management, Schmidt et al. [32,33] have argued that SHI-RHI by itself is insufficient because a data center with favorable global profiles (low SHI and high RHI) can still be subjected to local hotspots that hinder adequate thermal management. To address this concern, the following metric was proposed [32,33]:

$$\beta = \frac{\Delta T_{\text{inlet}}}{\Delta T_{\text{rack}}} = \frac{T_{\text{in}}^{\text{rack}} - T_{\text{sup}}}{T_{\text{out}}^{\text{rack}} - T_{\text{in}}^{\text{rack}}} \tag{3}$$

A value of $\beta=0$ indicates that no hot air is recirculated to the front of the rack, while a value of $\beta=1$ implies insufficient cold air supply so that air from the hot aisle is directly recirculated back to the inlet of the rack. A value of $\beta>1$ suggests that a local self-heating loop exists, which is causing the air to be heated even beyond the caloric heat gain due to heat addition from the rack. It would appear that rack-level approximations of SHI and RHI can perform the same function as $\beta$, and therefore use of either metric would suffice for purposes of thermal management. Subrack approximations of recirculation would require estimates of SHI or $\beta$ at corresponding granularities.

While useful for estimating thermal manageability for a given data center configuration, metrics such as SHI, $\beta$, the rack cooling index [34], etc., are still of limited use because limited information is gained regarding the energy efficiency of the system. For example, it is difficult to ascertain whether local hotspots are formed primarily due to poor CRAC performance, suboptimal equipment layout, unfavorable airflow patterns, etc. Other energy efficiency indicators for the data center have been proposed elsewhere [35–37], but these metrics provide no information about recirculation phenomena and corresponding impacts on the thermal manageability of data centers. Thus, there remains a gap with regard to an appropriate metric that fuses information about thermal manageability and energy efficiency while providing insight into methods of reducing recirculation in the data center airspace. This paper proposes such a metric using the thermodynamic con-

cept of exergy. The next section discusses, conceptually, how such an approach might fill the metrology gap with regard to energy-efficient data center thermal management.

## Exergy and Data Centers

The exergy of a system is a representation of the amount of useful work that can be obtained from a given quantity of energy. For example, the electricity supplied to the compute equipment is a very high quality of energy, as it can almost entirely be converted into work. Therefore, the electricity supplied to the data center has a high exergy value. On the other hand, heat is a relatively lower quality of energy, owing to the Carnot limitation on the amount of work that can be extracted from a heat source. So, the heat rejected by the racks inside the data center has a lower exergy value. Alternatively, the conversion of electricity to heat is an irreversible process: without any external input, the work available from the electricity can never be recovered once the conversion to heat has taken place. That is, exergy has been destroyed during the conversion of electricity to heat, so that the exergy content of the heat source will be lower than the exergy content of the electricity source.

Similarly, within the context of data center thermal management, there will be a difference in the exergy value depending on the temperature and velocity of the airflow in the data center. For example, relative to an ambient reference state, more work is theoretically available from a high-temperature exhaust stream in the hot aisle than a low-temperature input stream in the cold aisle. Or, the exergy value of a cold aisle with no recirculation will be lower than the exergy value of a cold aisle with recirculation where the average temperature is higher. Equivalently, the mixing of hot and cold air in the data center is an irreversible process—the streams cannot be separated into their original hot and cold aisles without any external work input—and therefore, any occurrence of recirculation will also be a source of exergy loss. The interested reader is referred to standard textbooks on thermodynamics [38,39] for a more detailed introduction to the concept of exergy.

Several authors have previously used exergy analysis to examine the energy efficiency of power plants [40], chemical systems [41], and complex manufacturing processes [42]. More recently, Carey and Shah [43] have assessed the energy efficiency of multiple generations of computer processors through an exergy analysis. Within the electronics cooling community, numerous authors have also taken similar second-law approaches, such as entropy generation minimization [44], to investigate the optimal design of heat sinks for maximum heat transfer with minimal losses [45–47] as well as the lowest fluid pumping power [48]. Thus, it may be expected that an exergy analysis could provide the desired indication of data center energy efficiency.

A more important question, perhaps, is whether the necessary information regarding data center thermal manageability can be discerned from an exergy-based metric of recirculation. Based on the previous discussion, owing to the irreversibility of the recirculation process, there is reason to believe that a map of exergy loss throughout the data center airspace can pinpoint locations of recirculation, thus providing an indication of data center thermal manageability. The next section discusses how such an exergy loss map could be created for a given data center. Subsequent sections explore the combination of this recirculation map with a broader exergy analysis to simultaneously evaluate the energy efficiency of the data center.

## Exergy-Based Modeling of Recirculation in Data Centers

**Model Development.** As discussed earlier, this paper proposes estimating the extent of recirculation in the data center airspace by measuring the exergy loss across the airspace. To computationally estimate this, a finite volume approach is used by dividing the physical volume of the room into a large mesh of smaller volumes, so that by evaluating the exergy loss of each cell against a common ground (reference) state, the total exergy loss of the airspace can be computed as the sum of all the individual cell exergy losses:

$$\dot{\Psi}_{d_{\text{air}}} = \sum_{i=1}^{N} \dot{\Psi}_{d_i} \tag{4}$$

where $N$ is the total number of cells in the room. The same rules used to define the grid for numerical thermofluidic analysis are used to govern the choice of mesh in the current analysis, i.e., the number, uniformity, and size of the cells chosen for the analysis depend on the thermal variability encountered within the system for a given data center setting. It is essential to choose a cell size that is small enough to capture field variations at length scales of room subregion dimensions. Beyond this, cell sizes should be chosen as a compromise between the required level of granularity (or the degree of accuracy necessary) and the desired speed of computation.

It should be noted that the total exergy loss estimate of Eq. (4) is proposed as a global metric of mixing in the airspace. The magnitude and location at which recirculation occurs will be represented by the exergy loss within a given cell of the grid, which requires knowledge about the exergy content of the cell (relative to the ground state). For a given control volume, the specific exergy of the system can be defined with respect to the ground state as

$$\psi = (h - h_0) + \frac{V^2}{2} + g(z - z_0) - T_0(s - s_0) \tag{5}$$

The subscript "0" corresponds to the ground (reference) state against which the system is operating. It is important that a common ground state be maintained throughout the second-law analysis, otherwise the summation of Eq. (4) will not be valid.

The exergy lost in each individual cell can then be calculated by performing an exergy balance for the individual cell

$$\frac{d\Psi_{cv}}{dt} = \sum_j \left(1 - \frac{T_0}{T_j}\right)\dot{Q}_j - \left(\dot{W}_{cv} - P_0\frac{dV_{cv}}{dt}\right) + \sum_{\text{in}} \dot{m}_i\psi_i - \sum_{\text{out}} \dot{m}_o\psi_o - \dot{\Psi}_d \tag{6}$$

where $j$ is the boundary across which heat $\dot{Q}_j$ is added at a temperature $T_j$. Note that the first term in Eq. (6) relates to the loss of exergy due to boundary heat transfer from high (processor) to low (ambient) temperature in the airspace of the data center, and is different from the exergy loss during heat dissipation in the rack itself (which is due to conversion of high-quality electrical work to low-quality heat at the processor temperature). Additionally, the walls of the racks are assumed to be insulated, so the heat addition will only occur as the air flows through the racks from inlet to outlet. For simplicity, parallel flowpaths are assumed through the racks, so that no internal mixing will occur within these cells.

The system is assumed to operate at steady state, and no changes occur to the control volume boundaries, so that

$$\dot{\Psi}_d = \sum_j \left(1 - \frac{T_0}{T_j}\right)\dot{Q}_j - \dot{W}_{cv} + \sum_{\text{in}} \dot{m}_i\psi_i - \sum_{\text{out}} \dot{m}_o\psi_o \tag{7}$$

Substituting for the specific exergy from Eq. (5),

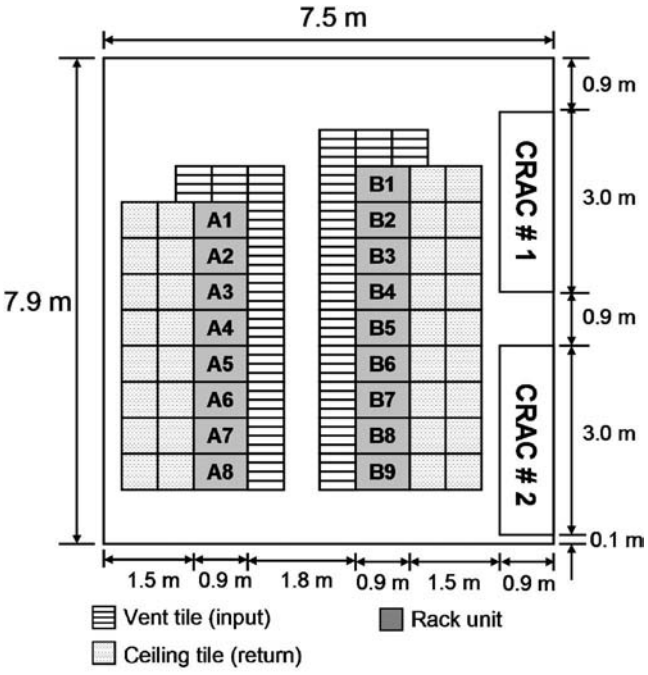


| Rack | Power (kW) |
|---|---|
| A1 | 2.0 |
| A2 | 2.6 |
| A3 | 2.6 |
| A4 | 2.6 |
| A5 | 2.6 |
| A6 | 3.2 |
| A7 | 3.2 |
| A8 | 0.0 |

| Rack | Power (kW) |
|---|---|
| B1 | 9.9 |
| B2 | 9.9 |
| B3 | 6.6 |
| B4 | 6.6 |
| B5 | 6.6 |
| B6 | 6.6 |
| B7 | 6.6 |
| B8 | 6.6 |
| B9 | 0.0 |

**Fig. 2 System layout and rack loading for test data center (top view). Each floor tile has an area of $0.6\times0.6$ m$^2$ ($2\times2$ ft$^2$). The floor-to-ceiling height is 2.7 m (9 ft), while the depth of the underfloor plenum is 0.6 m (2 ft) and the height of the ceiling return plenum is 1.2 m (4 ft).**

$$\dot{\Psi}_d = \sum_j \left(1 - \frac{T_0}{T_j}\right)\dot{Q}_j - \dot{W}_{cv} + \sum_{\text{in}} \dot{m}_i \left[ (h - h_0) + \frac{V^2}{2} + g(z - z_0) - T_0(s - s_0) \right]_{\text{in}} - \sum_{\text{out}} \dot{m}_o \left[ (h - h_0) + \frac{V^2}{2} + g(z - z_0) - T_0(s - s_0) \right]_{\text{out}} \quad (8)$$

Thus, for a cell at a given location, if the temperature and flow (pressure and velocity) properties at that point are known in addition to the system inputs (heat and work), then the exergy loss for the air flowing through the cell can be calculated per Eq. (8). Typical state-of-the-art thermofluidic analysis already involves a determination of the temperature and flow throughout the data center airspace; thus, only one additional calculation is required to gain the desired information about exergy loss in the system. Applying Eq. (8) to each cell of the numerical grid will provide a map of exergy loss throughout the data center and enable identification of local recirculation effects. The measure of total exergy loss per Eq. (4) provides a single metric that can be used to evaluate the overall recirculation patterns in the cold aisle or the entire data center.

**Application of Model.** For demonstration purposes, the model was applied to the data center shown in Fig. 2. Ceiling return mechanism was considered for all experimental and modeling cases, with the locations of return vents noted in Fig. 2. Air is supplied from two 105 kW (30 tons) Liebert FH600C-AAEI CRAC units, each of which has a maximum air flow rate of 7.9 m$^3$/s (17,100 cfm) per manufacturer specifications. The air enters the room either through low-flow vent tiles (which have dampeners that restrict maximum throughput to 0.3 m$^3$/s (750 cfm)) or high-flow vent tiles with no dampeners. The exact magnitude of flow through each tile will be a function of plenum pressure.

Heat input is provided from two rows of computing racks. The heat dissipation from each rack is specified using rack power measurements or from manufacturer specifications. The relevant heat loads are summarized in Fig. 2.

A base case scenario for the model was run with all of the CRAC units operating at 60% fan speed at a supply temperature of 16°C for a ground state corresponding to the supply temperature. The commercial CFD code FLOVENT™ [49] was used to numerically solve for the flow and temperature properties using an LVEL $k$-$\varepsilon$ model across a nonuniform grid of 569,772 cells. Grid independence and convergence criteria of subunity residuals were verified per the work of Patel et al. [13]. The model converged in roughly 6 h on an HP Proliant ML370 machine. For the established grid, the temperature and flow values were then postprocessed per the procedure outlined in Eqs. (4)–(8) to calculate the exergy loss values in each cell. Additional details regarding the computational model used for postprocessing can be found in the work of Shah [50].

Results from the model for temperature and exergy loss are shown in Figs. 3(*a*) and 3(*b*), respectively, at heights of 0.9 m (3 ft), 1.5 m (5 ft), 2.1 m (7 ft), and 2.7 m (9 ft) from the floor. At a height of 0.9 m (3 ft), the temperature distribution is as desired, with the hot aisles being slightly warmer than the cold aisles. No recirculation effects are noticed in the cold aisles. The same trend continues at a height of 1.5 m (5 ft), with the hot aisle being slightly warmer due to the mixing of exhausts from the servers loaded in the bottom and middle of the racks. At a height of 2.1 m (7 ft), the recirculation effects are clearly noticeable in the middle of the rows. The temperature map at 2.7 m (9 ft) suggests that this is due to recirculation over the top of the rack, although some recirculation around the end of the rows is also observable.

The exergy loss maps of Fig. 4(*b*) suggest similar trends of recirculation. At a height of 0.9 m (3 ft), some exergy loss is observed in the cold aisles due to nonuniform temperature of the supply air exiting from the plenum. However, the magnitude of this exergy loss is small (less than 50 W) and does not significantly impact the temperature of the cold aisle. Further, the effects of mixing are clearly observable in the hot aisles, where exergy is destroyed due to outlet temperature gradients caused by nonuniform heat loading of the racks. At a height of 1.5 m (5 ft), the supply air through the vent tiles is well mixed and therefore devoid of significant temperature gradients. As a result, almost no exergy loss is noticed in the cold aisle. The effects of recirculation are clearly evident at a height of 2.1 m (7 ft), where mixing in the cold aisle is noticeable in the middle of the Rows A and B. This corresponds to the observations from Fig. 4(*a*), where higher rack inlet temperatures were noticed in these locations. Lastly, at a height of 2.7 m (9 ft), it is interesting to note that the exergy loss is actually quite low even though the temperatures are high. This is because most of the high-temperature air in the hot aisles is removed through the ceiling vents, and although the temperatures in the cold aisle may be higher, there is not much mixing taking place at these locations. Some effects of recirculation are evident around the end of the rows, which is the cause of the higher temperatures observed in these locations in Fig. 3(*a*).

Thus, there is good qualitative agreement between the temperature-based and exergy-based predictions of recirculation

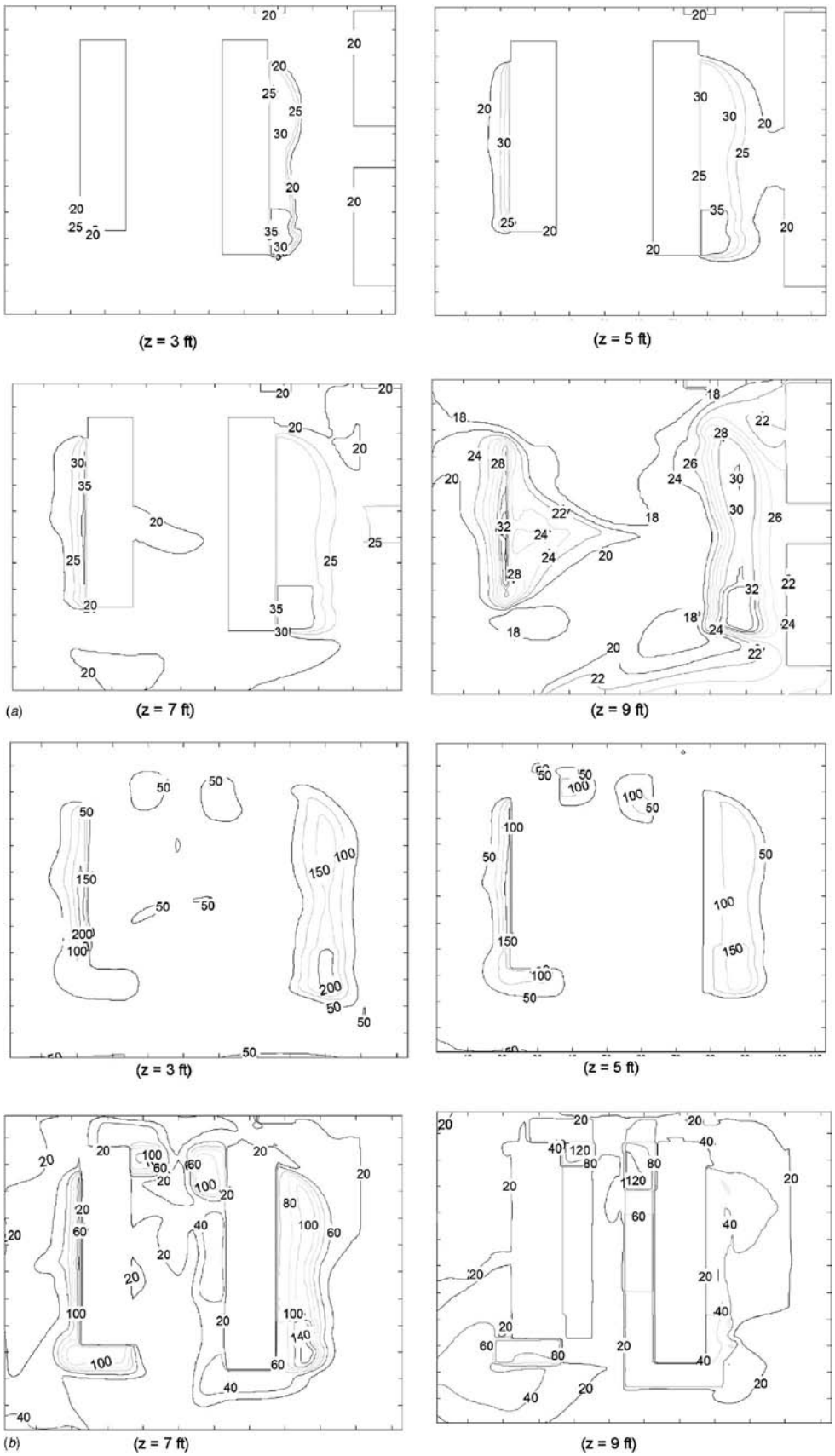


**Fig. 3 Results from numerical model (top view). Each map is a top view of the data center airspace at heights of 0.9 m (3 ft), 1.5 m (5 ft), 2.1 m (7 ft), 2.7 m (9 ft). (*a*) Temperature predictions (in °C) from model, and (*b*) map of exergy loss (in W) throughout data center. The locations of exergy destruction correspond well to hotspots or areas of recirculation estimated from the temperature map.**

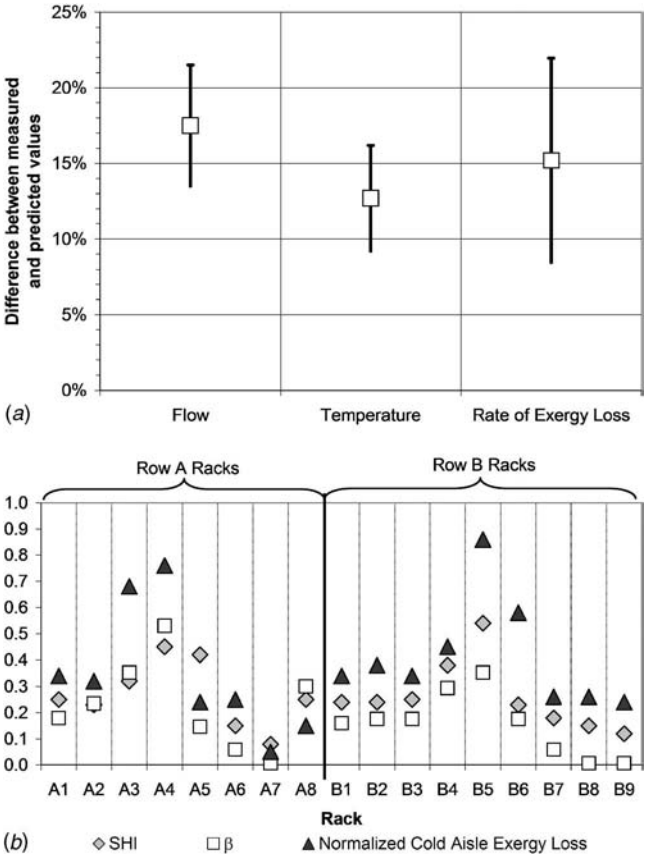


**Fig. 4 Experimental validation of model. (*a*) Comparison of predicted and measured values. (*b*) Comparison of rack-level estimates given by different metrics.**

patterns from the numerical model. The exergy-based predictions of recirculation agree with the temperature-based assessments, although the exergy loss model fuses information regarding flow and temperature into a single map to provide insight regarding the locations of mixing. To verify the numerical accuracy of these qualitative assessments, the predictions from the model were compared against actual measurements in the data center. The next section discusses this validation in further detail.

**Experimental Validation.** The exergy-based data center model discussed above essentially performs three computational operations in sequential order:

- flow approximation (based on conservation of mass and momentum)
- temperature estimation (based on energy balances)
- determination of system exergy loss (using Eq. (8), based on flow and temperature maps)

Thus, to estimate the accuracy of the exergy-based model, it is necessary to first verify the variability of the flow and temperature inputs provided to the exergy model. The error introduced during the exergy loss calculations can then be estimated through standard statistical analysis [51].

The input flow conditions through the vent tiles were measured using a flow hood (estimated to be accurate to within 5% of actual values). Measurements were also made with a handheld anemometer, empirically estimated to be within 20% of calibrated values, at several locations in the room. Handheld thermometers and type-K thermocouples (accurate to within $\pm 0.1^\circ$C per manufacturer specifications) are used to obtain temperature readings at the data collection points. The points of data collection were chosen to allow for assessment of model performance at different key locations of the system, including rack inlet, rack outlet, CRAC return, and potential hotspots in the hot aisles. Additional measurements were also made in the cold aisles to assist in the identification of locations of recirculation or short circuiting suggested by the model, yielding a total of 34 flow measurements and 102 temperature measurements throughout the data center.

Figure 4(*a*) shows a summary comparison of actual measurements and predicted values from the model. The mean difference between predicted and measured flow data is 18%, while the mean difference for temperature data is 13%. This is considered an acceptable level of accuracy for a first approximation. If further accuracy is desired, then finer meshes or more accurate flow modeling techniques should be considered.

Because exergy loss is calculated in the model based on system temperature and flow values, and since both of these quantities have already been validated, it is expected that predictions for exergy loss will also be within the same limits of accuracy. Nonetheless, to obtain a quantitative estimate of model accuracy with regard to prediction of exergy destruction, an indirect estimate of the actual exergy destruction in the physical airspace was obtained from the following equation:

$$\dot{\Psi}_{d_{\text{airspace}}} = \dot{\Psi}_{d^{\text{air}}_{\text{aisles}}} + \dot{\Psi}_{d^{\text{air}}_{\text{CRAC}}} + \dot{\Psi}_{d^{\text{air}}_{\text{racks}}} = \dot{\Psi}_{\text{sup}} - \dot{\Psi}_{\text{rec}} \tag{9}$$

The logic implicit to the expression of Eq. (9) is that any difference between the exergy supplied to the data center and the exergy recoverable from the data center must be due to the destruction of exergy in the air going through the data center (i.e., if no exergy were destroyed, then in the absence of useful work, all of the exergy supplied should be recoverable). This exergy loss has been assumed to arise from three major sources:

- *The exergy loss for the air in the hot and cold aisles.* For simplicity of nomenclature, it is assumed that the space above the rack units is part of the hot aisle, while any space between two rows of rack units comprises a cold aisle. This exergy loss is mostly due to mixing and cannot be measured directly in the data center.
- *The exergy loss as the air flows through the rack units*, which can be estimated based on a caloric heat balance across the rack using rack power measurements and inlet-outlet temperature/flow measurements.
- *The exergy loss as the air is refrigerated in the CRAC units*, which can be measured based on the fan speed and coefficient of performance (COP) of the CRAC unit.

All the known quantities can be substituted into Eq. (9), and an experimental estimate of the exergy loss for the airflow through the hot and cold aisles can then be obtained (this is the term predicted by the model of Eqs. (4)–(8), which needs to be experimentally verified). It should be noted that small errors in the exergy loss computed using Eq. (9) is to be expected, since some phenomena (such as exergy loss due to heat escape through walls or air leaks) will not be accounted for. However, the magnitude of these losses will be small, and as shown in Fig. 4(*a*), the estimated values based on measurements compare quite well to those predicted by the model. The uncertainty in estimating the difference between predicted and actual exergy loss values stems mostly from the uncertainty in temperature and flow measurements as well as the inaccuracy of flow and temperature predictions discussed earlier. Predictions of airspace exergy loss with higher accuracy would require the development of more accurate models for predicting temperature and flow.

The above validation is essentially a confirmation of the accuracy of the numerical values calculated by the model. It would also be desirable to obtain some type of validation regarding the viability of using airspace exergy loss as a metric to estimate recirculation effects in the data center. The existing state of the art utilizes the metrics of SHI (Eq. (1)) and $\beta$ (Eq. (3)) to measure recirculation. Both of these are temperature-based measures of the

infiltration of warm air into the cold aisle, and thus only represent thermal effects of mixing in the cold aisle (while the airspace exergy loss calculated in Eq. (4) includes thermal and fluidic mixing in both the hot and cold aisles). Therefore, to ensure a valid comparison, the exergy loss model was rerun for the data center of Fig. 2, and the total cold aisle thermal exergy loss was determined. To normalize these values, the exergy loss estimate was divided by the exergy supplied to the cold aisle (per Eq. (5)), assuming the ground state to be the external ambient. This normalized expression of exergy loss is scaled so that a value of 0 corresponds to no recirculation while a value of 1 would be a case where all the warm air from the hot aisle gets recirculated to the cold aisle. This exergy-based estimate of recirculation is then compared to rack-level averages of SHI and $\beta$ obtained by temperature measurements in the actual data center. Figure 4(*b*) summarizes the results of this evaluation. Although the magnitude of each metric on the normalized scale differs—which is to be expected, because each metric is defined differently—the trends of recirculation predicted by all the metrics are very similar. The highest SHI and $\beta$ values, which represent those racks with the highest inlet temperatures, also correspond to the racks with the highest exergy loss. Additionally, the exergy-based metric is more sensitive to recirculation than the temperature-based metrics.

To summarize, for the sample data center shown in Fig. 2, it has been shown that

- Recirculation trends suggested by temperature maps (Fig. 3(*a*)) or exergy loss maps (Fig. 3(*b*)) are qualitatively similar.
- Numerical error between estimated and predicted values are comparable for temperature and exergy loss (Fig. 4(*a*)).
- Quantitative estimates of recirculation from the exergy-based metrics agree with other temperature-based metrics (Fig. 4(*b*)).

These observations confirm that an exergy-based approach can provide, at a minimum, the same type of information regarding data center thermal manageability as the more traditional temperature-based metrics. The next section explores what information regarding data center energy efficiency is obtainable from the exergy analysis.

## Beyond the Data Center Airspace

To illustrate the need for considering energy efficiency beyond thermal manageability, consider a hypothetical data center environment where there is no recirculation. This has been achieved by rearranging appropriate vent tiles and overprovisioning the CRAC units to provide three times more cooling. While this data center might have excellent thermal manageability, the approach is hardly energy or cost efficient, owing to the large amount of electricity being supplied to the CRAC units. In such a configuration, although no thermal exergy is being destroyed in the airspace, large amounts of exergy would be destroyed in the CRAC units, because much electrical work is available in the air conditioners but not being used. A data center-level estimate of exergy loss, which includes the CRAC units could highlight such an occurrence. Similarly, recirculation-only estimates fail to give credit to data centers utilizing energy-efficient computer systems, which may have the same temperature gradients from hot aisle to cold aisle but consume less overall power per unit computation. Once again, a data center-level estimate of exergy loss, which includes the rack units, could compensate for such a scenario. Therefore, to evaluate the overall data center energy efficiency, the total exergy loss can be calculated as follows:

$$\dot{\Psi}_d = \dot{\Psi}_{d_{\text{racks}}} + \dot{\Psi}_{d_{\text{CRAC}}} + \dot{\Psi}_{d_{\text{airspace}}} \tag{10}$$

A discussion of how each of these terms can be evaluated follows.

**Airspace Exergy Loss.** The airspace exergy loss can be estimated using the finite volume model described earlier in this paper, or experimentally as discussed subsequent to Eq. (9). Note that for accounting purposes, the exergy loss in the airflow through the CRAC and rack units has been included in the airspace exergy loss rather than the component exergy loss terms.

**Computer-Room Air-Conditioning Unit Exergy Loss.** The CRAC units can be modeled as simple air-conditioning units, for which a basic second-law analysis yields the following exergy loss:

$$\dot{\Psi}_{d_{\text{CRAC}}} = \dot{m}_{\text{CRAC}}(\psi_{\text{ret}} - \psi_{\text{sup}}) - \dot{W}_{\text{CRAC}} \tag{11}$$

**Rack Unit Exergy Loss.** The only remaining challenge then is to estimate the exergy loss in the rack units. For simplicity, these are treated as a single computer unit dissipating heat at a uniform temperature. This assumption will be valid if

(i) All the servers in the rack are homogeneous. For racks with nonhomogeneous servers, the exergy loss occurring local to each server must be considered individually, and the total exergy loss of the rack can then be calculated as the sum of the exergy losses in these individual servers.
(ii) The load in the rack is uniformly distributed across the servers. For nonuniform loading, the effects of turbulence and buoyancy inside the rack can be significant. For example, Rolander et al. [52] show how an optimal arrangement of servers inside a rack can allow 50% higher loads compared to an arbitrary suboptimal configuration meeting the same thermal management criteria, while Rambo and Joshi [53] show how different server arrangements inside a single rack will lead to different thermal characteristics inside the cabinet. Inclusion of such considerations in the exergy model for racks could be achieved by approximating the entropy generation rate related to the airflow through the cabinet. After adding this to the entropy generated due to dissipation of heat in the cabinet, the Guoy–Stodola theorem could be invoked to predict the total rack exergy loss. For additional details, Bejan [44] elucidates how entropy generation and exergy loss are correlated.
(iii) The thermofluidic operating conditions (processor temperature, air flow rate etc.) internal to each server are the same. This assumption will be valid if all the servers have the same package-level thermal solution, which is likely to be the case for a homogeneously loaded rack per (i) and (ii) above.

Subject to the above assumptions, the rack can be assumed to behave like a single heat-dissipating component in a larger compute infrastructure. Then, as shown by Carey and Shah [43], the predominant exergy loss within the rack units will occur due to the conversion of high-quality electrical energy to low-quality thermal energy. Assuming that the electrical energy is entirely available for useful work, and that the heat dissipation equals the amount of electricity to the package, the exergy loss of the racks can be calculated as [43]

$$\dot{\Psi}_{d_{\text{racks}}} = \dot{W}_{\text{elec}} - \left(1 - \frac{T_0}{T_P}\right)\dot{Q} \approx \left(\frac{T_0}{T_P}\right)\dot{Q} \tag{12}$$

where $T_P$ is the temperature at which the heat is dissipated, in this case assumed to be the processor temperature. To be precise, the heat is actually transferred to the airflow after it has been dissipated through the package-level thermal solution. Shah et al. [54] have presented such a package-level exergy loss model, which takes into account the heat spreader, thermal interface material, and heat sink. At the data center level, however, the added exergy loss caused by the package-level thermal solution will be small (less than 1%), and is therefore neglected.

Equation (12) is a simplified version of the exergy loss in the

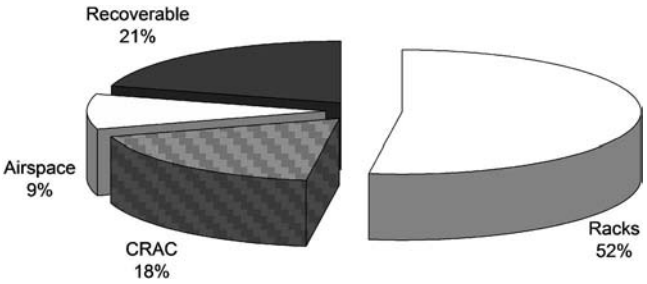


**Fig. 5 Exergy-based assessment of the entire data center. The majority of exergy loss occurs in the rack and CRAC units, although significant amount of exergy is also lost in the airspace. Nearly 21% of the supplied exergy is vented to the exhaust.**

rack units for the idealized case characterized by the assumptions (i)–(iii) above. For this example, a constant processor temperature of 85 °C was assumed in all the racks. If desired, subrack thermal models could be incorporated into the data center numerical model for a more accurate temperature estimate.

Having defined the exergy loss in the individual components, Eqs. (10)–(12) can be combined to evaluate the total exergy loss in the data center. Figure 5 shows the results for the sample data center analyzed earlier. The maximum exergy loss occurs in the rack units, owing to the irreversibility of converting electricity to heat. Exergy loss in the CRAC units mostly stems from the pressure drop and heat removal as the air flows from the return to supply vents. The airspace exergy loss is mostly due to recirculation and flow irreversibilities.

The insights from Fig. 5 are somewhat novel in terms of data center energy efficiency. First, the airspace—which has been such a focus of recent research—is the smallest source of inefficiency, although it is also the easiest to address (and arguably the one which can be most influenced by the data center operator after the remaining equipment has been installed). Second, there is scope for improvement in all the thermal management components of the data center, from the racks to the CRAC units, although the greatest long-term gain would arise from a type of disruptive improvement in rack power handling. Lastly, and perhaps most importantly, nearly 21% of the exergy being supplied is simply being vented through the exhaust. While practically reusing this energy in a cost-feasible manner may be challenging, the theoretical potential is interesting to notice.

For example, even if energy reuse is not possible, the above analysis suggests that additional equipment with an exergy consumption of 21% can theoretically be installed in the data center simply by optimizing of the existing thermal architecture. This additional exergy could be installed, as an example, in terms of additional compute power or redundant CRAC capacity. It should be noted that because the majority of the exergy supplied to the racks would be destroyed during conversion of electricity to heat, the actual compute capacity corresponding to this exergy supply would be lower, i.e., the above observation does not imply that it would be possible to obtain 21% additional compute capacity, but rather that the compute capacity for the given thermal architecture could be increased by a factor of $(0.21)(\eta_{\text{II}_{\text{racks}}})$. For the example data center analyzed above, this corresponds to roughly 2.8 kW of additional compute capacity, which could be installed without needing extra cooling capacity. It should be noted that the recirculation patterns of the system would likely change upon installation of the additional compute capacity, and a corresponding increase in airspace exergy loss may therefore offset some of the 2.8 kW availability. Additionally, a higher amount of recirculation may change the thermal manageability of the system. Therefore, a full thermal assessment—or equivalently, an assessment of the cold aisle exergy loss corresponding to the higher rack power—should be repeated to confirm the viability of installing this additional compute power in the data center. Nonetheless, the exergy analysis presented above provides an upper bound against which the appropriate thermal management criteria can be evaluated.

## Conclusions

This paper has demonstrated the viability of using exergy-based metrics for the concurrent assessment of the thermal manageability and energy efficiency of data centers. The conceptual approach was outlined from a second-law perspective, and a finite-volume computational model to predict data center exergy loss was demonstrated. Flow and temperature measurements from an actual data center were used to validate the numerical predictions of the model, and the viability of using exergy loss to predict recirculation patterns in data centers was verified by comparing rack-level estimates with existing metrics such as the SHI and $\beta$. Finally, the exergy loss of the airspace obtained from the model was combined with exergy loss predictions of the CRAC and rack units to obtain a net prediction of total data center exergy loss. Insights into the relative energy efficiencies of the different data center components were obtained from this analysis, which suggested the potential to install additional compute capacity without necessarily needing to increase the data center cooling capacity.

Thus, by considering the exergy loss among the different data center thermal management components (viz., cold aisle airspace, hot aisle airspace, CRAC units, and rack units), this paper has provided a metric to simultaneously evaluate the thermal manageability, energy efficiency, and potential for energy scavenging of the data center. The cold aisle exergy loss is a suitable metric for evaluating the temperature rise of rack inlet temperatures due to recirculation, while the net data center exergy loss provides a measure of energy efficiency across the data center thermal infrastructure. Building upon this foundation, future work will focus on investigating the optimal compromise between thermal manageability and energy efficiency considerations in the data center.

## Acknowledgment

The work presented in this paper was supported by a gift from the Hewlett Packard Company through the Center for Information Technology Research in the Interest of Society (CITRIS) at the University of California.

## Nomenclature

- cfm = cubic feet per minute
- $C_p$ = specific heat at constant pressure (J/kg K)
- $g$ = acceleration due to gravity ($m/s^2$)
- $h$ = specific enthalpy (J/kg)
- $\dot{m}$ = mass flow rate (kg/s)
- $N$ = total number of cells in finite-volume mesh
- $P$ = pressure ($N/m^2$)
- $\dot{Q}$ = rate of heat transfer (W)
- RHI = return heat index (Eq. (2)), nondimensional measure of recirculation proposed by Sharma et al. [27]
- $s$ = specific entropy (J/kg K)
- SHI = supply heat index (Eq. (1)), nondimensional measure of recirculation proposed by Sharma et al. [27]
- $T$ = absolute temperature (K)
- $V$ = velocity (m/s)
- $V$ = volume ($m^3$)
- $\dot{W}$ = power (W)
- $z$ = height (m)
- $\beta$ = nondimensional measure of recirculation (Eq. (3)), proposed by Schmidt et al. [29]
- $\eta_{\text{II}}$ = second-law thermodynamic efficiency
- $\Psi$ = exergy, available energy (J)

$\dot{\Psi}$ = rate of exergy transfer (W)

$\dot{\Psi}_d$ = rate of exergy destruction (W)

**Subscripts**

0 = ground state

air = related to air flow through the data center or the equipment

airspace = related to the airspace of the data center

aisles = related to the hot or cold aisles of the data center

CRAC = related to computer room air-conditioning unit

CV = control volume

elec = electrical

in, *i* = inlet

out, *o* = outlet

*P* = processor

racks = related to computer racks

rec = recoverable

ret = return

sup = supply

## References


[1] Patel, C. D., Bash, C. E., Sharma, R., Beitelmal, A., and Malone, C. G., 2005, "Smart Chip, System and Data Center Enabled by Advanced Flexible Cooling Resources," *Proceedings of the IEEE Semiconductor Thermal Management and Measurement Symposium (SEMITHERM)*, San Jose, CA.

[2] Patel, C. D., Sharma, R. K., Bash, C. E., and Beitelmal, A., 2002, "Thermal Considerations in Cooling Large Scale High Computer Density Data Centers," *Proceedings of the Eighth Intersociety Conference on Thermal and Thermomechanical Phenomena in Electronic Systems (ITHERM)*, San Diego, CA.

[3] Patel, C. D., and Shah, A. J., 2005, "Cost Model for Planning, Development and Operation of a Data Center," Hewlett Packard Laboratories, Palo Alto, CA, Technical Report No. HPL-2005-107R1.

[4] Sullivan, R. F., 2003, "Alternating Cold and Hot Aisles Provides More Reliable Cooling for Server Farms," White Paper by The Uptime Institute, Santa Fe, NM.

[5] American Power Conversion, 2003, "Avoidable Mistakes that Compromise Cooling Performance in Data Centers and Network Rooms," White Paper 49 by American Power Conversion, Washington, DC.

[6] ASHRAE, 2004, *Thermal Guidelines for Data Processing Environments*, Atlanta, GA.

[7] Shrivastava, S., Sammakia, B., Schmidt, R., and Iyengar, M., 2005, "Comparative Analysis of Different Data Center Airflow Management Configurations," *Proceedings of the ASME International Electronic Packaging Technical Conference and Exhibition (InterPACK)*, San Francisco, CA, Paper No. IPACK2005-73234.

[8] Iyengar, M., Schmidt, R., Sharma, A., McVicker, G., Shrivastava, S., Sri-Jayantha, S., Amemiya, Y., Dang, H., Chainer, T., and Sammakia, B., 2005, "Thermal Characterization of Non-Raised Floor Air Cooled Data Centers Using Numerical Modeling," *Proceedings of the Pacific Rim/ASME International Electronic Packaging Technical Conference and Exhibition (InterPACK)*, San Francisco, CA, Paper No. IPACK2005-73387.

[9] Wang, D., 2004, "A Passive Solution to a Difficult Data Center Problem," *Proceedings of the Intersociety Conference on Thermal and Thermomechanical Phenomena (ITHERM)*, San Diego, CA, pp. 586–592.

[10] Heydari, A., and Sabounchi, P., 2004, "Refrigeration Assisted Spot Cooling of a High Heat Density Data Center," *Proceedings of the Intersociety Conference on Thermal and Thermomechanical Phenomena (ITHERM)*, San Diego, CA, pp. 601–606.

[11] Schmidt, R., Chu, R., Ellsworth, M., Iyengar, M., Porter, D., Kamath, V., and Lehmann, B., 2005, "Maintaining Datacom Rack Inlet Air Temperatures With Water Cooled Heat Exchangers," *Proceedings of the ASME International Electronic Packaging Technical Conference and Exhibition (InterPACK)*, San Francisco, CA.

[12] Kang, S., Schmidt, R. R., Kelkar, K. M., Radmehr, A., and Patankar, S. V., 2000, "A Methodology for the Design of Perforated Tiles in a Raised Floor Data Center Using Computational Flow Analysis," *Proceedings of the Eighth Intersociety Conference on Thermal and Thermomechanical Phenomena in Electronic Systems (ITHERM)*, Las Vegas, NV.

[13] Patel, C. D., Bash, C. E., Belady, C., Stahl, L., and Sullivan, D., 2001, "Computational Fluid Dynamics Modeling of High Compute Density Data Centers to Assure System Inlet Air Specifications," *Proceedings of the Pacific Rim/ASME International Electronic Packaging Technical Conference and Exhibition (InterPACK)*, Kauai, HI.

[14] Schmidt, R., 2001, "Effect of Data Center Characteristics on Data Processing Equipment Inlet Temperatures," *Proceedings of the Pacific Rim/ASME International Electronic Packaging Technical Conference and Exhibition (InterPACK)*, Kauai, HI, Paper No. IPACK2001-15870.

[15] VanGilder, J. W., and Lee, T., 2003, "A Hybrid Flow Network-CFD Method for Achieving Any Desired Flow Partitioning Through Floor Tiles of a Raised-Floor Data Center," *Proceedings of the International Electronic Packaging Technical Conference and Exhibition (InterPACK)*, Maui, HI, Paper No. IPACK2003-35171.

[16] Schmidt, R., Karki, K., and Patankar, S., 2004, "Raised-Floor Data Center: Perforated Tile Flow Rates for Various Tile Layouts," *Proceedings of the Ninth Intersociety Conference on Thermal and Thermomechanical Phenomena in Electronic Systems (ITHERM)*, Las Vegas, NV.

[17] Karki, K. C., Radmehr, A., and Patankar, S. V., 2003, "Use of Computational Fluid Dynamics for Calculating Flow Rates Through Perforated Tiles in Raised-Floor Data Centers," HVAC&R Res., **9**(2), pp. 153–166.

[18] Karki, K. C., Patankar, S. V., and Radmehr, A., 2003, "Techniques for Controlling Airflow Distribution in Raised Floor Data Centers," *Proceedings of the Pacific Rim/ASME International Electronic Packaging Technical Conference and Exhibition (InterPACK)*, Maui, HI, Paper No. IPACK2003-35282.

[19] VanGilder, J. W., and Schmidt, R. R., 2005, "Airflow Uniformity Through Perforated Tiles in a Raised Floor Data Center," *Proceedings of the Pacific Rim/ASME International Electronic Packaging Technical Conference and Exhibition (InterPACK)*, San Francisco, CA, Paper No. IPACK2005-73375.

[20] Radmehr, A., Schmidt, R. R., Karki, K. C., and Patankar, S. V., 2005, "Distributed Leakage Flow in Raised Floor Data Centers," *Proceedings of the Pacific Rim/ASME International Electronic Packaging Technical Conference and Exhibition (InterPACK)*, San Francisco, CA, Paper No. IPACK2005-73273.

[21] Rambo, J. D., and Joshi, Y. K., 2004, "Supply Air Distribution From a Single Air Handling Unit in a Raised Floor Plenum Data Center," *Proceedings of the Joint Indian Society of Heat and Mass Transfer/American Society of Mechanical Engineers Heat and Mass Transfer Conference (ISHMT/ASME)*, Kalpakkam, India.

[22] Sharma, R. K., Bash, C. E., Patel, C. D., Friedrich, R. J., and Chase, J. S., 2003, "Balance of Power: Dynamic Thermal Management of Internet Data Centers," Hewlett Packard Laboratories, Palo Alto CA, Technical Report No. HPL-2003-5.

[23] Bhopte, S., Agonafer, D., Schmidt, R., and Sammakia, B., 2005, "Optimization of Data Center Room Layout to Minimize Rack Inlet Air Temperature," *Proceedings of the Pacific Rim/ASME International Electronic Packaging Technical Conference and Exhibition (InterPACK)*, San Francisco, CA, Paper No. IPACK2005-73027.

[24] Schmidt, R., and Iyengar, M., 2005, "Effect of Data Center Layout on Rack Inlet Air Temperatures," *Proceedings of the Pacific Rim/ASME International Electronic Packaging Technical Conference and Exhibition (InterPACK)*, San Francisco, CA, Paper No. IPACK2005-73385.

[25] Schmidt, R., and Cruz, E., 2002, "Raised Floor Computer Data Center: Effect on Rack Inlet Temperatures of Chilled Air Exiting Both the Hot and Cold Aisles," *Proceedings of the Intersociety Conference on Thermal and Thermomechanical Phenomena (ITHERM)*, San Diego, CA, pp. 580–594.

[26] Schmidt, R., and Cruz, E., 2002, "Raised Floor Computer Data Center: Effect on Rack Inlet Temperatures When High Powered Racks are Situated Amongst Lower Powered Racks," *Proceedings of the ASME International Mechanical Engineering Congress and Exposition (IMECE)*, New Orleans, LA.

[27] Schmidt, R., and Cruz, E., 2003, "Cluster of High Powered Racks Within a Raised Floor Computer Data Center: Effect of Perforated Tile Flow Distribution on Rack Inlet Air Temperatures," *Proceedings of the ASME International Mechanical Engineering Congress and Exposition (IMECE)*, Washington, DC, pp. 245–262.

[28] Schmidt, R., and Cruz, E., 2003, "Raised Floor Computer Data Center: Effect on Rack Inlet Temperatures when Adjacent Racks are Removed," *Proceedings of the Pacific Rim/ASME International Electronic Packaging Technical Conference and Exhibition (InterPACK)*, Maui, HI.

[29] Bash, C. E., Patel, C., and Sharma, R. K., 2003, "Efficient Thermal Management of Data Centers—Immediate and Long-Term Research Needs," HVAC&R Res., **9**(2), pp. 137–152.

[30] Sharma, R. K., Bash, C. E., and Patel, C. D., 2002, "Dimensionless Parameters for Evaluation of Thermal Design and Performance of Large-Scale Data Centers," *Proceedings of The Eighth ASME/AIAA Joint Thermophysics and Heat Transfer Conference*, St Louis, MO.

[31] Sharma, R. K., and Bash, C. E., 2002, "Dimensionless Parameters for Energy-Efficient Data Center Design," *Proceedings of the IMAPS Advanced Technology Workshop on Thermal Management (THERM ATW)*, Palo Alto, CA.

[32] Schmidt, R. R., Cruz, E. E., and Iyengar, M. K., 2005, "Challenges of Data Center Thermal Management," IBM J. Res. Dev., **49**(4/5), pp. 709–723.

[33] Schmidt, R., Iyengar, M., and Chu, R., 2005, "Meeting Data Center Temperature Requirements," ASHRAE J., **47**(4), pp. 44–49.

[34] Herrlin, M. K., 2005, "Rack Cooling Effectiveness in Data Centers and Telecom Central Offices: The Rack Cooling Index (RCI)," ASHRAE Trans., **111**(2), pp. 725–731.

[35] Aebischer, B., Eubank, H., and Tschudi, W., 2004, "Energy Efficiency Indicators for Data Centers," *International Conference on Improving Energy Efficiency in Commercial Buildings*, Frankfurt, Germany.

[36] Norota, M., Hayama, H., Enai, M., and Kishita, M., 2003, "Research on Efficiency of Air Conditioning System for Data Center," *Proceedings of the IEEE International Telecommunications Energy Conference (INTELEC)*, Yokohama, Japan, pp. 147–151.

[37] Mitchell-Jackson, J., Koomey, J. G., Nordman, B., and Blazek, M., 2001, "Data Center Power Requirements: Measurements From Silicon Valley," Energy-The International Journal, **28**(8), pp. 837–850.

[38] Bejan, A., 1997, *Advanced Engineering Thermodynamics*, 2nd ed., Wiley, New York.

[39] Çengel, Y. A., and Boles, M. A., 2001, *Thermodynamics: An Engineering Approach*, 4th ed., McGraw-Hill, Hightstown, NJ.
[40] Moran, M. J., 1982, *Availability Analysis: A Guide to Efficient Energy Use*, Prentice-Hall Inc., Englewood Cliffs, NJ.
[41] Szargut, J., Morris, D. R., and Steward, F. R., 1988, *Exergy Analysis of Thermal, Chemical and Metallurgical Processes*, Hemisphere, New York.
[42] Creyts, J. C., Carey, V. P., 1999, "Use of Extended Exergy Analysis to Evaluate the Environmental Performance of Machining Processes," Proc. Inst. Mech. Eng., Part E: J. Process Mech. Eng., **213**(4), pp. 247–264.
[43] Carey, V. P., and Shah, A. J., 2006, "The Exergy Cost of Information Processing—A Comparison of Computer-Based Technologies and Biological Systems," ASME J. Electron. Packag., **128**(4), pp. 346–352.
[44] Bejan, A. D., 1996, *Entropy Generation Minimization*, Wiley, New York, pp. 104–109.
[45] Lin, W. W., and Lee, D. J., 2000, "Second Law Analysis on a Flat Plate-Fin Array Under Crossflow," Int. Commun. Heat Mass Transfer, **27**(2), pp. 179–190.
[46] Culham, J. R., and Muzychka, Y. S., 2001, "Optimization of Plate Fin Heat Sinks Using Entropy Generation Minimization," IEEE Trans. Compon. Packag. Technol., **24**, pp. 159–165.
[47] Ogiso, K., 2001, "Assessment of Overall Cooling Performance in Thermal Design of Electronics Based on Thermodynamics," ASME J. Heat Transfer, **123**(5), pp. 999–1005.
[48] Bar-Cohen, A., and Iyengar, M., 2003, "Least-Energy Optimization of Air-Cooled Heat Sinks for Sustainable Development," IEEE Trans. Compon. Packag. Technol., **26**(1), pp. 16–25.
[49] FLOVENT vx.1, Software by Flomerics Ltd., 81 Bridge Road, Hampton Court, Surrey KT8 9HH, England, available http://www.flomerics.com/flovent/
[50] Shah, A. J., 2005, "Exergy-Based Analysis of Computer Thermal Management Systems," Ph.D. thesis, University of California, Berkeley.
[51] Moffat, R. J., 1988, "Describing the Uncertainties in Experimental Results," Exp. Therm. Fluid Sci., **1**, pp. 3–7.
[52] Rolander, N., Rambo, J., Joshi, Y., and Mistree, Y., 2005, "Robust Design of Air Cooled Server Cabinets for Thermal Efficiency," *Proceedings of the ASME International Electronic Packaging Technical Conference and Exhibition (InterPACK)*, San Francisco, CA, Paper No. IPACK2005-73171.
[53] Rambo, J., and Joshi, Y., 2005, "Thermal Performance Metrics for Arranging Forced Air Cooled Servers in a Data Processing Cabinet," ASME J. Electron. Packag., **127**(4), pp. 452–459.
[54] Shah, A. J., Carey, V. P., Bash, C. E., and Patel, C. D., 2006, "An Exergy-Based Figure of Merit for Electronic Packages," ASME J. Electron. Packag., **128**(4), pp. 360–369.

# Direct Numerical Simulation of Condensing Stratified Flow

**Djamel Lakehal**
Institute of Energy Technology,
ETH Zurich, Switzerland;
ASCOMP GmbH,
Zurich, Switzerland
e-mail: lakehal@ascomp.ch

**Marco Fulgosi**
Institute of Energy Technology,
ETH Zurich, Switzerland

**George Yadigaroglu**
Institute of Energy Technology,
ETH Zurich, Switzerland;
ASCOMP GmbH,
Zurich, Switzerland

*The paper discusses the results of a detailed direct numerical simulation study of condensing stratified flow, involving a sheared steam-water interface under various thermal and turbulent conditions. The flow system comprises a superheated steam and subcooled water flowing in opposite directions. The transport equations for the two fluids are alternately solved in separate domains and then coupled at the interface by imposing mass, momentum, and energy jump conditions with phase change. The effects induced by changes in the interfacial shear were analyzed by comparing the relevant statistical flow properties. New scaling laws for the normalized heat transfer coefficient (HTC), $K^+$, have been derived for both the steam and liquid phases. The steam-side law is found to compare with the passive-scalar law obtained hitherto by (Lakehal et al.(2003, "Direct Numerical Simulation of Turbulent Heat Transfer Across a Mobile, Sheared Gas-Liquid Interfaces," ASME J. Heat Transfer, **125**, pp. 1129–1139) in that HTC scales with $Pr^{-3/5}$. A close inspection of the transfer rates on the liquid side reveals a consistent relationship between $K^+$, the local wave deformation or curvature and the interfacial shear stress. The surface divergence model of Banerjee et al. (2004, "Surface Divergence Models for Scalar Exchange Between Turbulent Streams," Int. J. Multiphase Flow, **30**(8), pp. 965–977) is found to apply in the liquid phase, too.* [DOI: 10.1115/1.2789723]

*Keywords: DNS, phase change, heat transfer, two-phase flow, direct contact condensation*

## 1 Introduction

Condensation heat transfer parametrization is central to the computer-aided analysis of many systems, including nuclear reactor safety systems, using system codes or detailed two- and three-dimensional Navier–Stokes solvers. The thermal-hydraulic coupling of the liquid and vapor phases has resulted in a large number of correlations, but with less success with regard to the underpinning physical mechanisms. The key point is to characterize the transport mechanisms in wall and fluid-fluid boundary layers in the presence of mass exchange. For decades, the problem has been approached by investigating the very close subject of suction/blowing boundary layers, which has indeed helped in the understanding of some aspects of condensation. However, the analogy with coupled steam-water interfacial flows such as the ones dealt with herein can be limited by the presence of the deformable interface as compared to rigid walls.

Turbulent boundary layers with mass suction and/or blowing have been thoroughly studied both experimentally [1–4] and numerically [5–7]. However, most of the studies were focused on situations involving a flat and rigid boundary where the injection/suction rate was constant, occurring either uniformly or locally. It has been shown that blowing from the wall induces an apparent decrease in the skin friction, i.e., wall shear stress, reducing in turn the heat transfer coefficient (HTC) while suction exerts the opposite effect. In particular, Sumitani and Kasagi [5] performed direct numerical simulation (DNS) of closed channel flow with suction on one wall and blowing on the opposite. The simulation was conducted with a fixed pressure gradient. At the suction side, they observed an increase in the friction coefficient due to mass suction and, at the same time, an attenuation of the turbulence intensities; the opposite occurred at the injection side. Jimenez et al. [7] carried out DNS of closed channel flow where one wall was impermeable. A suction effect was created at the other wall by imposing vertical velocity fluctuations at the wall proportional to the wall pressure fluctuations. In order to keep the mass flow rate constant, the driving pressure gradient was continuously adjusted. The authors reported an increase of 40% in the friction coefficient at the suction side. This was primarily due to the fact that in the presence of suction, by increasing the pressure gradient the wall shear stress also increased, although the bulk velocity did not change much. Compared to the impermeable wall, they observed a small reduction in the streamwise turbulence intensity on the suction side and a significant increase for the spanwise and wall-normal components.

Since experimental investigations of condensation heat transfer are hindered by the difficulties in measuring the quantities of interest, particularly when subjected to high transfer rates, approaching the problem through DNS "experiments" is a viable alternative, even for the reduced turbulence intensity and/or subcooling and superheating thermal flow conditions that one can tackle at time. It is in this context that the present work has been undertaken, aiming toward a better understanding of turbulent transport at sheared deformable interfaces in the presence of condensation. The primary goal is to establish a data basis for the mean statistical flow properties on both sides of the interface. This should help clarify the coupling mechanisms of the fluxes between the phases. The second main motivation is to use the data basis for the development of heat transfer models and compare these to experiments.

To achieve these new objectives, our DNS tool used previously to study turbulent transport at interfaces [8] and to parametrize passive-scalar transport [9,10] has been modified to incorporate the proper interfacial/boundary conditions accounting for phase change. The modifications are described in Sec. 3. The results are presented in Secs. 4 and 5, first concentrating on the scaling and correlation between the interfacial transfer and shear, then on the transfer parametrization.

## 2 Modeling and Simulation Strategies

The geometry configuration of the problem is the same as the one studied hitherto by Lakehal et al. [9]. The modified boundary

Contributed by the Heat Transfer Division of ASME for publication in the JOURNAL OF HEAT TRANSFER. Manuscript received February 14, 2007; final manuscript received July 24, 2007; published online February 6, 2008. Review conducted by Raj M. Manglik.

  

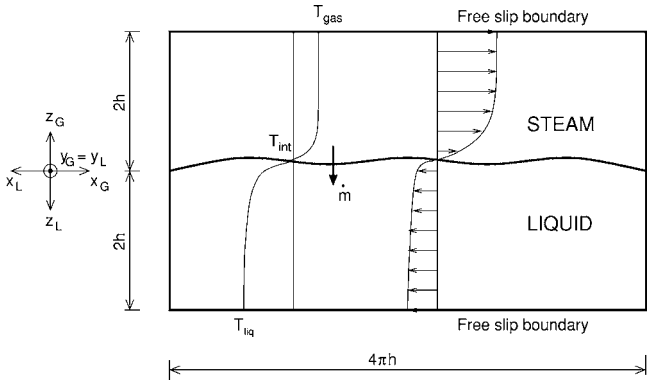


**Fig. 1 Sketch of the simulated vapor-liquid stratified flow**

conditions are now sketched in Fig. 1. The two phases flow countercurrently, separated by an interface free to deform in three dimensions. The flow domain is inclined by one degree in order to adjust for the pressure. What makes the present DNS different from suction/blowing boundary layer studies is the way the active mass transfer is handled. Experiments involving condensation heat transfer can be carried out in two ways: either by keeping the mass flow rates of the two phases constant or by keeping the pressure drop constant, and allowing the mass flow rates to vary. In the present work, the pressure gradients were kept constant, implying that the mass flow rates within the two computational domains are allowed to vary to satisfy the balance of forces. To satisfy the overall mass balance, the condensing mass flux at the interface is reinjected at the top of the vapor domain and removed from the bottom of the liquid domain.

**2.1 Transport Equations.** The steam and subcooled water phases (designated by the subscripts $G$ and $L$, respectively) are considered as Newtonian fluids, flowing in separate domains, and driven by an imposed constant mean pressure gradient. The reference quantities employed for normalization in each domain are the imposed shear velocity $u_\star=\sqrt{2h\Delta p/\rho}$, where $\Delta p$ is the initial pressure gradient driving the flow, the half-depth of each computational domain $h$, and the kinematic viscosity $\nu$. In contrast to the passive-scalar transfer problem of Lakehal et al. [9], and to the suction/blowing boundary layer problems evoked in the Introduction, this flow problem has two specific features to be taken into account in its setup and in the interpretation of the results. At the beginning of the simulation when the interface is flat, the viscous interfacial shear stress $\tau_{\text{int}}$ balances exactly the mean pressure gradient driving the flow, such that $u_\star$ is equal to the resulting shear velocity $u_\tau=\sqrt{\tau_{\text{int}}/\rho}$. As the interfacial waves start to form and develop, part of the energy is transferred into form drag, so that $u_\star<u_\tau$. The second important feature is the implication of the mass suction by condensation in the true and apparent interfacial shear unbalance: Condensation induces an extra shear at the interface acting in the opposite sense to $u_\star$.

The reference temperature $T_\star$ is defined as $T_\star=q_{\text{int}}/\rho c_p u_\star$, where $q_{\text{int}}$ represents the interfacial heat flux. The time is made nondimensional using $\nu/u_\star^2$, and the length scales are normalized using $u_\star/\nu$. In each computational domain, the shear Reynolds number is defined as $\text{Re}_\star=u_\star 2h/\nu$.

The normalized Navier–Stokes and energy equations governing the flow in each domain take the same form as in Ref. [9], but with modified interfacial and outer boundary conditions as explained in the next section. The velocity $\mathbf{u}^+$ is normalized by $u_\star$, the dynamic pressure $p^+$ is normalized by $\rho u_\star^2$, and the temperature is defined as $T^+=(T-T_{\text{int}})/T_\star$. The conventional notation $\mathbf{u}^+(x,y,z,t)=\mathbf{U}^+(z)+u^+(x,y,z,t)$ is adopted to decompose the velocity and temperature fields into mean and fluctuating (turbulent) components.

**2.2 Boundary Conditions.** In the presence of phase change due to condensation, the interfacial and boundary conditions need to account for the mass exchange between the two phases. The thermal-hydraulic coupling between the vapor and liquid becomes more complicated, and the interfacial continuity conditions should include extra terms in the transfer direction. These terms involve the condensation rate, i.e., the interfacial mass flux, which is here determined by solving the interfacial energy continuity conditions. The interfacial jump conditions do not constitute a closed system of equations because they should be supplemented by interfacial constitutive laws, which specify the kinematic, dynamic, and thermal coupling between the two phases.

Using the reference quantities introduced previously, the interfacial jump conditions introduced in Ref. [9] should be recast in a nondimensional form as (note that for simplicity, the overbars, subscripts $+$, and primes are dropped out)

$$\Gamma=\frac{\text{Ja}_L}{\text{Re}_\star\text{Pr}_L}\nabla T_{L,\text{int}}\cdot\mathbf{n}+\frac{1}{\mathcal{R}}\frac{\text{Ja}_G}{\text{Re}_\star\text{Pr}_G}\nabla T_{G,\text{int}}\cdot\mathbf{n}$$

$$\left(\mathbf{u}_G-\frac{1}{\mathcal{R}}\mathbf{u}_L\right)\cdot\mathbf{n}=\Gamma\frac{\mathcal{R}^2-1}{\mathcal{R}}$$

$$\left(\mathbf{u}_G-\frac{1}{\mathcal{R}}\mathbf{u}_L\right)\cdot\mathbf{t}_i=0\quad i=1,2$$

$$p_L-p_G+\frac{1}{\text{Fr}}f=\frac{1}{\text{Re}_\star}((\sigma_L-\sigma_G)\cdot\mathbf{n})\cdot\mathbf{n}-\frac{1}{\text{We}}\nabla\cdot\mathbf{n}+\Gamma^2(\mathcal{R}^2-1)$$

$$((\sigma_G-\sigma_L)\cdot\mathbf{n})\cdot\mathbf{t}_i=0\quad i=1,2$$

$$T_G=T_L=T_{\text{sat}} \tag{1}$$

where the first expression relates to the energy, the second and third expressions relate to the mass, and the fourth and fifth to the momentum. At the outer boundaries, the following conditions were imposed:

$$\frac{\partial u_k}{\partial z}=\frac{\partial v_k}{\partial z}=\frac{\partial T_k}{\partial z}=\frac{\partial p_k}{\partial z}=0;\quad k=G,L$$

$$w_G=-\mathcal{R}\Gamma\quad w_L=\Gamma \tag{2}$$

where $\Gamma$ is the nondimensional condensation rate, Ja is the Jakob number, a parameter that measures the rate of subcooling/superheating, We is the Weber number that accounts for the surface tension effect, and Fr is the Froude number that accounts for gravity. These nondimensional numbers are defined as

$$\Gamma=\frac{\dot m}{\rho_L u_{\star_L}}\quad \text{Ja}_G=\frac{c_{p_G}\Delta T_{\text{sup}}}{\mathcal{H}}\quad \text{Ja}_L=\frac{c_{p_L}\Delta T_{\text{sub}}}{\mathcal{H}}$$

$$\text{We}=\frac{\rho_L h u_{\star_L}^2}{\gamma}\quad \text{Fr}=\frac{\rho_L u_{\star_L}^2}{gh(\rho_L-\rho_G)}\quad \text{Re}_\star=\frac{u_{\star_G}2h}{\nu_G}=\frac{u_{\star_L}2h}{\nu_L}$$

### 2.3 Simulations

*2.3.1 Numerical Approach.* The governing equations are solved using a collocation pseudospectral technique employing Fourier series in the homogeneous, streamwise, and spanwise directions and Chebychev polynomials in the nonuniform direction normal to the interface. The physical domain is mapped into a rectangular parallelepiped at each time step. Mass, momentum, and energy equations are first solved separately in each domain, then coupled at the interface using Eqs. (1). The coupling at the interface is performed once the topology equation for the interface has been solved: $\partial F/\partial t+\mathbf{u}\cdot\nabla F=0$, where $F$ denotes the surface elevation above and below the zero level. Procedures for dealiasing the solutions based on the two-thirds rule apply in this context,

**Table 1 Matrix of runs performed**

| Case | $u_{\star_G}$ (m/s) | $h$ (m) | We ($10^{-4}$) | Fr ($10^{-5}$) | $\mathrm{Pr}_G$ | $\mathrm{Pr}_L$ | $\mathrm{Ja}_G$ | $\mathrm{Ja}_L$ | $\Delta T_{\mathrm{sub}_L}$ (K) |
|---|---|---|---|---|---|---|---|---|---|
| R1 | 0.0126 | 0.0250 | 2.20 | 1.90 | 0.95 | 1.15 | 0.020 | 0.000 | 0.12 |
| C11 | 0.0126 | 0.0250 | 2.20 | 1.90 | 0.95 | 1.15 | 0.020 | 0.010 | 10.00 |
| C12 | 0.0126 | 0.0250 | 2.20 | 1.90 | 0.95 | 1.17 | 0.020 | 0.020 | 20.00 |
| R2 | 0.0378 | 0.0080 | 6.60 | 5.13 | 0.95 | 1.17 | 0.020 | 0.000 | 0.13 |
| C21 | 0.0378 | 0.0080 | 6.60 | 5.13 | 0.95 | 1.15 | 0.020 | 0.010 | 10.00 |
| C22 | 0.0378 | 0.0080 | 6.60 | 5.13 | 0.95 | 1.17 | 0.020 | 0.020 | 20.00 |

too.

A modified version of the two-step fractional time splitting method of Temmam is employed [9]. The convective term is treated explicitly by reference to the Adams–Bashforth (AB) scheme. The viscous term is implicit and discretized using the Crank–Nicholson (CN) semi-implicit scheme. The time marching is second-order accurate in the computation of the intermediate velocity, the value of which is corrected in the next step by solving the Poisson equation for the pressure. The energy equation is also solved using a second-order accurate time differencing scheme, where the explicit convective term is discretized using the AB scheme, and the implicit diffusive term is discretized by use of the CN scheme.

As capillary waves do not produce significant domain distortions, the grid resolution for each domain was found to be appropriate to resolve the flows. The grids employed here are the same as those used in the previous work [9], for close-to-unity Prandlt numbers and same shear Reynolds number (171). As it was previously demonstrated in the context of the isothermal flow field simulation, the energy spectra of the three velocity components have shown no energy accumulation at high wave numbers, confirming that this resolution is sufficiently accurate for the solution of both the velocity and thermal fields. Doubling the grid resolution in the interface-normal direction did not affect the results.

*2.3.2 Simulation Setup*. The simulations have been performed using constant pressure gradients driving the two flows. Different choices for the reference velocity are possible: the shear velocity $u_\star$ based on the mean pressure gradient and the friction velocity $u_\tau$ based on the viscous stress at the interface. When the interface is flat and there is no mass exchange, $u_\tau = u_\star$. In the presence of waves, the mean pressure gradient based on $u_\star$ remains necessarily constant, while as a portion of the drag is absorbed by waves, the so-called "form drag," $u_\tau$, is reduced. This is further exacerbated when mass is exchanged between phases through condensation. In both cases, $u_\tau < u_\star$. To adjust to the pressure gradient, the computational domain is slightly tilted (by 1 deg).

The vapor and liquid phases consist of water vapor and liquid water, respectively. The interface is assumed to be at the saturation state corresponding to a pressure of 5 bars and a temperature of 425.15 K. The superheating in the vapor is kept constant ($\Delta T_{\mathrm{sup}} = 20$ K) for two different levels of subcooling in the liquid, namely, $\Delta T_{\mathrm{sub}_1} = 10$ K and $\Delta T_{\mathrm{sub}_2} = 20$ K. The vapor and water physical properties (density, viscosity, heat capacity, and thermal conductivity) have been evaluated at $T_G^0 = T_{\mathrm{sat}} + \Delta T_{\mathrm{sup}}$ for the vapor and at $T_L^0 = T_{\mathrm{sat}} - \Delta T_{\mathrm{sub}}$ for the water. The surface tension was evaluated at the saturation temperature. Since the variations in density due the variation of the subcooling are negligible, the simulations were performed with $\mathcal{R} = \sqrt{\rho_L/\rho_G} = 18.4$. The shear-based Reynolds number, $\mathrm{Re}_\star$ was set to 171 in both phases for all simulations.

For the purpose of the present study, it was decided to vary the interfacial shear by reducing the height of the computational domain, keeping the shear-based Reynolds number constant.

Each simulation can be characterized by specifying the following nondimensional numbers defined previously: $\mathrm{Re}_{\star_G} = \mathrm{Re}_{\star_L}$, $\mathrm{Pr}_G$, $\mathrm{Pr}_L$, $\mathrm{Ja}_G$, $\mathrm{Ja}_L$, We, Fr, and $\mathcal{R}$. To understand the effect of the waves on the condensation process, two sets of three different simulations have been performed. In the first set, which comprises the runs identified by R1, C11, and C12 in Table 1, the flow conditions are such that the interface separating the vapor and liquid phases is virtually flat. R1 is the reference case without condensation, whereas C11 and C21 indicate the cases with water subcooling of $\Delta T_{\mathrm{sub}_1} = 10$ K and $\Delta T_{\mathrm{sub}_2} = 20$ K, respectively. The same convention applies to the second set of simulations (identified by R2, C21, and C22 in Table 1), where the shear velocity is three times larger than that in the previous set, so that the interface is deformed by capillary waves.

It must be noticed that since the values of $\mathcal{R}$, We, and Fr for the condensing stratified flow are different from those employed to study turbulence at the sheared air-water interface [8], the reference cases R1 and R2 have been added to analyze the results consistently. In these reference cases, the subcooling of the water was small enough to preclude condensation.

The dimensions of the computational domains (in nondimensional space) and the grid resolution employed for the present simulations, for both the flow and the temperature fields, are equal to those of grid R1 employed for the passive heat transfer problem (i.e., $\Delta x^+ = 16.77$, $\Delta y^+ = 8.38$, $\Delta z^+ = 0.102 - 4.191$). The time step used is $0.024 u_\star^2/\nu$ nondimensional time units, and the databases are collected over a time interval of $5760 u_\star^2/\nu$ nondimensional time units (240,000 time steps), with a sampling frequency of $2.88 u_\star^2/\nu$ (one every 120 steps), so that 2000 flow fields are collected in each simulation, for each phase.

## 3 Heat Transfer Mechanisms

**3.1 Interface Coupling.** The nondimensional HTC in the two phases can be defined as

$$K^+ = \frac{q_{\mathrm{int}}}{\rho c_p \Delta \bar{T} u_\star} \quad \text{or} \quad K_\tau^+ = \frac{q_{\mathrm{int}}}{\rho c_p \Delta \bar{T} u_\tau}, \tag{4}$$

when the velocity scale used for the normalization is $u_\tau$. The difference between the interfacial liquid and vapor heat fluxes produces the rate of condensation, i.e., $\dot{m}\mathcal{H} = q_{\mathrm{int},L} - q_{\mathrm{int},G}$.

To proceed with the analysis, we first examine snapshots of the HTC patterns at the interface and compare these with the corresponding shear stress patterns. The same analysis has been performed for the passive-scalar transport DNS [9]. Here, attention is placed upon the shear-HTC relationship at the flat and wavy interfaces in the presence of condensation and for the cases C12 and C22. Before analyzing selected snapshots of the thermal flow field, it is worth discussing Fig. 2, where contours of the joint probability density function (jpdf) of the normalized interfacial stress and HTC (at all points of the interface) are plotted for both the vapor and the liquid phases, for case R2. Similar patterns for the jpdfs were observed for all the cases under investigation. These patterns clearly show that the shear-HTC coupling mechanisms in the two phases are different. On the vapor side, the contours of the jpdf are inclined by about 45 deg, meaning that the regions over the interface where the maximum heat transfer takes place coincide with those of maximum shear stress [9,10]. In the liquid, the jpdf presents a broader area, and with lower values

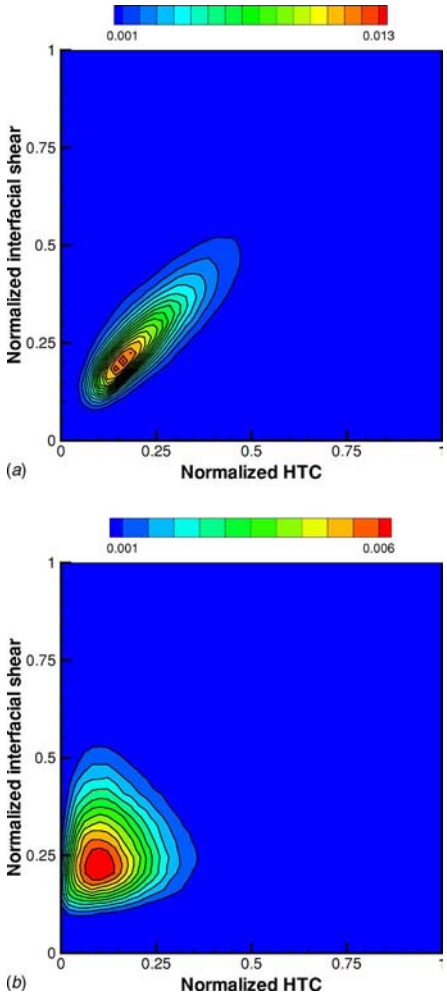


**Fig. 2 jpdf of normalized interfacial shear stress and HTC (Case R2)**

of the normalized HTC (i.e., <30%). By comparing both the vapor- and liquid-side jpdfs for all the cases investigated, it has been observed that these distribution patterns do not vary, meaning that the shear-HTC correlation at the interface is not affected by either interfacial deformation or condensation.

The situation described above also becomes evident when comparing the instantaneous distributions of the interfacial shear stress and of the HTC. For the vapor side, Fig. 3 shows instantaneous snapshots of the normalized HTC and of the interfacial stress. It is clear that the regions of high interfacial stress, generated by sweeps and first-quadrant events, correlate well with the regions of high heat transfer. This correlation between shear and heat transfer is not evident on the liquid side (Fig. 4). In this case, the pattern of the shear remains streaky, whereas it looks more patchy for heat transfer.

**3.2 Quadrant Analysis.** Since in a turbulent boundary layer, momentum, heat, and mass transfer are controlled by the Reynolds stresses, the quadrant analysis of the Reynolds stress $\overline{uw}$ Fulgosi [8] is an excellent measure of the dynamic coupling and associated transfer at the interface. Briefly, this analysis splits the Reynolds stress into four different contributions based on the sign of $u$ and $w$: two events that contribute to positive Reynolds stress production, i.e., ejections (II quadrant events) and sweeps (IV quadrant events), and two other, I and III quadrant events, giving rise to negative Reynolds stress production.

The probability distribution of each event and of coupled events is examined as a function of the interfacial stress. The study could be performed considering only 28 independent flow realizations within a time interval of $600u_\star^2/\nu$. The event probability distribution analysis has been first conducted for the R1 case using all the 2000 recorded independent flow realizations, and then has been extended to the other cases (i.e., R2, C21, and C22). The sampling method consists of placing five monitor planes parallel to the interface (covering the entire streamwise and spanwise extensions of the computational domains) within a layer of about 12 wall units on both sides of the interface. In order to count only the events that are *strongly coherent*, an event is stored at the location $(\hat{x},\hat{y})$ when there, the same type of instantaneous event simultaneously occurs. The following information was collected:

1. the type of event
2. the local value of the normalized interfacial stress (i.e., the shear level at the point $(\hat{x},\hat{y})$ lying on the interface)
3. the "Reynolds stress content" of the event, i.e., $\Sigma_i\overline{uw}$, the sum being extended only to those planes (at least 4) where the strongly coherent event has been detected
4. the type of coupled event, if any, and its Reynolds stress content, the sum now being extended to all the planes lying in both computational domains

The events were then analyzed irrespective of their spatial and temporal locations. Figure 5 presents the pdf distributions in the vapor and in the liquid phases for the cases without interfacial condensation, i.e., R1 for the flat interface and R2 for the wavy interface. In both cases, the larger fraction of the heat flux is carried by sweeps (fourth-quadrant events), i.e., 68.7% and 69.3% for R1 and R2, respectively, even though their probability is lower than that of sweeps, i.e., $p_{II}=0.408$ and $p_{IV}=0.378$ in R1 and $p_{II}=0.398$ and $p_{IV}=0.369$ in R2. This implies that the heat transfer occurs predominantly through the fluid pumped toward the interface by sweeps and removed from there by ejections. First- and third-quadrant events play only a marginal role, both in terms of probability and heat content. In the liquid, the sweeps still carry the largest contribution to heat transfer, 63.5% ($p_{IV}=0.393$) and 62.7% ($p_{IV}=0.334$) in R1 and R2, respectively, but first- and third-quadrant events are of the same order as ejections. In particular, it was found that $p_I=0.152$ (11.2%), $p_{II}=0.345$ (17.7%), and $p_{III}=0.110$ (7.6%) for the flat interface, and $p_I=0.211$ (12.7%), $p_{II}=0.293$ (12.6%), and $p_{III}=0.162$ (12.0%) for the wavy one. It follows that the waviness of the interface, which was seen to promote first- and third-quadrant events, also participates in the transfer mechanisms, in line with the findings of the analysis for the Reynolds stress.

With moderate interfacial condensation (Fig. 6), nothing significantly different is observed in the vapor phase for both the flat and wavy interfaces. At the liquid side with the flat interface, i.e., C11, the probabilities of first- and third-quadrant events slightly increase, $p_I=0.173$ and $p_{III}=0.128$, compared to the case without condensation. However, their contribution to the heat transfer remains almost unchanged, 11.2% and 9.0%, respectively, meaning that sweeps and ejections are the main mechanisms driving the transfer. At the wavy interface, sweeps decrease their contribution, i.e., 58% ($p_{IV}=0.346$), being replaced by the other three events, particularly $p_I=0.213$ (13.2%), $p_{II}=0.293$ (14.1%), and $p_{III}=0.148$ (14.7%). A further increase in the condensation rate (see Fig. 7) does not show any significant variation in the probabilities and heat contents, for both phases, either.

## 4 Heat Transfer Coefficient

One of the major objectives of this study is to understand which velocity scale is relevant for the HTC at the interface, in the presence of condensation. For the problem considered here, a study of the scaling law for the HTC as a function of the Prandtl number is not feasible because the variation of this parameter is

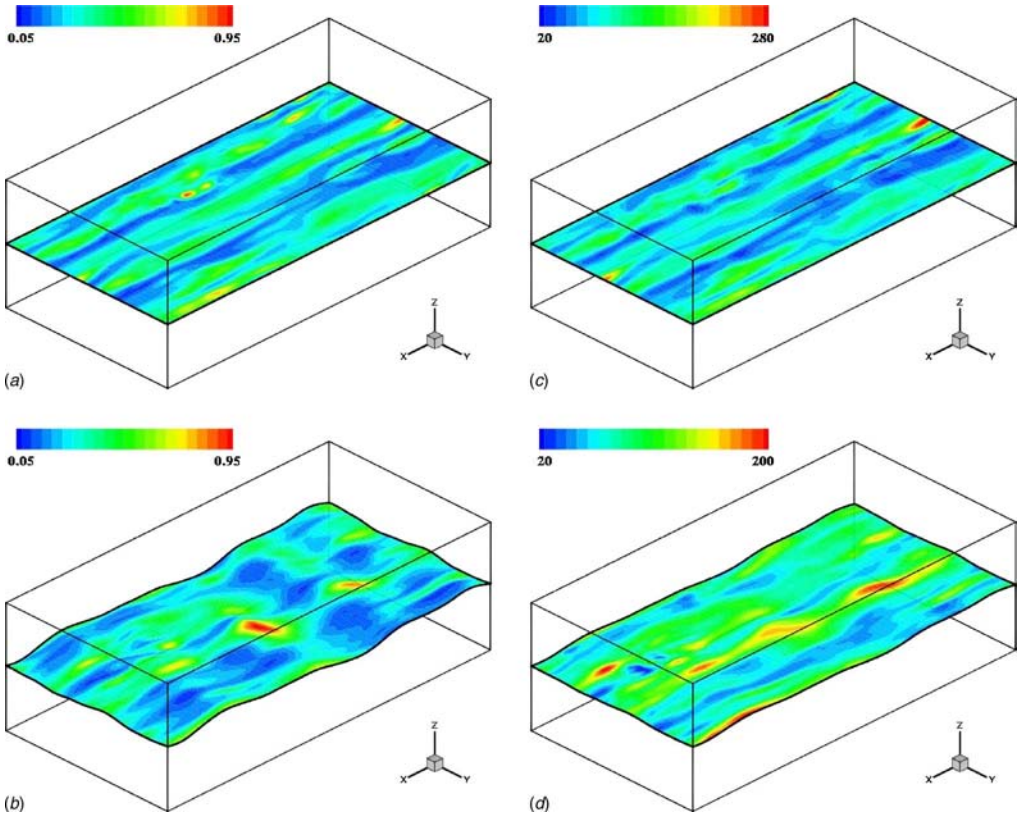


**Fig. 3 Instantaneous contours of the normalized HTC and of the interfacial shear stress in the vapor phase**

negligible; thus, the objective is restricted to the establishment of the best suited velocity scale that should be used to normalize the condensation heat transfer process.

It has been shown in the previous section that the total interfacial shear stress changes because of the interfacial condensation, as well as for the presence of interfacial waves; the frictional drag then is reduced, and so does the frictional velocity $u_\tau$. The HTC, scaled with both $u_\star$ and $u_\tau$, obtained by the present DNS simulations are reported in Table 2, where the ratio $u_\tau/u_\star$ as well as the Prandtl number have been included for completeness. For the cases without interfacial condensation, i.e., R1 and R2, the resulting values for both phases are in line with the results reported by Lombardi et al. [11], for the case of passive-scalar transfer at the flat and wavy interfaces; the differences are in the range of the statistical error, i.e., $\pm 10\%$.

**4.1 Vapor Side.** In the DNS of passive heat transfer [9], we have shown that for low-to-moderate Pr numbers (i.e., 1–10), the HTC in the vapor phase scales with the frictional velocity $u_\tau$ as

$$\frac{K_G \mathrm{Pr}^{0.6}}{u_{\tau_G}} = C \tag{5}$$

where $C=0.058$. From Fig. 8, it can be argued that the condensation heat transfer is better represented when the HTC is normalized by the friction velocity rather than with $u_\star$. As depicted in this figure, when the R1 and R2 data are connected together with Eq. (5), the value of the constant is slightly larger, i.e., $C=0.0615$. The small difference in the value of the constant might be due to the fact that the vapor-liquid density ratio employed in the present simulations is smaller than the one considered in Ref. [9] (18.4 versus 29.9). Moreover, we observe the condensation C result data to fall slightly below the line connecting the R1 and R2 cases. A twofold effect of the liquid subcooling can be observed: On one side, it reduces slightly the transfer coefficient (i.e., shift in the vertical direction), and on the other, it results in a reduction of the friction velocity (i.e., shift in the horizontal direction).

**4.2 Liquid Side.** The liquid-side heat transfer is more interesting from the engineering point of view as it controls the condensation process. For the liquid phase, in the case of high-Schmidt (Sc) passive mass transfer, De Angelis et al. [13] developed a relationship between frictional velocity and scalar exchange rate based on the surface renewal theory, i.e., derived a scaling law for the transfer velocity based on the surface renewal theory, i.e.,

$$\frac{K_L \mathrm{Sc}^{0.5}}{u_{\tau_L}} = 0.108 - 0.158 \tag{6}$$

De Angelis et al. [13] have shown that this expression holds also in the presence of small interfacial capillary waves if the shear velocity due only to frictional drag is used as the characteristic velocity scale. It was concluded that Eq. (6) is inadequate for the prediction of the transfer rates in the case of low-Sc numbers.

The results obtained for the liquid side in the present simulations are plotted in Fig. 9. It is interesting to observe that in the presence of condensation, the HTC remains roughly unaffected by the rate of condensation for both groups of low and high viscous shears. Since the total shears velocity is fixed, consequently, an *apparent* scaling of the HTC with $u_\star$ can be observed. This apparent behavior is opposite to what was observed in passive heat/mass transfer problems, where the transfer coefficient was seen to better scale with the frictional velocity $u_\tau$.

Assuming the conventional Prandtl number dependence for the transfer coefficient, the DNS results for the R1 and R2 cases without condensation can be fitted by

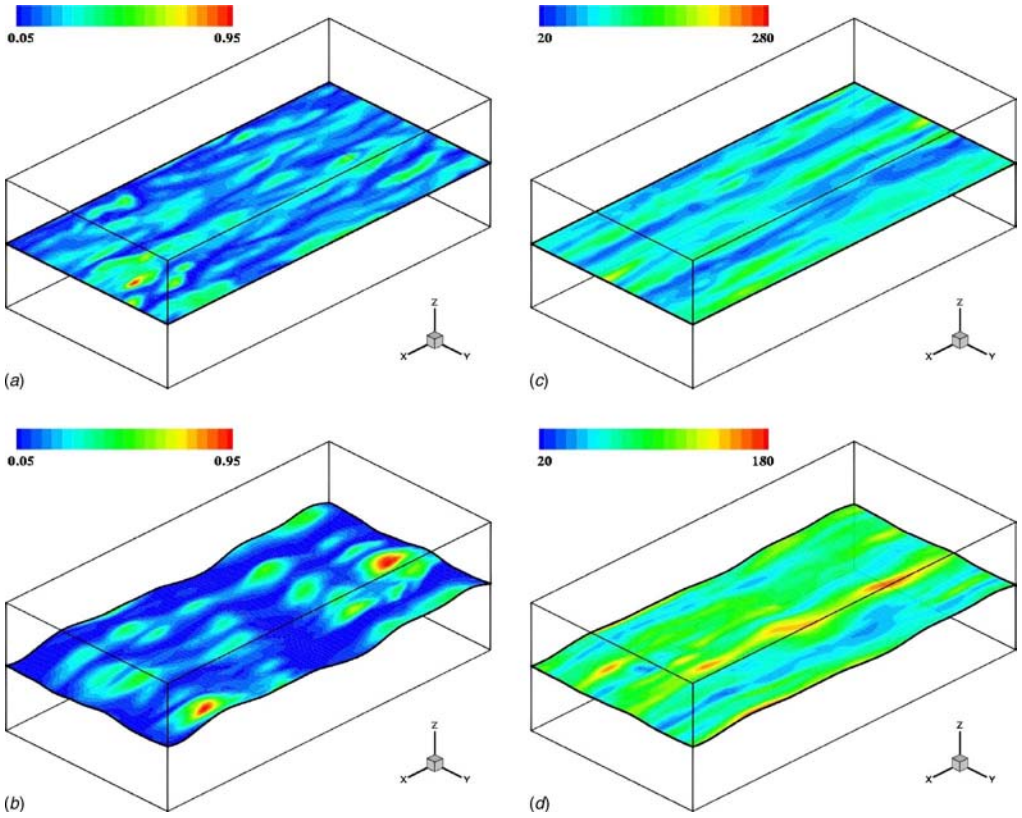


**Fig. 4 Instantaneous contours of the normalized HTC and of the interfacial shear stress in the liquid phase**

$$\frac{K_L \mathrm{Pr}^{0.5}}{u_{\tau_L}} = 0.079 \tag{7}$$

If the C points were obtained in the absence of mass exchange effects, one would have expected them to correlate with $u_\tau$ and fall on the straight line joining R1 and R2, given by Eq. (7). In this light, one can argue that the vertical distance between the points C and the R1-R2 line represents an augmentation of heat transfer due to the combined effects of mass exchange (for all the C points) and possibly also of the interfacial waviness (for points C21 and C22 only). This is depicted in Fig. 10, where $\Delta K_L$ is the difference between the value of $K_L$ obtained from the present DNS and the value of $K_L$ as if it were on the line connecting R1-R2. As it can be observed, if the low-viscous-shear points C11 and C12 (flat interface) are connected with lines passing through the origin, a first observation that can be made is that the slopes of these two lines are proportional to the subcooling or the condensation rate, as could have been expected. Second, the points C21 and C22 lie above these lines: one could argue that the extra augmentation of $K_L$ in these two last cases might be due to the waviness of the interface. At this point, the fact that at both $u_\tau$ levels the HTC remains roughly constant seems to be fortuitous.

We now compare interesting to compare the values of the liquid-side HTC inferred from the present DNS to those delivered by some "well known" correlations for condensation heat transfer available in the literature, some of which have already been introduced in the Introduction. For example, the turbulence-centered model proposed by Kim and Bankoff [14] can be slightly reformulated by introducing the height of the liquid layer and the frictional velocity as turbulent characteristic length and velocity scales. Since the length scale associated with the wave motion can be directly obtained from the DNS data, their model expression may be rewritten as

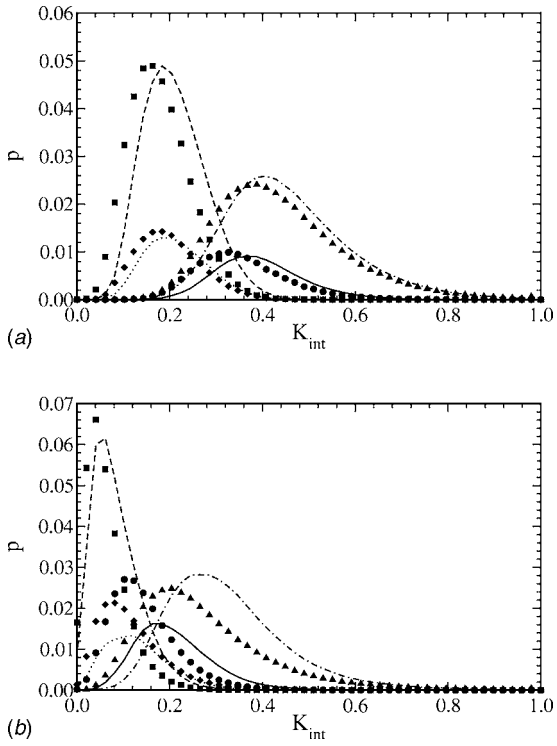


**Fig. 5 Probability distribution of "strongly coherent" $\overline{uw}$ events versus normalized HTC at the interface. Lines and symbols are used to identify R1 and R2, respectively. (—) and (●), I quadrant events; (---) and (□), II quadrant events; (···) and (◇), III quadrant events; (-·-) and (△), IV quadrant events.**

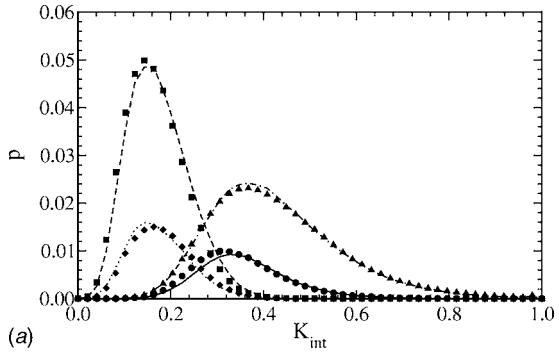


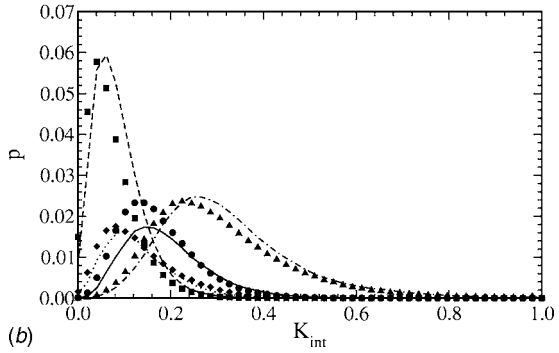


**Fig. 6 Probability distribution of strongly coherent $\overline{uw}$ events versus normalized HTC at the interface. Lines and symbols are used to identify C11 and C12, respectively. (—) and (●), I quadrant events; (---) and (black □), II quadrant events; (···) and (black ◇), III quadrant events; (-·-) and (black △), IV quadrant events.**

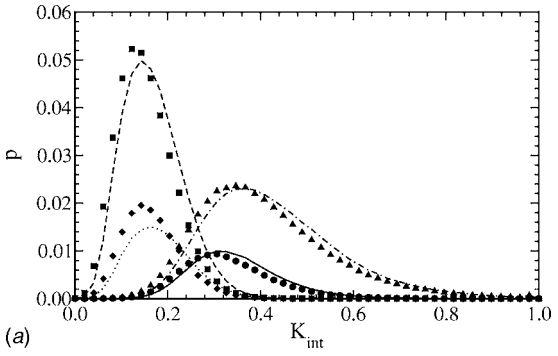


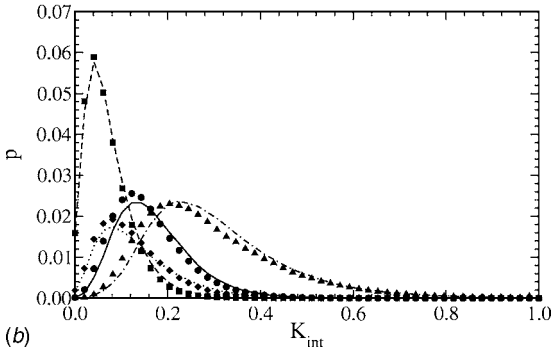


**Fig. 7 Probability distribution of strongly coherent $\overline{uw}$ events versus normalized HTC at the interface. Lines and symbols are used to identify C21 and C22, respectively. (—) and(●), I quadrant events; (- - -) and (black □), II quadrant events; (···) and (black ◇), III quadrant events; (-·-) and (black △), IV quadrant events.**

$$\frac{K_L \mathrm{Pr}^{0.5}}{u_{\tau_L}} = 0.113\left(\frac{ak}{k_{\max}}\right)^{0.12} \tag{8}$$

where $ak$ is the wave slope. From the present DNS database, an averaged value of $(ak/k_{\max})^{0.12}=0.672$ has been obtained, which reduces the previous equation to

$$\frac{K_L \mathrm{Pr}^{0.5}}{u_{\tau_L}} = 0.088 \tag{9}$$

Other correlations available in the literature include the one suggested by Carpenter and Colburn [15], who performed experiments on film condensation inside vertical tubes and proposed a model expression that can be recast in the form

$$\frac{K_L \mathrm{Pr}^{0.5}}{u_{\tau_L}} = 0.043 \tag{10}$$

Soliman et al. [16] also experimented on film condensation inside vertical tubes but considered the relative contributions of friction, momentum, and gravity to the shear stress; they proposed to correlate the HTC as follows:

$$\frac{K_L \mathrm{Pr}^{0.35}}{u_{\tau_L}} = 0.036 \tag{11}$$

Finally, the correlation proposed by Linehan [17] does not account for the dependency on the Prandtl number; using the present DNS results, their expression can be rewritten, however, as

$$\frac{K_L}{u_{\tau_L}} = 0.070 \tag{12}$$

The results of this comparison are discussed in the context of Fig. 11. As can be observed, the present DNS results are in good agreement with the model of Kim and Bankoff [14], whereas the other correlations give lower predictions for the condensation HTC.

The message here is that only models that incorporate a measure for surface deformations are capable of providing the best results. This is in line with what we have later found when exploring the so-called surface divergence model (SDM) [10] incorporating such information through the surface curvature.

**4.3 Surface Divergence Model.** In our previous contributions to this subject [10], we have unexpectedly found the SDM of Banerjee [12] to also apply for the scalar transport parametrization at sheared interfaces, although it was primarily thought for isotropic, homogeneous turbulence conditions and nonsheared interfaces. In the modified form of the SDM model, the interfacial mass transfer reads [10]

$$\frac{K\mathrm{Sc}^{0.5}}{U_\infty} = C\mathrm{Re}_t^{-0.5}[(\nabla \cdot \mathbf{u}_{\mathrm{tang}} - 2w' \nabla \cdot \mathbf{n})^2]_{\mathrm{int}}^{0.25} \tag{13}$$

where $C$ is a model constant of the order of unity, and the quantity between square brackets is the square of the surface divergence field tangential to the interface (known as the dilation term) due to the fluctuating motions. Velocity fluctuations are indeed possible at deformable sheared interfaces, such that the two-dimensional continuity equation cannot be satisfied. This term physically represents the signature of the interfacial deformation caused by sweep events that bring bulk fluid toward the interface. The right-hand-side term is normalized using the integral velocity and length scales of the far field turbulence, i.e., $U_\infty$ and $\Lambda_\infty$, and $\mathrm{Re}_t = U_\infty \Lambda_\infty / \nu$ is the turbulent Reynolds number.

The above form requires a closure for the right-hand-side term.

**Table 2 Values of the HTC derived from the present DNS**

| | | Vapor | | | | Liquid | | | |
|---|---|---|---|---|---|---|---|---|---|
| Case | $u_\tau/u_\star$ | Pr | $K$ ($10^4$ m/s) | $K^+$ | $K_\tau^+$ | Pr | $K$ ($10^5$ m/s) | $K^+$ | $K_\tau^+$ |
| R1 | 1.00 | 0.95 | 7.875 | 0.0625 | 0.0625 | 1.15 | 4.978 | 0.0727 | 0.0727 |
| C11 | 0.91 | 0.95 | 7.056 | 0.0560 | 0.0615 | 1.15 | 4.958 | 0.0724 | 0.0796 |
| C12 | 0.84 | 0.95 | 6.301 | 0.0500 | 0.0595 | 1.17 | 4.876 | 0.0712 | 0.0848 |
| R2 | 0.98 | 0.95 | 23.701 | 0.0627 | 0.0640 | 1.17 | 14.894 | 0.0725 | 0.0740 |
| C21 | 0.90 | 0.95 | 21.281 | 0.0563 | 0.0626 | 1.15 | 15.162 | 0.0742 | 0.0824 |
| C22 | 0.83 | 0.95 | 18.673 | 0.0494 | 0.0595 | 1.17 | 15.058 | 0.0733 | 0.0883 |

This has been intuitively made based on the Hunt–Graham blocking theory [12] and later on validated against the DNS data [10], as shown in Fig. 12,

$$\frac{K\mathrm{Sc}^{0.5}}{U_\infty} = C\mathrm{Re}_t^{-1/2}[0.3(2.83\mathrm{Re}_t^{3/4} - 2.14\mathrm{Re}_t^{2/3})]^{1/4} \qquad (14)$$

The scaling between the DNS based surface dilation term shown in the above figure (from earlier work) and the Hunt–Graham blocking theory is also expected to apply under phase-change conditions, in which case the model can be tested and compared to the DNS data. The result of this comparison is shown in Fig. 13, where the results obtained by the model of Eq. (14) for all interfacial shear velocities reported in Table 1 are compared to the true DNS data. The agreement between the two sets of data is excellent for the range of turbulence (shear Reynolds number) and thermal conditions (subcooling and superheating rates) employed in this work. The comparison is made with the $C$ constant equal to 0.35, which was found to be better suited for Sc/Pr numbers of the order of unity; an augmented value of $C=0.45$ should be employed for higher Sc/Pr values. What is important to note is that the turbulent Reynolds number appearing in Eq. (14) is the actual one, and should be smaller than the initial value.

## 5 Interfacial Friction

To use the correlation for the HTC proposed in the previous paragraph, the interfacial shear velocity should be known. From an engineering point of view, the value of the interfacial shear stress is not a priori known, but it is more likely that some global parameters, such as the turbulence Reynolds numbers or the bulk velocities of the two phases, are available and can be used to estimate the interfacial friction velocity.

An approach to estimate the friction factor for condensing stratified steam water has been proposed by Linehan [17] and,

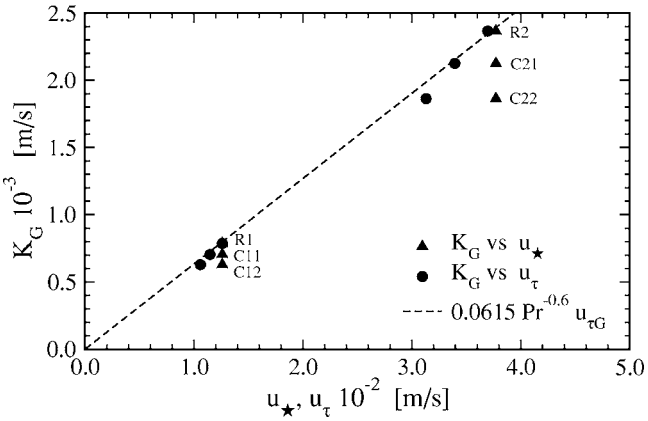


**Fig. 8 Vapor-side dimensional heat transfer velocity plotted versus the shear and friction velocities**

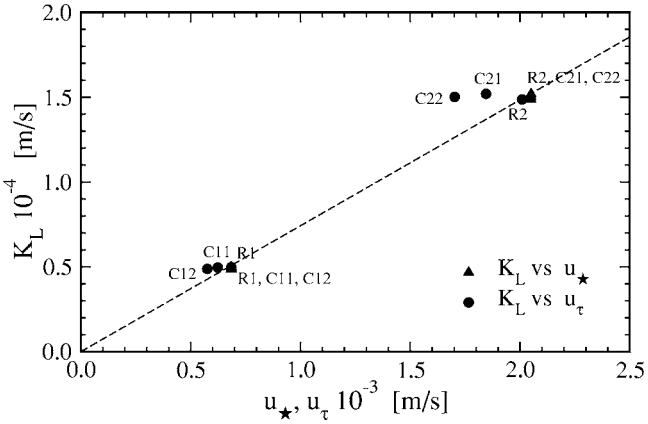


**Fig. 9 Liquid-side dimensional heat transfer velocity versus the shear and friction velocities**

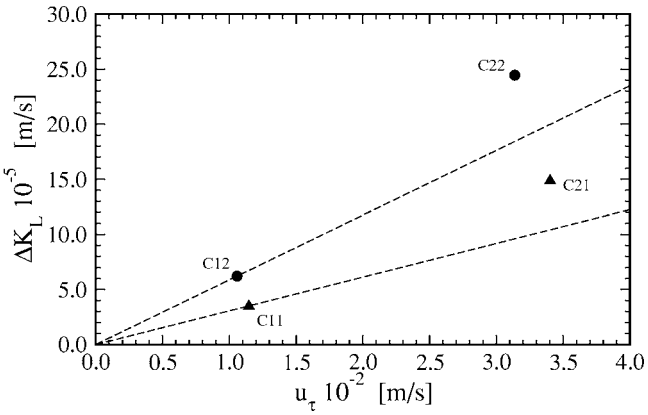


**Fig. 10 Effect of liquid subcooling and interfacial waviness**

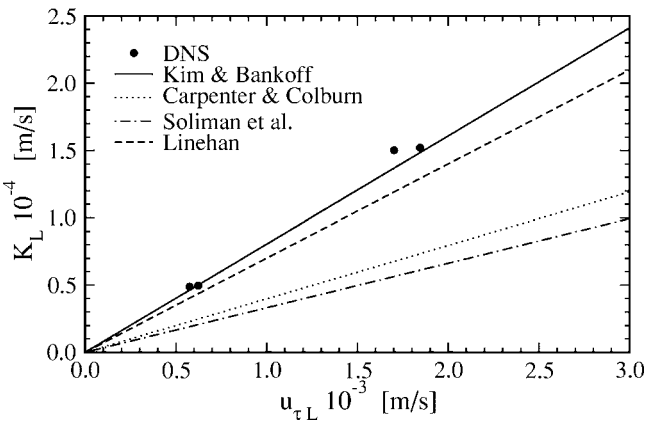


**Fig. 11 Comparison of the liquid-side DNS data with other correlations**

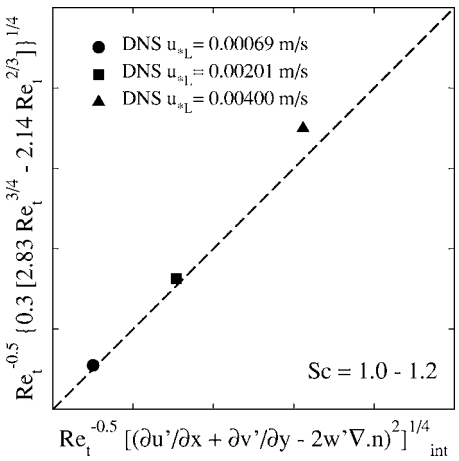


**Fig. 12 Comparison of the surface term with the dilation contribution to the Hunt–Graham blocking theory**

subsequently, by Kim et al. [18]. Observing that the shear stress at the interface, in the presence of condensation, is influenced by the mass exchange, these authors proposed the relation

$$\tau_{\text{int}} = \tau_{\text{int},a} - (\bar{u}_G - \bar{u}_{\text{int}})\dot{m} \tag{15}$$

where $\tau_{\text{int},a}$ represents the interfacial shear without condensation and $\dot{m}$ is the rate of condensation. The second term on the right-hand side of Eq. (15) represents the interfacial momentum transfer, in which the difference $(\bar{u}_G - \bar{u}_{\text{int}})$ is the relative vapor velocity with respect to the moving interface, $\bar{u}_{\text{bulk}_G}$. In nondimensional form, Eq. (15) can be rewritten as

$$f = f_a - \phi \tag{16}$$

where

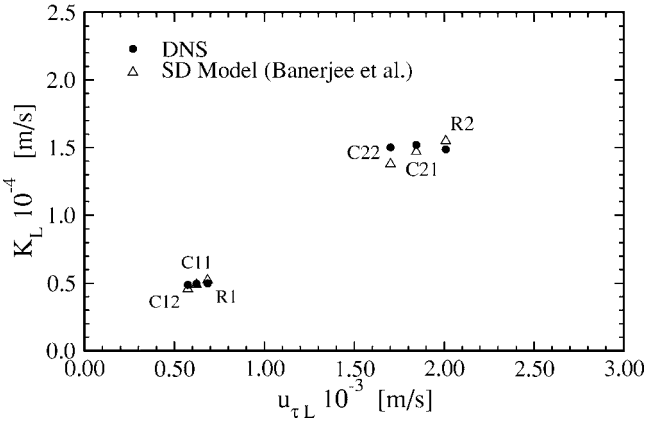


**Fig. 13 HTC parametrization by means of the SDM model**

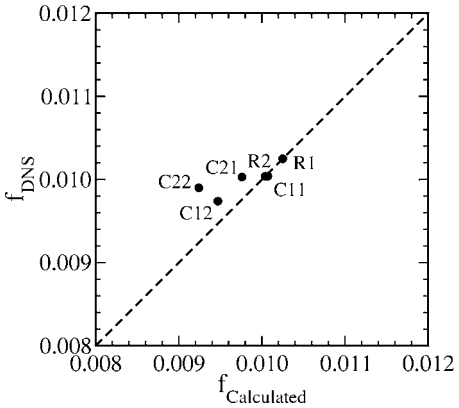


**Fig. 14 Comparison of the computed interfacial friction factors with the values obtained using Eq. (16)**

$$f = 2\left(\frac{u_{\tau_G}}{\bar{u}_{\text{bulk}_G}}\right)^2 = \frac{2\tau^+_{\text{int}}}{\bar{u}^{+2}_{\text{bulk}_G}} \quad \phi = \frac{2\dot{m}}{\rho_G \bar{u}_{\text{bulk}_G}} = \frac{2\Gamma^+_G}{\bar{u}^+_{\text{bulk}_G}} \tag{17}$$

The values of the friction factor obtained from Eq. (16) using the DNS values for the interfacial shear without condensation (from the R1 and R2 cases) and the rate of condensation, are reported in Table 3 and plotted in Fig. 14.

It can be observed that the DNS predictions of shear with condensation are in good agreement with the values predicted by Eq. (16); although small differences are noticeable in the cases of wavy interface or large subcooling, the results confirm that in the presence of condensation, the interfacial shear stress is influenced by the mass exchange, as proposed by Kim et al. [18].

## 6 Conclusions

This new DNS database for the steam-water stratified flow has been exploited to understand the importance of the relative driving mechanisms for the condensation heat transfer in both phases. It has been observed that the heat transfer mechanisms in the two phases are different and do not depend significantly on either the interfacial deformation or condensation. In the vapor, the heat transfer correlates locally with the interfacial shear. On the liquid side, however, the shear stress patterns do not clearly indicate mass transfer rates, nor do they indicate ejections and sweeps. The probability analysis of the quadrant events as a function of interfacial heat transfer has shown that in both phases, the heat transfer occurs predominantly through the fluid pumped toward the interface by sweeps and then removed by ejections. First- and third-quadrant events play only a marginal role.

On the gas side, condensation heat transfer is well represented when the HTC is normalized with the friction velocity. The scaling law obtained for passive heat transfer reported in Ref. [9] still holds. In the liquid phase, the DNS results provided a condensation HTC that remains roughly constant for a given total shear velocity $u_\star$ (or pressure gradient). However, an augmentation of heat transfer due to the combined effects of mass exchange and interfacial waviness has been observed. The DNS data compare well with the correlation of Ref. [14] for similar experimental

**Table 3 Friction factors**

| Case | $\tau^+_{\text{int}}$ | $\bar{u}^+_{\text{bulk}_G}$ | $\Gamma^+_G$ | $\phi$ | $f_a$ | $f$ | $f_{\text{DNS}}$ |
|---|---|---|---|---|---|---|---|
| R1 | 1.00 | 13.968 | 0.0000 | 0.00000 | 0.01025 | 0.01025 | 0.01025 |
| C11 | 0.83 | 12.842 | 0.0132 | 0.00206 | 0.01213 | 0.01007 | 0.01004 |
| C12 | 0.71 | 12.034 | 0.0261 | 0.00434 | 0.01381 | 0.00947 | 0.00974 |
| R2 | 0.96 | 13.833 | 0.0000 | 0.00000 | 0.01004 | 0.01004 | 0.01004 |
| C21 | 0.81 | 12.706 | 0.0136 | 0.00214 | 0.01190 | 0.00976 | 0.01003 |
| C22 | 0.69 | 11.798 | 0.0269 | 0.00456 | 0.01380 | 0.00924 | 0.00990 |

conditions. The SDM of [10] is found to apply in the liquid phase, too, with an excellent agreement with the low-to-mild interfacial shear regime in particular.

The DNS data confirm that in the presence of condensation the interfacial shear stress is influenced by the mass exchange, and a correction factor based on the rate of condensation is needed to correctly predict the variation of the friction coefficient.

## Acknowledgment

This work was partially supported by (Euratom 6th Framework) EU program NURESIM (www.nuresim.org). Prof. Sanjoy Banerjee from UCSB is gratefully acknowledged for his contribution to this work.

## Nomenclature

- $a$ = wave amplitude
- $ak$ = wave slope
- $c_p$ = heat capacity
- $f$ = friction coefficient
- Fr = Froude number
- $h$ = half-depth of each domain
- Ja = Jakob number
- $k$ = wave number
- $K^+$ = nondimensional transfer coefficient
- $\dot{m}$ = mass flow rate
- $\mathbf{n}$ = surface normal vector
- $p^+ = p/\rho u_\star^2$ = nondimensional dynamic pressure
- Pr = Prandtl number
- $q_{\text{int}}$ = interfacial heat flux
- $\mathcal{R} = \sqrt{\rho_L/\rho_G}$ = density ratio
- Re = Reynolds number
- $\text{Re}_\star = u_\star 2h/\nu$ = imposed shear Reynolds number
- $\text{Re}_\tau = u_\tau 2h/\nu$ = resulting shear Reynolds number
- $\text{Re}_t = U_{\text{inf}}\Lambda_{\text{inf}}/\nu$ = turbulent Reynolds number
- Sc = Schmidt number
- $\mathbf{t}_i$ = tangential unit vectors
- $t^+ = \nu/u_\star^2$ = nondimensional time unit
- $T_\star = q_{\text{int}}/\rho c_p u_\star$ = reference temperature
- $T^+ = (T - T_{\text{int}})/T_\star$ = nondimensional temperature
- $\mathbf{u}^+$ = nondimensional instantaneous velocity
- $\mathbf{U}^+$ = nondimensional time averaged velocity
- $u^+$ = fluctuating velocity
- $\mathbf{u}^+ = \mathbf{u}/u_\star$ = nondimensional velocity
- $u_\tau = \sqrt{\tau_{\text{int}}/\rho}$ = resulting shear velocity
- $u_\star = \sqrt{\tau_\star/\rho}$ = imposed shear velocity
- We = Weber number

## Greek Letters

- $\Delta x^+$ = nondimensional grid units
- $\Delta T_{\text{sup}}$ = superheating
- $\Delta T_{\text{sub}}$ = subcooling
- $\Delta p$ = pressure gradient driving the flow
- $\mathcal{H}$ = latent heat of phase change
- $\gamma$ = surface tension coefficient
- $\Gamma$ = nondimensional condensation rate
- $\Lambda_{\text{inf}}$ = integral length scale
- $\nu$ = viscosity
- $\rho$ = density
- $\sigma$ = viscous stress
- $\tau_{\text{int}} = \mu du/dz_{\text{int}}$ = resulting interfacial shear stress
- $\tau_\star = 2h\Delta p$ = imposed interfacial shear stress

## Subscripts

- bulk = bulk
- int = interfacial
- $\text{int}_a$ = without condensation
- $\infty$ = integral
- sup = superheating
- sub = subcooling
- $L$ = liquid
- $G$ = gas/vapor

## References

[1] Seban, R. A., and Back, L. H., 1961, "Velocity and Temperature Profiles in a Wall Jet," Int. J. Heat Mass Transfer, **3**, pp. 255–265.

[2] Moffat, R. J., and Kays, W. M., 1968, "The Turbulent Boundary on Porous Plate: Experimental Heat Transfer With Uniform Blowing and Suction," Int. J. Heat Mass Transfer, **11**, pp. 1547–1566.

[3] Faraco-Medeiros, M. A., and Silva-Freire, A. P., 1992, "The Transfer of Heat in Turbulent Boundary Layers With Injection or Suction: Universal Laws and Stanton Number Equations," Int. J. Heat Mass Transfer, **35**, pp. 991–995.

[4] Chan, T., and Yuen, M. C., 1990 "The Effect of Air on Condensation of Stratified Concurrent Steam Water-Flow," ASME J. Heat Transfer, **112**, pp. 1092–1095.

[5] Sumitani, Y., and Kasagi, N., 1995, "Direct Numerical Simulation of Turbulent Transport With Uniform Wall Injection and Suction," AIAA J., **33**, pp. 1220–1228.

[6] Park, J., and Choi, H., 1999, "Effect of Uniform Blowing and Suction From a Spanwise Slot on a Turbulent Boundary Layer," Phys. Fluids, **11**, pp. 3095–3105.

[7] Jimenez, J., Uhlmann, M., Pinelli, A., and Kawahara, G., 2001, "Turbulent Shear Flow over Active and Passive Porous Surfaces," J. Fluid Mech., **442**, pp. 89–117.

[8] Fulgosi, M., Lakehal, D., Banerjee, S., and De Angelis, V., 2003, "Direct Numerical Simulation of Turbulence in a Sheared Air-Water Flow With Deformable Interface," J. Fluid Mech., **482**, pp. 319–345.

[9] Lakehal, D., Fulgosi, M., Yadigaroglu, G., and Banerjee, S., 2003, "Direct Numerical Simulation of Turbulent Heat Transfer Across a Mobile, Sheared Gas-Liquid Interface," ASME J. Heat Transfer, **125**, pp. 1129–1139.

[10] Banerjee, S., Lakehal, D., and Fulgosi, M., 2004, "Surface Divergence Models for Scalar Exchange Between Turbulent Streams," Int. J. Multiphase Flow, **30**(8), pp. 965–977.

[11] Lombardi, P., De Angelis, V., and Banerjee, S., 1996, "Direct Numerical Simulation of Near-Interface Turbulence in Coupled Gas-Liquid Flow," Phys. Fluids, **8**, pp. 1643–1665.

[12] Banerjee, S., 1990, "Turbulence Structure and Transport Mechanisms at Interfaces," *Ninth International Heat Transfer Conference*, p. 395.

[13] De Angelis, V., Lombardi, P., Andreussi, P., and Banerjee, S., 1997, "Microphysiscs of Scalar Transfer at Air-Water Interfaces," in *Proceedings of Wind-Over-Wave Couplings: Perspectives and Prospects*, S. G. Sajjadi, N. H. Thomas, and J. C. R. Hunt, eds., Oxford University Press, New York.

[14] Kim, H. J., and Bankoff, S. G., 1983, "Local Heat Transfer Coefficient for Condensation in Stratified Countercurrent Steam-Water Flows," ASME J. Heat Transfer, **105**, pp. 706–712.

[15] Carpenter, E. F., and Colburn, A. P., 1951, "The Effect of Vapor Velocity on Condensation Inside Tubes," *Proceedings of the General Discussion on Heat Transfer*, Institute of Mechanical Engineers, London, pp. 20–26.

[16] Soliman, M., Schuster, J. R., and Berenson, P. J., 1968, "A General Heat Transfer Correlation for Annular Flow Condensation," ASME J. Heat Transfer **90**, pp. 267–276.

[17] Linehan, J. H., 1968, "The Interaction of Two-Dimensional Stratified Turbulent Air-Water and Steam-Water Flows," Ph.D. thesis, Department of Mechanical Engineering, University of Wisconsin.

[18] Kim, H. J., Lee, S. C., and Bankoff, S. G., 1985, "Heat Transfer and Interfacial Drag in Countercurrent Steam-Water Stratified Flow," Int. J. Multiphase Flow, **11**, pp. 593–606.

# Temperature Scalings and Profiles in Forced Convection Turbulent Boundary Layers

**Xia Wang**[1]
Department of Mechanical Engineering,
Oakland University,
Rochester, MI 48309
e-mail: wang@oakland.edu

**Luciano Castillo**

**Guillermo Araya**

Department of Mechanical Engineering,
Aerospace and Nuclear Engineering,
Rensselaer Polytechnic Institute,
Troy, NY 12180

*Based on the theory of similarity analysis and the analogy between momentum and energy transport equations, the temperature scalings have been derived for forced convection turbulent boundary layers. These scalings are shown to be able to remove the effects of Reynolds number and the pressure gradient on the temperature profile. Furthermore, using the near-asymptotic method and the scalings from the similarity analysis, a power law solution is obtained for the temperature profile in the overlap region. Subsequently, a composite temperature profile is found by further introducing the functions in the wake region and in the near-the-wall region. The proposed composite temperature profile can describe the entire boundary layer from the wall all the way to the outer edge of the turbulent boundary layer at finite Re number. The experimental data and direct numerical simulation (DNS) data with zero pressure gradient and adverse pressure gradient are used to confirm the accuracy of the scalings and the proposed composite temperature profiles. Comparison with the theoretical profiles by Kader (1981, "Temperature and Concentration Profiles in Fully Turbulent Boundary Layers," Int. J. Heat Mass Transfer, **24**, pp. 1541–1544; 1991, "Heat and Mass Transfer in Pressure-Gradient Boundary Layers," Int. J. Heat Mass Transfer, **34**, pp. 2837–2857) shows that the current theory yields a higher accuracy. The error in the mean temperature profile is within 5% when the present theory is compared to the experimental data. Meanwhile, the Stanton number is calculated using the energy and momentum integral equations and the newly proposed composite temperature profile. The calculated Stanton number is consistent with previous experimental results and the DNS data, and the error of the present prediction is less than 5%. In addition, the growth of the thermal boundary layer is obtained from the theory and the average error is less than 5% for the range of Reynolds numbers between $5\times10^5$ and $5\times10^6$ when compared with the empirical correlation for the experimental data of isothermal boundary layer conditions.*
[DOI: 10.1115/1.2813781]

*Keywords: turbulent boundary layer, similarity analysis, forced convection heat transfer, temperature scaling*

## 1 Introduction

Heat transfer in turbulent boundary layers has attracted many researchers due to its various applications in industry such as in heat exchangers, gas turbine blades, aircrafts, electronic cooling, and so on. However, this phenomenon remains unsolved due to the complexity of nonlinear turbulent quantities. The problem of forced convection turbulent boundary layer flow is worse in the case of pressure gradient flows, particulary in adverse pressure gradient (APG) flow.

Experimental investigations related to forced convection turbulent boundary layers were mainly performed during and before the 1970s. Analytical studies and numerical simulations have been the main tool to investigate heat transfer problems in boundary layer flows. Due to high computing cost and limitation of low Reynolds number flows, many complex flows in engineering applications are not well understood by numerical simulations alone, Gad-el-hak [1]. Therefore, dimensional analysis and similarity analysis are still useful tools in understanding the basic physics of heat transfer in turbulent boundary flows including high Reynolds number problems. Using dimensional analysis, Perry et al. [2] investigated the velocity and temperature profiles in turbulent boundary layers subject to the APG. A half-power law was found for the velocity profile and an inverse-half-power law for the temperature profile in the region of the pressure gradient layer. Furthermore, Afzal [3] derived the same power law using the matched asymptotic expansion method. These power laws were limited to describe the temperature profile in a small overlap region and cannot be used to describe the entire boundary layer. Kader [4] later proposed the following equations to describe the temperature profile in the zero pressure gradient (ZPG) turbulent boundary layers as

$$\frac{T_W - T}{T_\tau} = P_r y^+ \exp(-\Gamma) + \left\{ 2.12 \ln\left[ (1+y^+) \frac{2.5(2-\bar{y})}{1+4(1-\bar{y})^2} \right] + \beta(P_r) \right\} \exp\left( -\frac{1}{\Gamma} \right) \tag{1}$$

where $y^+ = y u_\tau / \nu$, $\bar{y} = y/\delta$, $\Gamma = 10^{-2}(P_r y^+)^4/(1+5P_r^3 y^+)$, and $\beta(P_r) = (3.85P_r^{1/3} - 1.3)^2 + 2.12 \ln P_r$. This equation was derived assuming that a single temperature scaling exists in the overlap region. A decade later, Kader [5] investigated the temperature profile of turbulent boundary layer flow subject to pressure gradient using dimensional analysis and the asymptotic method. The boundary layer was divided into three regions, and each region was described by a given formulation. Moreover, these equations were derived based on the assumption of a moving-equilibrium bound-

[1]Corresponding author.

Contributed by the Heat Transfer Division of ASME for publication in the JOURNAL OF HEAT TRANSFER. Manuscript received June 13, 2006; final manuscript received May 30, 2007; published online February 4, 2008. Review conducted by Anthony M. Jacobi.

  

ary layer, which means that for a given value of the streamwise location $x$, all the characteristics of the fluid flow depend on the local value of the position of $x$ only. However, recent investigators argued that the downstream flow cannot forget its upstream history, and the upstream conditions, such as the tripping wire (its shape, size, and location) and the wind tunnel speed will have some effects on the development of the downstream flow, Erm and Joubert [6], Castillo and Johansson [7], and Castillo and Walker [8].

Instead of using conventional dimensionless analysis or similarity analysis, Churchill et al. [9,10] proposed an algebraic model to scale the mean turbulence quantities, turbulence Reynolds stresses, and turbulence heat flux. Le and Papavassiliou [11] used the theory of Churchill et al. [9,10] to develop a temperature profile for low Re turbulent flow. Moreover, Wei et al. [12,13] developed the so-called "multiscale analysis" in order to study the structure of the turbulent boundary layer with and without heat transfer. Different from all the previous studies, George and coworkers introduced the near-asymptotic method [14,15]. George [14] used a near-asymptotic method in order to derive the solution of the velocity profile in the overlap region. By matching the profiles in the inner and outer regions at the finite Re number, a velocity profile can be obtained. This approach is opposite to the classical method in which the velocity profiles are obtained in the limit of infinite Reynolds number. Using the near-asymptotic method, George and Castillo [15] derived a power law solution for the velocity profile in the overlap region of a ZPG turbulent boundary layer. They further proposed a composite velocity profile for the same type of flow. George et al. [16] discussed that a power law solution should also exist to describe the temperature profile in the overlap region of a thermal boundary layer. In the current investigation, the temperature scaling derived by Wang and Castillo [17] will be reviewed first. Then using the new temperature scalings proposed by Wang and Castillo [17], a new power law solution will be derived for the temperature profile in the overlap region by applying the near-asymptotic theory. Furthermore, a composite temperature profile is constructed by introducing a new wake function for the outer region and a function describing the near-wall region. In addition, this composite temperature profile will be verified using the ZPG and APG experimental data of Blackwell [18], Reynolds [19] and the direct numerical simulation (DNS) data of Kong et al. [20]. Also, the theoretical profiles of Kader [4,5] will be used for comparison and verification of the present theory. A unique feature of the proposed new composite temperature profile is its validity at the finite Re number over the entire thermal boundary layer (i.e., from the near-the-wall region to the outer region). In addition, this new composite temperature profile will be applied to the energy integral equation to calculate the heat transfer law.

## 2 Theory

**2.1 Temperature Scalings From Similarity Analysis.** In the limit as the Reynolds number goes to the infinity, the boundary layer equations become independent of the Reynolds number, Schlichting and Gersten [21], George and Castillo [15]. Therefore, any scaling or function representing the boundary layer solutions must also be independent of the Reynolds number in this limit. Consequently, the inner and outer scalings of turbulent boundary layers can also be determined in this limit (i.e., the asymptotic invariance principle: AIP proposed by George and Castillo [15]). Most recently, Wang and Castillo [17] applied this theory to forced convection turbulent boundary layers with and without external pressure gradient. Two different scalings are derived for the inner and outer regions, respectively. The temperature profiles can be written in inner and outer variables and given as

$$\frac{T_w - T}{T_{si}} = g_{si}(y_T^+; \delta_T^+) \tag{2}$$

$$\frac{T - T_\infty}{T_{so}} = g_{so}(\bar{y}_T; \delta_T^+) \tag{3}$$

Substituting Eqs. (2) and (3) into the inner and outer thermal turbulent boundary layers in the limit as $\delta_T^+ \to \infty$, the new inner and outer temperature scalings are found to be

$$T_{si} = \mathrm{Pr}\sqrt{\mathrm{St}}(T_W - T_\infty) \tag{4}$$

$$T_{so} = \frac{\delta_T^*}{\delta_T}(T_W - T_\infty) \tag{5}$$

The variables $y_T^+$ and $\bar{y}_T$ are the inner and outer similarity length scales, respectively, defined as

$$y_T^+ = \frac{yU_\infty}{\nu}\sqrt{\mathrm{St}} \tag{6}$$

$$\bar{y}_T = \frac{y}{\delta_T} \tag{7}$$

The ratio of inner to outer similarity length scales is denoted by $\delta_T^+$ and given as

$$\delta_T^+ = \frac{y_T^+}{\bar{y}_T} = \frac{\delta_T U_\infty}{\nu}\sqrt{\mathrm{St}} \tag{8}$$

The outer temperature scaling $T_{so}$ includes the term $\delta_T^*/\delta_T$, which is the ratio of the thermal displacement thickness $\delta_T^*$ to the thermal boundary layer thickness $\delta_T$. The thermal displacement thickness $\delta_T^*$ is defined as

$$\delta_T^* = \int_0^\infty \frac{T - T_\infty}{T_w - T_\infty} dy \tag{9}$$

Figures 2 and 3 show the comparison between the classical scaling and the new scaling using the ZPG and APG forced convection experimental data by Blackwell [18]. The APG experiments were performed in such a way that a power law relationship between the free stream velocity $U_\infty$ and the streamwise distance $x$ exists, i.e., $U_\infty \sim x^m$, where the power law coefficient $m$ represents the strength of the pressure gradient. A different value of $m$ means that the flow is subject to different strengths of the pressure gradient. The ZPG data are also from the experiment by Blackwell [18]. The Reynolds number based on $\theta$ varies between 515 and 2805 and the upstream wind tunnel speed is given by $U_o \approx 10$ m/s.

In the classical scaling, both the inner and outer temperature profiles were scaled with $T_\tau = q_w/\rho C p u_\tau$ where $q_w$ is the heat flux imposed at the wall and $u_\tau$ is the friction velocity. For example, Fig. 2(*a*) shows various ZPG and APG experimental data in classical variables (i.e., $T_\tau$ and $U_\tau$). Clearly, the profiles do not collapse into a single curve as one may expect in the classical view. For the experimental data with different strengths of the pressure gradient, the profiles collapse into a single curve for a given external strength of the pressure gradient; however, the collapsed profiles show different shapes as the pressure gradient changes. In contrast, the temperature profiles dimensionalized by the new scaling $T_{si} = P_r(T_w - T_\infty)\mathrm{St}^{1/2}$ show an excellent collapse over the entire boundary layer as presented in Fig. 2(*b*). Notice that all the experimental data with different Reynolds numbers and pressure gradients collapse into the same curve, especially in the near-the-wall region. Thus, the new scaling is able to capture the influences of the local heat transfer and the external pressure gradient. This fact will be shown later to play a crucial role in determining the functional forms of the temperature profiles $g_{si}$ and $g_{so}$.

Figures 3(*a*) and 3(*b*) show the same experimental data plotted in outer variables. Figure 3(*a*) shows the temperature profiles normalized by the friction temperature $T_\tau$, as given by the classical approach. Notice that for the experimental data with fixed up-

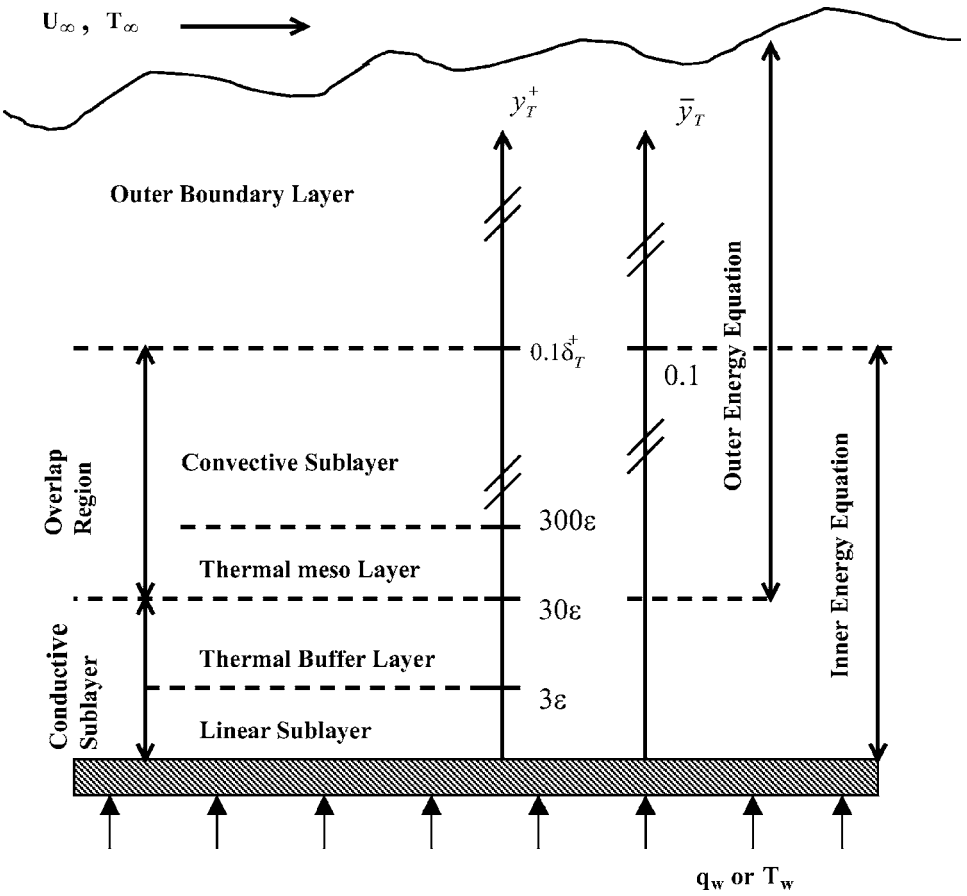


**Fig. 1 Schematic showing various regions inside the thermal boundary layer**

stream conditions and pressure gradient, the profiles collapse into one single curve. However, each of these profiles has different shapes from each other due to different external pressure gradients imposed on the flow. On the other hand, Fig. 3(*b*) shows the same experimental data using the new outer scaling $T_{so}=\delta_T^*/\delta_T(T_W-T_\infty)$. Clearly, the new scaling, compared to the classical scaling, removes all the effects of pressure gradient and the dependence on the Reynolds number given by $\delta_T^+$ in the outer flow. Therefore, all profiles collapse into a single curve regardless of these effects.

Consequently, Figs. 2(*b*) and 3(*b*) indicate that an asymptotic temperature profile exists when the profiles are scaled by the new inner and outer scalings. Nevertheless, there may be a weak dependence in the overlap region on the Reynolds number.

**2.2 Temperature Profiles in the Overlap Region.** Proper temperature scalings have been reviewed in the previous section; these scalings are able to remove most of the effects from the Reynolds number dependence and different strengths of pressure gradients. In this section, an analytical function will be derived to describe the entire temperature profile from the near-the-wall region up to the outer region of the boundary layer.

The inner and outer temperature scalings will be used in order to determine the functional dependence in the overlap region (i.e., the common region between the inner and outer flows given in Fig. 1). Figure 1 shows the diagram of different layers within the thermal boundary layer, which corresponds to various regions within the velocity layer discussed by George and Castillo [15]. According to George and Castillo [15], an overlap region is found for the velocity boundary layer within the range of $30<y^+<0.1\delta^+$. For the thermal boundary layer, an overlap region can be similarly transformed from the velocity overlap region as $30\varepsilon<y_T^+<0.1\delta^+\varepsilon$ considering $y_T^+=y^+\varepsilon$, where $\varepsilon=\sqrt{\mathrm{St}/(C_f/2)}$. The overlap region includes two sublayers: one is the convective sublayer where the conduction term has almost no effect; the other one is the thermal mesolayer where the conduction term is not negligible, and it has certain effects on the turbulent heat flux term. The temperature scalings and the functions for the inner and outer flows will be employed together in order to build the composite temperature.

George and Castillo [15] proposed the near-asymptotic method to investigate the velocity profile in the ZPG boundary layer flow. This theory will be applied for the temperature profile in the overlap region of turbulent boundary layers. According to the near-asymptotic theory, the following conditions or assumptions should be satisfied. First, at the finite Re number given by $\delta_T^+$, the temperature profile scaled in either inner or outer variables can describe the flow everywhere inside the boundary layer. Therefore, at finite Reynolds number, the inner temperature profile of Eq. (2) and the outer temperature profile of Eq. (3) must match each other, and it follows that

$$Q_T(\delta_T^+)=P_T(\delta_T^+)g_{si}+g_{so} \tag{10}$$

where

$$Q_T(\delta_T^+)=\frac{T_w-T_\infty}{T_{so}} \quad P_T(\delta_T^+)=\frac{T_{si}}{T_{so}} \tag{11}$$

for all values of $y$ and $\delta_T^+$. Second, the temperature derivatives with respect to the vertical position $y$ should also be the same whether the temperature profile is expressed in terms of inner variables or outer variables at finite Re number. Consequently, for the fixed Re number given by $\delta_T^+$, the temperature derivatives must match each other between the inner and outer regions, and it follows that

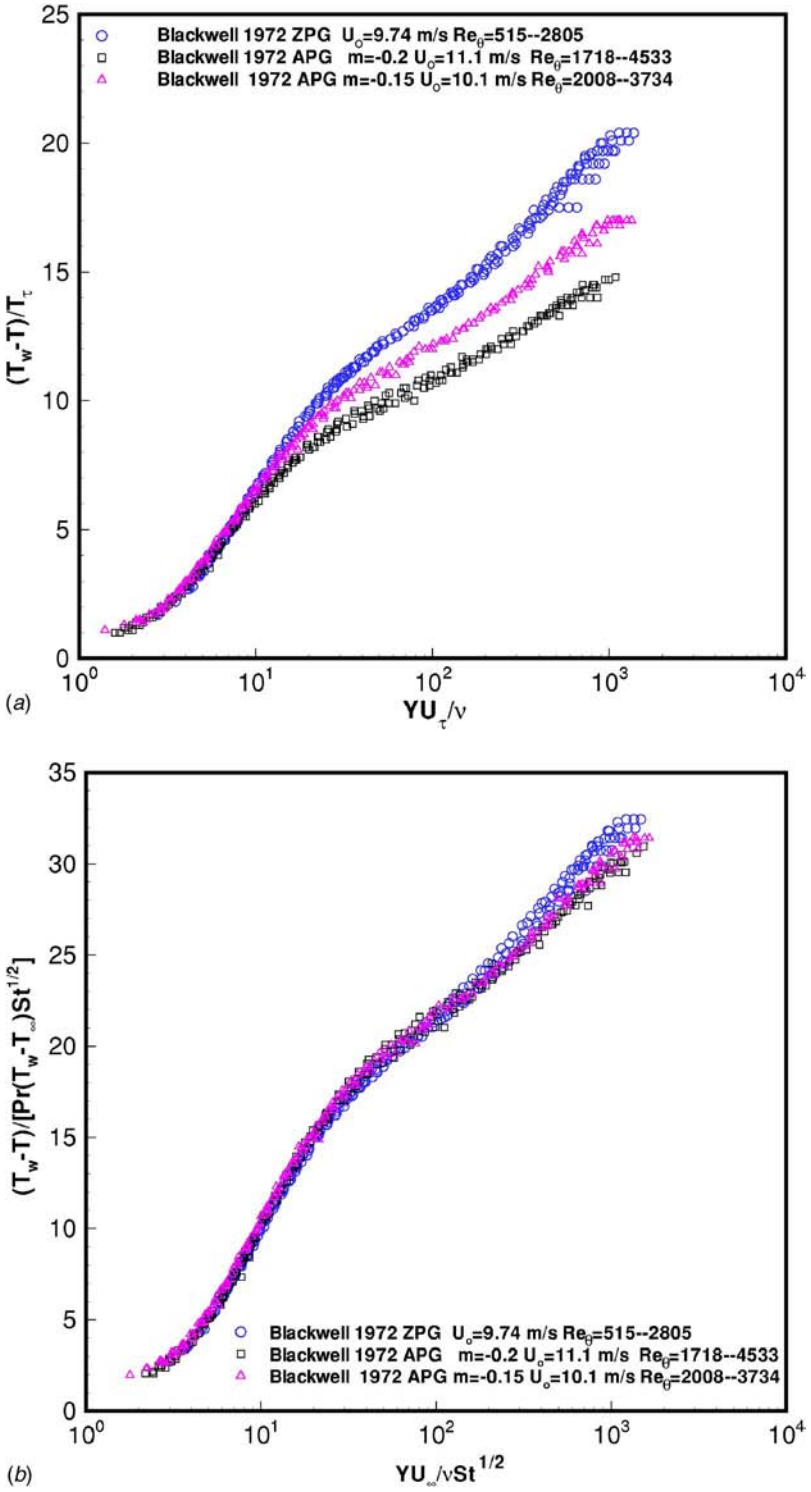


**Fig. 2 Comparisons of the temperature profiles in inner variables using the classical scaling and present scaling for ZPG and APG flows**

$$\bar{y}_T \left.\frac{\partial g_{so}}{\partial \bar{y}_T}\right|_{\delta_T^+} = -P_T(\delta_T^+) y_T^+ \left.\frac{\partial g_{si}}{\partial y_T^+}\right|_{\delta_T^+} \tag{12}$$

Since the overlap region cannot be maintained in a certain vertical position with the change of the downstream position $x$ due to the fact that the boundary layer continues to grow in this direction, an intermediate variable $\tilde{y}_T$ is introduced. This intermediate variable $\tilde{y}_T$ can be fixed in the overlap region all the way to the limit of $\mathrm{Re}\to\infty$, regardless of what is happening in the physical space according to George and Castillo [15]. Using this intermediate variable $\tilde{y}_T$, the inner and outer length scales should take the following forms;

$$y_T^+ = \tilde{y}_T \delta_T^{+n} \quad \bar{y}_T = \tilde{y}_T \delta_T^{+n-1} \tag{13}$$

where $0<n<1$. In the limit as $\delta_T^+\to\infty$, $\bar{y}_T\to 0$ and $y_T^+\to\infty$ while $\tilde{y}_T$ remains fixed in the overlap region along the boundary layer.

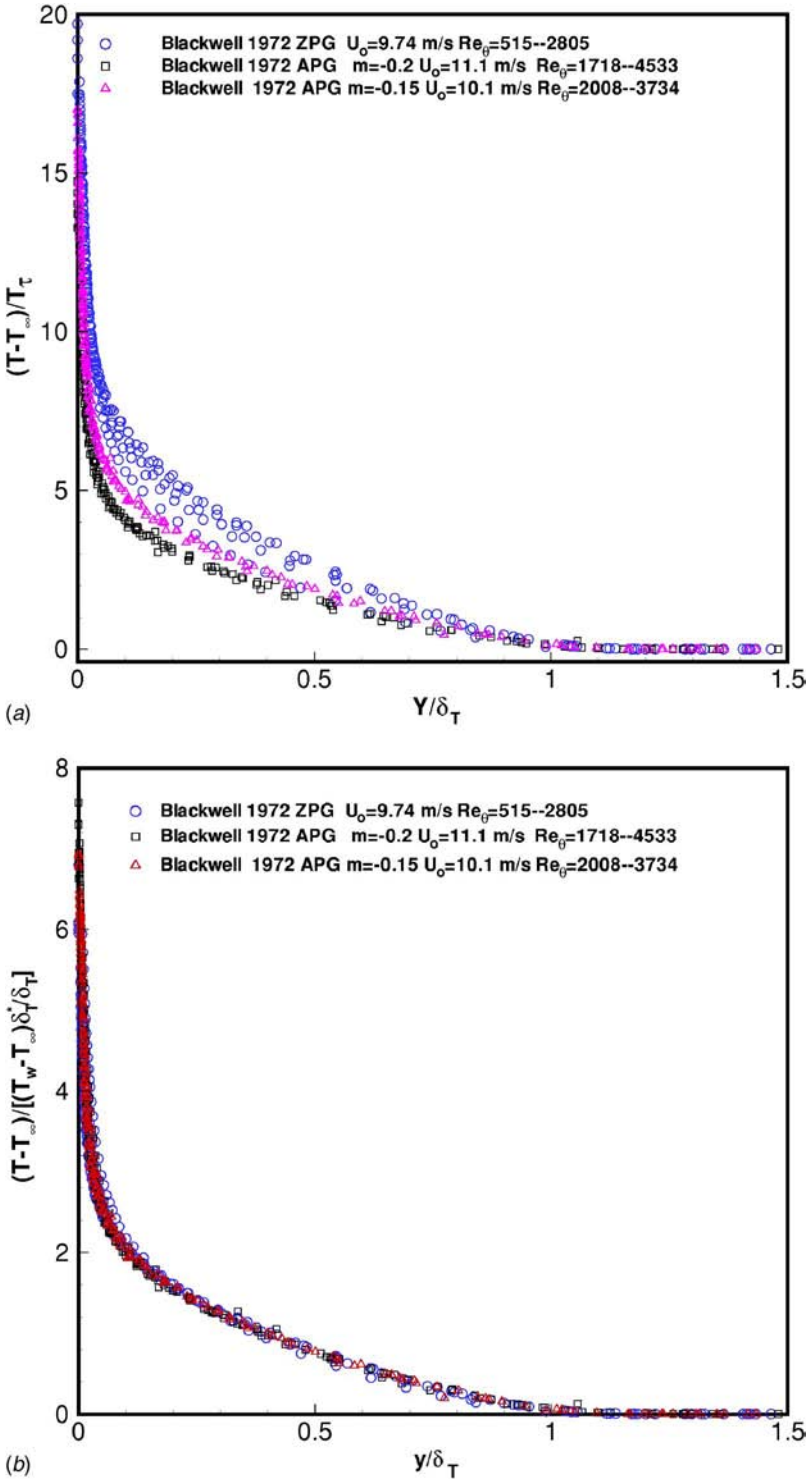


**Fig. 3 Comparisons of the temperature profiles in outer variables using the classical scaling and present scaling for ZPG and APG flows**

Therefore, the matching condition of Eq. (10) can be transformed in terms of the intermediate variable $\tilde{y}_T$ and given by

$$Q_T(\delta_T^+) = P_T(\delta_T^+) g_{si}(\tilde{y}_T \delta_T^{+n}; \delta_T^+) + g_{so}(\tilde{y}_T \delta_T^{+n-1}; \delta_T^+) \tag{14}$$

where the variables $P_T$ and $Q_T$ have the same definitions as given by Eq. (11). Differentiating Eq. (14) with respect to $\delta_T^+$ for the fixed $\tilde{y}_T$ yields

$$\left.\frac{dQ_T}{d\delta_T^+}\right|_{\tilde{y}_T} = \frac{dP_T}{d\delta_T^+} g_{si} + P_T \left[ \left.\frac{\partial g_{si}}{\partial y_T^+}\right|_{\delta_T^+} n\tilde{y}_T \delta_T^{+n+1} + \left.\frac{\partial g_{si}}{\partial \delta_T^+}\right|_{y_T^+} + \left.\frac{\partial g_{so}}{\partial \bar{y}_T}\right|_{\delta_T^+} (n-1)\tilde{y}_T \delta_T^{+n-2} + \left.\frac{\partial g_{so}}{\partial \delta_T^+}\right|_{\bar{y}_T} \right] \tag{15}$$

and clearing terms by using Eqs. (10) and (12)–(14), it follows that

$$\bar{y}_T \left.\frac{\partial g_{so}}{\partial \bar{y}_T}\right|_{\delta_T^+} = g_{so}\gamma_T + \phi_T + g_{so}\left(S_{oT} - S_{iT} + \frac{Q_T}{g_{so}}S_{iT}\right) \tag{16}$$

where

$$\gamma_T(\delta_T^+) = -\frac{\delta_T^+}{P_T(\delta_T^+)}\frac{dP_T(\delta_T^+)}{d\delta_T^+} \tag{17}$$

$$\phi_T(\delta_T^+) = -Q_T(\delta_T^+)\gamma_T - \delta_T^+\frac{dQ_T(\delta_T^+)}{d\delta_T^+} \tag{18}$$

$$S_{iT}(y_T^+, \delta_T^+) = \frac{1}{g_{si}}\left.\frac{\partial g_{si}}{\partial \delta_T^+}\right|_{y_T^+} \tag{19}$$

$$S_{oT}(\bar{y}_T, \delta_T^+) = \frac{1}{g_{so}}\left.\frac{\partial g_{so}}{\partial \delta_T^+}\right|_{\bar{y}_T} \tag{20}$$

Observe that the variables $S_{iT}$ and $S_{oT}$, as defined in Eqs. (19) and (20), represent how fast the functions $g_{si}$ and $g_{so}$ change with respect to $\delta_T^+$ for a fixed $y$ position, respectively. Both of them will vanish identically in the limit of $\delta_T^+ \to \infty$. Meanwhile, when the temperature profiles are normalized using the new scalings, as shown in Figs. 2(*b*) and 3(*d*), the temperature profiles $g_{si}$ in inner variables and $g_{so}$ in outer variables have a very weak dependence on $\delta_T^+$ in the overlap region. Therefore, the following relationship $S_{oT}=S_{iT}\cong 0$ exists in the overlap region and Eq. (16) can be written as

$$\bar{y}_T \left.\frac{\partial g_{so}}{\partial \bar{y}_T}\right|_{\delta_T^+} \cong g_{so}\gamma_T + \phi_T \tag{21}$$

The solution of Eq. (21) is a first order approximation of the outer profile, $g_{so}$. Consequently, in the overlap region, a power law solution is obtained by integrating Eq. (21) as

$$\frac{T - T_\infty}{T_{so}} = g_{so}(\bar{y}_T, \delta_T^+)|_{\text{overlap}} = C_{oT}(\delta_T^+)(\bar{y}_T + \bar{a}_T)^{\gamma_T(\delta_T^+)} + B_{oT}(\delta_T^+) \tag{22}$$

where $B_{oT}(\delta_T^+) = -\phi_T/\gamma_T$. Similarly, a power law solution expressed in inner variables can be formulated in a similar way and has the following form:

$$\frac{T_w - T}{T_{si}} = g_{si}(y_T^+, \delta_T^+)|_{\text{overlap}} = C_{iT}(\delta_T^+)(y_T^+ + a_T^+)^{\gamma_T(\delta_T^+)} + B_{iT}(\delta_T^+) \tag{23}$$

where $B_{iT}(\delta_T^+) = -\varphi_T/\gamma_T$ with $\varphi_T = \delta_T^+/P_T(dQ_T/d\delta_T^+)$, which is also a first-order approximation to the temperature profiles in the overlap region. The parameters $a_T^+$ and $\bar{a}_T$ in Eqs. (22) and (23) arise from the fact that the results should be independent of the origin shift according to George and Castillo [15] and Oberlack [22]. George and Castillo [15] used a value of −16 for $a^+$ in the ZPG velocity profile. Here, $a_T^+$ and $\bar{a}_T$ can be simply transformed from $a^+$ by $a_T^+ = \varepsilon a^+$ with $\varepsilon = \sqrt{\text{St}/(Cf/2)}$ and $\bar{a}_T = a^+(\delta/\delta_T)(1/\delta^+)$. Other coefficients such as $C_{oT}$, $C_{iT}$, $\gamma_T$, $B_{iT}$, and $B_{oT}$ are the functions of $\delta_T^+$ only. Matching the outer profile Eq. (22) and the inner profile Eq. (23) yields the following constraints given as

$$\ln \delta_T^+ \frac{d\gamma_T}{d\ln \delta_T^+} = \frac{d\ln(-C_{oT}/C_{iT})}{d\ln \delta_T^+} \tag{24}$$

and

$$B_{oT} = \delta_T/\delta_T^*(1 - \text{Pr}\sqrt{\text{St}}B_{iT}) \tag{25}$$

The solutions of the constraint given in Eq. (24) are as follows:

$$\gamma_T = \gamma_{T\infty} + \frac{\alpha A}{(\ln \delta_T^+)^{1+\alpha}} \tag{26}$$

$$\frac{C_{oT}}{C_{iT}} = \frac{C_{oT\infty}}{C_{iT\infty}}\exp\left[\frac{(1+\alpha)A}{(\ln \delta_T^+)^\alpha}\right] \tag{27}$$

where the coefficients $A=2.9$ and $\alpha=0.46$, which use the same value as the case of the velocity profile discussed by George and Castillo [15]. The coefficients $\gamma_{T\infty}$, $C_{oT\infty}$, and $C_{iT\infty}$ are the asymptotic values of $\gamma_T$, $C_{oT}$, and $C_{iT}$. These asymptotic constants will be determined from the experimental data of Blackwell [18] in the later sections.

**2.3 Temperature Profiles in the Inner Region.** In the region very close to the wall, the heat conduction term is a first order term compared to convection terms in the governing equation. Monin and Yaglom [23] have shown that the Taylor expansion of the mean temperature profile in the sublayer region has the form of

$$\frac{T_W - T}{T_\tau} = \text{Pr}[y^+ - C_4(y^+)^4 + C_5(y^+)^5 + \cdots] \tag{28}$$

where $T_\tau = q_w/\rho C_p u_\tau$. In this investigation, this Taylor's expansion will be used. A filter function of the exponential form will be adopted considering the fact that the combination of the near-wall expansion, Eq. (28), and the overlap expansion, Eq. (23), is valid up to $y^+ \cong 15$. George and Castillo [15] used a similar idea to form the inner velocity profile. An expression, which can describe the inner temperature profile, is given as

$$\frac{T_W - T}{T_W - T_\infty} = \text{Pr St}\frac{U_\infty}{u_\tau}\underbrace{[y^+ - C_4(y^+)^4 + C_5(y^+)^5]\exp[-d(y^+)^6]}_{\text{near-the-wall region}} + \text{Pr}\sqrt{\text{St}}(1 - \exp[-d(y^+)^6]) \times \underbrace{\left\{C_{iT}y_T^{+\gamma_T}\left[1 + \gamma_T a_T^+ y_T^{+-1} + \frac{1}{2}\gamma_T(\gamma_T - 1)a_T^{+2}y_T^{+-2}\right] + B_{iT}\right\}}_{\text{overlap region}} \tag{29}$$

in which the coefficients $C_4 \cong 1\times 10^{-4}$, $C_5 \cong 3\times 10^{-6}$, and the damping coefficient $d = 1\times 10^{-7}$ were obtained from the experimental data in the inner region ($0 \leqslant y^+ \leqslant 15$).

**2.4 Temperature Profiles in the Outer Region.** In order to ensure that the temperature profile is best represented in the wake region and that all the boundary conditions are satisfied, a polynomial wake function is proposed. In the present investigation, the suggested thermal wake function takes the polynomial form of $w_T(\bar{y}_T) = w_m\bar{y}_T^2 + w_n\bar{y}_T^3$, which is similar to the one used by Kader [5] and Granville [24]. Combining the power law solution in the overlap region in outer variables and the new wake function, the outer composite temperature profile is then given as,

$$\frac{T - T_\infty}{T_W - T_\infty} = \underbrace{\frac{\delta_T^*}{\delta_T}[C_{oT}(\bar{y}_T + \bar{a}_T)^{\gamma_T} + B_{oT}]}_{\text{overlap region}} + \underbrace{w_T(\bar{y}_T)}_{\text{wake region}} \tag{30}$$

The coefficients $w_m$ and $w_n$ appearing in the wake function $w(\bar{y}_T)$ depend on $\delta_T^+$, which is contrary to the assumed constant values given as $w_m=6$ and $w_n=-4$, by Kader [5] and Granville [24]. In the present derivation, the coefficients $w_m$ and $w_n$ are determined such that they satisfy the boundary layer conditions given as

$$y = \delta_T(\text{or } \bar{y}_T = 1) \Rightarrow \frac{dT}{dy} = 0 \quad \frac{T - T_\infty}{T_W - T_\infty} = 0 \tag{31}$$

Thus, using the above boundary conditions, Eqs. (31) and (30), the analytical forms of $w_m$ and $w_n$ are obtained as

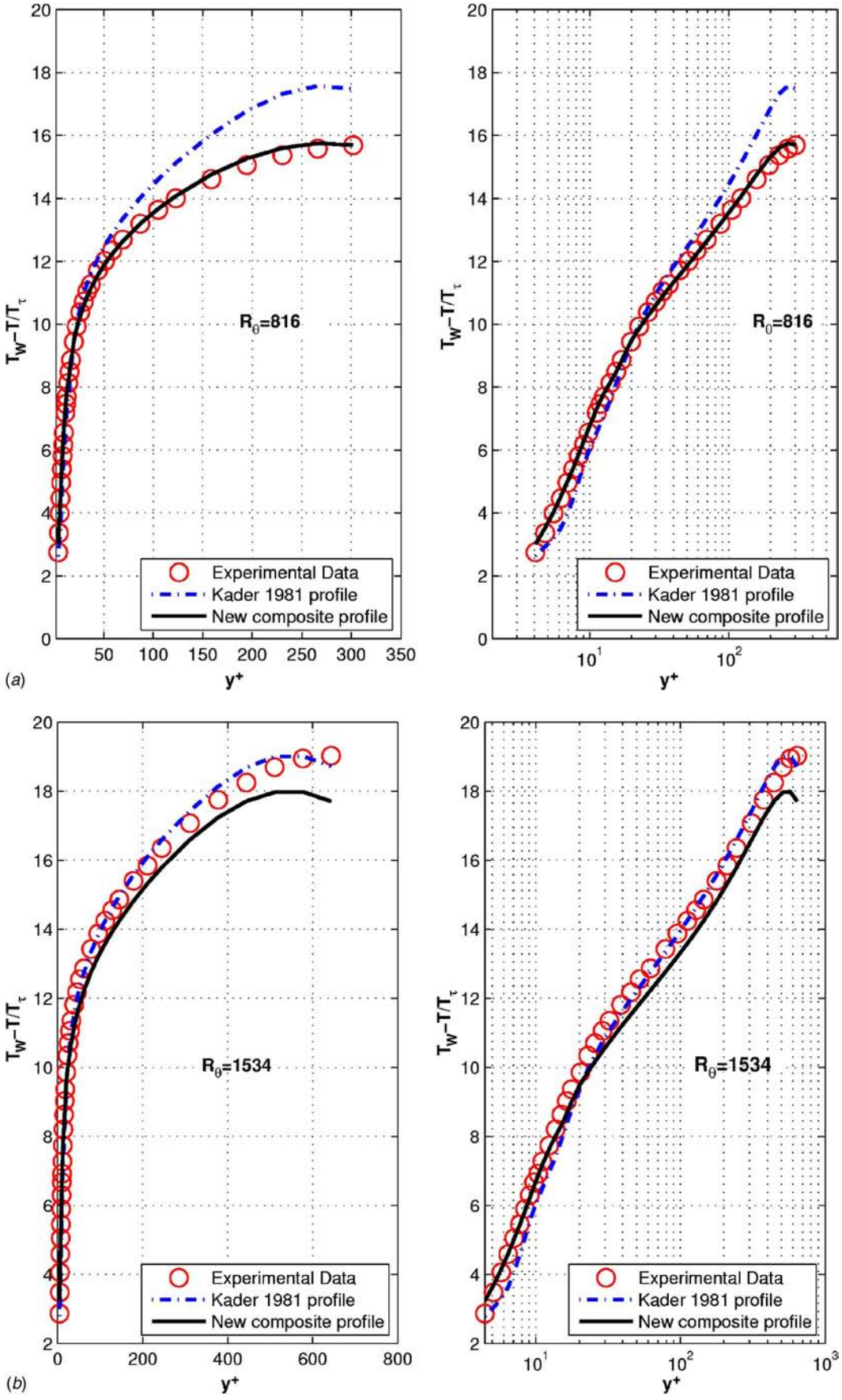


**Fig. 4 The composite temperature profile of ZPG flows: Blackwell [18]**

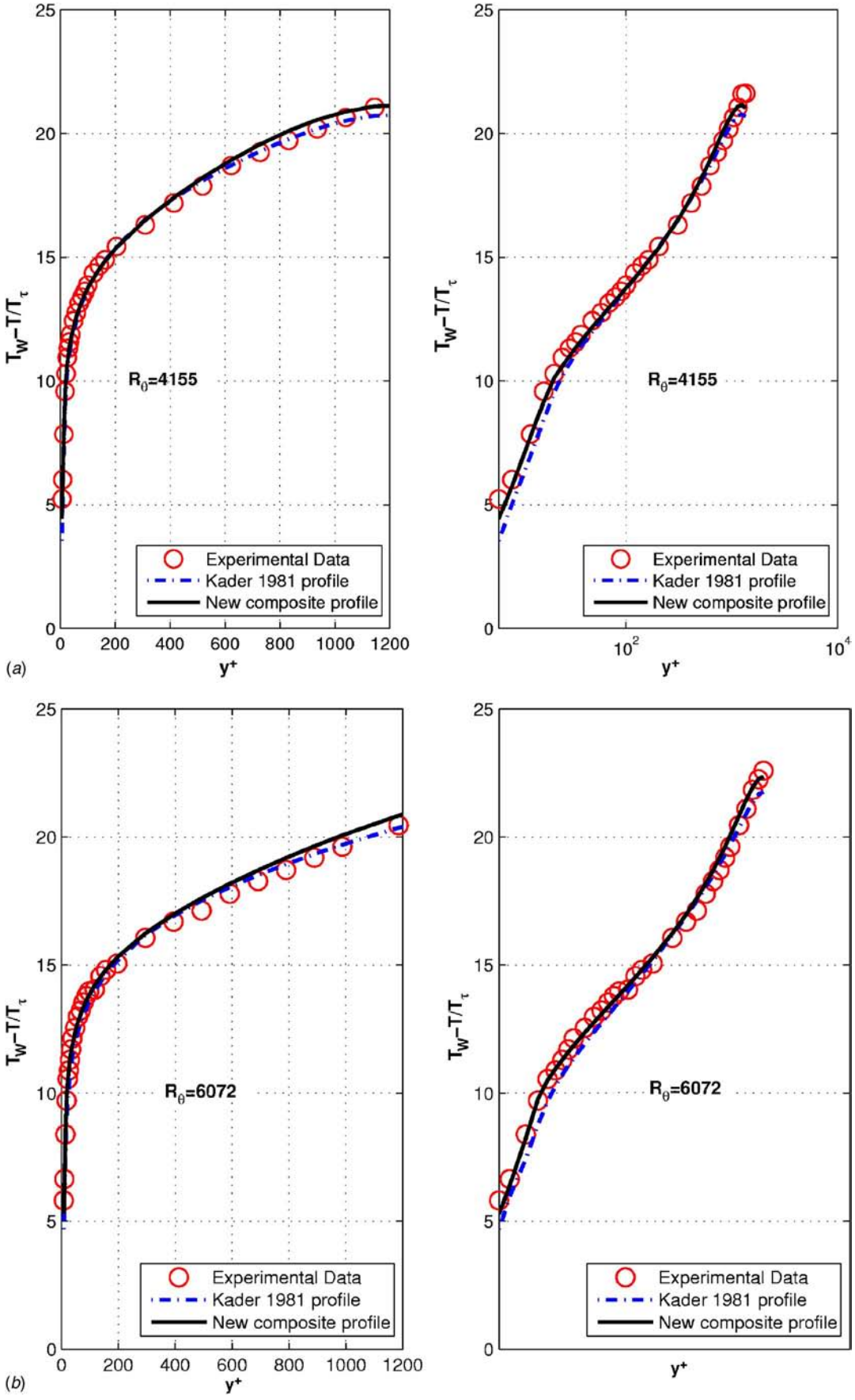


**Fig. 5 The composite temperature profile of ZPG flows: Reynolds [19]**

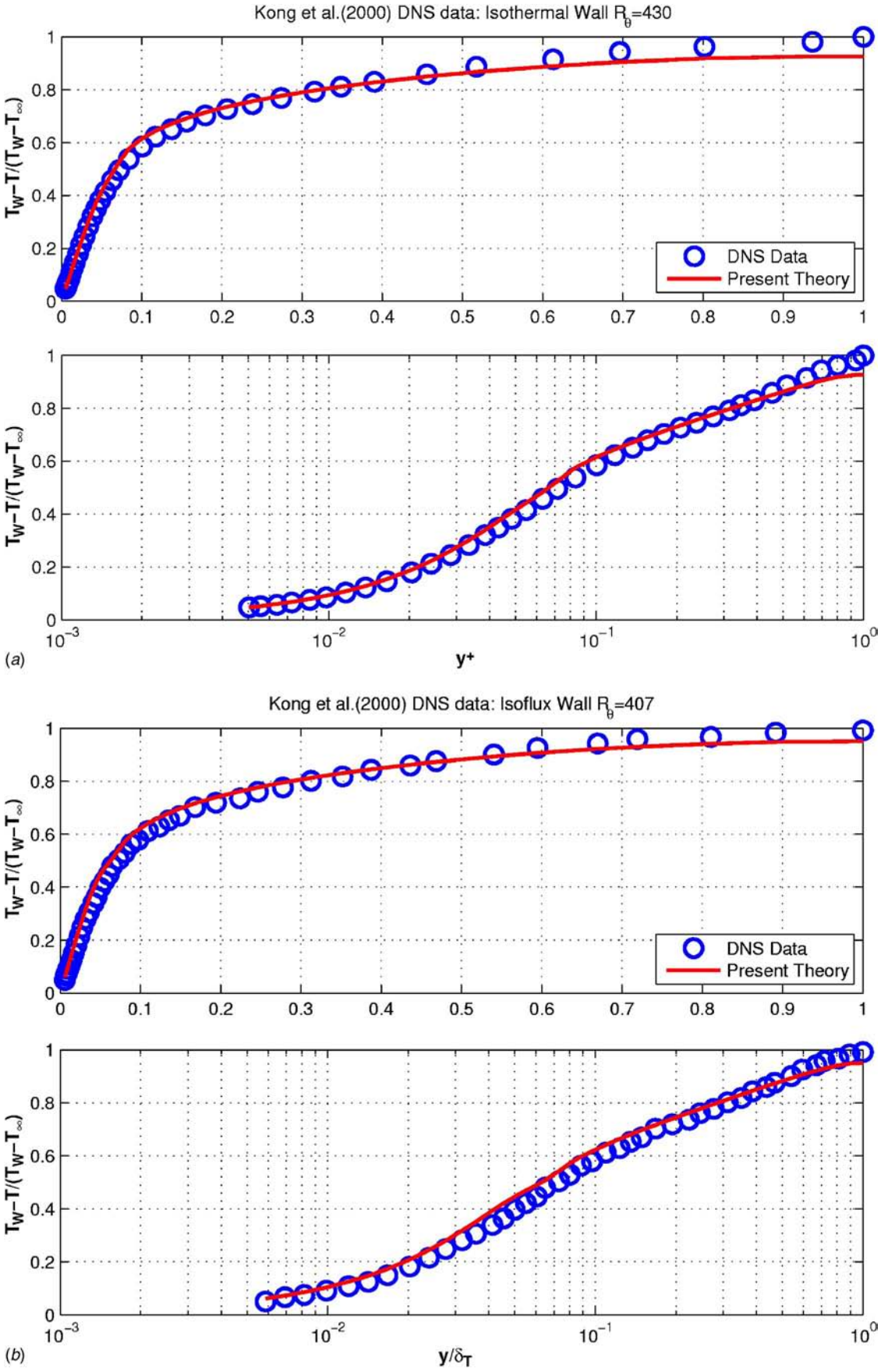


**Fig. 6 The composite temperature profile of DNS data for ZPG flows: Kong et al. [20]**

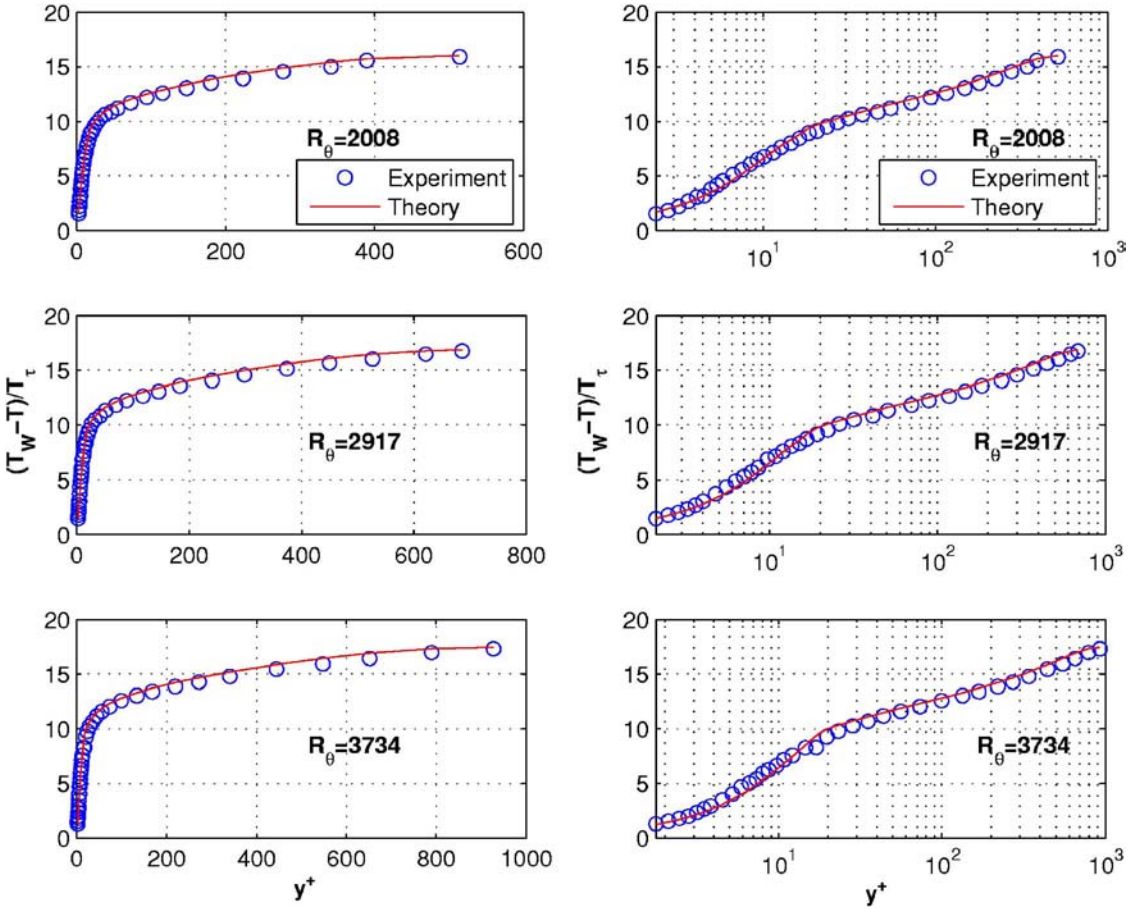


**Fig. 7 The new composite temperature profile for APG flow: Blackwell [18] $m=-0.15$**

$$w_m = -\frac{\delta_T^*}{\delta_T}[3C_{oT}(1+\bar{a}_T)^{\gamma_T} + 3B_{oT} - C_{oT}\gamma_T(1+\bar{a}_T)^{\gamma_T-1}] \quad (32)$$

$$w_n = -\frac{\delta_T^*}{\delta_T}[C_{oT}\gamma_T(1+\bar{a}_T)^{\gamma_T-1} - 2C_{oT}(1+\bar{a}_T)^{\gamma_T} - 2B_{oT}] \quad (33)$$

where $\delta_T^*/\delta_T$ is actually an integration of the dimensionalized temperature profile from the inner wall to the boundary layer edge. A constant value of $\delta_T^+/\delta_T \approx 1.45$ is obtained from the experimental data of Blackwell [18]. This constant value will be used for the other data as well.

**2.5 Composite Temperature Profiles.** Using the inner temperature profile, Eq. (29), and the outer temperature profile, Eq. (30), it is possible to construct a composite profile that describes the entire boundary layer at the finite $\delta_T^+$ number. This composite temperature profile is composed of the inner profile and the outer profile, but the profile in the overlap region, Eq. (22) or (23), has to be subtracted once to avoid repeating according to Van Dyke [25]. Hence, the composite temperature profile can be constructed in terms of the outer variables as

$$\frac{T_W - T}{T_W - T_\infty} = \underbrace{\left[1 - \frac{\delta_T^*}{\delta_T} g_{so}(\bar{y}_T, \delta_T^+)\right]}_{\text{outer region}} + \Pr\sqrt{\text{St}}\underbrace{[g_{si}(\bar{y}_T\hat{\delta}_T^+, \delta_T^+)}_{\text{inner region}}$$
$$\underbrace{- C_{iT}(\bar{y}_T\hat{\delta}_T^+ + a_T^+)^{\gamma_T} - B_{iT}]}_{\text{overlap region}} \quad (34)$$

Notice that the inner length scale $y^+$ can be expressed in outer variables as $y^+ = (\delta_T U_\tau/\nu)\bar{y}_T = \bar{y}_T\hat{\delta}_T^+$. Thus, using Eqs. (29)–(33), the composite profile, Eq. (34), can be rewritten in inner variables as

$$\frac{T_W - T}{T_\tau} = \frac{T_W - T_\infty}{T_\tau}\Bigg\{-[w_m(y^+/\hat{\delta}_T^+)^2 + w_n(y^+/\hat{\delta}_T^+)^3] + \Pr\text{St}\frac{U_\infty}{U_\tau}$$
$$\times\exp[-dy^{+6}][y^+ - C_4y^{+4} + C_5y^{+5}]$$
$$+ \Pr\sqrt{\text{St}}\Bigg\{B_{iT} + C_{iT}(y^+\varepsilon)^{\gamma_T}\Bigg[1 + \gamma_T a_T^+(y^+\varepsilon)^{-1}$$
$$+ \frac{1}{2}\gamma_T(\gamma_T - 1)a_T^{+2}(y^+\varepsilon)^{-2}\Bigg]\Bigg\}\{1 - \exp[-dy^{+6}]\}\Bigg\} \quad (35)$$

In order to use Eq. (35), the variables listed in Table 1 should be obtained from the experiments or prescribed.

This profile will be verified with the experimental data and the DNS data, and will be compared with the theoretical profile of Kader [5] shown in the Appendix of this paper.

## 3 Results

**3.1 Coefficients of the Composite Temperature Profiles.** In order to describe the experimental data using the composite pro-

**Table 1 Variables collected from experimental data**

| | |
|---|---|
| Temperature information | $T_W$, $T_\tau$, $T_\infty$ |
| Velocity information | $U_\tau$, $U_\infty$ |
| Property of fluids | Pr, $\nu$, $\rho$ |
| Boundary layer information | $\delta$, $\delta_T$ |

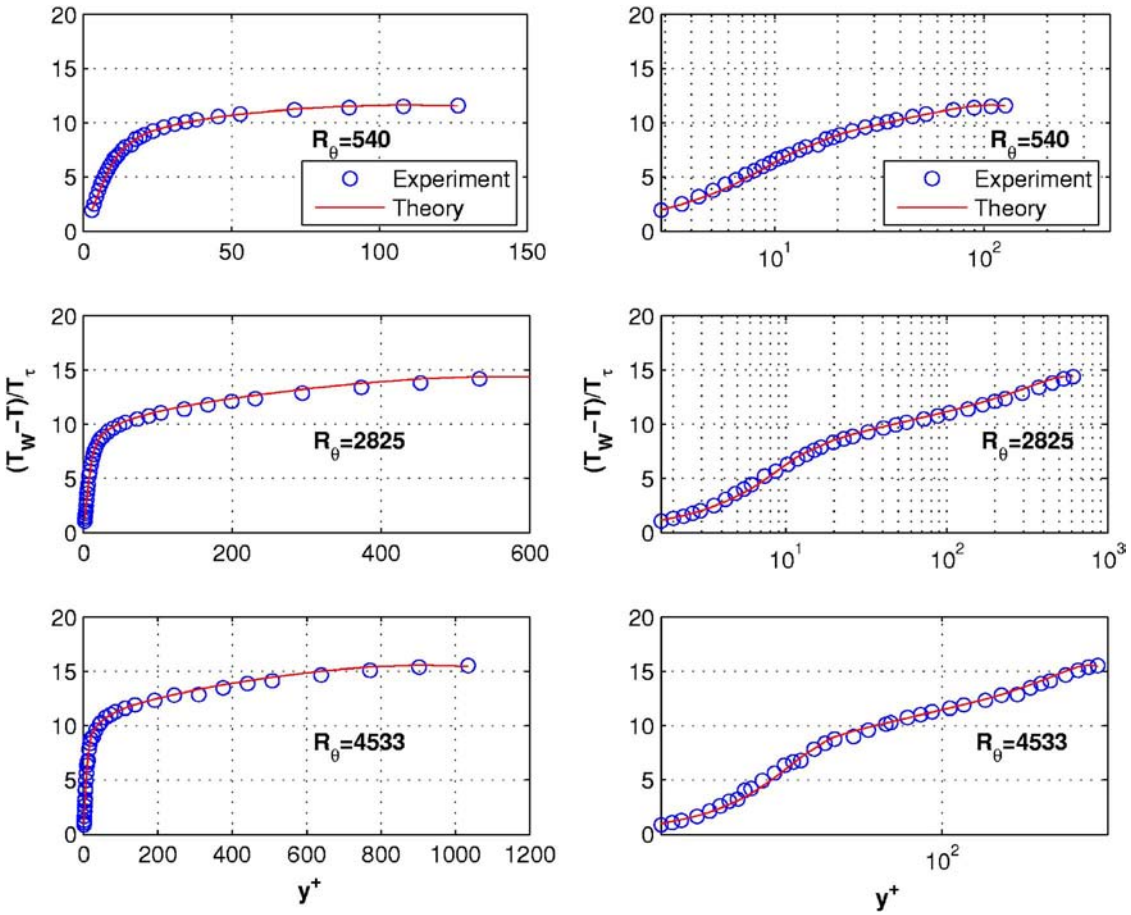


**Fig. 8 The new composite temperature profile for APG flow: Blackwell [18] $m=-0.2$**

file, Eq. (35), the correlations of $C_{oT}$, $C_{iT}$, and $\gamma_T$ need to be determined along with the constraints enforced by Eq. (24). By optimizing the experimental data of Blackwell [18], it was found that the outer coefficients $B_{oT}$ and $C_{oT}$ can be approximately described as

$$\frac{C_{oT}}{C_{oT\infty}} = 1 - 1.32\exp(-0.0226\delta_T^+) \tag{36}$$

$$\frac{B_{oT}}{B_{oT\infty}} = 1 - 0.4\exp(-0.0049\delta_T^+) \tag{37}$$

where $B_{oT\infty}=5.05$ and $C_{oT\infty}=-4.67$ for APG boundary layer flow and $B_{oT\infty}=5.9$ and $C_{oT\infty}=-5.4$ for ZPG boundary layer flow. Then, using Eqs. (27) and (36), $C_{iT}/C_{iT\infty}$ is now given as

$$\frac{C_{iT}}{C_{iT\infty}} = [1 - 1.32\exp(-0.0226\delta_T^+)]\exp\left[\frac{(1+\alpha)A}{(\ln\delta_T^+)^\alpha}\right] \tag{38}$$

Using the constraint given by Eqs. (25) and (37), $B_{iT}$ is then given as

$$B_{iT} = \frac{1}{\mathrm{Pr}\sqrt{\mathrm{St}}}\left\{1 - \frac{\delta_T^*}{\delta_T}B_{oT\infty}[1 - 0.4\exp(-0.0049\delta_T^+)]\right\} \tag{39}$$

Note that the slight difference of the coefficients between the APG and ZPG flows is due to major effects of the pressure gradient on the outer flow. The asymptotic value of the power coefficient $\gamma_{T\infty}$ is found to be a constant of 0.0827, which is same for both ZPG and APG flows considered here. Table 2 summarizes the coefficients for the composite profile, Eq. (35), for all the experimental data by Blackwell [18] with both ZPG and APG.

**3.2 Temperature Profiles.** Figure 4 compares Kader's composite profile given in the appendix with the new composite profile of Eq. (35) for the ZPG experimental data of Blackwell [18]. The reason why we used the composite profile in the inner variable is that it is convenient to compare the new results with Kader's results since the composite profile proposed by Kader is given in inner variables. In Fig. 4, the circle represents the experimental data, the dash line Kader's log-law composite profile, and the solid line the current power law composite profile. Notice that the new composite profile can describe the experimental data through the entire boundary layer within an error of less than 5%, while Kader's log law with an average error of 8%. Especially, Kader's log-law composite profile cannot predict the low Reynolds number flow well in the outer region as magnified in Fig. 4.

Figure 5 shows the ZPG experimental data of Reynolds [19] for the new composite profile of Eq. (35) and Kader's composite profile (details of this function can be found in the Appendix). Reynolds's experiment focused exclusively on the convective heat

**Table 2 The values of various coefficients in the composite profile**

| $C_4$ | $C_5$ | $d$ | $\alpha$ | $A$ |
|---|---|---|---|---|
| $1\times10^{-4}$ | $3\times10^{-6}$ | $1\times10^{-7}$ | 0.46 | 2.9 |
| $\gamma_{T\infty}$ | $-\frac{C_{oT\infty}}{C_{iT\infty}}$ | $B_{oT\infty}$ | $C_{oT\infty}$ | |
| 0.0829 | −0.12 | 5.9(ZPG)<br>5.05(APG) | −5.4 (ZPG)<br>−4.67 (APG) | |

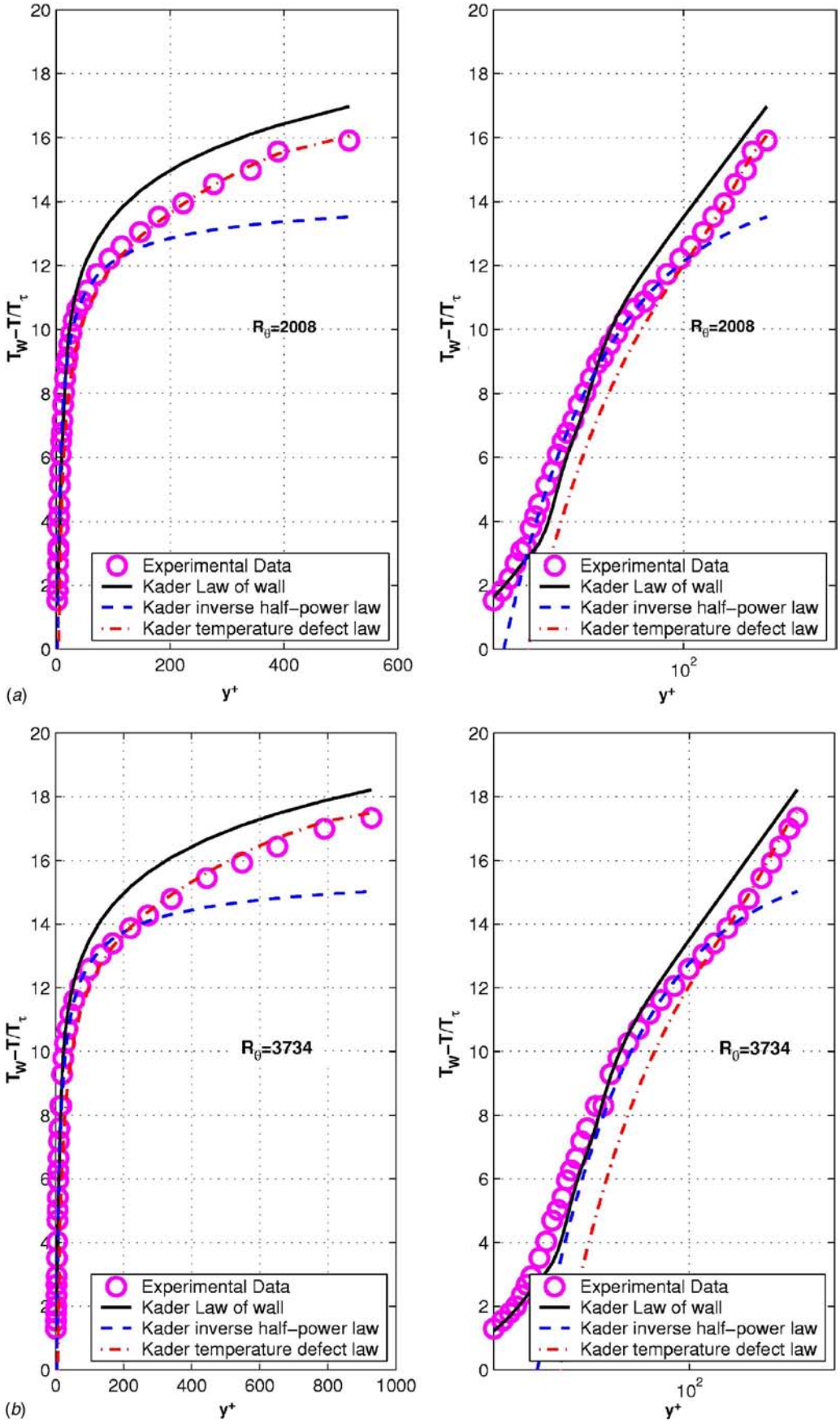


**Fig. 9 Kader's composite temperature profile for APG flows: Blackwell [18] $m=-0.15$**

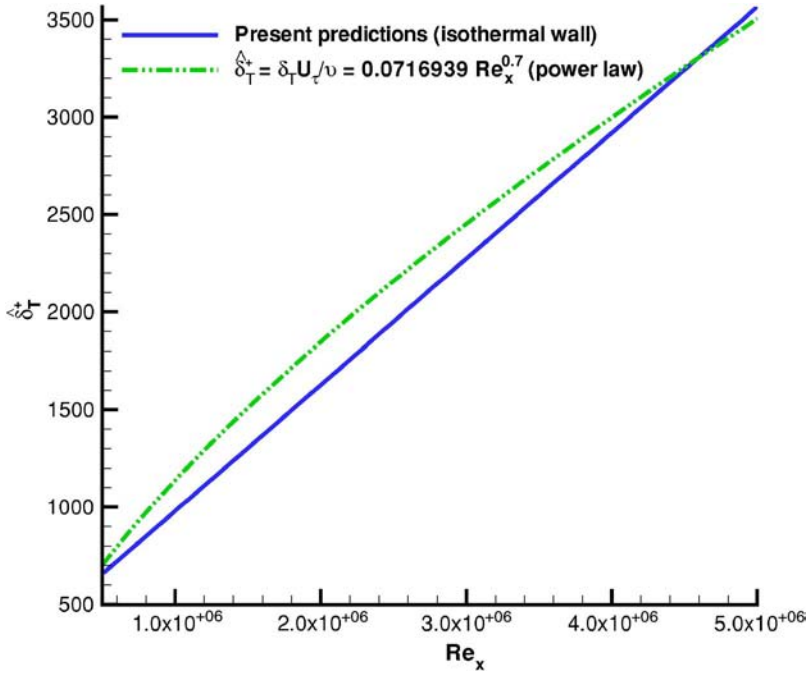


**Fig. 10 Reynolds number based on the thermal boundary layer thickness versus Reynolds number based on the *x* coordinate**

transfer from a flat plate (i.e., there is no change in the external pressure). The upstream velocity is around 30 m/s and the Reynolds number based on the momentum thickness is up to 6072. As shown in Fig. 5, the new composite profile performs better than Kader's profile in describing the experimental data, especially in the inner region. It is important to observe that this set of data was not used at all in calculating the coefficients shown in Table 2. Therefore, the accuracy of the composite profile (at least for the ZPG flow) is actually independent of the data used (i.e., Blackwell data). Moreover, it can also be generalized to describe the data with different Reynolds numbers.

Furthermore, Fig. 6 shows another independent verification of the proposed temperature profile using the DNS data by Kong et al. [20] for $Re_\theta$=407 and $Re_\theta$=430. Figure 6(*a*) shows the comparisons of the ZPG flow data on an isothermal condition and the proposed composite profile. The new composite profile can predict this DNS temperature profile very well with an average error of less than 2%. Particularly, the proposed composite profile can predict the inner region and overlap region very well. In the wake region, the maximum error between the theory and the DNS data is 8.3%. Similarly, Fig. 6(*b*) shows the comparison between the proposed temperature profile and the DNS data with a constant heat flux condition. The average error between these two profiles is less than 5%. However, in the near-the-wall region, the maximum error between the theory and the DNS data is up to 18%, which is mainly due to the fact that at such low Reynolds number, the boundary layer does not have an overlap region and is mainly composed of mesolayer.

Figures 7 and 8 show the results using the new composite profile Eq. (35) for APG flows subject to different strengths of the pressure gradients with $m=-0.15$ and $m=-0.2$, respectively. As shown in these figures, a single new composite profile can describe the entire boundary layer very well, and the average error is less than 5%. Also, a single value of each coefficient listed in Table 2 works for both APG and ZPG flows but with different Reynolds numbers.

Figure 9 shows some examples of the same experimental data but using Kader's temperature profiles [5]. The circle represents the experimental data, the solid line Kader's law of the wall (i.e., Eq. (1) in the Appendix), the dash line Kader's inverse half-power law (i.e., Eq. (A2) in the Appendix), and the dash dot line Kader's defect law (i.e., Eq. (A3) in Appendix). Notice that the exact region where each of these laws is valid cannot be determined beforehand. Therefore, each of these profiles is plotted here through the entire boundary layer. As shown in the semilog plot on the right side, Kader's defect law can only describe the outer part of the boundary layer. Kader's inverse half-power law shows a good fit for the data in the "overlap" region. However, Kader's log law shows a poor prediction in the near-wall region, which is very important in predictions of heat transfer on the wall. Therefore, the new composite profile has the obvious advantages over Kader's profiles in describing the entire boundary layer profile, especially the inner region, which is very crucial to predict the heat transfer law.

**3.3 Heat Transfer Law.** The current composite temperature profile can be applied to derive the heat transfer law. Using the integral forms of the momentum and energy equations, the Stanton number is solved for turbulent boundary layers over a flat surface.

The integral forms of momentum and energy equations in inner variables are given below as

$$\frac{d}{d\,\mathrm{Re}_x}\left[\frac{1}{(u_\tau U_\infty)}\int_0^{\delta^+}\frac{U}{U_\infty}\left(1-\frac{U}{U_\infty}\right)dy^+\right]=\left(\frac{u_\tau}{U_\infty}\right)^2 \tag{40}$$

$$\frac{d}{d\,\mathrm{Re}_x}\left[\frac{q_w}{(u_\tau U_\infty)^2}\int_0^{\hat{\delta}_T^+}\frac{U}{U_\infty}\left[\left(\frac{T_w-T_\infty}{T_\tau}\right)-\left(\frac{T_w-T}{T_\tau}\right)\right]dy^+\right]=q_w \tag{41}$$

First, the momentum equation (40) is solved by considering a Runge–Kutta procedure and using the velocity composite profile, $UU_\infty$, as well as an expression for $u_\tau U_\infty$ as a function of $\delta^+$, developed by George and Castillo [15]. In this way, the variation of the hydrodynamic boundary layer thickness as a function of the

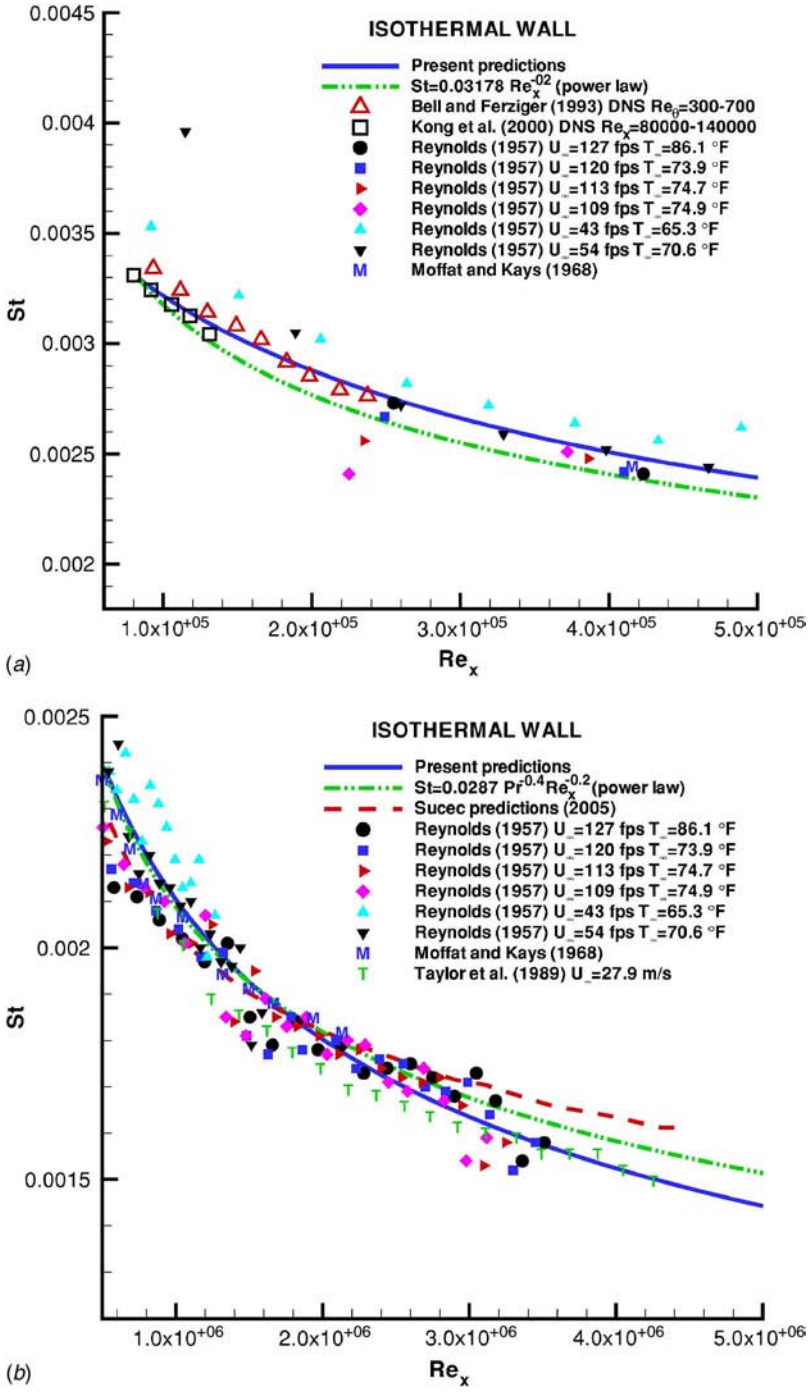


**Fig. 11 Stanton number calculated by the composite temperature profile and the integral energy equation for the isothermal data**

streamwise direction $x$ (or $\mathrm{Re}_x = xU_\infty/\nu$) is calculated along the flat plate.

Then, with the hydrodynamic solution ($\delta = f(\mathrm{Re}_x)$), the corresponding velocity profile by George and Castillo [15] and the temperature profiles developed in the present analysis given by Eq. (35), the energy equation (41) is solved in a similar manner to determine the variation of the thermal boundary layer thickness along the flat plate. Figure 10 shows the variation of the thermal boundary layer thickness normalized by the friction velocity versus the Reynolds number based on the $x$ coordinate ($\mathrm{Re}_x = xU_\infty\upsilon$) for a boundary layer flow on a flat with an isothermal wall. A comparison is performed with an empirical equation obtained from different power law curves proposed by White [26]. By using equations from White's [26] (i.e., Eqs. (6-112a) and (6-112b) of book) plus a hydrodynamic/thermal boundary layer thickness ratio in a flat plate at Pr=0.7, the following expressions are obtained:

$$C_f = 0.0592\,\mathrm{Re}_x^{-1/5} \tag{42}$$

$$\frac{\delta}{x} = 0.37\,\mathrm{Re}_x^{-1/5} \tag{43}$$

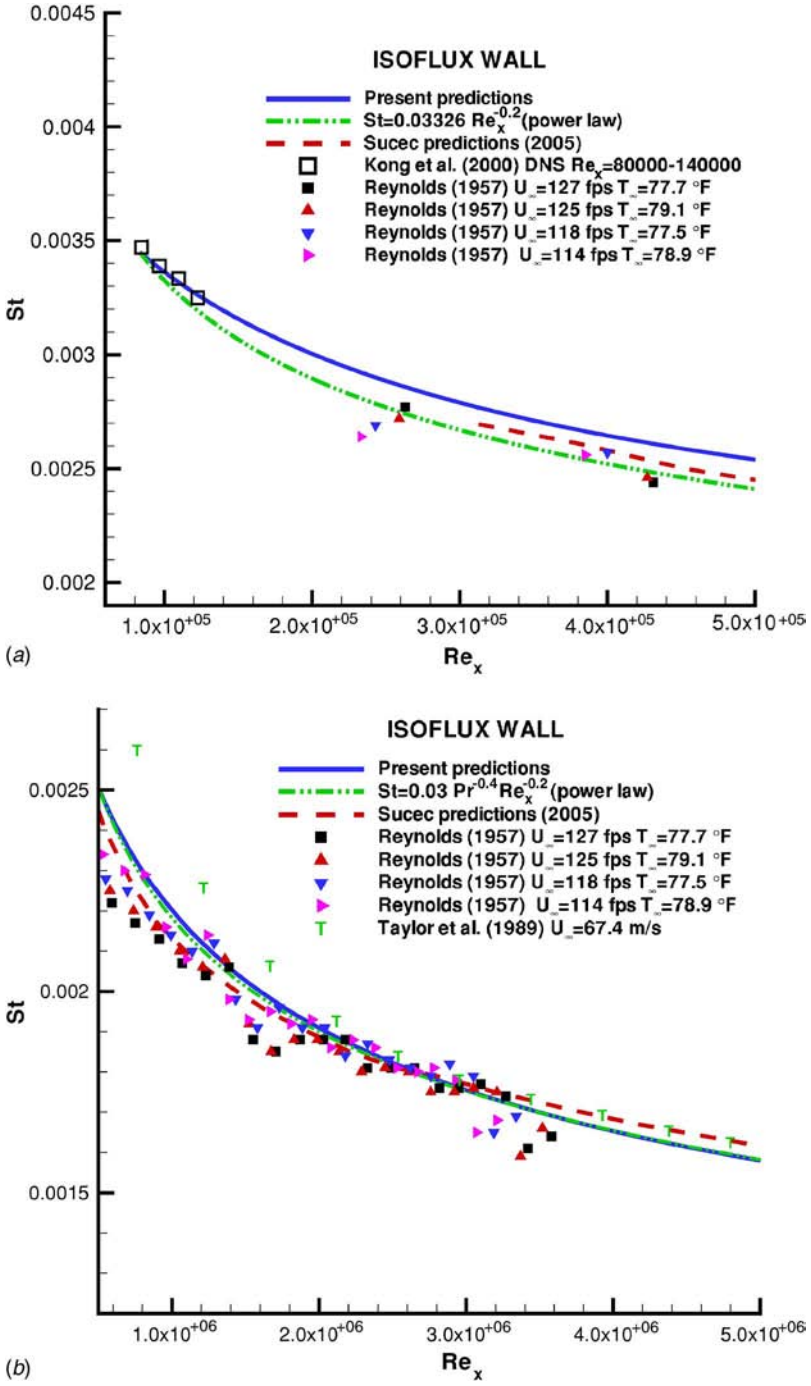


**Fig. 12 Stanton number calculated by the composite temperature profile and the integral energy equation for the isoflux data**

$$\frac{\delta}{\delta_T} \approx \mathrm{Pr}^{1/3} \tag{44}$$

$$\hat{\delta}_T^+ = 0.0716939\ \mathrm{Re}_x^{0.7} \tag{45}$$

According to Fig. 10, the maximum relative error is approximately 15% at $\mathrm{Re}_x$ equal to $2\times10^6$. For the range of Reynolds numbers considered, i.e., from $5\times10^5$ to $5\times10^6$, the average uncertainty is approximately 5%.

In solving both governing equations, it is necessary to start the marching process along the flat plate from a known point or initial conditions, i.e., finite values of the velocity and thermal boundary layer thicknesses must be specified at some location. At the leading edge of the flat plate, both thicknesses are considered zero. To avoid the discontinuity of the Stanton number at this point (infinity), calculations are started from a downstream point.

Finally, the thermal solution $\delta_T^+ = f(\mathrm{Re}_x)$ is substituted into the heat transfer law given as below

$$\sqrt{\mathrm{St}} = \frac{1}{\mathrm{Pr}}\frac{\delta_T^*}{\delta_T}\left(-\frac{C_{oT\infty}}{C_{iT\infty}}\right)\exp\left[\frac{A}{(\ln\ \delta_T^+)^\alpha}\right]\delta_T^{+-\gamma_{T\infty}} \tag{46}$$

which is obtained by matching the outer profile, Eq. (22), and the inner profile, Eq. (23), in the overlap region.

The roots of the nonlinear equation (46) are solved by the bisection method and represent the Stanton numbers at different Reynolds numbers.

Figures 11 and 12 show a comparison of the Stanton number predictions on air as a function of the Reynolds number based on the $x$ coordinate with an empirical power law, numerical results, and experimental data. All data are grouped according to different wall conditions (isothermal and isoflux) and Reynolds numbers (low and high).

Figure 11($a$) shows the results of Stanton numbers obtained at low Reynolds numbers ($80,000 < \mathrm{Re}_x < 500,000$) for an isothermal wall. A comparison is made with the empirical power law for low $\mathrm{Re}_x$ from Kays and Crawford [27], the DNS results from Bell and Ferziger [28] and Kong et al. [20], and experimental data from Reynolds [19] and Moffat and Kays [29]. The maximum deviation of the present predictions from the power law is around 4.3% at $\mathrm{Re}_x \sim 250,000$. However, the present predictions depict a better agreement with DNS results as well as with experimental data than the power law. Similarly, for the isoflux wall condition at low $\mathrm{Re}_x$, as shown in Fig. 11($b$), it is observed that there is a good agreement with DNS data from Kong et al. [20]. On the other hand, as the $\mathrm{Re}_x$ increases, the power law is a little bit closer to the experimental data from Reynolds [19] and Sucec's predictions [30] (who used the combined law of the wall and the wake function of Coles for solving the integral forms of the momentum and energy equations) than our predictions.

Figure 12($a$) depicts the results for the isothermal boundary condition at high $\mathrm{Re}_x$. The present predictions show a good agreement with the power law curve from Kays and Crawford [27] (i.e., Eqs. (12)–(14) of the book, which are valid for the range $500,000 < \mathrm{Re}_x < 5,000,000$). At higher Reynolds numbers, a slight increasing separation of the present calculations with respect to the empirical profile is observed; however, a similar trend is seen in Sucec's predictions [30]. However, the present simulations show a better agreement in this zone of high Reynolds numbers with experimental data from Taylor et al. [31] than those of Sucec [30]. Experimental data from Reynolds [19] exhibit a significant level of dispersion, which is probably due to the different upstream conditions considered. In a similar way, Figure 12($b$) shows the variation of the Stanton number at high $\mathrm{Re}_x$ but at an isoflux wall condition. An almost perfect agreement between the present predictions and the empirical power law from Kays and Crawford [27] (i.e., Eqs. (12)–(27), which are valid for the range $500,000 < \mathrm{Re}_x < 5,000,000$) is appreciated. When comparing with experimental data from Taylor et al. [31], some disagreement is obtained at lower Reynolds numbers (in the range $500,000 < \mathrm{Re}_x < 1,500,000$). A better match with experimental data from Taylor et al. [31] is observed at higher Reynolds numbers, not only for our numerical predictions but also for the Sucec's calculations. As in the isothermal case, Reynolds' experiments [19] show some dispersion, which can be reached a maximum deviation of 6% with respect to the power law. Therefore, an accurate comparison becomes difficult. In general, present predictions and Reynolds' experiments [19] show a similar trend, especially in the range of $\mathrm{Re}_x = 1,800,000 - 3,000,000$.

## 4 Conclusions

Two temperature scalings, proposed by Wang and Castillo [17], were reviewed and applied for the forced convection turbulent boundary layer by using the theory of similarity analysis and the analogy between the momentum and energy transport equations. The new temperature scalings were shown to be able to collapse the temperature profile better than the single temperature scaling proposed in the classical theory. Particulary, these scalings were able to remove the effects of Reynolds number dependence and pressure gradient on both inner and outer flows. Using the near-asymptotic theory and the new temperature scalings, a new power law solution has been obtained for the temperature profile in the overlap region by matching the inner and outer temperature profiles. Moreover, a function describing the inner region was proposed similar to the inner velocity profile proposed by George and Castillo [15], and a new wake function was proposed, which satisfies the boundary conditions in the outer region of the boundary layer. Furthermore, a composite temperature profile was formed, which is able to describe the flow over the entire boundary layer at finite Reynolds number.

This new composite temperature profile was verified by using the experimental data, the DNS data, and the theoretical profile by Kader [4,5]. It was shown that the present temperature profile shows a better prediction with an average error of less than 5% than Kader's prediction for the the same experimental data. The new composite temperature profile was also independently verified using the DNS data and the experimental data from Reynolds [19], which were not used in determining the coefficients in the temperature profile. As a result, the new composite profile shows a very good agreement with experimental and DNS data with an average error of less than 5%.

Furthermore, the new temperature composite profile was combined with the integral momentum and energy equation to calculate the Stanton number and the boundary layer growth along the streamwise direction. Various DNS data and experimental data under isothermal or isoflux boundary conditions have been used to test the newly calculated Stanton number, respectively. It was shown that the Stanton number in the power law form can predict the experimental data or the DNS data with an average error of 5%.


## Acknowledgment

The authors are very thankful to Dr. Ramona Travis from NASA Stennis Space Center for her continuous support of many of our projects.


## Nomenclature

$C_f/2$ = skin friction coefficient

$g_{so}, g_{si}$ = outer and inner temperature functions

Pr = Prandtl number, $\mathrm{Pr} = \nu/\alpha$

Pe = Peclet number, $\mathrm{Pe} = U_\infty \delta/\alpha$

$\mathrm{Re}_\delta$ = Reynolds number, $\mathrm{Re}_\delta = U_\infty \delta/\nu$

$\mathrm{Re}_\theta$ = Reynolds number based on momentum thickness, $\mathrm{Re} = U_\infty \theta/\nu$

$\mathrm{Re}_x$ = Reynolds number based on streamwise direction $x$, $U_\infty x/\nu$

$\mathrm{Re}_{\delta_T}$ = Reynolds number based on thermal boundary layer thickness $\delta_T$, $U_\infty \delta_T/\nu$

St = Stanton number, $\mathrm{St} = q_w/\rho C_p U_\infty (T_W - T_\infty)$

$T_{so}, T_{si}$ = outer and inner temperature scaling

$T_\tau$ = friction temperature, $T_\tau = q_w/\rho C_p u_\tau$

$T_\infty$ = free stream temperature

$T_w$ = wall temperature

$U_\infty$ = free stream velocity

$u_\tau$ = friction velocity, $u_\tau = \sqrt{\tau_w/\rho}$

$\bar{y}$ = outer velocity similarity length scale, $y/\delta$

$\bar{y}_T$ = outer temperature similarity length scale, $y/\delta_T$

$y^+$ = inner velocity similarity length scale, $yU_\tau/\nu$

$y_T^+$ = inner temperature similarity length scale, $yU\infty/\nu\sqrt{\mathrm{St}}$

### Greek Symbols

$\alpha$ = thermal diffusivity, $\alpha = k/\rho Cp$

$\delta$ = momentum boundary layer thickness, i.e., $\delta_{99}$

$\delta_T$ = thermal boundary layer thickness

$\delta_T^*$ = thermal displacement thickness, $\delta_T^* = \int_0^\infty T - T_\infty / T_W - T_\infty dy$

$\delta_T^+$ = ratio of outer to inner temperature length scales, i.e., $\delta_T U_\infty/\nu\sqrt{\mathrm{St}}$

$\hat{\delta}_T^+$ = ratio of classical outer to inner temperature length scales, i.e., $\delta_T U_\tau/\nu$
$\nu$ = kinematic viscosity, $\mu/rho$

**Subscripts**

$si$ = inner thermal boundary layer
$so$ = outer thermal boundary layer
$W$ = at the wall
$\infty$ = free stream

## Appendix

Kader [5] proposed the temperature profile for the turbulent boundary layer with pressure gradient. He divided the pressure gradient flow in three regions, and each region is characterized by the following equations:

- the inner region: $0 \leqslant y^+ \leqslant y_1 u*/\nu$ (the thermal law of the wall),

$$\frac{T_W - T}{T_\tau} = \Pr y^+ \times \exp(-G) + \{\beta(\Pr) + 2.12\ln(1+y^+)\}\exp(-1/G) \tag{A1}$$

- the pressure gradient region: $y_1\gamma/u_*^2 \leqslant \xi \leqslant y_2\gamma/u_*^2$ (the inverse-half-power law)

$$\frac{T_W - T}{T_\tau} = -K_1^{(\theta)}/\sqrt{\xi} + K_2^{(\theta)} \tag{A2}$$

- the outer region: $y_2/H \leqslant \eta \leqslant 1$ (the temperature defect law)

$$\frac{T_W - T}{T_\tau} = \frac{T_W - T_o}{T_\tau} - \frac{3\sqrt{Z}}{1+Z}\left(\frac{1}{\eta} - 1\right) + \frac{2.12}{1+Z}\ln\eta - \frac{15 - 3.5\sqrt{Z}}{20+Z}(2 - 6\eta^2 + 4\eta^3) \tag{A3}$$

where the coefficients $G$, $\beta(\Pr)$, $K_1^{(\theta)}$, $K_2^{(\theta)}$, the length scales $\xi$, $\eta$, $Z$, and the pressure parameter $\gamma = 1/\rho|dP/dx|$ can be found in Kader [5]. The vertical position $y_1$ is the ordinate of the intersection point for the law of the wall, Eq. (A1), and the inverse half-power law, Eq. (A2). The position $y_2$ represents the intersection point of the inverse half-power law and the temperature defect law, Eq. (A3). However, $y_1$ and $y_2$ cannot be determined unless the experimental data are plotted for all three regions. This is a major disadvantage of Kader's profile since these points ($y_1$ or $y_2$) may depend on the Pe number. It is worthwhile mentioning that Kader's work includes the effects of different Pr numbers.

## References


[1] Gad-el-Hak, M., 2000, *Flow Control: Passive, Active and Reactive Flow Management*, Cambridge University Press, Cambridge.
[2] Perry, A. E., Bell, J. B., and Joubert, P. N., 1966, "Velocity and Temperature Profiles in Adverse Pressure Gradient Turbulent Boundary Layers," J. Fluid Mech., **25**, pp. 299–320.
[3] Afzal, N., 1982, "Thermal Turbulent Boundary Layer Under Strong Adverse Pressure Gradient Near Separation, J. Heat Transfer," ASME J. Heat Transfer **104**, pp. 397–402.
[4] Kader, B. A., 1981, "Temperature and Concentration Profiles in Fully Turbulent Boundary Layers," Int. J. Heat Mass Transfer, **24**, pp. 1541–1544.
[5] Kader, B. A., 1991, "Heat and Mass Transfer in Pressure-Gradient Boundary Layers," Int. J. Heat Mass Transfer, **34**, pp. 2837–2857.
[6] Erm, L. P., and Joubert, P. N., 1991, "Low-Reynolds-Number Turbulent Boundary Layers," J. Fluid Mech., **230**, pp. 1–44.
[7] Castillo, L., and Johansson, G., 2002, "The Effects of the Upstream Conditions in a Low Reynolds Number Turbulent Boundary Layer With Zero Pressure Gradient," J. Turbul., **3**, pp. 1–19.
[8] Castillo, L., and Walker, D., 2002, "The Effect of the Upstream Conditions on the Outer Flow of Turbulent Boundary Layers," AIAA J., **40**, pp. 1292–1299.
[9] Churchill, S. W., and Chan, C., 1995, "Turbulent Flow in Channels in Terms of the Turbulent Shear and Normal Stresses," AIChE J., **41**, pp. 2513–2521.
[10] Churchill, S. W., Yu, B., and Kawaguchi, Y., 2005, "The Accuracy and Parametric Sensitivity of Algebraic Models for Turbulent Flow and Convection," Int. J. Heat Mass Transfer, **48**, pp. 5488–5503.
[11] Le, P. M., and Papavassiliou, D. V., 2006, "On Temperature Prediction at Low Re Turbulent Flows Using the Churchill Turbulent Heat Flux Correlation," Int. J. Heat Mass Transfer, **49**, pp. 3681–3690.
[12] Wei, T., Fife, P., Klewicki, J., and McMurtry, P., 2005, "Properties of the Mean Momentum Balance in Turbulent Boundary Layer, Pipe and Channel Flows," J. Fluid Mech., **522**, pp. 303–327.
[13] Wei, T., Fife, P., Klewicki, J., McMurtry, P., 2005, "Scaling Heat Transfer in Fully Developed Turbulent Channel Flow," Int. J. Heat Mass Transfer, **48**, pp. 5284–5296.
[14] George, W. K., 1995, *Some New Ideas for Similarity of Turbulent Shear Flows, Turbulence, Heat and Mass Tansfer*, Begell House, New York.
[15] George, W. K., and Castillo, L., 1997, "Zero Pressure Gradient Turbulent Boundary Layer," Appl. Mech. Rev., **50**, pp. 689–729.
[16] George, W. K., Wosnik, M., and Castillo, L., 1997, "Similarity Analysis for Forced Convection Thermal Boundary Layer," *10th International Symposium in Transport Phenomena in Thermal Science and Process Engineering*, Kyoto, Japan, Vol. 1, pp. 239–244.
[17] Wang, X., and Castillo, L., 2003, "Asymptotic Solutions in Forced Convection Turbulent Boundary Layers," J. Turbul., **4**, pp. 1–18.
[18] Blackwell, B. F., 1972, "The Turbulent Boundary Layer on a Porous Plate: An Experimental Study of the Heat Transfer Behavior with Adverse Pressure Gradients," Ph.D. thesis, Stanford University, Palo Alto.
[19] Reynolds, W. C., 1957, "Heat Transer in the Turbulent Incompressible Boundary Layer with Constant and Variable Wall Temperature," Ph.D. thesis, Stanford University, Palo Alto.
[20] Kong, H., Choi, H., and Lee, J., 2000, "Direct Numerical Simulation of Turbulent Thermal Boundary Layers," Phys. Fluids, **12**, pp. 2555–2568.
[21] Schlichting, H., and Gersten, K., 2000, *Boundary Layer Theory*, Springer, New York.
[22] Oberlack, M., 1996, "Symmetries in Turbulent Boundary Layer Flows," *Annual Research Briefs*, Center for Turbulence Research, Stanford University/ NASA Ames, pp. 183–197.
[23] Monin, A. S., and Yaglom, A. M., 1971, *Statistic Fluid Mechanics*, MIT, pp. 327–347.
[24] Granville, P., 1976, "A Modified Law of the Wake for Turbulent Shear Layers," ASME J. Fluids Eng., **98**, pp. 578–580.
[25] Van Dyke, M., 1964, *Perturbation Methods in Fluid Mechanics*, Academic, New York.
[26] White, F. M., 1974, *Viscous Fluid Flow*, 1st ed., McGraw-Hill, New York.
[27] Kays, W. M., and Crawford, M. E., 1993, *Convective Heat and Mass Transfer*, 3rd ed. McGraw-Hill, New York.
[28] Bell, D. M., and Ferziger, J. H., 1993, "Turbulent Boundary Layer DNS With Passive Scalars," *Near-Wall Turbulent Flows*, R. M. C. So, C. G. Speziale, and B. E. Launder, eds., Elsevier, Amsterdam, pp. 327–336.
[29] Kays, W. M., 1994, "Turbulent Prandtl Number-Where Are We?," ASME J. Heat Transfer, **116**, pp. 284–295.
[30] Sucec, J., 2005, "Calculation of Turbulent Boundary Layers Using Equilibrium Thermal Wakes," ASME J. Heat Transfer, **127**, pp. 159–164.
[31] Taylor, R. P., Love, P. H., Coleman, H. W., and Hosni, M. H., 1989, "The Effect of Step Changes in the Thermal Boundary Condition on Heat Transfer in the Incompressible Flat Plate Turbulent Boundary Layer," *Proceedings of the 1989 National Heat Transfer Conference*, Vol. 107, pp. 9–16.

# Heat Transfer Enhancement of Air Flowing Across Grooved Channels: Joint Effects of Channel Height and Groove Depth

**El Hassan Ridouane**
e-mail: eridouan@cems.uvm.edu

**Antonio Campo**

Department of Mechanical Engineering,
The University of Vermont,
Burlington, VT 05405

*A numerical study was conducted to investigate convective heat transfer and laminar fluid flow in the developing region of two-dimensional parallel-plate channels with arrays of transverse hemicircular grooves cut into the plates. Air with uniform velocity and temperature enters the channel whose plates are at a uniform temperature. The finite-volume method is used to perform the computational analysis accounting for the traditional second-order-accurate QUICK and SIMPLE schemes. Steady-state results are presented for parallel-plate channels with and without hemicircular grooves for comparison purposes. The study revolves around four controlling parameters: (1) the height of the channel, (2) the relative groove depth, (3) the number of grooves, and (4) the Reynolds number. A prototypical* 120-cm-*long channel contains two series of 3, 6, and 12 transverse grooves with four relative groove depths $\delta/D$ of 0.125, 0.25, 0.375, and 0.5. Three ratios of channel height to groove print diameter $H/D$ of 0.5, 1, and 2 are employed. Computations are performed for Reynolds numbers based on the hydraulic diameter ranging from 1000 to 2500. It is found that the grooves enhance local heat transfer relative to a flat passage at locations near their downstream edge. The maximum heat transfer enhancement occurs at an optimal depth of the grooves. For purposes of engineering design, generalized correlation equations for the Nusselt number in terms of the pertinent Re, $\delta/D$, and the number of grooves N were constructed using nonlinear regression theory.* [DOI: 10.1115/1.2790022]

*Keywords: parallel-plate channel, hemicircular grooves, enhanced heat transfer, vortex patterns, finite-volume methodology*

## 1 Introduction

Improvements in heat transfer augmentation levels in internal passages are useful in a variety of practical applications, including combustion chamber liners, and passages for internal cooling of turbine airfoils in gas turbine engines. In most parallel-plate channels, it is typical that the viscous fluids flow laminarly due to the combination of small-to-moderate dimensions and low velocities. The direct consequence of these factors is that the heat transfer coefficients turn out to be extremely low [1–6]. To overcome the prevalent heat transfer rates that are insufficient, one idea that has been traditionally contemplated in applied research scenarios is to install transverse fins (or ribs) onto the parallel plates normal to the main fluid flow. From thermal physics, the appendage of these fins brings forward a threefold objective: (1) to interrupt the hydrodynamic boundary layer in a periodic manner, (2) to add surface area, and (3) to invigorate the fluid mixing. Further, the partial blockage of the channel cross section increases the fluid velocity in the central part causing the flow to deflect and impinge against the large bounding plates and also against the attached fins. Obviously, the tortuous flow structure versus the heat transfer features will be highly sensitive to the layout of the fin arrangement.

Representative papers by Berner et al. [7], Webb and Ramadhyani [8], Kelkar and Patankar [9], Lazaridis [10], and Cheng and Huang [11] have dealt with the numerical computation of the heat/fluid flow characteristics in parallel-plate channels with a bundle of normal fins attached onto the bounding plates. These studies have predicted the heat transfer rates and the companion flow friction under the assumption of periodic fully developed flow. A concluding remark was that the fin lengths and the fin separation play an important role indicating that this issue had to be treated in more depth. From the standpoint of heat transfer augmentation, the consensus reached in these papers was that the staggered fin arrangement outperforms the in-line fin arrangement by a significant margin. From the physics of fluids, this trait is somehow expected because the staggered fin arrangement can force the fluid flow to deflect and impinge upon the opposite bounding plates of the channel. In contrast, the in-line fin arrangement makes the passing flow detach from the channel plates, hence reducing the heat transfer performance. In general, when compared against the base line case of a smooth parallel-plate channel, all of the papers consistently signaled that appreciable levels of heat transfer enhancement were achievable but only at the expense of creating costly pressure drops. As a consequence, this action elevates the power requirement for the pump needed to sustain the desired fluid flow in a particular channel chosen. One important comment made in Ref. [8] was that the heat transfer invigoration for gases ($\mathrm{Pr} \approx 0.7$) is not sufficient to offset the enormous pressure drop penalty that occurs. Nevertheless, from an optimistic framework, the heat transfer augmentation may be probably justified for moderate-to-high Prandtl number fluids ($\mathrm{Pr} \gg 1$) such as water, oil glycerin, and fluorocarbons.

Ghaddar et al. [12] studied an idealized two-dimensional isothermal cyclic flow in parallel-plate channels with integrated circuit protrusions. Their results showed the existence of a critical Reynolds number above which cyclic flow oscillations are ob-

Contributed by the Heat Transfer Division of ASME for publication in the JOURNAL OF HEAT TRANSFER. Manuscript received November 30, 2006; final manuscript received June 15, 2007; published online February 4, 2008. Review conducted by Anthony M. Jacobi.

  

served with increased fluid transport. Ghaddar et al. [13] used two-dimensional non-isothermal predictive methods to illustrate the potential for naturally enhancing heat transfer by exploiting the unsteadiness observed previously by Ghaddar et al. [12]. Amon and Mikic [14] and Amon [15] extended the above work [12,13], and embarked on the comparison of heat transfer enhancement for flows where oscillations are induced passively and naturally above the critical Reynolds number value.

The present study deliberately avoids the flow perturbation concept caused by inserting an array of inward fins located perpendicular to the channel plates. Instead, the study focuses on the opposite idea, that is adding an array of transverse grooves (i.e., cavities pointing outward) onto the parallel plates forming the channels. Related articles that touch upon this subject are those of Wirtz et al. [16], Greiner et al. [17–20], and McGarry et al. [21]. Navier–Stokes simulations of two-dimensional and three-dimensional flow and augmented convection in a fully developed, symmetrically grooved passage were performed by Greiner et al. [17–20] using the spectral element technique. The evolution of the velocity and temperature fields was presented for Reynolds numbers ranging from 180 up to 1800. The two-dimensional simulations conducted by the authors did not accurately predict the spatially and temporally averaged friction factor for $\mathrm{Re} > 400$, or the heat transfer for $\mathrm{Re} > 1000$. At low Reynolds number flows, the two geometric configurations showed little or no heat transfer enhancement in comparison with the standard smooth parallel-plate channel. However, with gradual increments in the Reynolds number, longitudinal vortices appeared, and these vortices increased in size giving rise to appreciable heat transfer intensification.

In recent years, attention has been turned to semispherical dimples impressed on the surfaces of parallel-plate passages. It has been demonstrated that these attachments produced important heat transfer enhancement with relatively small pressure drop penalties [22–24]. These authors considered different dimple shapes and layouts to obtain maximum heat transfer with minimal pressure drop accretion. Won and Ligrani [25] and Park et al. [26] studied numerically the turbulent air flow in asymmetrical channels with dimples placed on the bottom and a smooth upper plate. The computations were carried out with a standard $k$-$\varepsilon$ turbulence model under the platform of the commercial code FLUENT. Their numerical results showed the presence of centrally located vortex pairs near the spanwise edges of the individual dimples. Also, the fluid within and near the vortices contains augmented magnitudes of eddy diffusivity for momentum and heat.

The body of the present paper is divided into three sections. The first section describes the two proposed grooved systems along with the mathematical formulation for both. The computational procedure, the grid sensitivity analysis, and the code validation are explained in the second section. A discussion of the velocity and temperature fields via velocity vector plots and isotemperature plots is reserved for the third section. All the calculations are performed assuming that the flow is steady. Also included in this section is the quantification of the ultimate design quantity, the mean heat transfer coefficient, or its equivalent, the mean Nusselt number. Undoubtedly, this cumulus of local and global information will provide valuable guidance to engineers engaged in the design of ducts for heat exchange devices and/or electronic equipment.

## 2 Problem Description

The schematic in Fig. 1 illustrates a two-dimensional parallel-plate channel containing a series of equally spaced, variable-depth transverse grooves placed onto each plate. Two basic configurations were studied, one with symmetric grooves in Fig. 1(*a*) and the other with nonsymmetric or staggered grooves in Fig. 1(*b*). Also, two series with 6 and 12 hemicylindrical transverse cavities are studied. For these tests, the total length of the channel is maintained and the distance between the cavities is varied. The spacing between the cavities for 6 and 12 cavity geometries is described in Fig. 1(*c*). Shown also in the companion Fig. 2 are the geometric details of the grooves considered. The channel is 120 cm long with variable height $H$, which can be 1 cm, 2 cm or 4 cm. The groove width is $D=2$ cm with four groove depths $\delta$ such that $\delta/D=0.125$, 0.25, 0.375, and 0.5. Three ratios of channel height to groove width of $H/D=0.5$, 1, and 2 are employed. At this juncture, it is worth noting that the hydraulic diameter $D_h$ does not account for the localized increased cross sections caused by the sequence of grooves. This decision is beneficial because it permits a direct comparison of the magnitudes of the heat transfer coefficients for grooved channels with that for the smooth channel retaining the same value of Re, the base line case. Six combinations consisting of 3, 6, and 12 grooves with in-line and staggered arrangements are studied. For these tests, as already mentioned, the length of the parallel-plate channel is maintained constant while the distance between two consecutive grooves is varied.

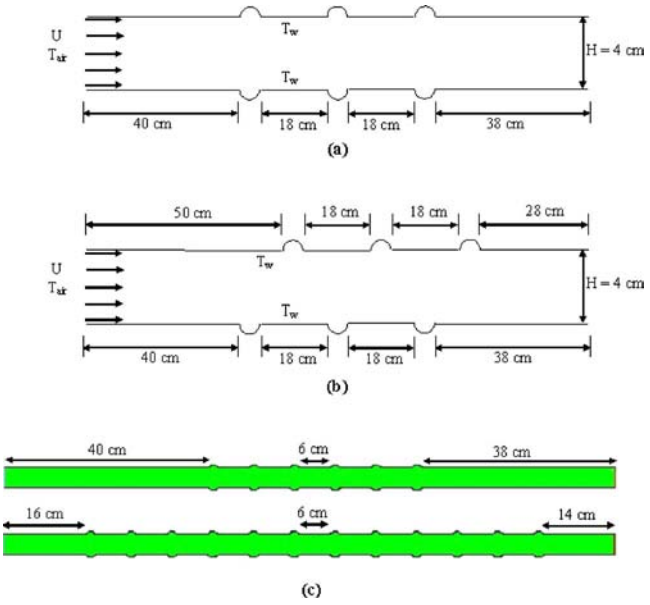


**Fig. 1 Schematic of the physical systems: (*a*) symmetric arrangement, (*b*) staggered arrangement, and (*c*) spacing between 6 and 12 cavities**

## 3 Computational Procedure

The computational grid is developed using quadrilateral elements aligned with the main airflow direction. This layout seeks to reduce the numerical diffusion errors and thus improve the quality of the numerical predictions for velocity and temperature. The regions near the plates and near the grooved surfaces are meshed with fine grids to resolve the typical high velocity and temperature gradients that normally occur there. To attain grid-independent solutions, a critical test will be conducted on a channel with 12 grooves with the largest relative depth $\delta/D=0.5$. Herein, a total of 155,000 quadrilateral elements is employed for the entire flow domain. For other configuration combinations with the relative depths $\delta/D$ of 0.25 and 0.5, the grid-independent mesh sizes are summarized in Table 1. By performing a grid sensitivity analysis, numerical errors are minimized to ascertain that the proper number of quadrilateral elements is employed. The numerical uncer-

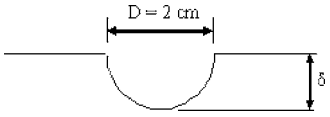


**Fig. 2 Geometry of the hemicircular grooves**

**Table 1 Computational grids employed for different channels with relative cavity depths $\delta/D$ of 0.25 and 0.5**

| Number of cavities | Relative cavity depth $\delta/D$ | Mesh |
|---|---|---|
| 0 | 0 | 88,000 |
| 3 | 0.25 | 109,000 |
| | 0.5 | 113,000 |
| 6 | 0.25 | 122,000 |
| | 0.5 | 128,000 |
| 12 | 0.25 | 141,000 |
| | 0.5 | 155,000 |

tainty for the axial and transverse velocity components was less than 2%, while for the local wall heat flux, it was less than 4%. A portion of the computational grid around the second groove of a three-groove channel employed is shown in Fig. 3.

The finite-volume method attributable to Patankar [27] is implemented to perform the computational analysis, with the tandem of second-order-accurate QUICK and SIMPLE schemes used for the discretization of the convective term in the conservation equations and the pressure-velocity coupling, respectively.

Under the assumption of no fluid slippage at the channel plates, the full, steady, two-dimensional conservation of mass and momentum equations are written in vector form as

$$\nabla \cdot (\rho v) = 0 \tag{1}$$

$$\nabla \cdot (\rho v v) = -\nabla p + \nabla \cdot (\nu \nabla v) = 0 \tag{2}$$

A uniform velocity was imposed for the inlet boundary condition and a constant pressure of zero gauge for the outlet boundary condition.

The conservation of energy equation in vector form is

$$\nabla \cdot (\rho c_P v T) = \nabla \cdot (k \nabla T) \tag{3}$$

Constant temperature boundary conditions are assigned to this equation. The plate temperature including the groove surfaces is maintained at $T_w = 320$ K, whereas the air enters the channel at a lower temperature $T_i = 280$ K, creating a temperature imbalance of $\Delta T = T_w - T_i = 40$ K.

In the above system of Eq. (1)–(3), the relation between the air density $\rho$ and the temperature $T$ obeys the ideal gas equation of state. The air viscosity $\mu$ and the air thermal conductivity $k$ are permitted to vary according to the standard power law described in Ref. [28]. The air specific heat capacity $c_p$ is taken as constant over the expected temperature range $\Delta T$.

Local convergence was assessed by point monitoring the axial velocity $u$ and the temperature $T$ in the vicinity of the first and last grooves at each plate. Global convergence was monitored by the residuals of the mass, momentum, and energy conservation equations (1)–(3) by setting its variations to less than $10^{-6}$.

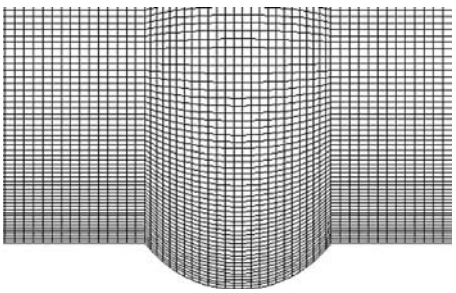

**Fig. 3 A portion of the computational grid showing the distribution of elements in a groove/channel with $\delta/D = 0.25$ on the lower plate of a channel with three grooves onto each plate**

Validation of the numerical code was done by reproducing the simultaneous development of velocity and temperature $u(x,y)$, $v(x,y)$, and $T(x,y)$ in a simple parallel-plate channel with smooth surfaces. For this fundamental case, the set of boundary conditions involves constant inlet velocity, constant inlet temperature, and equal plate temperatures. Based on the same hydraulic diameter, good agreement for the axially changing friction factor and the axially changing Nusselt number reported in Ref. [29] was found. For a fully developed condition, the asymptotic friction factor $f_\infty \mathrm{Re}/4 = 24$ and the asymptotic Nusselt number $\mathrm{Nu}_\infty = 7.54$ are recovered.

All numerical computations are steady and performed for Reynolds numbers based on the channel hydraulic diameter ranging from 1000 to 2500. The Prandtl number for air is set at 0.7.

## 4 Channel With Fixed Height $H = 4$ cm

**4.1 Fluid Flow.** Figure 4 depicts the airflow structure induced by the grooves incrusted onto the plates of the channel. Shown in Figs. 4(*a*) and 4(*b*) on the left are the velocity vector plots near the lower surface of the central groove in a channel with three grooves with a relative groove depth $\delta/D = 0.25$ at Reynolds numbers of 1000 and 2500, respectively. The observed flow inside the groove region is representative of flows in other two grooves throughout the channel domain. Vortical structures are observable leading to fluid recirculation in the clockwise direction (counterclockwise direction for grooves on the top plate). The velocity vector sizes are proportional to the velocity magnitudes. Within the groove, the velocity magnitudes are much smaller than the average velocity in the channel. However, the velocity vectors are largest in the central region of the channel as well as downstream of the groove. When the Reynolds number is increased to 2500, the qualitative structure of the vortex in Fig. 4(*b*) stays the same as in Fig. 4(*a*) despite an increment in the velocity magnitudes by a factor of 2.

The right parts of Fig. 4 display the isotherm contours for the same two Reynolds numbers cited above 1000 and 2500. The effect of the vortex formation on the temperature distribution can clearly be seen in the regions where the vortices form. The presence of high temperature gradients is noticeable on the flat surface downstream.

For a fixed Re, doubling the relative groove depth $\delta/D$ from 0.25 to 0.5 results in a larger vortex size, but owing smaller velocity magnitudes. The thermal boundary layer is not as thin near the downstream rim of the groove and on flat surface downstream as for $\delta/D = 0.25$.

The effect of the hydraulic diameter (not presented) on the flow is characterized by high fluid velocities as $D_h$ decreases, implying a high vortex strength. For all cases considered, the groove arrangements (symmetrical or staggered) do not seem to affect the flow structure.

**4.2 Heat Transfer.** Relying on the same grooved channel, the comparison between the symmetrical and staggered groove arrangements revealed subtle differences in terms of heat transfer. In light of this, the results for the staggered arrangements will be presented for the channel with three grooves only. Here again, the Reynolds numbers attaining intermediate values from 1000 to 2500 have been tested with each type of groove array and relative groove depth.

*4.2.1 Local Wall Heat Flux.* Preliminary heat transfer results are obtained with a smooth parallel-plate channel at the same Reynolds numbers. These base line values constitute a reliable base line solution for comparison. The height $H$ in the grooved parallel-plate channel is measured between the flat portions of the plates. The two-part Fig. 5 displays the axial variation of the wall heat flux $q_w$ in the smooth channel and in a channel with 12

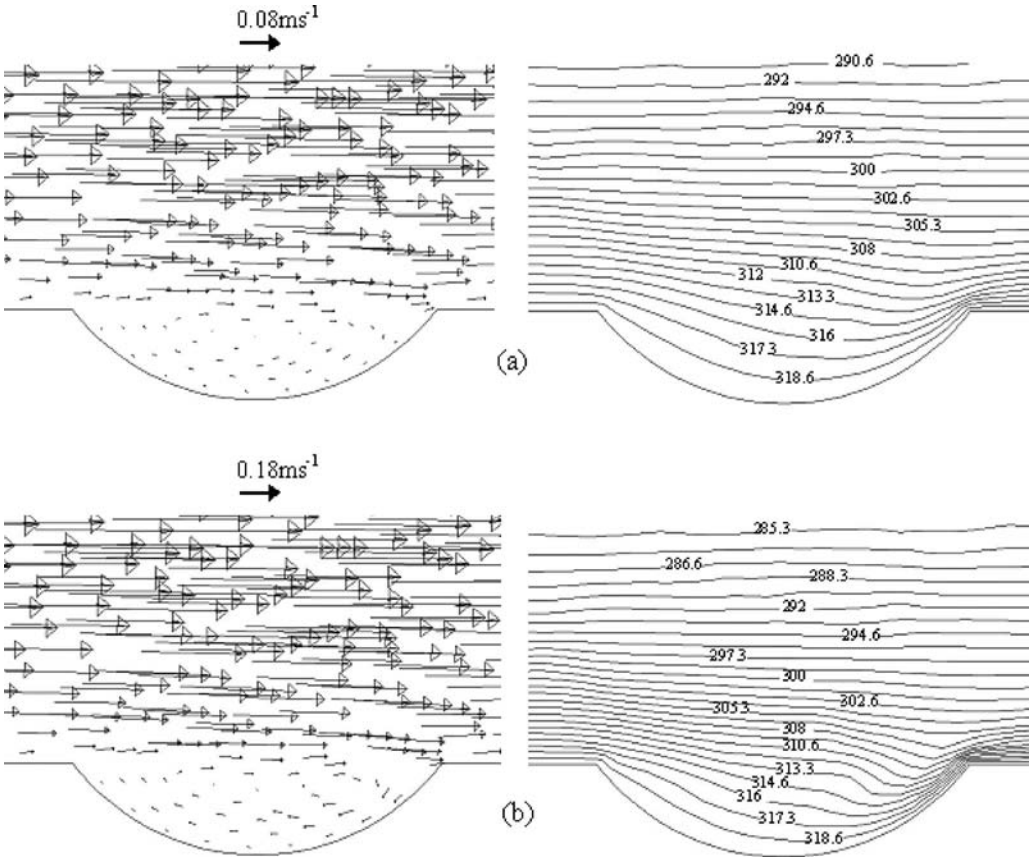


**Fig. 4 Velocity vectors and isotherms inside a shallow groove with half radius depth $\delta/D=0.25$: (*a*) Re=1000($\bar{u}=0.198$ m s$^{-1}$) and (*b*) Re=2500 ($\bar{u}=0.496$ m s$^{-1}$)**

grooves for two relative groove depths $\delta/D=0.25$ and 0.5 at a given Re=2500. Note that in the figure, the air moves from left to right.

As expected, the thin thermal boundary layer in the standard channel with smooth plates produces very high local heat flux $q_w$ at the origin of the entrance region. In the vicinity of $x=0$, $q_w$ decreases rapidly and approaches asymptotically the fully developed condition given in Ref. [29].

Inspection of Fig. 5(*a*) reveals that the shape of the $q_w$ curves related to channels with grooves is very complex. The $q_w$ curve is in general characterized by an oscillatory line composed of pronounced peaks preceded by moderate valleys at each groove. For a better scrutiny between the two contrasting curves (smooth channel versus grooved channel), results are zoomed in Fig. 5(*b*) for the first groove starting at $x=0.16$ m and for the second groove starting at $x=0.24$ m. It is noticeable that the peaks for the highest local heat fluxes are located downstream of the grooves. This is due to the high vorticity that takes place at these particular locations. Valleys with low local heat flux are then located within the two grooves. The tendency exhibited by the numerical $q_w$ results has been confirmed experimentally by Mahmood and Ligrani [22] and Burgess et al. [30] for a somewhat related channel but having hemispherical dimples.

Regarding the $q_w$ curve around the first groove with $\delta/D=0.25$, the minimum $q_w$ is about 150 W/m$^2$ less than the counterpart $q_w$ for the standard channel. However, the maximum $q_w$ is about 500 W/m$^2$ higher. The effect of the relative depth on the heat flux is obvious and the $q_w$ curve related to $\delta/D=0.5$ lies always underneath its counterpart curve related to $\delta/D=0.25$. This result is attributed to the fact that stronger vortex exists in the shallow groove. One further point should be noted about the groove locations with respect to the channel inlet: The magnitude of the extreme values of the peaks rises as the cavity location is closer to the inlet. However, the heat transfer enhancement compared to the standard channel stays invariant with respect to the groove locations because both increments in the extreme values compensate each other.

*4.2.2 Mean Nusselt Number*. The mean Nusselt number is defined as

$$\overline{\mathrm{Nu}}=\frac{Q}{(T_w-T_i)}\left(\frac{D_h}{k}\right) \tag{4}$$

where $Q$ is the mean wall heat flux per total area and $k$ is the air thermal conductivity evaluated at the reference temperature $T_0=(T_w+T_i)/2$. The other two quantities $(T_w-T_i)$ and $D_h$ appearing in Eq. (4) are fixed.

Collectively, Fig. 6 illustrates the monotonic increasing (almost linear) variations of the mean Nusselt number Nu with the Reynolds number Re for the two related channels, one with three symmetric grooves and the other with three staggered grooves. Here, the emphasis is put on the heat transfer enhancement of the two distinct groove arrangements.

The lowermost Nu-curve representative of the smooth channel presents the expected monotonic increase with Re in the whole Re range. This Nu-Re relation has been confirmed with the literature values of Ref. [29].

The semicircular grooves with relative depth $\delta/D=0.5$ supply a very limited heat transfer enhancement as reflected in a Nu value of about 5% at a low Re=1000 and of 6% at a high Re=2500. It can be anticipated that for practical purposes, both arrangements, symmetrical and staggered, presented similar levels of heat transfer enhancement.

When the relative groove depth is halved to $\delta/D=0.25$, the pair

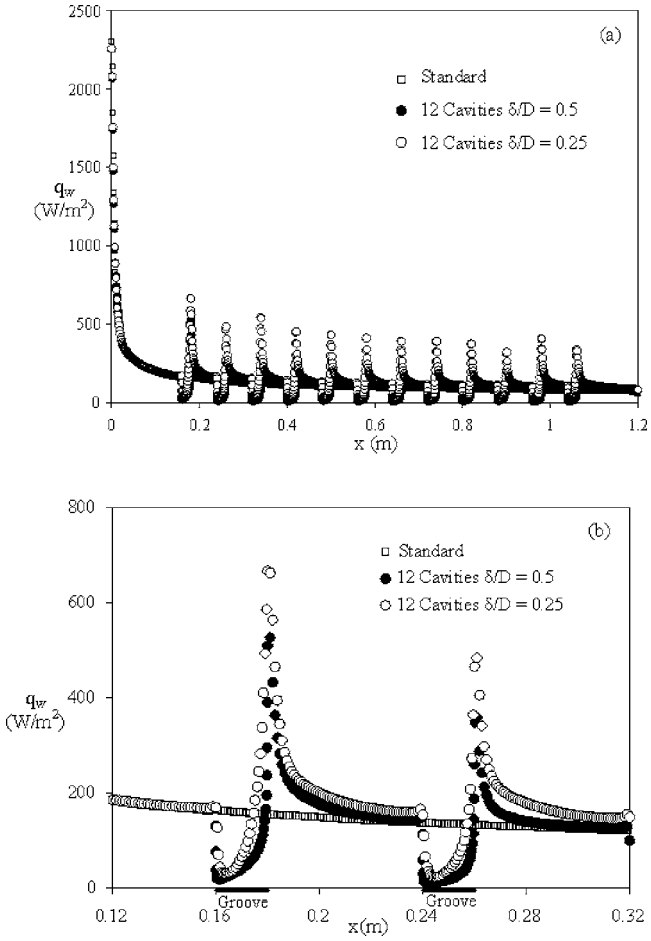


**Fig. 5 Local wall heat flux along the upper plate of the channel with 12 grooves at Re=2500 ($\bar{u}$=0.496 m s$^{-1}$)**

of Nu curves for the two arrangements climbs up resulting in a remarkable heat transfer enhancement. In numbers, the heat transfer enhancement via Nu goes up to about 9% at a low Re=1000 and to about 13% at a high Re=2500. These numbers are taken in reference to the smooth parallel-plate channel.

Applying nonlinear regression analysis to the numerical-generated data represented by the two-valued function Nu=$f$ (Re, $\delta/D$) produces the generalized correlation equation

$$\mathrm{Nu} = 3.55283 + 0.0032562\mathrm{Re} - 0.00000033\mathrm{Re}^2 + 0.498(\delta/D) + 0.00329956\mathrm{Re}(\delta/D) - 0.0065511\mathrm{Re}(\delta/D)^2 \quad (5)$$

This equation has a correlation coefficient $R^2$=1 and a maximum error of 0.46% between the numerical and the predicted Nu. To summarize, Eq. (5) is valid for simultaneous airflow and temperature development in a parallel-plate channel with symmetrical or staggered arrangements for three grooves and $\delta/D$=0.25 or 0.5 satisfying the Re interval $1000 \leq \mathrm{Re} \leq 2500$.

Having discussed the numerical results for the first channel owing to three grooves and knowing that the in-line and staggered arrangements give nearly similar heat transfer enhancements as witnessed in Fig. 6, the presentation of results is being reconsidered and shortened for higher number of grooves.

To scrutinize the role that the number of symmetrical grooves plays on the total heat transfer, two series of grooved channels were considered: one with 6 grooves and the other with 12 grooves. The outcome of the Nu-Re family of curves is illustrated in Fig. 7. Here again, the lowest Nu curve for the standard smooth channel constitutes the base line case for comparison purposes. For a relative groove depth $\delta/D$=0.5, the mean Nusselt number increases slightly but remains invariant with the number of grooves used either 6 or 12. This comportment leads to nearly equal heat transfer performance for each Re chosen. However, as the relative groove depth decreases to $\delta/D$=0.25, the gain in heat transfer grows significantly as the number of grooves is increased from 6 to 12. Heat transfer enhancement of about 18% for the channel with 6 grooves is observed at a high Re=2500, climbing up to about 30% for the channel with 12 grooves. In contrast, the Nu increment at a low Re=1000 for 12 grooves with $\delta/D$=0.25 is a moderate 12%.

A generalized correlation equation able to handle the variations of the mean Nusselt number Nu caused by changes in the three parameters: (1) the Reynolds number, (2) the relative groove depth $\delta/D$, and the number of grooves $N$ is

$$\mathrm{Nu} = 2.12 + 0.00454\mathrm{Re} + 5.10(\delta/D) + 0.0955N - 0.00382\mathrm{Re}(\delta/D) + 0.0000532\mathrm{Re}N - 0.359N(\delta/D) - 0.00000028\mathrm{Re}^2 \quad (6)$$

Because the regression coefficient $R^2$=0.999 and the maximum relative error stays within 1.3%, there is a good agreement between the numerical data and the correlated predictions. The restrictions imposed on Eq. (6) are continuous Re in the interval

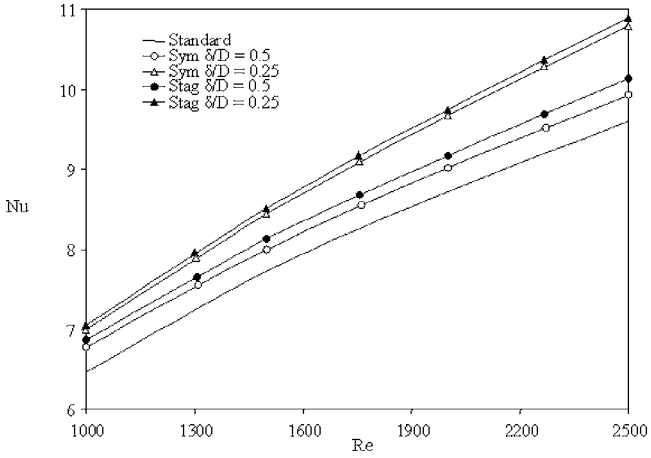


**Fig. 6 Variations of the mean Nusselt number with Re for the two arrangements and different relative groove depths in a channel with three grooves**

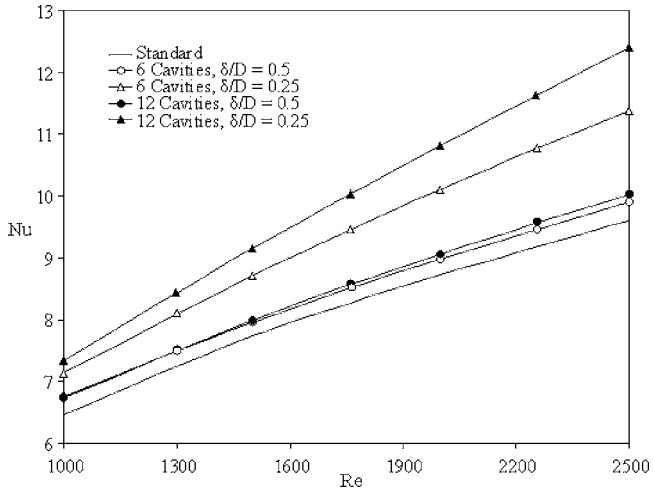


**Fig. 7 Variations of the mean Nusselt number of channel with 6 and 12 grooves with Re for different relative groove depths**

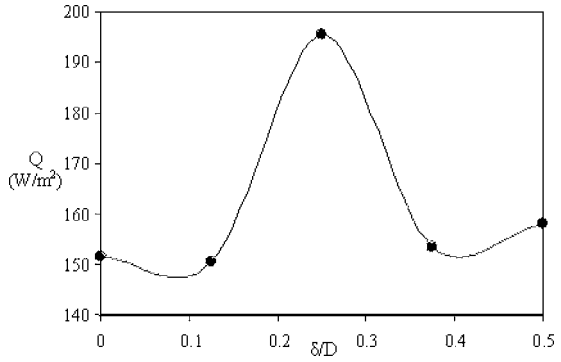


**Fig. 8 Optimal groove depth that maximizes the heat transfer through the channel**

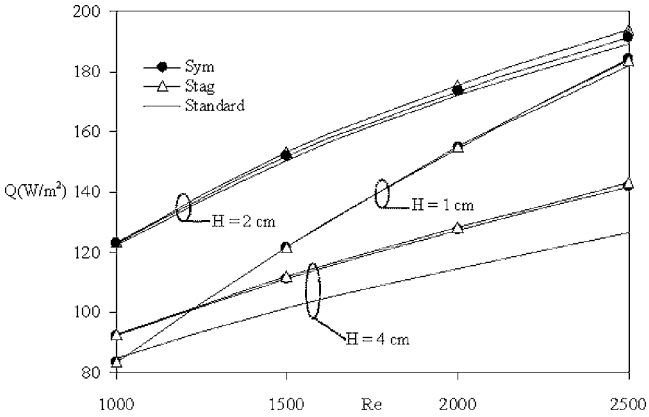


**Fig. 9 Evolution of the mean wall heat flux with Reynolds parametrized by the channel height and groove arrangement. Three relative heights of the channel are considered, $H/D$=0.5, 1, and 2.**

$1000 \leq \mathrm{Re} \leq 2500$, together with discrete $\delta/D=0.25$ or 0.5, and discrete $N=6$ or 12.

*4.2.3 Optimal Groove Depth*. From the heat transfer results presented above, it is clear that the enhancement over a flat plate increases as the groove depth goes to zero. However, if the depth is zero, this will match the flat plate with the minimum heat transfer. Consequently, there must be some optimum groove depth that maximizes the heat transfer. Tests were conducted in a channel with 12 grooves at Re=2500 for various groove depths $\delta/D$ of 0.125, 0.25, 0.375, and 0.5. The outcome of these tests in terms of the mean heat flux $Q$ is presented in Fig. 8 as a function of $\delta/D$. The trend of this curve shows that there is an optimum value of the groove depth $\delta/D=0.25$. For deeper or shallower grooves, the mean heat is not affected by the depth and stays almost constant.

## 5 Optimal Channel Height

It may be speculated that once the channel length is fixed, the interweaving of the channel height, the groove width, and the groove depth may have a direct bearing on the heat transfer rates. This issue may be viewed as an optimization analysis with the goal of maximizing the heat transfer rates. For conciseness, it seems logical to do the optimization analysis for the best relative depth found, i.e., $\delta/D=0.25$. Three different relative height-to-width ratios $H/D=0.5$, 1, and 2 ($D=2$ cm) were tested.

As the height $H$ decreases, the effect of $H$ on the fluid flow is accompanied by stronger vortices on each cavity, but the qualitative flow structure remains unaltered as witnessed earlier in Fig. 4 for the case of $H=4$ cm.

The influence that $H$ exerts on the heat transfer is presented by way of the variations of the mean wall heat flux per total area, $Q$, versus Re. The collection of $Q$-Re plots parametrized by $H$ is illustrated in Fig. 9. For a fixed channel height, three tests were conducted; one on a standard smooth channel, another on the symmetrical grooved channel, and another on the staggered grooved channel. The results of nine tests, three for each height, are compared in this figure. The heat transfer enhancement induced by the addition of the grooves is proportional to the channel height. In fact, at high Re of 2500, an enhancement of about 13% has been found when $H=4$ cm. This value is decreased to 3% and 1.5% when $H$ is reduced to 2 cm and 1 cm, respectively. The differences in terms of the heat transferred through the walls, when the grooves are arranged in a symmetrical or staggered fashion, are maximal for $H=2$ cm and minimal for $H=1$ cm, but still very limited (less than 2%). In addition, regardless of the channel structure (smooth or with grooves), $Q$ is higher for the intermediate $H=2$ cm and lower for the widest channel with $H=4$ cm. The narrow channel with $H=1$ cm lies between the two and behaves as the widest channel at low Re and as the intermediate channel at high Re.

## 6 Conclusions

Two-dimensional laminar forced convection with air across parallel-plate channels with a sequence of grooves placed on both plates has been numerically predicted using the finite-volume method and correlated using nonlinear regression analysis. These data are given to provide information on the effects of the number of grooves, the groove depth, and the channel height on the local flow structure characteristics, and on local and mean surface heat flux distributions. Three series of 3, 6, and 12 symmetrical and staggered rows of hemicylindrical grooves were placed on each plate of the channel. The Reynolds number based on the hydraulic diameter ranges from 1000 to 2500. The ratios of channel height to groove print diameter, $H/D$, are 0.5, 1, and 2. Four different groove depths, $\delta/D=0.125$, 0.25, 0.375, and 0.5, are considered.

Steady-state results show that the flow recirculation zone exists in each groove and the vortices get stronger as the groove depth decreases. Regardless of the groove depth and Reynolds number, each groove contains only one single vortex that rotates clockwise within grooves that are placed on the bottom wall and in the opposite direction within grooves on the upper wall. This phenomena lead to local wall heat flux augmentations, which are especially pronounced near the downstream rim of each groove. Local wall heat flux augmentations also develop as the vertical fluid advects colder fluid from the central part of channel to regions near the heated cavity surface. This intensifies as the groove depth approaches the optimal depth $\delta/D=0.25$ that maximizes the heat transfer through the channel.

The mean Nusselt number results show that both arrangements (symmetrical or staggered) provide similar results. In addition, when $\delta/D$ is far from its optimal value of 0.25, the number of grooves placed on each wall does not affect the mean Nusselt number. However, these quantities increase as the number of cavities goes from 3 to 12 when the cavities have the optimum depth $\delta/D=0.25$. Overall, this system can achieve heat transfer enhancements of about 30% relative to the smooth surface.

## Nomenclature

$c_p$ = air specific heat capacity, kJ kg$^{-1}$ K$^{-1}$
$D$ = groove width, m
$D_h$ = hydraulic diameter (=2$H$), m
$H$ = channel height, m
$h$ = mean heat transfer coefficient, W m$^{-2}$ K$^{-1}$
$k$ = air thermal conductivity, W m$^{-1}$ K$^{-1}$
$L$ = length of plate plus perimeter of grooves, m
Nu = mean Nusselt number (=$hD_h/k$)
$p$ = static pressure, Pa

Pr = Prandtl number ($=\nu/\alpha$)
$q_w$ = local wall heat flux, W m$^{-2}$
$Q$ = mean wall heat flux, W m$^{-2}$
Re = Reynolds number ($=\bar{u}D_h/\nu$)
$T$ = temperature, K
$\bar{u}$ = mean axial velocity, m s$^{-1}$
$\vec{\mathbf{v}}$ = velocity vector, m s$^{-1}$
$x,y$ = axial and transverse coordinates, m

### Greek Symbols

$\alpha$ = air thermal diffusivity, m$^2$ s$^{-1}$
$\delta$ = groove depth, m
$\nu$ = air kinematic viscosity, m$^2$ s$^{-1}$
$\rho$ = air density, kg m$^{-3}$

### Subscripts

$i$ = condition at the channel inlet
$w$ = condition at the channel plate

## References


[1] Gnielinski, V., 1998, "Forced Convection in Ducts," *Handbook of Heat Exchanger Design*, G. F. Hewitt, ed., Begell House, New York, Chap. 4.
[2] Sekulic, D. P., and Shah, R. K., 2002, *Fundamentals of Heat Exchanger Design*, Wiley, New York.
[3] Simons, R. E., Antonnetti, V. W., Nakayawa, W., and Oktay, S., 1997, "Heat Transfer in Electronic Packages," *Handbook of Microelectronics Packaging*, 2nd ed., R. R. Tummala, ed., Chapman and Hall, New York, pp. 1.315–1.403.
[4] Bar-Cohen, A., Watwe, A. A., and Prasher, R. S., 2003, "Heat Transfer in Electronic Equipment," *Handbook of Heat Transfer*, A. Bejan and A. D. Kraus, eds., Wiley, New York, Chap. 13.
[5] Chung, Y. M., Tucker, P. G., and Luo, K. H., 2001, "Large-Eddy Simulation of Complex Internal Flows," *Direct and Large-Eddy Simulations IV*, B. J.Geurts, R. Friedrich and O. Metais, eds., Kluwer Academic, The Netherlands.
[6] Chung, Y. M., Luo, K. H., and Sandham, N. D., 2002, "Numerical Study of Momentum and Heat Transfer in Unsteady Impinging Jets," Int. J. Heat Fluid Flow, **23**, pp. 592–600.
[7] Berner, C., Durst, F., and McEligot, D. M., 1984, "Flow Around Baffles," ASME J. Heat Transfer, **106**, pp. 743–749.
[8] Webb, B. W., and Ramadhyani, S., 1985, "Conjugate Heat Transfer in a Channel With Staggered Ribs," Int. J. Heat Mass Transfer, **28**, pp. 1679–1687.
[9] Kelkar, K. M., and Patankar, S. V., 1987, "Numerical Prediction of Flow and Heat Transfer in a Parallel-Plate Channel With Staggered Fins," ASME J. Heat Transfer, **109**, pp. 25–30.
[10] Lazardis, A., 1988, "Heat Transfer Correlation for Flow in a Parallel-Plate Channel With Staggered Fins," ASME J. Heat Transfer, **110**, pp. 801–802.
[11] Cheng, C. H., and Huang, W. H., 1989, "Laminar Forced Convection Flows in Horizontal Channels With Transverse Fins Placed in the Entrance Region," Numer. Heat Transfer, Part A, **16**, pp. 77–100.
[12] Ghaddar, N. K., Karczak, K. Z., Mikic, B. B., and Patera, A. T., 1986, "Numerical Investigation of Incompressible Flow in Grooved Channels, Part 1. Stability and Self-Sustained Oscillations," J. Fluid Mech., **163**, pp. 99–127.
[13] Ghaddar, N. K., Megan, M., Mikic, B. B., and Patera, A. T., 1986, "Numerical Investigation of Incompressible Flow in Grooved Channels, Part 2. Resonance and Oscillatory Heat-Transfer Enhancement," J. Fluid Mech., **168**, pp. 541–567.
[14] Amon, C. H., and Mikic, B. B., 1990, "Numerical Prediction of Convective Heat Transfer in Self-Sustained Oscillatory Flows," J. Thermophys. Heat Transfer, **4**, pp. 239–246.
[15] Amon, C. H., 1992, "Heat Transfer Enhancement by Flow Destabilization in Electronic Chip Configurations," ASME J. Electron. Packag., **144**, pp. 35–40.
[16] Wirtz, R. A., Huang, F., and Greiner, M., 1999, "Correlation of Fully Developed Heat Transfer and Pressure Drop in a Symmetrically Grooved Channel," ASME J. Heat Transfer, **121**, pp. 236–238.
[17] Greiner, M., 1987, "Flow Field Destabilization and Heat Transfer Enhancement in Grooved Channels," FED (Am. Soc. Mech. Eng.), **52**, pp. 131–138.
[18] Greiner, M., Faulkner, R. J., Van, V. T., Tufo, H. M., and Fischer, P. F., 2000, "Simulations of Three-Dimensional Flow and Heat Transfer in a Symmetrically Grooved Channel," ASME J. Heat Transfer, **122**, pp. 653–660.
[19] Greiner, M., Fischer, P. F., Tufo, H. M., and Wirtz, R. A., 2002, "Three-Dimensional Simulations of Enhanced Heat Transfer in a Flat Passage Downstream From a Grooved Channel," ASME J. Heat Transfer, **124**, pp. 169–176.
[20] Greiner, M., Fischer, P. F., and Tufo, H. M., 2002, "Two-Dimensional Simulations of Enhanced Heat Transfer in an Intermittently Grooved Channel," ASME J. Heat Transfer, **124**, pp. 538–545.
[21] McGarry, M., Campo, A., and Hitt, D. L., 2004, "Numerical Simulations of Heat and Fluid Flow in Grooved Channels With Curved Vanes," Numer. Heat Transfer, Part A, **46**, pp. 41–54.
[22] Mahmood, P. M., and Ligrani, P. M., 2002, "Heat Transfer in a Dimpled Channel: Combined Influences of Aspect Ratio, Temperature Ratio, Reynolds Number, and Flow Structure," Int. J. Heat Mass Transfer, **45**, pp. 2011–2020.
[23] Ligrani, P. M., Harrison, J. L., Mahmood, G. I., and Hill, M. L., 2001, "Flow Structure Due to Dimple Depressions on a Channel Surface," Phys. Fluids, **13**, pp. 3442–3451.
[24] Mahmood, G. I., Hill, M. L., Nilson, D. L., Ligrani, P. M., Moon, H. K., and Glezer, B., 2001, "Local Heat Transfer and Flow Structure on and Above a Dimpled Surface in a Channel," ASME J. Turbomach., **123**, pp. 115–123.
[25] Won, S. Y., and Ligrani, P. M., 2004, "Numerical Predictions of Flow Structure and Local Nusselt Number Ratios Along and Above Dimpled Surfaces With Different Dimple Depths in a Channel," Numer. Heat Transfer, Part A, **46**, pp. 549–570.
[26] Park, J., Desam, P. R., and Ligrani, P. M., 2004, "Numerical Predictions of Flow Structure Above a Dimpled Surface in a Channel," Numer. Heat Transfer, Part A, **45**, pp. 1–20.
[27] Patankar, S. V., 1980, *Numerical Heat Transfer and Fluid Flow* Hemisphere, Washington, DC.
[28] Poling, B. E., Prausnitz, J. M. and O'Connell, J. P., 2001, *The Properties of Gases and Liquids*, McGraw-Hill, New York, pp. A.5–A.19.
[29] Shah, R. K., and London, L. A., 1978, *Laminar Flow and Heat Transfer in Ducts*, Academic, New York.
[30] Burgess, N. K., Oliveira, M. M., and Ligrani, P. M., 2004, "Nusselt Number Behavior on Deep Dimpled Surfaces Within a Channel," ASME J. Heat Transfer, **125**, pp. 11–18.

# Influence of a Coflowing Ambient Stream on a Turbulent Axisymmetric Buoyant Jet

**S. Habli**
e-mail: sabra.habli@fsm.rnu.tn

**N. Mahjoub Said**

**H. Mahmoud**

**H. Mhiri**

Unité de thermique et environnement,
Ecole Nationale d'Ingénieurs de Monastir,
route de Ouardanine,
5020 Monastir, Tunisie

**G. Le Palec**

**Ph. Bournot**

Equipe IMFT,
Institut de Mécanique de Marseille,
UNIMECA, 60 rue Joliot-Curie,
Technopôle de Château-Gombert,
13453 Marseille Cedex 13, France

*This paper reports numerical results on turbulent buoyant axisymmetric jets in a coflowing ambient stream. The objective of this study is to compare the performance of the Reynolds stress algebraic model (ASM) with that of the k-ε turbulence model in predicting the flow field. A finite difference method has been used to solve a system of coupled partial differential equations. A comparison has been carried out between the numerical results obtained in the present work and experimental and numerical data reported in the literature. It has been found that the two investigated models reasonably predict the mean flow properties of the flow field. Nevertheless, the ASM proves to be better than the k-ε method to predict the effects of buoyancy and the turbulence structure. It has been found that the increase of the coflow can slow the development of the jet to the state of similarity of mean characteristic profiles. A jet with a ratio of coflow velocity $\bar{u}_\infty$ to jet discharge velocity $\bar{u}_0$ less than 0.05 has developed to closely approximate a free jet in a stagnant medium while a jet with higher $\bar{u}_\infty/\bar{u}_0$ ratio never reaches a similarity state. In buoyant jets, only a flow with $u_\infty/u_0 \leqslant 0.05$ reaches a similarity state. Buoyancy ensures that the similarity region begins at a distance closer to the nozzle exit than if the medium is stagnant.* [DOI: 10.1115/1.2804930]

*Keywords: axisymmetric jet, buoyant jet/turbulent jet, co-flowing stream, algebraic Reynolds stress model of turbulence (ASM), k-ε model, buoyancy, similarity, forced convection/free convection*

## 1 Introduction

The simplest configuration of a jet is the free jet in stagnant surroundings. In the presence of an external stream, jets are classified as counterflow or coflow [1–11]. A coflow jet is formed when a jet, with an exit velocity $\bar{u}_0$, develops within an outer stream flowing at a velocity $\bar{u}_\infty$ in the same direction as the jet. Turbulent coflowing jets are used in several industrial applications such as combustors, mixers, etc.

The effect of a coflow on turbulent jet mixing behavior has been investigated by several authors. For co-flows having an infinite radial extent, the modification of the jet behavior from that of a free jet is often characterized in terms of a momentum radius $\theta$ [12]. The flow is accepted to behave as a free jet when $\theta$ becomes large ($\theta \to \infty$) and as a wake flow up to the point where $\theta$ approaches zero. Working with a jet in a coflowing stream reduces errors in the regions of high turbulence levels, such as the edge of the jet in a medium at rest, but at the expense of destroying the similarity for mean flow characteristics [1].

A flow with $\bar{u}_\infty/\bar{u}_0$ ratio less than 5% develops a similarity of the mean flow behavior [5], while one with higher $\bar{u}_\infty/\bar{u}_0$ ratio never reaches such state. The axisymmetric geometry of the round jet confers properties to the flow that make it a good problem for discriminating between turbulence models. Even with the development of direct numerical simulation (DNS) and large eddy simulation (LES) for turbulent flows, the most popular models for round jets and industrial flows are based on the two equation of Reynolds averaged Navier–Stokes (RANS). The $k$-$\varepsilon$ model [10,13–15], based on the Boussinesq approximation of the Reynolds stress tensors introduced by the conservation equations (where isotropic turbulence is assumed), is one of these. The $k$-$\varepsilon$ model used with the standard constants, however, overestimates the spreading rate of a round jet [13,15]. This is called the "round-jet anomaly" [13]. Attempts at overcoming the round jet anomaly have almost invariably involved the modification of the closure coefficients of the $k$-$\varepsilon$ model [7,10,16] and are not applicable for general flows.

The algebraic stress model (ASM) is derived from the simplified Reynolds stress equation [14,15,17,18]. This model provides a mechanism by which the anisotropic turbulence distribution can be computed without the large computational effort required for the Reynolds stress transport equation model. In flows where the Reynolds stress anisotropy varies slowly in time and space, the traditional ASM approach is to neglect the total transport of the diffusion and the convection terms in the transport equation for the Reynolds stress anisotropy [19]. This form of the ASM is easy to solve, converges relatively quickly, and is numerically robust. The ASM is used in large domains and requires minimal computational expense, an important feature for industrial flow predictions. This model is known to be simple, stable, and easy to implement for the boundary layer flow [20]. Further, it can model several flow types where simple models fail for example, flow affected by buoyancy such as turbulent axisymmetric buoyant jets in a medium at rest [15]. In the following, two things are examined. The first is the influence of the $k$-$\varepsilon$ model and the ASM for prediction of a turbulent axisymmetric coflowing jet. The second is the investigation of the effect of a coflowing ambient stream on the behavior of the jet flow. A comparison with a jet in a medium at rest is carried out.

## 2 Numerical Modeling

**2.1 Governing Equations.** In the following, a vertical turbulent jet flowing from an axisymmetric nozzle is considered. The jet flow has a velocity $\bar{u}_0$, an initial temperature $\bar{T}_0$, and a density

Contributed by the Heat Transfer Division of ASME for publication in the JOURNAL OF HEAT TRANSFER. Manuscript received May 25, 2006; final manuscript received June 1, 2007; published online February 4, 2008. Review conducted by Louis C. Burmeister.

  

**Table 1 Diffusion and source terms for the ($k-\varepsilon$) model**

| $\phi$ | $D_\phi$ | $S_\phi$ |
|---|---|---|
| $k$ | $v_t/\sigma_k$ | $P-\varepsilon$ |
| $\varepsilon$ | $v_t/\sigma_\varepsilon$ | $\varepsilon/k(c_{\varepsilon 1}P-c_{\varepsilon 2}\varepsilon)$ |

**Table 2 Model coefficients in the ($k$-$\varepsilon$) model**

| $c_\mu$ | $\sigma_k$ | $\sigma_\varepsilon$ | $c_{\varepsilon 1}$ | $c_{\varepsilon 2}$ | $\sigma_T$ |
|---|---|---|---|---|---|
| 0.09 | 1.0 | 1.3 | 1.44 | 1.92 | 0.95 |

$\rho_0$. The jet is discharging into a nonturbulent coflowing air stream. The axial pressure gradient is often assumed to be zero, consistent with the thin shear layer approximation [20,21]. The flow is steady and satisfies Boussinesq approximations. The continuity, momentum, and energy equations for the mean velocity are

$$\frac{\partial(r\bar{u})}{\partial x}+\frac{\partial(r\bar{v})}{\partial r}=0$$

$$\bar{u}\frac{\partial\bar{u}}{\partial x}+\bar{v}\frac{\partial\bar{u}}{\partial r}=\frac{1}{r}\frac{\partial}{\partial r}(-r\overline{u'v'})+g\beta(\overline{T-T_0})$$

$$\bar{u}\frac{\partial\bar{T}}{\partial x}+\bar{v}\frac{\partial\bar{T}}{\partial r}=\frac{1}{r}\frac{\partial}{\partial r}(-r\overline{v'T'}) \tag{1}$$

The above equations are written in a form valid for the axisymmetric boundary layer flow. The Reynolds number is assumed to be high, so that viscous diffusion can be neglected compared to turbulent diffusion and the turbulence is fully developed. Generally speaking, the fully developed turbulence assumption cannot be sustained if the Reynolds number falls below a critical value, $\mathrm{Re}_c=10^4$ [22]. This value must be viewed as a necessary, but not sufficient, condition for the turbulence to be fully developed since depend on the details of the flow. In the results obtained by Ricou and Spalding [23], the value of Re=25,000 is found to remove the effect of the Reynolds number on the behavior of the jet. Ebrahimi and Klein [24] show that Reynolds number has no effect on the centerline development of the axisymmetric jet for $\mathrm{Re}\geqslant 50{,}000$. Measurements reported by Grandmaison et al. [25] in free jets reveal that the Reynolds number effects on the jet development are negligible for $\mathrm{Re}>50{,}000$. Pitts et al. [3] investigated the effect of the Reynolds number on the centerline scalar mixing behavior of the axisymmetric coflow jet emerging from a long pipe. It has been demonstrated that the effect of the Reynolds number on the centerline development of the flow decreases as the Reynolds number increases. For the smooth contraction nozzle, it has been reported by Malmström et al. [26] that the far field centerline mean velocity decay factor increases with the Reynolds number, particularly for $\mathrm{Re}<\mathrm{Re}_c$. In the present study, uniform exit profiles obtained from a contraction nozzle are adopted so that for high Reynolds number ($\mathrm{Re}>\mathrm{Re}_c$) turbulence can be assumed fully developed.

Two turbulence models are used to obtain a closed system: the ($k$-$\varepsilon$) model and the ASM. In these models, the parabolized conservations equations can be expressed in the following way:

$$\underbrace{\frac{\partial(\bar{u}\phi)}{\partial x}+\frac{1}{r}\frac{\partial(r\bar{v}\phi)}{\partial r}}_{\text{Convection}}=\underbrace{\frac{1}{r}\frac{\partial}{\partial r}\left(rD_\phi\frac{\partial\phi}{\partial r}\right)}_{\text{Diffusion}}+S_\phi \tag{2}$$

where $\phi$ is a general dependent variable, $S_\phi$ is the source term, and $D_\phi$ is the coefficient of the turbulent diffusion.

**2.2 $k$-$\varepsilon$ Model.** Equations (1) and (2) are solved in this model, $\phi$ standing for $k$ or $\varepsilon$. In the generalized equation (2), the turbulent diffusion term is $D_\phi=\nu_t/\sigma_\phi$ and the source terms are given in Table 1 with $P=-u'v'\partial\bar{u}/\partial r$ being the production term of turbulent kinetic energy.

The first order $k$-$\varepsilon$ model is closed by expressions for Reynolds stress and turbulent heat flux [10,13–15]:

$$\overline{u'v'}=-v_t\frac{\partial\bar{u}}{\partial r}\quad\overline{v'T'}=-\frac{v_t}{\sigma_t}\frac{\partial\bar{T}}{\partial r}\quad\text{with } v_t=c_\mu\frac{k^2}{\varepsilon} \tag{3}$$

This model requires the use of different empirical constants (Table 2). Better prediction of the expansion of round jets are obtained using the following correction functions [17]:

$$c_{\mu m}=c_\mu[1-0.465H] \tag{4}$$

$$c_{\varepsilon 2m}=c_{\varepsilon 2}[1-0.035H]\quad\text{with } H=\left|\frac{y_{0,5\bar{u}}}{\bar{u}_{c_{\mathrm{ex}}}}\frac{\partial\bar{u}_c}{\partial x}\right|^{1/5} \tag{4}$$

**2.3 Stress Algebraic Model.** $\phi=k$, $\varepsilon$, or $\overline{T'^2}$. The ASM yields algebraic equations for Reynolds stresses ($\overline{u_i'u_j'}$) and turbulent heat fluxes ($\overline{u_i'T'}$). The equations solved in this model are Eqs. (1) and (2). In the generalized equation (2), the turbulent diffusion term $D_\phi$ and the source terms are given in Table 3, with $P=-\overline{u'v'}\partial\bar{u}/\partial r$ being the production term of turbulent kinetic energy and $G=g\beta\overline{u'T'}$ being the buoyancy production term.

In the ASM, the algebraic relations for Reynolds stresses and turbulent heat flux satisfy the following equations [14,15,17]:

$$\overline{v'^2}=c_2k$$

$$-\overline{u'v'}=\frac{1-c_0\dfrac{\overline{v'^2}}{k}}{c_1}\left(1+\frac{k}{\varepsilon}\frac{g\beta}{c_h}\frac{\partial\bar{T}/\partial r}{\partial\bar{u}/\partial r}\right)\frac{k^2}{\varepsilon}\frac{\partial\bar{u}}{\partial r} \tag{5}$$

$$-\overline{v'T'}=\frac{1}{c_h}\frac{\overline{v'^2}}{k}\frac{k^2}{\varepsilon}\frac{\partial\bar{T}}{\partial r}$$

$$\overline{u'T'}=\frac{k}{c_h\varepsilon}\left(-\overline{u'T'}\frac{\partial\bar{T}}{\partial r}-(1-c_{h1})\overline{v'T'}\frac{\partial\bar{u}}{\partial r}+g\beta(1-c_{h1}\overline{T'^2})\right)$$

This model includes 11 empirical constants (Table 4).

To better predict the expansion of round jets by ASM, functions of correction are proposed [17]:

**Table 3 Diffusion and source terms for the ASM**

| $\phi$ | $D_\phi$ | $S_\phi$ |
|---|---|---|
| $k$ | $c_k\dfrac{k}{\varepsilon}\overline{v'^2}$ | $P+G-\varepsilon$ |
| $\varepsilon$ | $c_\varepsilon\dfrac{k}{\varepsilon}\overline{v'^2}$ | $\dfrac{\varepsilon}{k}(c_{\varepsilon 1}(P+G)-c_{\varepsilon 2}\varepsilon)$ |
| $\overline{T'^2}$ | $c_T\dfrac{k^2}{\varepsilon}$ | $-2\overline{v'T'}\dfrac{\partial\bar{T}}{\partial r}-c_{T1}\dfrac{\varepsilon}{k}\overline{T'^2}$ |

**Table 4 Model coefficients in the ASM**

| $c_0$ | $c_1$ | $C_2$ | $c_\varepsilon$ | $C_{\varepsilon 1}$ | $c_{\varepsilon 2}$ | $c_k$ | $c_T$ | $c_{T1}$ | $c_h$ | $c_{h1}$ |
|---|---|---|---|---|---|---|---|---|---|---|
| 0.55 | 2.2 | 0.53 | 0.15 | 1.43 | 1.92 | 0.225 | 0.13 | 1.25 | 3.2 | 0.5 |

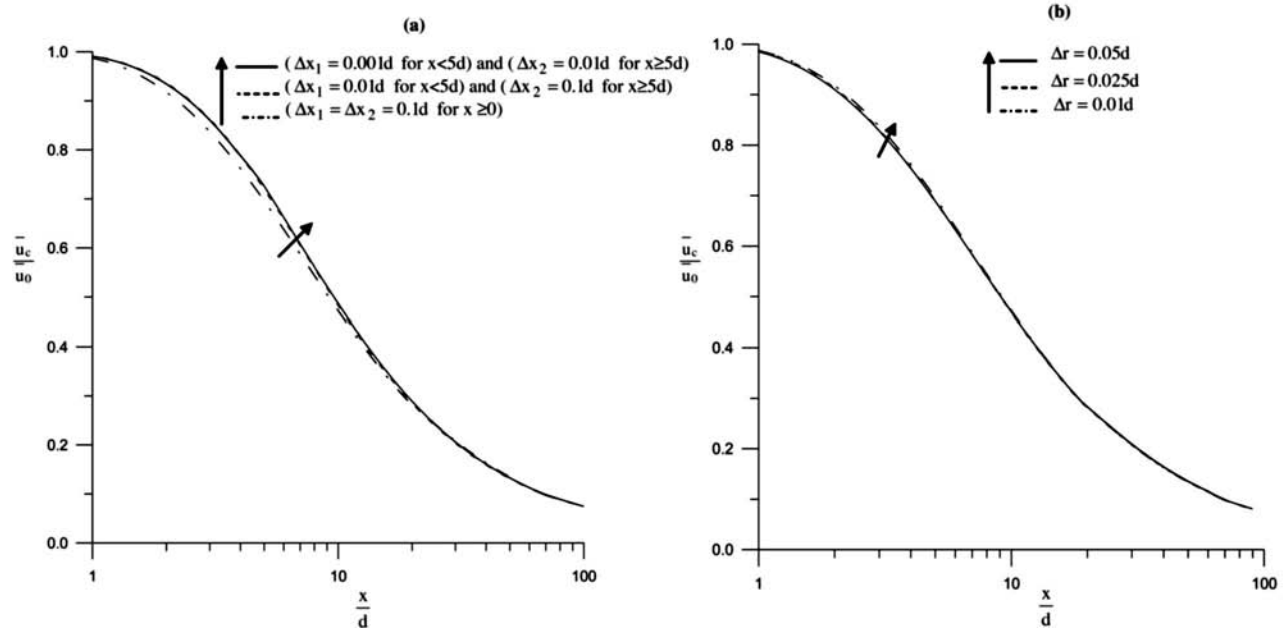


**Fig. 1 Effect of the grid on the centerline longitudinal distribution of velocity: $u_{co}=0.01$. (*a*) Effect of the axial step on the flow: $\Delta r=0.025d$. (*b*) Effect of the radial step on the flow: ($\Delta x_1=0.001d$ for $x>5d$) and ($\Delta x_2=0.01d$ for $x\geqslant 5d$).**

$$-\overline{u'v'}=\left[\frac{1-c_0}{c_1}\frac{\overline{v'^2}}{k}\left(1+\frac{k}{\varepsilon}\frac{g\beta}{c_h}\frac{\partial\bar{T}/\partial r}{\partial\bar{u}/\partial r}\right)\frac{k^2}{\varepsilon}\frac{\partial\bar{u}}{\partial r}\right](1-0.465H)) \quad c_{\varepsilon 2m}=c_{\varepsilon 2}[1-0.035H] \tag{6}$$

and

$$H=\left|\frac{y_{0,5\bar{u}}}{\bar{u}_{c_{ex}}}\frac{\partial\bar{u}_c}{\partial x}\right|^{1/5}$$

**2.4 Boundary Conditions.** The foregoing system of equations is completed with the following boundary conditions:

$$\text{For } x>0:\begin{cases}\bar{v}=\dfrac{\partial\bar{u}}{\partial r}=\dfrac{\partial\bar{T}}{\partial r}=\dfrac{\partial k}{\partial r}=\dfrac{\partial\varepsilon}{\partial r}=\dfrac{\partial\overline{T'^2}}{\partial r}=0 & \text{for } r=0\\ \bar{u}-\bar{u}_\infty,\overline{T-T_\infty},k,\varepsilon,\overline{T'^2}\to 0 & \text{for } r\to\infty\end{cases} \tag{7}$$

Resolution of the governing equations associated with their boundary conditions (Eq. (7)) can be carried out only by considering the initial conditions. In this work, uniform initial conditions are assumed:

$$\text{For } x=0:\ v=0 \text{ and}\begin{cases}\dfrac{\bar{u}}{u_0}=\dfrac{\overline{T-T_\infty}}{T_0-T_\infty}=1 \quad \dfrac{k}{u_0^2}=0.05 \quad \dfrac{\varepsilon d}{u_0^3}=0.02 \quad \dfrac{\overline{T'^2}}{T_0-T_\infty{}^2}=0.05 & \text{for } 0\leqslant\dfrac{r}{d}<0.05\\ \bar{u}-\bar{u}_\infty,\overline{T-T_\infty},k,\varepsilon,\overline{T'^2}\to 0 & \text{for } \dfrac{r}{d}\geqslant 0.5\end{cases} \tag{8}$$

## 3 Numerical Method

The finite difference equations for the governing equations were solved iteratively by using a parabolized marching algorithm in the flow direction until convergence was achieved for all variables [27]. This method used a staggered grid for numerical stability, the continuity equation is discretized at the $(i+1/2,j+1/2)$ node, while the other equations are discretized at the $(i+1/2,j)$ node. The iterative process was brought to an end when the relative change of $\phi$ between two successive iterations was lower than $10^{-5}$ for each node of the grid.

A nonuniform axial forward step was utilized. In this direction, we tested different steps (Fig. 1(*a*)). Then, we showed that taking $\Delta x_1=0.001d$ for $x<5d$ and $\Delta x_2=0.01d$ for $x\geqslant 5d$ is sufficient to obtain a numerical solution independent of the grid. In the radial direction, $\Delta r=0.025d$ is sufficient (Fig. 1(*b*)).

## 4 Results and Discussion

**4.1 Comparison Between Computation Results and Experimental Data.** The first stage of calculation consisted primarily in testing the developed programs. Then, we undertook a parametric study of the effect of the coflowing stream on the behavior of the jet flow.

*4.1.1 Forced Jet.* To validate numerical computations, the results obtained using the two turbulence models are compared with the experimental data in free or coflow jets. The initial conditions used for the numerical calculation correspond closely to those found experimentally by Antoine et al. [8].

In Fig. 2, the centerline longitudinal excess velocities obtained from the two turbulence models are in close agreement. Examination of this figure shows reasonable agreement with experimental

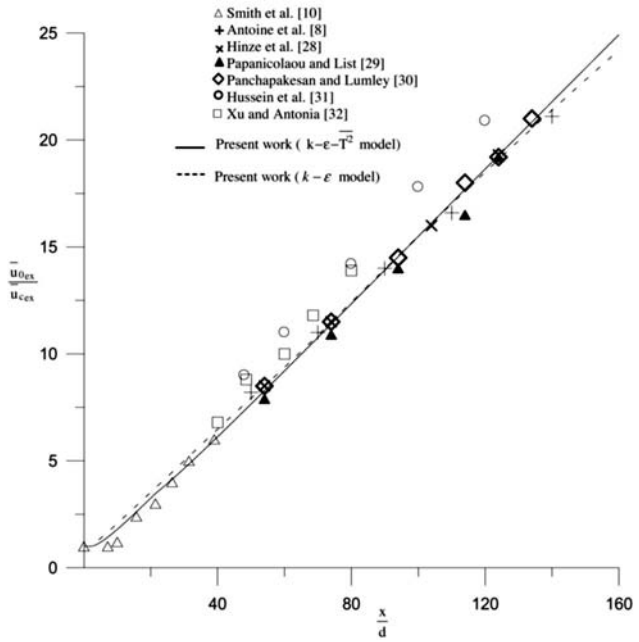


**Fig. 2 Longitudinal distributions of the centerline excess velocity**

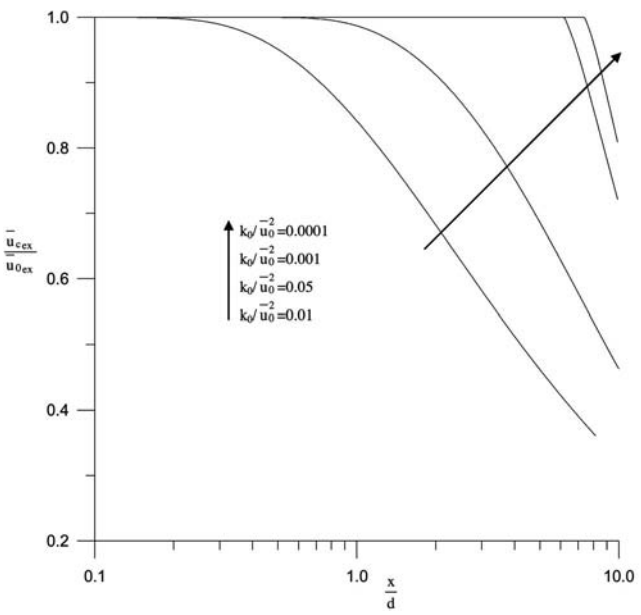


**Fig. 3 Potential core for different initial intensity of the turbulent kinetic energy: $u_{co}=0.01$**

data such as those reported in Refs. [10,8,28–30], while some disparity is observed in comparing to the data sets of Refs. [31,32] corresponding to free jets.

The potential core length of the present numerical models ends at about $2d$, whereas in the experimental data reported in Ref. [33] it ends at about $5d$ and in the numerical study reported in Ref. [10] at about $10d$. The potential core length is strongly affected by the conditions at the nozzle, namely, the Reynolds number, density ratio of the injected fluid to the ambient fluid [3,4], etc. The parameters used in simulation are not identical to those of the experiment since the potential core depends on the competition between the inertial and viscous forces. In addition, the initial turbulence intensity affects strongly the flow characteristics in the region adjacent to the jet exit [7,33]. In Fig. 3, the effect of different initial intensity of turbulence is illustrated. The figure shows that the lower the initial turbulence intensity, the greater the length of the potential core.

The centerline longitudinal excess velocity can be written as a hyperbolic law in the similarity region: $\bar{u}_{0_{ex}}/\bar{u}_{c_{ex}}=1/K_u(x-x_0/d)$. The constants $K_u$ and $x_0$ ($x_0$ is a virtual origin) determined by the two turbulence models are compared to those measured by several other authors in Table 5. The virtual origin from the ASM is nearer values reported in Refs. [29,31,34] for free jets than the value reported in Ref. [8] for a coflowing stream. The virtual origin from the $k$-$\varepsilon$ model is significantly smaller than other reported data. The values of the virtual origin (reported in Table 5) show a considerable scatter. Such variations are not unexpected because the location of the virtual origin is sensitive to the variation of Reynolds number, the velocity profiles and intensities at the jet exit, and the density ratio of the injected fluid to the ambient fluid [3,4]. These parameters varied from study to study.

A comparison between the numerical radial distribution of the longitudinal velocity and the experimental data of a jet in a medium at rest [30,35] or in a coflowing stream [8] is shown in Fig. 4. The velocity profiles appear to be Gaussian. The ASM predicts lower velocities near the centerline and the core of the jet than the $k$-$\varepsilon$ model, while it predicts higher velocities at the jet edge. Especially, near the edge, the ASM correlates more closely with experimental data of Refs. [8,30,35].

In the established region, the profile of the half-radius of the longitudinal velocity $y_{0.5\bar{u}}$ is expressed as $y_{0.5\bar{u}}=K_y(x/d)$. The present results, reported in Table 5, are compared with the experimental data. The analysis of these data shows that the spreading rates of the jet from the two turbulence models are in close agreement. The correlation is better with the experimental data of Antoine et al. [8] in a coflowing stream than in free jets. The spreading rates are about 50% lower than those determined in free jets (Table 5). It is believed that these low rates of the spreading are due to the coflowing stream tending to reduce the jet expansion.

The longitudinal decay of the centerline excess temperature obtained from the two turbulence models is shown in Fig. 5 and compared with the experimental study of Mi et al. [9]. In this study [9], temperature was used as a marker to identify the scalar since, when buoyancy effects are negligible, the temperature field is known to behave similarly to any passive scalar field. In the study of Van der Hegge Zijnen [36,37], temperature and concentration measurements are compared and it has been found that the diffusion of heat is similar to that of mass. Data from the study of Mi et al. [9], for a Grashof number$=210^{-5}$, are small enough that the buoyancy is negligible and the temperature acts as a passive scalar field. These data agree better with results from the ASM than with those from the $k$-$\varepsilon$ model. However, the decay rate of the centerline excess temperature from the ASM is about 15% higher than the experimental data.

The centerline excess temperature can be written in the similarity region, as a hyperbolic law: $\Delta\bar{T}_0/\Delta\bar{T}_c=1/K_T((x-x_0^{(T)})/d)$, where $K_T$ and $x_0^{(T)}$ in Table 5 are compared to those of other authors. $K_T$ determined from the ASM agrees well with the value measured by Mi et al. [9]. This value is about 30% lower than the value measured by Antoine et al. [8] in a coflowing stream. $K_T$ from the $k$-$\varepsilon$ model matches the experimental data of Antoine et al. [8] more closely, being only about 15% higher than the experimental value [8]. There is a large scatter between the experimental and the numerical results for the prediction of the thermal virtual origin. The virtual origin from the ASM is significantly different from that of Antoine et al. [8]. The $k$-$\varepsilon$ model predicts a thermal virtual origin close to that found by Antoine et al. [8]. This discrepancy can be attributed to the difference in initial conditions between experiment and simulation [3,9].

A comparison of the radial distribution of the normalized excess temperature is shown in Fig. 6. It is shown that the tempera-

**Table 5 Flow parameter for an axisymmetric turbulent jet**

| Authors | Present Results (ASM) | Present Results ($k-\varepsilon$) | [34] | [8] | [28] | [29] | [30] | [31] (HW) | [31] (LDA) | [35] | [9] | [2] |
|---|---|---|---|---|---|---|---|---|---|---|---|---|
| Field of measurements | | | $x/d<45$ | $x/d<140$ | $x/d<140$ | $x/d<120$ | $x/d<150$ | $x/d<120$ | $x/d<120$ | $x/d<100$ | $x/d<46$ | $x/d=30$ to 90 |
| $u_{co}$ | 0.05 | 0.05 | 0 | 0.05 | 0 | 0 | 0 | 0 | 0 | 0 | 0 | 0.004 |
| $K_u$ | 6.37 | 6.71 | 10.8 | 6.83 | 6.39 | 6.71 | 6.06 | — | 5.9 | — | | |
| $x_0$ | $1.39d$ | $-3.14d$ | $2.4d$ | $4.9d$ | $0.6d$ | $2.56d$ | 0 | — | $2.7d$ | — | | |
| $K_y$ | 0.056 | 0.055 | 0.106 | 0.064 | 0.082 | 0.104 | 0.116 | 0.094 | 0.102 | 0.086 | | |
| $K_T$ | 4.54 | 7.75 | | 6.76 | 5.27 | 6.33 | 2.41 | | | | 4.56 | 5.11 |
| $x_0^{(T)}$ | $-1.59d$ | $-5.75d$ | | $-11d$ | $0.8d$ | $6d$ | | | | | $4.25d$ | $-3.7d$ |
| $(\overline{u'v'}/\overline{u}^2_{c_{ex}})_m$ | 0.0225 | 0.0220 | | 0.0225 | | | 0.0190 | | 0.0211 | 0.0155 | | |
| $(\overline{v'T}/\Delta\overline{T}_c\overline{u}_{c_{ex}})_m$ | 0.03 | 0.022 | | 0.03 | | | 0.02 | | | | | |

ture profiles of the $k$-$\varepsilon$ model are narrower than those of the ASM. It is clear from Fig. 6 that the ASM provides the best agreement with the results of Refs. [8,30], but results of Dowling and Dimotakis [2] lie between the $k$-$\varepsilon$ model and the ASM predictions. Differences between the simulation and the experimental data are most apparent near the edge of the jet, where the real flow is intermittently turbulent and laminar because the radial velocity distribution depends on the mechanisms of turbulent motion for experimental data [38]. Comparison of Figs. 4 and 6 shows that the temperature field obtained from the ASM extends farther than the velocity, as a law, observed by different authors [14,17,18].

The normalized radial distribution of the Reynolds shear stress $(\overline{u'v'}/\overline{u}^2_{c_{ex}})$ is shown in Fig. 7 where it is compared to data measured by several authors. The maximum values of the normalized Reynolds shear stress from the two models, reported in Table 5, are in close agreement with the results of Antoine et al. [8] for measurements in the rage of $70 \leqslant x/d \leqslant 140$. Furthermore, $(\overline{u'v'}/\overline{u}^2_{c_{ex}})_m$ in the present study is reached at $x/d \approx 120$ for the ASM and at $x/d \approx 90$ for the $k$-$\varepsilon$ model. We note that similarity is not completely reached for the two turbulence models at these distances even for a higher axial distance. In fact, calculations have shown [39] that complete similarity is only possible when $\overline{u}_\infty/\overline{u} \to 0$ (pure jet behavior) or $(\overline{u}_\infty/\overline{u} \to 1)$ (pure wake behavior) and neither is the case here.

The maximum value of the normalized Reynolds shear stress obtained with the ASM is located at $(r/x \approx 0.04)$. This value is close to data reported by authors of Refs. [30,31] in free jets and 20% lower than experimental data in coflow jets [8]. Still, the value obtained with $k$-$\varepsilon$ model $(r/x \approx 0.045)$ matches better the experimental data of Antoine et al. [8], which is located at $(r/x \approx 0.05)$. The radial turbulent flux from the ASM is higher in Fig. 8($a$) than the results of Ref. [30] obtained in a helium jet discharging in the air. Further, a horizontal shift (20%) is observed compared to the experimental data of Antoine et al. [8]. The radial turbulent flux from the $k$-$\varepsilon$ model (Fig. 8($b$)), matches better with the experimental data of Panohapakesan and Lumley [30] obtained in a free jet than that obtained in the coflow [8].

The maximum value of $(\overline{v'T}/\Delta T\overline{u}_{c_{ex}})_m$ (Table 5), obtained from the ASM, is higher than that from the $k$-$\varepsilon$ model. The maximum value from the ASM is close to the value obtained by Antoine et al. [8] in the coflow and greater than other reported data (0.019 [40]; 0.015 [41]). This difference can be attributed to the presence of a coflowing stream rather than to the absence of a complete similarity in a coflowing stream [8,39]. From the $k$-$\varepsilon$ model, the

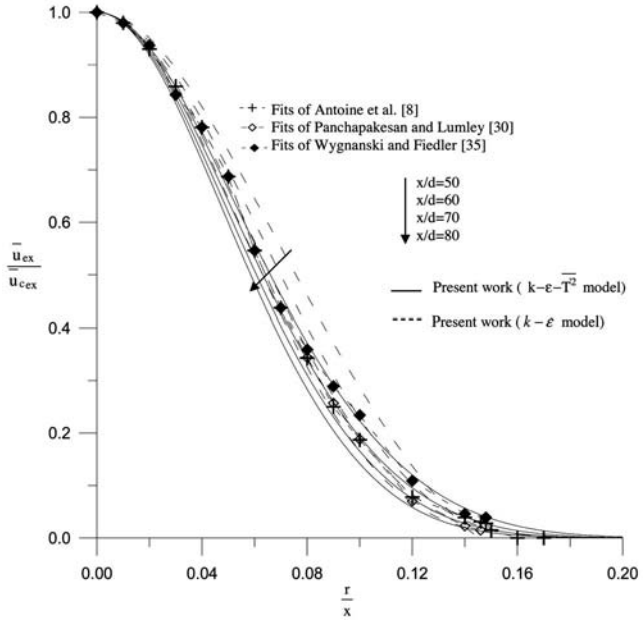


**Fig. 4 Radial distributions of the longitudinal excess velocity**

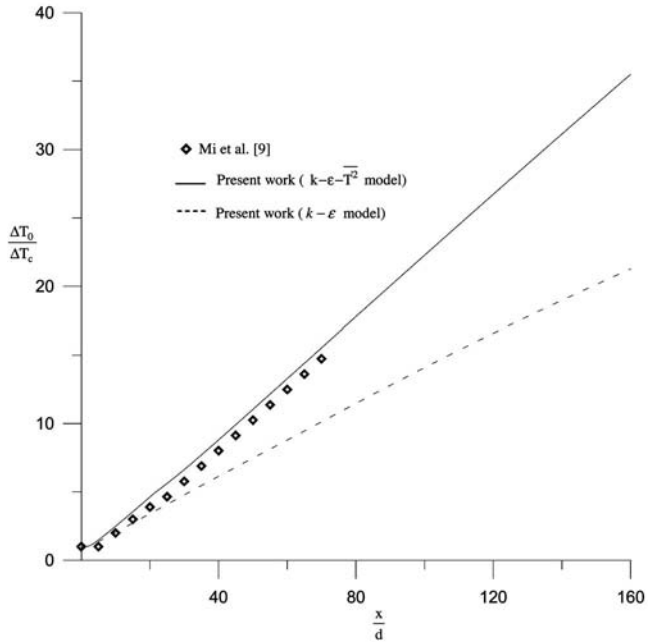


**Fig. 5 Longitudinal distributions of centerline excess temperature**

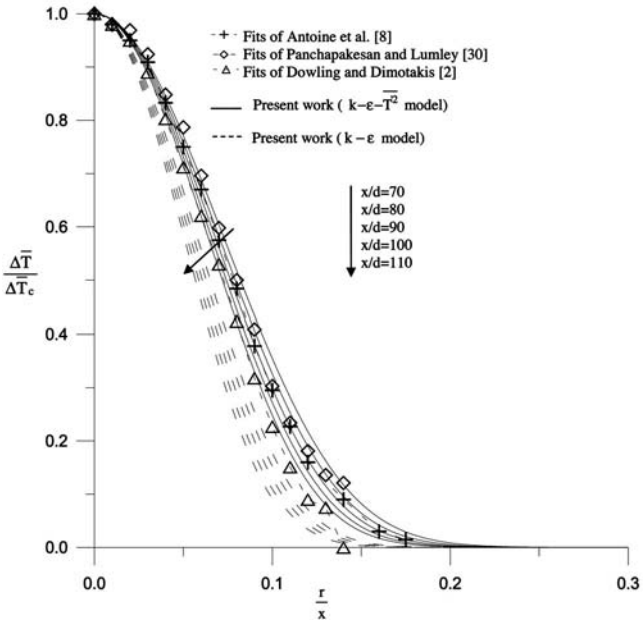


**Fig. 6 Radial distributions of the longitudinal excess temperature**

maximum value of the radial turbulent flux is smaller than that in the coflow data [8] and it is closer to the values measured in a free jet [30,40,41]. Nevertheless, as for the normalized Reynolds shear stress, similarity is not completely reached even for a higher axial distance. This tendency can be attributed to the absence of complete similarity solutions in a coflowing stream [8,39].

*4.1.2 Buoyant Jet*. To validate the numerical computations, results obtained from the ASM are compared with results from the $k$-$\varepsilon$ model in a buoyant jet. Calculations starts at the nozzle exit where uniform profiles were assumed (Eq. (8)) [14] with $u_{co}=0.01$.

Figure 9 shows the variation of centerline numerical profiles with height. Variables are normalized by Fr as suggested by Martynenko et al. [14]. The effect of Fr on the centerline profiles is clearly illustrated in this figure. As Fr increases, the length of the transition region increases. Further, downstream from the jet exit, the centerline dimensionless variables for all Fr calculated become the same and parallel. This means that all predictions are essentially independent of Fr in the plume region. In this region, the behavior of numerical solutions at the jet axis can be approximated by the known power solution [14]:

$$\frac{\overline{u}_{0_{ex}}}{\overline{u}_{0_{ex}}}\mathrm{Fr}^{1/2}=A_u\left(\frac{x}{d}\mathrm{Fr}^{-1/2}\right)^{-1/3} \qquad \frac{\Delta T_c}{\Delta T_0}\mathrm{Fr}^{1/2}=A_\theta\left(\frac{x}{d}\mathrm{Fr}^{-1/2}\right)^{-5/3}$$

$$\frac{k_c}{k_0}\mathrm{Fr}=A_k\left(\frac{x}{d}\mathrm{Fr}^{-1/2}\right)^{-2/3}$$

Coefficients $A_u$, $A_\theta$, and $A_k$ from the present study and reported by different authors [14,42–44] are given in Table 6.

The predictions from the ASM agree reasonably with the numerical results of Martynenko et al. [14]. From the $k$-$\varepsilon$ model, the coefficients do not provide a satisfactory agreement between the theory and the experiment. However, as Martynenko et al. [14] noted, the calculated $A_\theta$ factor from the ASM is almost 21% lower than the experimentally obtained factor [42–44]. From the $k$-$\varepsilon$ model, the $A_\theta$ factor computed is almost 32% higher [42–44].

On the whole, the ASM predicts the characteristics of a jet in a coflowing stream with a sufficient accuracy. It performs at least as well as the $k$-$\varepsilon$ model to predict the mean flow properties of the dynamic field and the ASM is better than the $k$-$\varepsilon$ model to model buoyancy and the turbulence structure.

**4.2 Influence of the Coflowing Stream Velocity.** The main objective of this numerical study is to examine the effect of the coflowing ambient stream on the behavior of the axisymmetric

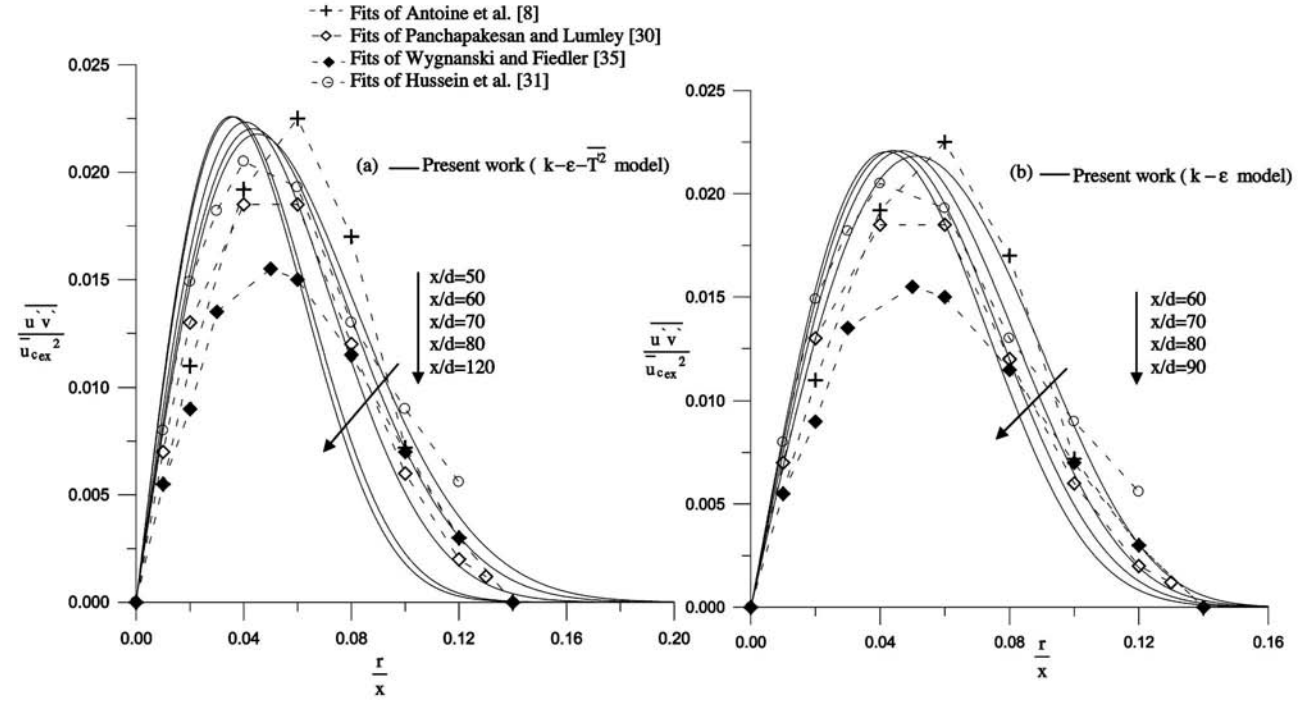


**Fig. 7 Radial distributions of the Reynolds shear stress**

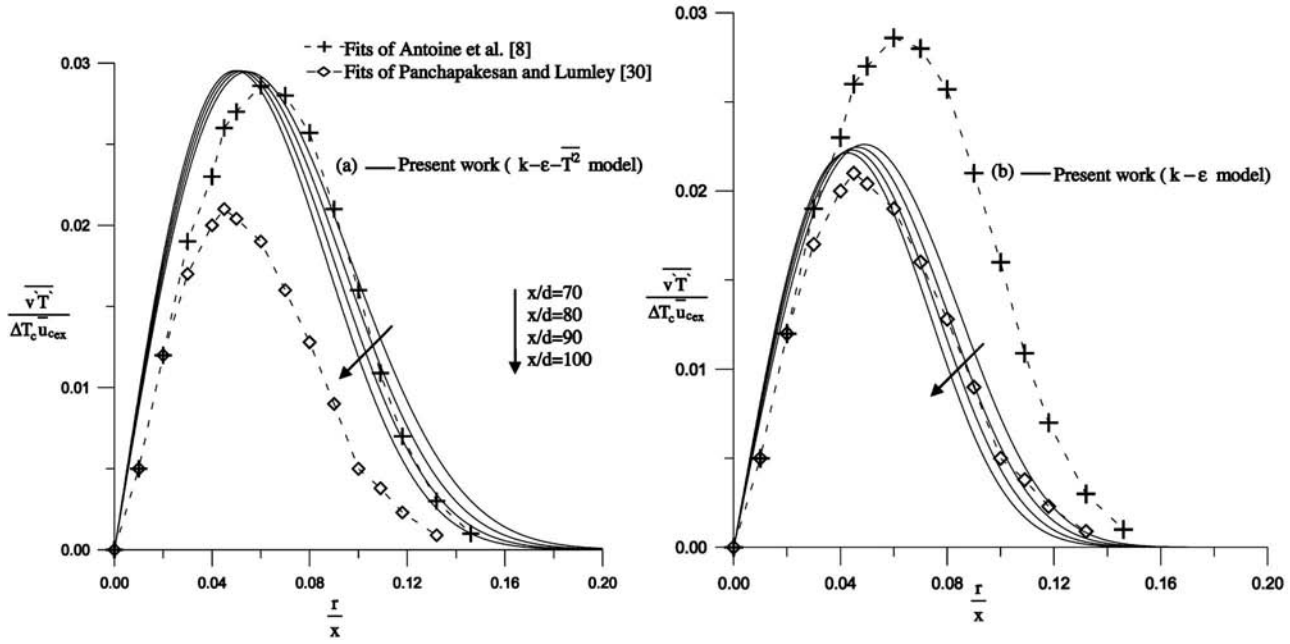


**Fig. 8 Radial distributions of the heat flux**

turbulent jet in comparison with a jet in a medium at rest ($u_{co}=0$). The results to be presented in the following are obtained for $k_0/\bar{u}_0^2=0.05$ and $\varepsilon_0 d/\bar{u}_0^3=0.02$ [14] and from the ASM.

*4.2.1 Forced Jet.* Figure 10 illustrates the distribution of the centerline longitudinal velocity for different coflowing streams. This figure shows that the centerline longitudinal velocity is almost constant in the potential core area and is independent of the coflow stream effect. Further downstream, the decay rate of the centerline longitudinal velocity is slower for high coflow streams. A light increase of the coflowing stream velocity (for $u_{co}<5\%$) modifies slightly the centerline longitudinal velocity profiles. So, the coflowing jet behaves like a jet in a medium at rest for $u_{co}<5\%$. With a ratio of a free-stream velocity higher than or equal to 5%, the centerline longitudinal velocity far from the nozzle exit is greater than that for a stagnant medium.

In Fig. 11, we represent the longitudinal excess velocity ($\bar{u}_{ex}=u-u_\infty$) normalized by the centerline longitudinal excess velocity ($\bar{u}_{c_{ex}}=u_c-u_\infty$) to show the effect of the coflow on the establishment of the similarity region. The abscissa has been normalized by the axial distance ($(x-x_o)/r$) rather than the half-radius. Normalization by the half-radius $y_{0.5\bar{u}}$, defined in the nomenclature, makes it difficult to detect any difference in ($\bar{u}_{ex}/\bar{u}_{c_{ex}}$) [31,9].

Figure 11(*a*) shows radial profiles of ($\bar{u}_{ex}/\bar{u}_{c_{ex}}$) at several downstream stations for $u_{co}=0.01$. For $x/d\geq 80$, the normalized excess velocity is independent of $x$ and the profiles take Gaussian forms: $(\bar{u}_{ex}/\bar{u}_{c_{ex}})=\exp[-A(r/(x-x_0))^2]$, where $A$ is determined from a fit of the numerical data. The constant $A$ obtained from the present study is found to be 105. This value is approximately 24% lower than that given by Sautet and Stepowski [4] ($A=138.88$) for jets of hydrogen-nitrogen mixtures discharged into a coflow. This difference can be attributed to the fact that the investigation of Sautet and Stepowski [4] is restricted to the region near the nozzle ($5\leq x/d\leq 20$) where buoyancy and coflow have negligible effects.

According to Habli et al. [15], the established region of an axisymmetric jet emerging in a medium at rest begins at $x/d\approx 50$, whereas this zone begins at $x/d=70$ according to Wygnan-

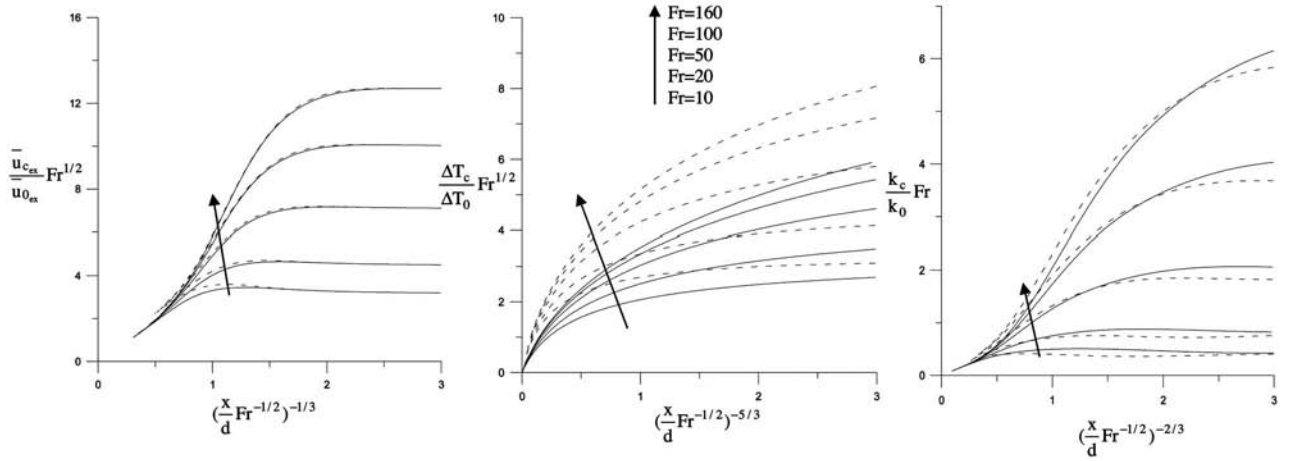


**Fig. 9 Centerline distributions of numerical solutions for a buoyant jet: $u_{co}=0.01$**

**Table 6 Coefficients of a buoyant turbulent round jet in the plume region**

| Authors | $A_u$ | $A_\theta$ | $A_k$ |
|---|---|---|---|
| Present work (ASM) | 3.7 | 7.35 | 0.91 |
| Present work ($k$-$\varepsilon$) | 4.48 | 12.35 | 1.06 |
| Ref. [14] | 3.18, 3.27, 3.16 | 5.85, 5.47, 5.85 | 0.78, 0.79 |
| Ref. [42] | 3.5 | 9.35 | — |
| Ref. [43] | 3.4 | 9.4 | — |
| Ref. [44] | — | 9.46 | --- |

ski and Fielder [35]. In fact, the initial conditions can have an effect on the development of the similarity state [7,9]. Thus, for $u_{co}=0.01$, the coflowing jet behaves like a free jet. Nevertheless, for $u_{co}\geq 0.05$ (Figs. 11(*a*) and 11(*c*)), profiles of the normalized longitudinal excess velocity do not coincide even at high values of $(x\text{-}x_o)/r$. This confirms the absence of a complete similarity in the presence of significant coflowing streams [13,39].

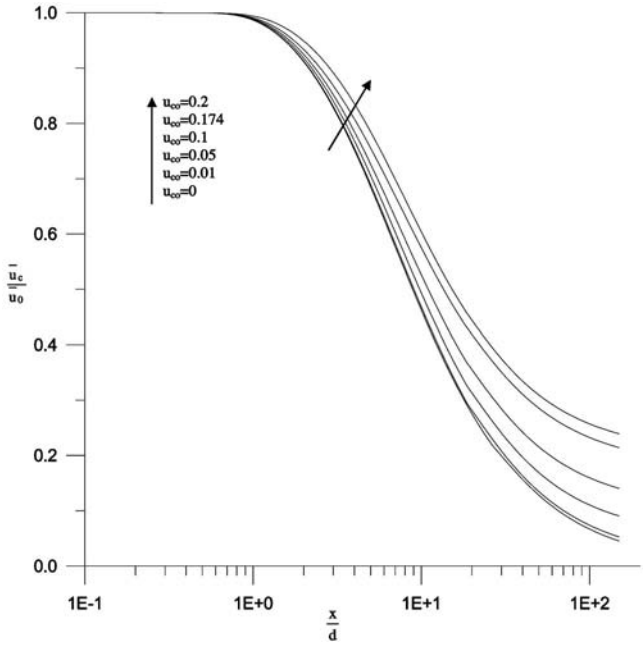


**Fig. 10 Axial distributions of the centerline longitudinal velocity for different velocity coflows**

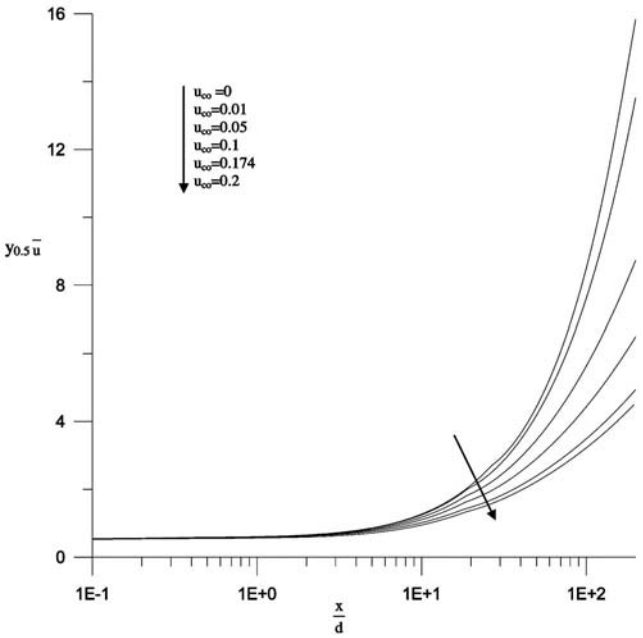


**Fig. 12 Axial distributions of the dynamic half-radius of the jet for different coflows**

Figure 12 shows the longitudinal distribution of the dynamic half-radius of the jet for different coflowing streams. The main visible effect of the coflow is the jet decay rate reduction in comparison with a free jet. The dynamic half-radius profiles coincide in the area close to the nozzle exit. This means that the effect of the coflowing stream is negligible in this area. For $u_{co}=0.01$, the coflowing stream influence on the jet becomes noticeable for $x/d>20$. For a higher velocity, the coflowing stream influence starts to be conspicuous very close to the jet exit.

The influence of the coflow stream also acts on the turbulent properties field such as the kinetic energy of turbulence $k_c/\bar{u}_0^2$ (Fig. 13(*a*)). This figure shows that the coflowing stream has no influence on the turbulent kinetic energy in the areas close to and far from the nozzle exit. Just downstream of the inlet jet, there is a local minimum and a local maximum for $k_c/\bar{u}_0^2$ followed by a decrease of the turbulent kinetic energy.

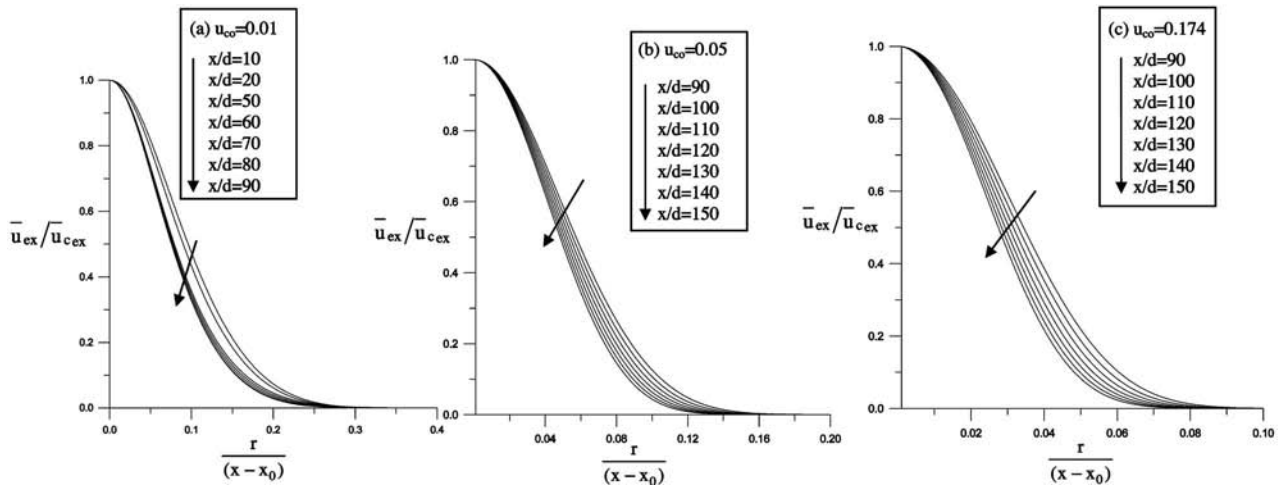


**Fig. 11 Radial distributions of the excess velocity at several downstream stations and for different coflowing streams**

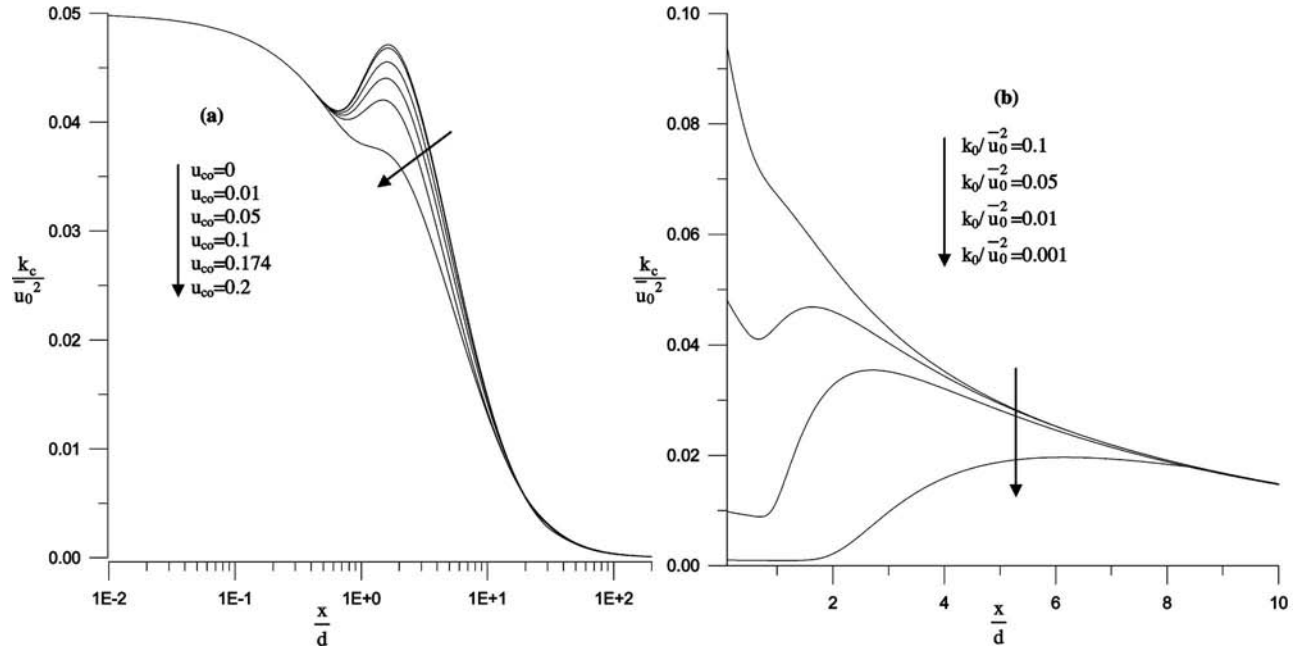


**Fig. 13 Axial distributions of the turbulence kinetic energy for (*a*) different coflows and (*b*) different levels of $k_0/\bar{u}_0^2$: $u_{co}$ =0.01**

In Fig. 13(*b*), we examine the effect of the initial level of turbulence over the kinetic energy development at the jet axis in the near field. This figure shows that a prescription of different levels of the kinetic energy exerts a strong influence only on the region adjacent to the outlet. In this region, for $(k_c/\bar{u}_0{}^2 >= 0.01)$, the centerline kinetic energy presents a minimum followed by a local maximum. For $(k_c/\bar{u}_0{}^2 = 0.001)$, the centerline kinetic energy remains constant then it reaches a maximum followed by a decrease of this parameter. The position of this maximum is considered to be where the axial velocity has the largest gradient in the axial direction, i.e., at the potential core ends [11].

In Table 7, we report the maximum values of the normalized Reynolds shear stress obtained for different coflowing velocities. This table shows that the introduction of a disturbance in the ambient stream generates an increase in the Reynolds shear stress. Inflow conditions can have a long-lived downstream effect on the development of the turbulent flow field [6]. For $u_{co}=0.01$; the value of $(\overline{u'v'}/\bar{u}_{c_{ex}}^2)_m$ is comparable to values determined in a jet in a quiescent ambient by different authors of Refs. [30,31].

Budget for the Turbulent Kinetic Energy Under the mentioned hypothesis in the numerical modeling paragraph, the transport equation for the kinetic energy of turbulence (ASM) in forced convection (i.e., $\phi=k$ in the generalized equation (2)) can be written in the following way:

$$\underbrace{\bar{u}\frac{\partial k}{\partial x}+\bar{v}\frac{\partial k}{\partial r}}_{\text{Convection}}=\underbrace{\frac{1}{r}\frac{\partial}{\partial r}\left(rD_k\frac{\partial k}{\partial r}\right)}_{\text{Diffusion}}+S_k$$

where $D_k(D_k=c_k k/\varepsilon\overline{v'^2})$ is the turbulent diffusion term, $S_k(S_k = P_{\text{Production}}-\varepsilon_{\text{Dissipation}})$ being the source term. $D_k$ and $S_k$ are given in Table 3.

The radial distribution of the budget for the turbulent kinetic energy transport equation normalized by $(y_{0.5\bar{u}}/\bar{u}_{c_{ex}}^3)$ is presented in Fig. 14, at several downstream stations for $u_{co}=0.01$. As is the convention, positive quantities denote a loss (or flux out of the control volume) and negative quantities denote a gain (or flux into the control volume). The diffusion term was obtained by difference, i.e., Diffusion=(Convection-Production-Dissipation).

In the vicinity of the jet exit, Fig. 14(a) reveals a strong imbalance of the flow since dissipation and diffusion are of the same sign and order but convection and production are of different signs, although of the same order. The strong production of turbulent energy, as well as the strong viscous dissipation of energy, can be seen in the core of the jet $(r/x\approx 1)$. The convection term in the turbulent kinetic energy equation acts to transport energy from the edges of the jet toward the centerline, while the diffusion term acts to transport turbulence energy away from the region of peak production toward the jet centerline as well as toward the jet edges. Near the outer edges of the jet, as discussed by Tennekes

**Table 7 Maximum values of the Reynolds shear stress**

| | $u_{co}=0$ | $u_{co}=0.01$ | $u_{co}=0.05$ | $u_{co}=0.1$ | $u_{co}=0.174$ | $u_{co}=0.2$ |
|---|---|---|---|---|---|---|
| $\left(\frac{\overline{u'v'}}{\bar{u}_{c_{ex}}^2}\right)_m$ | 0.018 [15]; 0.0190 [30] 0.0211 [31]; 0.0155 [35] | 0.020 | 0.022 | 0.0246 | 0.0247 | 0.0248 |

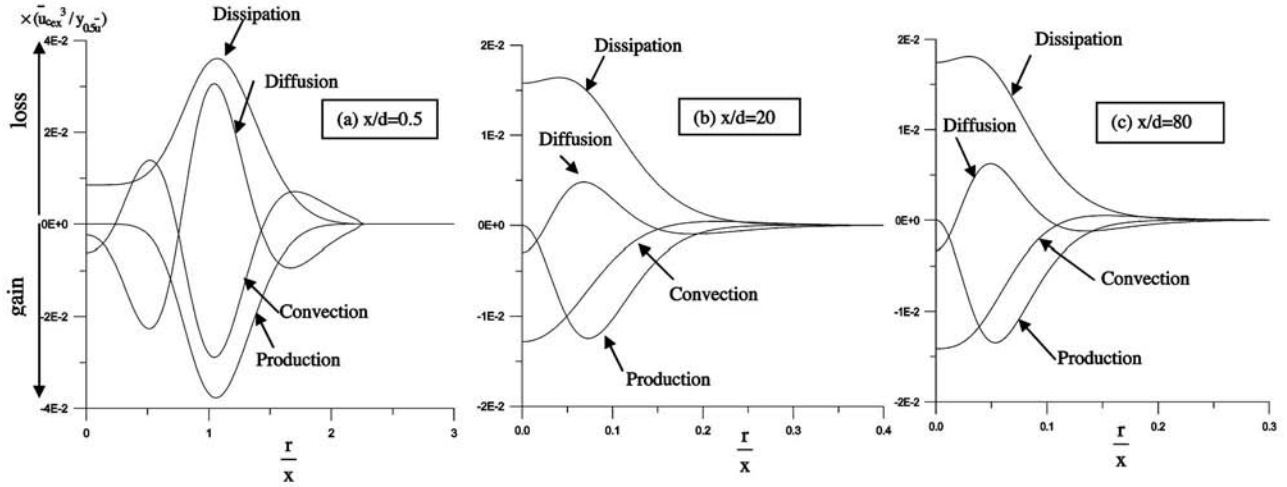


**Fig. 14 Radial distributions of the budget for the turbulent kinetic energy transport equation at several downstream stations: $u_{co}=0.01$**

and Lumley [45], the balance is predominantly between the diffusion term and the convection. At this point in the jet, the diffusion term acts to spread turbulent energy outwards toward the jet edges while the convection due to the entrainment velocity transports energy inwards. In the intermediate station of the jet (Fig. 14(*b*)), the production decreases in amplitude. The diffusion of energy, while remaining important, decreases gradually. On the other hand, dissipation tends to be the predominant transport mechanism. For $x/d=80$ (Fig. 14(*c*)), in the fully developed region of the jet, the maximum value of production and dissipation move toward the jet axis. At the centerline, the production term is zero so the convection and diffusion terms are the sole means by which turbulence energy is present at the core of the jet. The production has a maximum at $r/x\approx 0.053$ (Fig. 14(*c*)), which corresponds to the regions of peak shear stress. This value is close to the values of Hussein et al. ($r/x\approx 0.051$) [31] and Wygnanski and Fiedler ($r/x\approx 0.052$) [35]. The convection has its maximum on the centerline; it is as large as the dissipation. At $r/x>0.12$ ($r/x>0.117$ [35]), the convection changes its sign and becomes a loss to the budget. At $r/x\approx 0.11$ ($r/x>0.12$ [35]), the dissipation is balanced solely by the production. In fact, the budget suggests dividing the flow into two regions. In the outer region ($r/x>0.1$), the mechanisms of production and dissipation approximately balance each other and the flow can be considered in a local equilibrium. In the inner region ($r/x<0.1$), this is not true.

In general, the turbulent-energy balance compares well with the energy balance given by Wygnanski and Fiedler [35] despite the difference observed on the axis of the jet, which is mainly due to the production term, which is not equal to zero in experimental studies [31,35]. To take account of this, Minh et al. [46] introduced generation terms of second order to ensure that the production term is different from zero.

In the experimental studies in the past, it has been necessary to make various approximations regarding the term in the turbulent kinetic energy equation in order to estimate their balance. Ramparian and Chandrasekhara [47] did not measure the dissipation directly, but they estimated it using the energy spectra of $\overline{u'^2}$. On the other hand, Gutmark and Vygnanski [48] estimated the dissipation using the isotropic assumption.

The different normalized terms of the budget for the turbulent kinetic energy are plotted for the different coflowing stream velocities (Fig. 15) and similar observations can be made. Close to the axis and in the core region, the co-flow has a little influence on the different terms of the kinetic energy balance. Nevertheless, this figure shows that when the co-flowing stream velocity is increased, the maxima of the diffusion and production terms move towards the jet axis. Away from the core region, the increase of the co-flowing stream velocity leads to a significant reduction of the dissipation and the production.

*4.2.2 Buoyant Coflowing Jet*. Figure 16 shows, respectively, the longitudinal distribution for different Froude numbers of the centerline excess velocity (*a*) and the dynamic half-radius $y_{0.5\bar{u}}$ (*b*). In a buoyant jet, three distinct regions exist. The first is an initial nonbuoyant region called pure jet, where the buoyancy and coflow effects are not important and which occurs near the jet exit. In this region, the axis velocity (Fig. 16(*a*)) and the dynamic half-radius (Fig 16(*b*)) remain constant and approximately equal to their values at the nozzle exit for different Froude numbers. This is followed by a second, transition, region where the buoyancy and the inertia play equally important roles in determining the characteristics of the jet. Here, the coflow effect is no longer

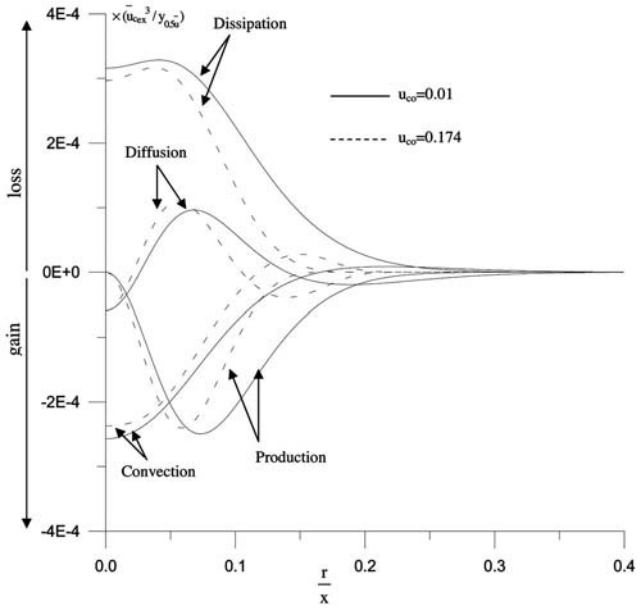


**Fig. 15 Radial distributions of the budget for the turbulent kinetic energy transport equation for different coflowing streams: $x/d=20$**

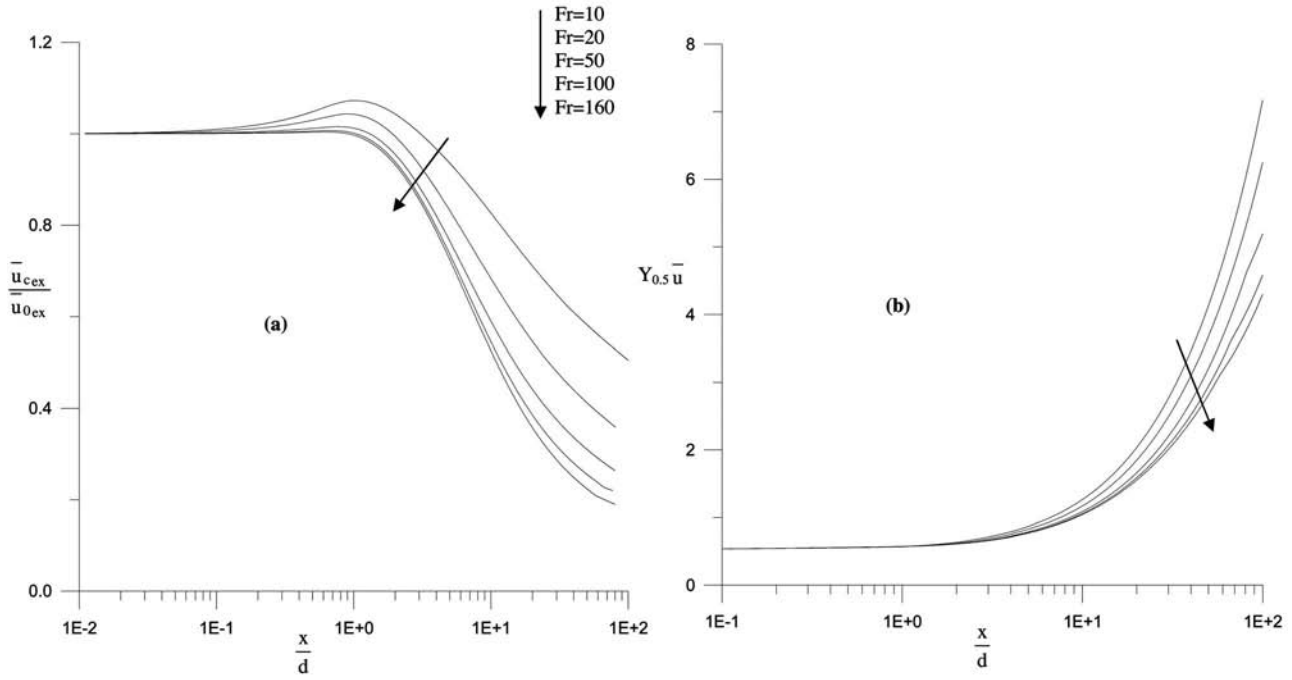


**Fig. 16 Longitudinal distributions for different Froude numbers of (*a*) the centerline excess velocity and (*b*) the dynamic half-radius: $u_{co}=0.174$**

negligible. In this region, the axis velocity can go over its value and the growth of the dynamic half-radius is slow. The third region, where the flow is far from the source, is a plume; the coflow effect is important, the effects of inertia are neglected, and the buoyancy becomes the only important parameter. In this region, the axis velocity decreases with the distance $x$ and the inverse decay rate of the dynamic half-radius is highlighted for small Froude numbers.

The longitudinal distribution of the centerline excess temperature (*a*) and the longitudinal distribution of the thermal half-radius $y_{0.5\bar{T}}$ (*b*) are depicted in Fig. 17, for different Froude numbers. In a region close to the nozzle exit, Fig 17(*a*) reveals no effect of Froude number. As the Froude number increases, the length of the initial region increases. In the transition and plume regions, the decay rate of the centerline excess temperature is lower for higher values of the Froude number. When the Froude number increases, the drive of ambient air becomes more important and conse-

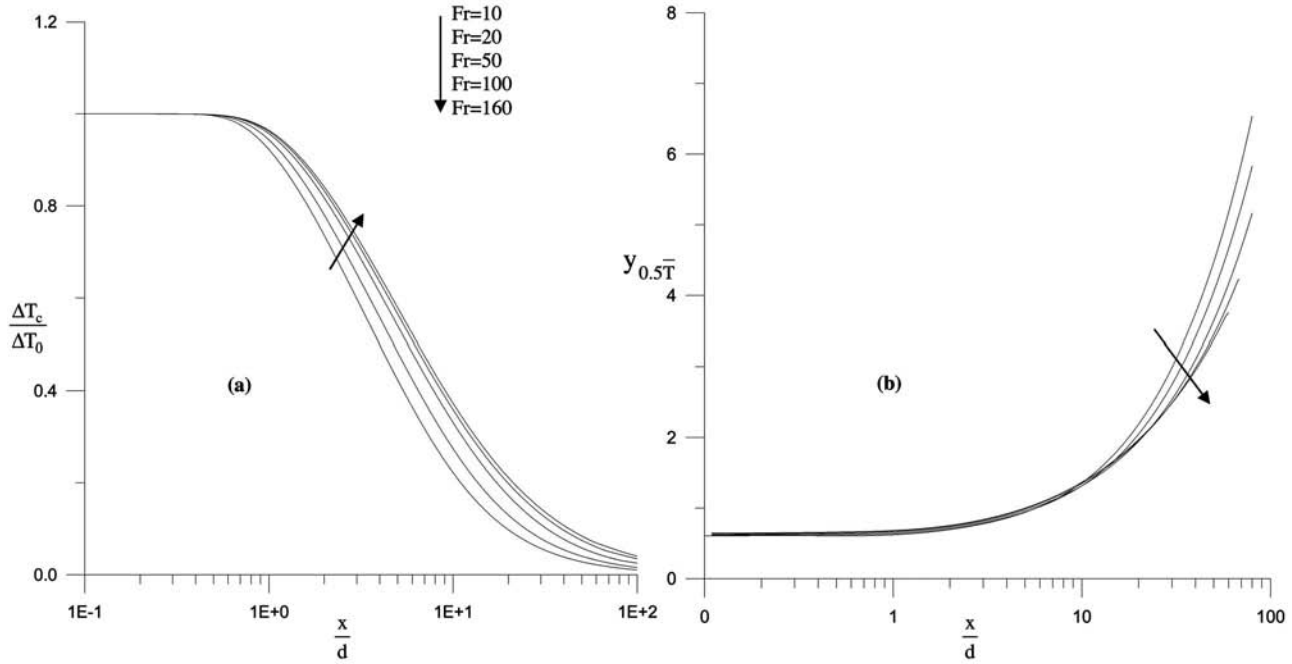


**Fig. 17 Longitudinal distributions for different Froude numbers of (*a*) the centerline excess temperature and (*b*) the thermal half-radius: $u_{co}=0.174$**

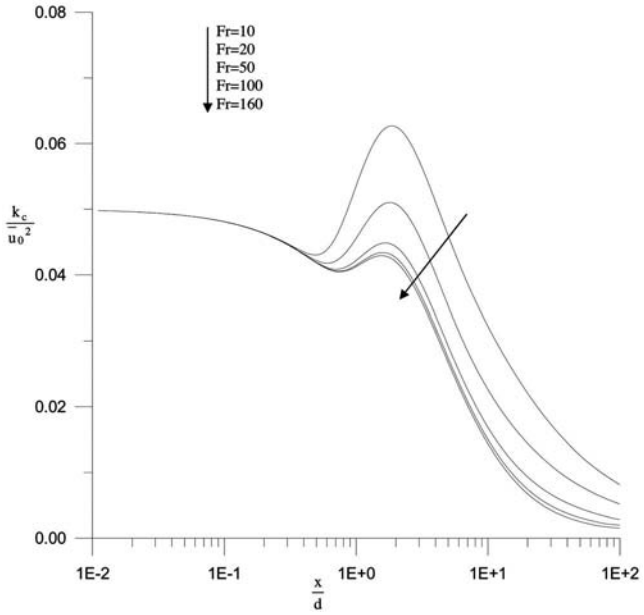


**Fig. 18 Longitudinal distributions of the turbulent kinetic energy for different Froude numbers: $u_{co}=0.174$**

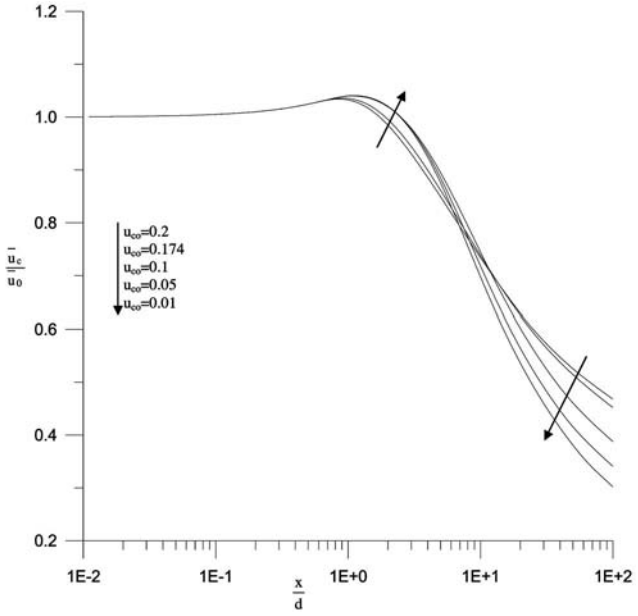


**Fig. 19 Centerline longitudinal distributions of the velocity for different coflowing streams: Fr=20**

quently the cooling of the flow is faster.

Figure 17(*b*) shows agreement between different results for all Froude numbers, only in the vicinity of the nozzle exit. Far from the jet exit, the decay rate of thermal half-radius is lower for higher values of the Froude number.

We represent the distribution of the turbulent kinetic energy according to the Froude number in Fig. 18. Profiles of the kinetic energy are the same in an area close to the nozzle exit. A little further from this zone, the shift between the profiles appears and the increase of the Froude number leads to a significant reduction on the centerline turbulent kinetic energy. Considering the importance of the inertia in the potential core area, the increase of buoyancy does not have any effect on this area. However, in the buoyant jet (transition and plume regions) buoyancy play an important role, which translates to a significant reduction in the turbulent kinetic energy, particularly its maximum value, when free convection decreases.

Figure 19 shows the longitudinal distribution of the centerline velocity with different coflow streams in free convection (Fr =20). In fact, in a vertical buoyant jet, two parameters play important roles: the initial momentum flux and the buoyancy flux. To estimate the different behavior, a function of a dimensionless parameter has been characterized in a jet in a medium at rest [42] ($x_1=\mathrm{Fr}^{-1/2}(\rho_0/\rho_\infty)^{-1/4}(x/d)$). For $x_1<0.5$, the flow is a pure jet, whereas it is a plume when $x_1>5$ [42]. However, the results of Papanicolaou and List [29] show that the flow is a pure jet for $x_1<1$.

As seen in Fig. 19, for $x/d<1$ the flow is a pure jet (value is 50% smaller than the data of Chen and Rodi [42] and compares well the data of Papanicolaou and List [29]). In this region, coflow does not have any influence on the flow and the velocity remains constant and approximately equal to its value at the nozzle exit. For $x/d>20$ (9% smaller than the data of Chen and Rodi [42]), the buoyancy and coflow effects are important. So, in this region the decay of the centerline longitudinal velocity is slowed down by buoyancy and coflow. However, in the transition region, inertial forces, buoyancy forces, and coflow play equally important roles in determining the characteristic of the flow. Thus, decay laws are not well defined in this region.

The similarity region of mean characteristics for different velocity coflows is determined from the profiles of the longitudinal excess velocity normalized by the centerline longitudinal excess velocity for Fr=20 (Fig. 20). Similarity is established when the normalized radial excess velocity becomes independent of $x$. Results are summarized in Table 8.

Table 8 shows that the increase of the coflow can slow the development of the jet to a similarity state [6]. The similarity region starts at a distance closer to the nozzle exit when we consider buoyant jet in comparison with a forced jet. It is also noted that for $(u_\infty/u_0)=0.05$ a similarity state is reached contrary to a forced jet. In addition, in buoyant jets in a medium at rest, similarity occurred for $x_1\approx 5$ for mean characteristics [14]. For Fr =20 and $u_{co}=0$, similarity occurred for $x/d\approx 22$ [14]. Thus, for $u_{co}=0.01$ (Table 6), the coflowing jet behaves like a free jet.

A similar effect of coflow on the longitudinal distribution of the centerline velocity is observed on the longitudinal distribution of the centerline excess temperature (Fig. 21(*a*)). This figure shows an agreement between results for different coflowing streams in the pure jet ($x/d<1$). In the plume region ($x/d>20$), there is a slight influence of the coflow on the centerline excess temperature. In this region, the decay rate of the centerline excess temperature is slowed by the buoyancy and coflow effects. In the transition region, buoyancy forces, inertial forces, and coflow influence the distribution of the excess temperature.

The profiles of the thermal half-radius (Fig. 21(*b*)) are the same for all velocity coflowing streams in the area close to the nozzle exit because of the absence of buoyancy and coflow effects. Far from the jet exit, the spreading rate of the temperature is reduced by the increase of the coflow.

The effect of coflowing streams on the normalized longitudinal distribution of the centerline turbulent kinetic energy $(k_c/\bar{u}_0^2)$ is presented in Fig. 22. It can be seen that the profiles of the centerline turbulent kinetic energy are the same in the pure jet region as for the other parameters because the coflow and buoyancy effects do not have any influence on the flow in this region. In the intermediate region, the centerline turbulent kinetic energy is affected by buoyancy forces, inertia forces, and coflow. In the plume region, the decay rate of the kinetic energy on the centerline axis $(k_c/\bar{u}_0^2)$ is faster for higher coflow streams.

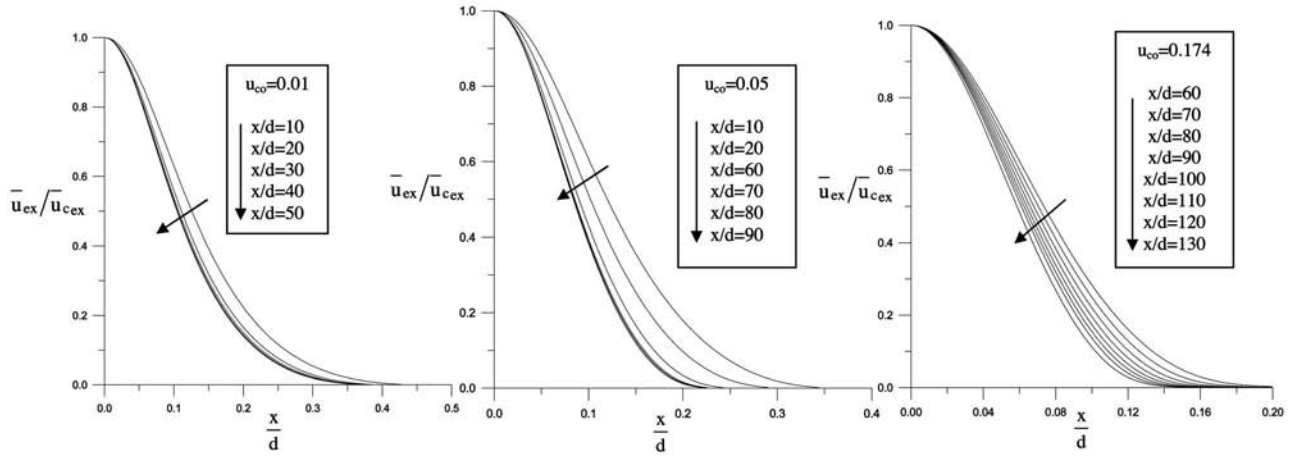


**Fig. 20 Radial distributions of the excess velocity at several downstream stations and for different coflowing streams: Fr =20**

## 5 Conclusion

In the present paper, results of a numerical investigation of the behavior of a buoyant turbulent axisymmetric jet discharged in a coflowing ambient stream are presented. The performance of the ASM is compared with the $k$-$\varepsilon$ model for predicting the development of the flow field. Numerical results from the investigated models are compared with experimental and numerical data reported in the literature. The results from the ASM enable a sufficient reproduction of this jet flow. It performs at least as well as the $k$-$\varepsilon$ model in predicting the mean flow properties of the dynamic field, and is better than the $k$-$\varepsilon$ model in modeling buoyancy and the turbulence structure.

In forced convection, numerical results show that the axisymmetric jet discharged in a coflowing stream develops to closely approximate the similarity of mean characteristic distributions of a free jet for $u_{co} < 0.05$, while a jet with a higher rate of a coflowing stream never reaches similarity state.

In a buoyant coflowing jet, three regions exist. The first is an initial nonbuoyant region, where buoyancy and coflow effect are not important, and occurs near the jet exit. In this region, different characteristics of the jet remain constant at approximately their values at the nozzle exit for different Froude numbers and coflow streams. In the second, transition, region buoyancy and inertial forces are of comparable importance in determining the characteristics of the jet. In this region, the flow is very much affected by

**Table 8 Established region for different coflowing streams (Fr=20)**

| $u_{co}$ | 0.01 | 0.05 | 0.174 |
|---|---|---|---|
| Similarity region ($x/d$) | 30 | 70 | — |

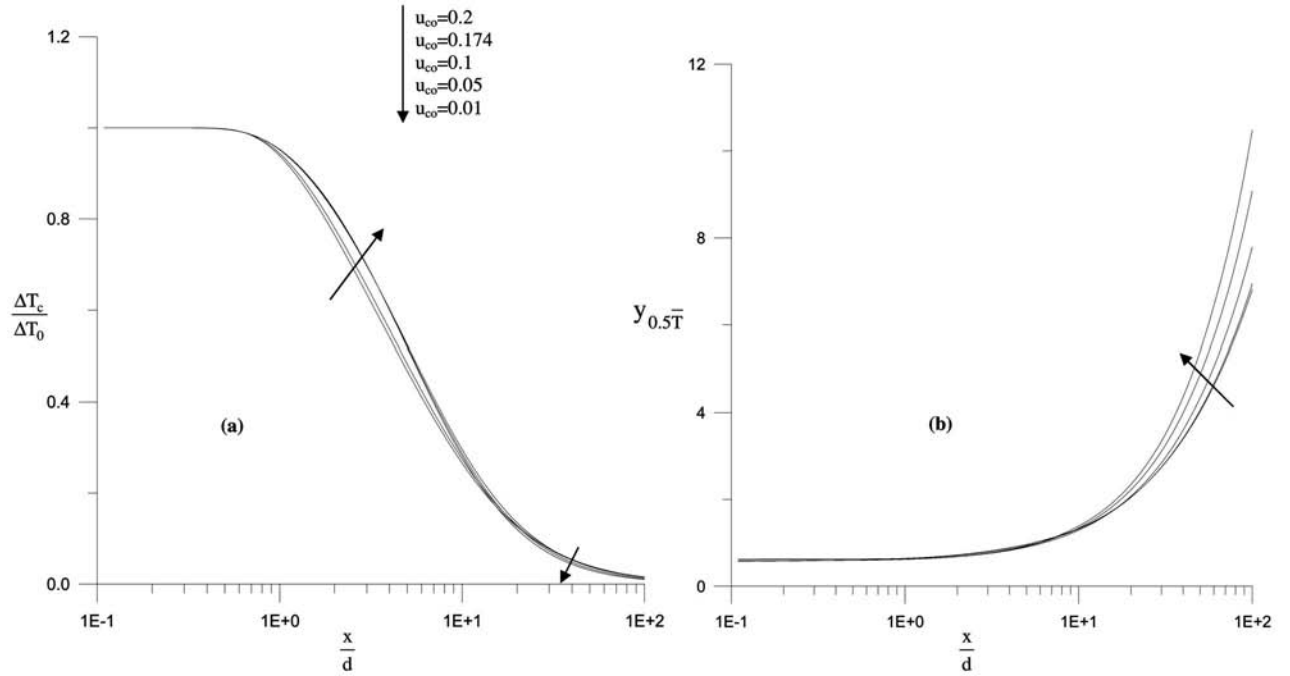


**Fig. 21 Longitudinal distributions for different co-flowing streams of (*a*) the centerline excess temperature and (*b*) the thermal half-radius: Fr=20**

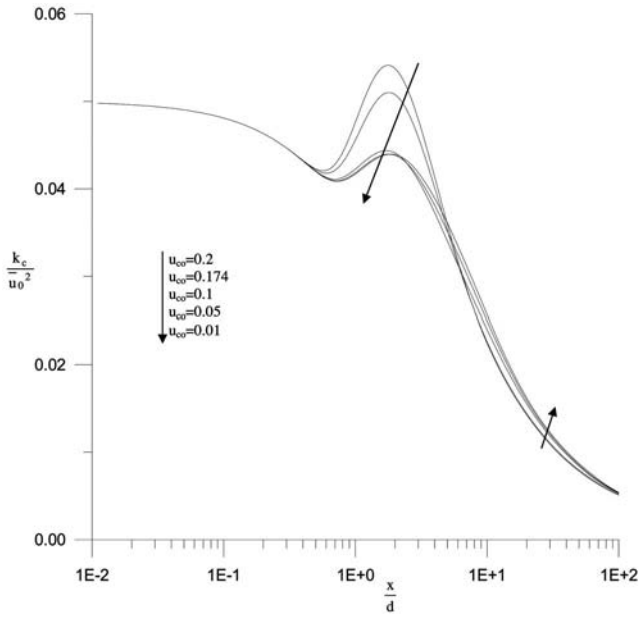


**Fig. 22 Longitudinal distributions of the centerline turbulent kinetic energy for different coflowing streams: Fr=20**

buoyancy forces, inertia forces, and the coflow effect. The third region, where the flow is far from the source, is a plume and the buoyancy and coflow effects are important. In this region, the mean characteristics of the flow field are slowed down by buoyancy and coflow, whereas the decay rate of the kinetic energy is reduced for higher coflows.

A region of similarity in velocity and temperature distributions, in a buoyant jet, starts at a distance closer to the nozzle exit in comparison with a forced jet. For $u_\infty/u_0=0.05$ a similarity state is reached contrary to the case for a forced jet. Increasing of the coflowing stream can slow the development of the jet to a similarity state.

## Nomenclature

$c_\mu, c_{\varepsilon 1}, c_{\varepsilon 2}$ = coefficients in the ($k$-$\varepsilon$) model
$c_0, c_1, c_2, c_\varepsilon, c_{\varepsilon 1}, c_{\varepsilon 2}$,
$c_k, c_T, c_{T1}, c_h, c_{h1}$ = coefficients in the ASM
$c_{\mu m}, c_{\varepsilon 2m}$ = correction functions
$D$ = diffusion term
$D_\phi$ = coefficient of turbulent diffusion
$d$ = nozzle diameter (m)
Fr = Froude number $u_0^2/g\beta\Delta T_0 d$
$g$ = gravitational acceleration ($\mathrm{m\cdot s^{-2}}$)
$G$ = production term due to buoyancy
$i, j$ = axial and radial nodes
$K_u, K_y, K_T$ = velocity, dynamic half-radius, and thermal decay rates
$k$ = turbulent kinetic energy ($\mathrm{m^2\ s^{-2}}$)
$P$ = production term
Re = Reynolds number $u_0 d/\nu$
$\mathrm{Re}_c$ = critical value of Reynolds number
$S_\phi$ = source term
$\overline{T'^2}$ = mean square temperature fluctuation ($\mathrm{K^2}$)
$\bar{T}$ = mean temperature, $\Delta T=\overline{T-T_\infty}$ (K)
$u, v$ = axial and radial components of velocity, respectively ($\mathrm{m\ s^{-1}}$)
$\bar{u}, \bar{v}$ = mean axial and radial components of velocity, respectively ($\mathrm{m\ s^{-1}}$)
$\Delta x, \Delta r$ = axial and radial steps (m)
$\overline{u'v'}$ = turbulent shear stress ($\mathrm{m^2/s^2}$)
$\overline{v'^2}$ = normal Reynolds stress
$\overline{v'T'}, \overline{u'T'}$ = turbulent heat flow
$x, r$ = axial and radial coordinates (m)
$x_0$ = dynamic virtual origin
$x_0^{(T)}$ = thermal virtual origin
$x_1$ = dimensionless function ($x_1=\mathrm{Fr}^{-1/2}(\rho_0/\rho_\infty)^{-1/4}(x/d)$)
$y_{0.5\bar{u}}$ = dynamic jet half-radius, value of radius at which mean axial velocity excess is half of the centerline axial velocity excess (m)
$y_{0.5\bar{T}}$ = thermal jet half-radius, value of radius at which the mean temperature is equal to half its value at the centerline (m)
$u_{\mathrm{co}}$ = $\bar{u}_\infty/\bar{u}_0$
$u_{\mathrm{ex}}$ = $u-u_\infty$ $\mathrm{m\ s^{-1}}$

### Greek Symbols

$\beta$ = coefficient of volumetric expansion ($\mathrm{K^{-1}}$)
$\varepsilon$ = dissipation rate ($\mathrm{m^2\ s^{-3}}$)
$\nu_t$ = kinematic eddy viscosity($\mathrm{m^2\cdot s^{-1}}$)
$\phi$ = generalized variable
$\rho$ = fluid density
$\sigma_k, \sigma_\varepsilon, \sigma_T$ = turbulent Prandtl numbers
$\theta$ = momentum radius [$\theta=(\pi(d/2)^2(\bar{u}_0/\bar{u}_\infty-1)\bar{u}_0/\bar{u}_\infty/\pi\bar{u}_\infty^2)$]

### Subscripts

$c$ = centerline value
$\infty$ = ambient fluid
0 = value at the jet exit
$m$ = maximum value
ex = excess

### Superscripts

$-$ = average
$'$ = fluctuation

## References


[1] Antonia, R. A., and Bilger, R. W., 1973, "An Experimental Investigation of an Axisymmetric Jet in a Co-Flowing Air Stream," J. Fluid Mech., **61**, pp. 805–822.

[2] Dowling, D. R., and Dimotakis, P. E., 1990, "Similarity of the Concentration Field of Gas-Phase Turbulent Jets," J. Fluid Mech., **218**, pp. 109–141.

[3] Pitts, W. M., 1991, "Reynolds Number Effects on the Centerline Mixing Behavior of Axisymmetric Turbulent Jets," Exp. Fluids, **11**, pp. 135–144.

[4] Sautet, J. C., and Stepowski, D., 1995, "Dynamic Behavior of Variable-Density, Turbulent Jets in Their Near Development Fields," Phys. Fluids, **7**(11), pp. 2796–2806.

[5] Nickels, T. B., and Perry, A. E., 1996, "An Experimental and Theoretical Study of the Turbulent Co-Flowing Jet," J. Fluid Mech., **309**, pp. 157–182.

[6] LaRue, J. C., Ly, T., Rahai, H., and Jan, P. Y., 1997, "On Similarity of a Plane Turbulent Jet in a Co-Flowing Stream," *Proceedings of the 11th Symposium on Turbulent Shear Flows*, Springer, New York, Vol. 3, pp. 25. 11–25.16.

[7] Morgans, R. C., Dally, B. B., Nathan, G. J., Lanspeary, P. V., and Fletcher, D. F., 1999, "Application of the Revised Wilcox (1998) k-w Turbulence Model to a Jet in Co-Flow," *Second International Conference on CFD in the Minerals and Process Industries CSIRO*, Melbourne, Australia, pp. 479–484.

[8] Antoine, Yan, Lemoine, F., and Lebouché, M., 2001, "Turbulent Transport of a Passive Scalar in a Round Jet Discharging Into a Co-Flowing Stream," Eur. J. Mech. B/Fluids, **20**, pp. 275–301.

[9] Mi, J., Nobes, D. S., and Nathan, G. J., 2001, "Influence of Jet Exit Conditions on the Passive Scalar Field of an Axisymmetric Free Jet," J. Fluid Mech., **432**, pp. 91–125.

[10] Smith, E. J., Mi, J., Nathan, G. J., and Dally, B. B., 2004, "Preliminary Examination of a Round Jet Initial Condition Anomaly for the $k$-$\varepsilon$ Turbulence Model," *15th Australasian Fluid Mechanics Conference*, The University of Sydney, Sydney, Australia.

[11] Imine, B., Saber-Bendhina, A., Imine, O., and Gazzah, M. H., 2005, "Effects of a Directed Co-Flow on a Non-Reactive Turbulent Jet with Variable Density," Heat Mass Transfer, **42**, pp. 39–50.

[12] Reichardt, H., 1964, "Turbulente Strahlausbreitung in gleichgerichteter Grundstromung," Forsch. Ingenieurwes., **30**, pp. 133–164.

[13] Pope, S. B., 1978, "An Explanation of the Round Jet/Plane Jet Anomaly," AIAA J., **16**, pp. 279–281.

[14] Martynenko, O. G., and Korovkin, V. N., 1994, "Flow and Heat Transfer in

Round Vertical Buoyant Jets," Int. J. Heat Mass Transfer, **37**(1), pp. 51–58.
[15] Habli, S., Mhiri, H., El Golli, S., Le Palec, G., and Bournot, P., 2001, "Etude numérique des conditions d'émission sur un écoulement de type jet axisymétrique turbulent," Int. J. Therm. Sci., **40**, pp. 497–511.
[16] Gerge, W. K., Wang, H., Wollblad, C., and Johansson, T. G., 2001, "Homogenous Turbulence and Its Relations to Realizable Flows," *14th AFMC*, Adelaide, Australia, pp. 41–48.
[17] Chen, C. J., and Nikitopoulos, C. P., 1979, "On the Near Field Characteristics of Axisymmetric Turbulent Buoyant Jets in a Uniform Environment," Int. J. Heat Mass Transfer, **22**, pp. 245–255.
[18] Chen, C. J., and Chen, C. H., 1979, "On Prediction and Unified Correction for Decay of Vertical Buoyant Jets," Trans. ASME, Ser. C: J. Heat Transfer, **101**, pp. 245–255.
[19] Ville, Hämäläinen, 2001, "Implementing an Explicit Algebraic Reynolds Stress Model Into the Three-Dimensional FINFLO Flow Solver," Report B-52.
[20] Lars, D., 2003, "An Introduction to Turbulence Models," Department of Thermo and Fluid Dynamics, Chalmers University of Technology Göteborg, Sweden.
[21] Schlichting, H., 1979, *Boundary-Layer Theory*, 7th ed., McGraw-Hill, New York.
[22] Dimotakis, P. E., 1993, "Some Issues on Turbulent Mixing and Turbulence," *Turbulence Symposium in Honor of W. C. Reynolds' 60th Birthday*, Monterey, CA, pp. 1–34.
[23] Ricou, F. P., and Spalding, D. B., 1961, "Measurements of Entrainment by Axisymmetric Turbulent Jets," J. Fluid Mech., **11**, 21–32.
[24] Ebrahimi, I., and Kleine, R., 1977, "Konzentrationsfelder in Isothermermen Luft-Freistrahlen," Forsch. Ingenieurwes., **43**, pp. 25–30.
[25] Grandmaison, E. W., Rathgeber, D. E., and Becker, H. A., 1982, "Some Characteristics of Concentration Fluctuations in Free Turbulent Jets," Can. J. Chem. Eng., **60**, pp. 212–219.
[26] Malmström, T. G., Kirkpatrick, A. T., Christensen, B., and Knappmiller, K. D., 1997, "Centerline Velocity Decay Measurements in Low-Velocity Axisymmetric Jets," J. Fluid Mech., **346**, pp. 363–377.
[27] Patankar, S. V., and Spalding, D. B., 1972, "A Calculation Procedure for Heat, Mass and Momentum Transfer in Three-Dimensional Parabolic Flows," Int. J. Heat Mass Transfer, **15**, pp. 1787–1806.
[28] Hinze, J. O., and Van Der Hegge Zijnen, B. G., 1949, "Transport of Heat and Matter in the Turbulent Mixing Zone of an Axially Symmetrical Jet," Appl. Sci. Res., Sect. A, **1**, pp. 425–461.
[29] Papanicolaou, P. N., and List, E. J., 1988, "Investigations of Round Vertical Turbulent Buoyant Jets," J. Fluid Mech., **195**, pp. 341–391.
[30] Panchapakesan, N. R., and Lumley, J. L., 1993, "Turbulence Measurements in Axisymmetric Jets of Air and Helium. Part 2: Helium Jet," J. Fluid Mech., **246**(2), pp. 225–247.
[31] Hussein, J., Capp, P., and George, K., 1994, "Velocity Measurements in a High Reynolds Number, Momentum Conserving Axisymmetric Turbulent Jet," J. Fluid Mech., **258**, pp. 31–75.
[32] Xu, G., and Antonia, R. A., 2002, "The Effect of Different Initial Conditions on a Turbulent Round Jet," Exp. Fluids, **33**, pp. 677–683.
[33] Mi, J., Nathan, G. J., and Nobes, D. S., 2001, "Mixing Characteristics of Axisymmetric Free Jets From a Contoured Nozzle, an Orifice Plate and a Pipe," ASME J. Fluids Eng., **123**, pp. 878–883.
[34] Becker, H. A., Hottel, H. C., and Williams, G. C., 1967, "The Nozzle-Fluid Concentration Field of the Round Turbulent Free Jet," J. Fluid Mech., **30**, pp. 285–303.
[35] Wygnanski, I., and Fiedler, H., 1969, "Some Measurements in the Self Preserving Jet," J. Fluid Mech., **38**, pp. 577–621.
[36] Van Der Hegge Zijnen, B. G., 1958, "Measurements of the Velocity Distribution in a Plane Turbulent Jet of Air," Appl. Sci. Res., Sect. A, **7**, pp. 256–276.
[37] Van Der Hegge Zijnen, B. G., 1958, "Measurements of Turbulence in a Plane Jet of Air by the Diffusion Method and by the Hot-Wire Method," Appl. Sci. Res., Sect. A, **7**, pp. 293–313.
[38] Wilcox, D., 1998, *Turbulence Modeling for CFD*, DCW Industries, La Cañada, CA.
[39] Hinze, J. O., 1979, *Turbulence*, 2nd ed., McGraw-Hill, New York.
[40] Chua, L. P., and Antonia, R. A., 1986, "The Turbulent Interaction Region of Circular Jet," Int. Commun. Heat Mass Transfer, **13**, pp. 545–558.
[41] Chevray, R., and Tutu, N. K., 1977, "Intermittency and Preferential Transport of Heat in a Round Jet," J. Fluid Mech., **88**(1), pp. 133–160.
[42] Chen, C. J., and Rodi, W., 1980, "Vertical Turbulent Buoyant Jets," *A Review of Experimental Data*, Pergamon, New York.
[43] Oginio, F., Takeuchi, H., Kudo, I., and Mizushina, T., 1980, "Heated Jet Discharged Vertically Into Ambients of Uniform and Linear Temperature Profiles," Int. J. Heat Mass Transfer, **23**, pp. 1581–1588.
[44] Papanicolaou, P. N., and List, E. J., 1987, "Statistical and Spectral Properties of Tracer Concentration in Round Buoyant Jet," Int. J. Heat Mass Transfer, **30**, 1059–1071.
[45] Tennekes, H., and Lumley, J. L., 1972, *A First Course in Turbulence*, MIT, Cambridge, MA.
[46] Minh, H. Ha., and Chassaing, P., 1978, "Restructuration d'écoulements turbulents," J. Mécanique, **17**(3), 359–386.
[47] Ramparian, B. R., and Chandrasekhara, M. S., 1985, "LDA Measurements in Plane Turbulent Jets," ASME J. Fluids Eng., **107**, pp. 264–271.
[48] Gutmark, E., and Wygnanski, I., 1976, "The Planar Turbulent Jet," J. Fluid Mech., **73**, pp. 465–495.

# Influence of Inelastic Scattering at Metal-Dielectric Interfaces

**Patrick E. Hopkins**

**Pamela M. Norris**[1]
e-mail: pamela@virginia.edu

Department of Mechanical and Aerospace Engineering,
University of Virginia,
P.O. Box 400746,
Charlottesville, VA 22904-4746

**Robert J. Stevens**
Department of Mechanical Engineering,
Rochester Institute of Technology,
76 Lomb Memorial Drive,
Rochester, NY 14623-5604

*Thermal boundary conductance is becoming increasingly important in microelectronic device design and thermal management. Although there has been much success in predicting and modeling thermal boundary conductance at low temperatures, the current models applied at temperatures more common in device operation are not adequate due to our current limited understanding of phonon transport channels. In this study, the scattering processes across* Cr/Si, $Al/Al_2O_3$, $Pt/Al_2O_3$, *and* Pt/AlN *interfaces were examined by transient thermoreflectance testing at high temperatures. At high temperatures, traditional models predict the thermal boundary conductance to be relatively constant in these systems due to assumptions about phonon elastic scattering. Experiments, however, show an increase in the conductance indicating inelastic phonon processes. Previous molecular dynamic simulations of simple interfaces indicate the presence of inelastic scattering, which increases interfacial transport linearly with temperature. The trends predicted computationally are similar to those found during experimental testing, exposing the role of multiple-phonon processes in thermal boundary conductance at high temperatures.* [DOI: 10.1115/1.2787025]

*Keywords: thermal boundary conductance, diffuse mismatch model, inelastic scattering, nanoscale, solid interfaces*

## Introduction

The ongoing trend of miniaturization of devices with structures on nanometer length scales has given rise to new challenges in the science and engineering of thermal transport and management. As these length scales continue to decrease, heat transport around active regions in these devices is enhanced/restricted by interfaces between materials and the structures surrounding them. Therefore, the issue of thermal management is becoming more critical in device engineering and reliability [1], particularly in thermoelectrics [2,3], thin-film high temperature superconductors [4,5], vertical cavity surface emitting lasers [6], and optical data storage media [7]. An ever increasing challenge in the development of these devices is successfully accounting for the temperature drop $\Delta T$ across the interface caused by, for example, the transport properties of the different materials [8], the presence of gaps and voids in the lattice structure due to nonperfect contacts [2], or a disordered region of the materials resulting from device fabrication conditions [9]. In any case, this temperature drop is characterized by the thermal boundary conductance $h_{BD}$ which is the conductance per unit area that relates the heat flux across the interface, $q_{BD}$, to the temperature drop $\Delta T$ across the interface. This is mathematically expressed as $q_{BD}=h_{BD}\Delta T$.

## Background

An understanding of the basic transport mechanisms involved in thermal boundary conductance is critical to the design and engineering of nanostructured devices. The main resistance to interfacial transport in the majority of these devices is phonon scattering between two materials, which has been successfully predicted by various models in limiting cases. Little proposed the acoustic mismatch model (AMM) to account for the specular scattering of phonons at an interface between two materials at low temperatures [10,11]. The root of the AMM theory is the wave nature of phonon transport. At low temperatures (when the dominant phonon wavelength is long) and at perfect interfaces, an incident phonon at a boundary of two materials can be treated as a plane wave, and the reflection and transmission probabilities can be analyzed similar to that of photons (Snell's law) [10,11]. This approach assumes that the phonon is transmitted or reflected at the interface (not scattered), an assumption that is valid when predicting $h_{BD}$ at low temperatures ($T<7$ K) and at ideal interfaces where specular scattering is probable [9]. However, this ideal case only represents a very limited population of interfaces in modern devices, which may operate at higher temperatures and have disordered regions near the interface that would induce diffuse scattering. To account for this type of phonon scattering, Swartz and Pohl developed the diffuse mismatch model (DMM) to predict $h_{BD}$ at more realistic interfaces [12].

The DMM provides a quick and simple estimation of $h_{BD}$ for an interface between the two materials [12]. To apply the DMM in its simplest form, the following assumptions must be made [13]: (1) phonons are elastically scattered, i.e., when a phonon from Side 1 with frequency $\omega$ scatters at the interface, it can only emit a phonon into Side 2 with the same frequency $\omega$ (for discussions, Side 1 will refer to the softer material with lower phonon velocities and Side 2 will refer to the stiffer material with higher phonon velocities); (2) phonon scattering is completely diffuse, i.e., a scattered phonon has no memory of the mode (longitudinal or transverse) or direction of the incident phonon; and (3) the materials on both sides of the interface are elastically isotropic, i.e., the longitudinal and transverse acoustic velocities are constant in all crystallographic directions. This model has been shown to predict conductance across higher temperature interfaces ($T>15$ K) relatively well [9,12]. However, at much higher temperatures (as $T$ approaches $T_{room}$), the DMM has been shown to either underpredict or overpredict experimental data, depending on the material systems [8,13–15]. The overprediction of the DMM has been associated with multiple elastic scattering events occurring from material mixing around the boundary in materials systems where the Debye temperature, $\theta_D$, of both materials is greater than $T_{room}$ [16–19]. The underprediction of the DMM in material systems where $\theta_D$ of one material is less than $T_{room}$ has been attributed to inelastic phonon scattering processes, which is the focus of this paper.

[1]Corresponding author.

Contributed by the Heat Transfer Division of ASME for publication in the JOURNAL OF HEAT TRANSFER. Manuscript received July 24, 2006; final manuscript received June 14, 2007; published online February 4, 2008. Review conducted by Suresh V. Garimella.

  

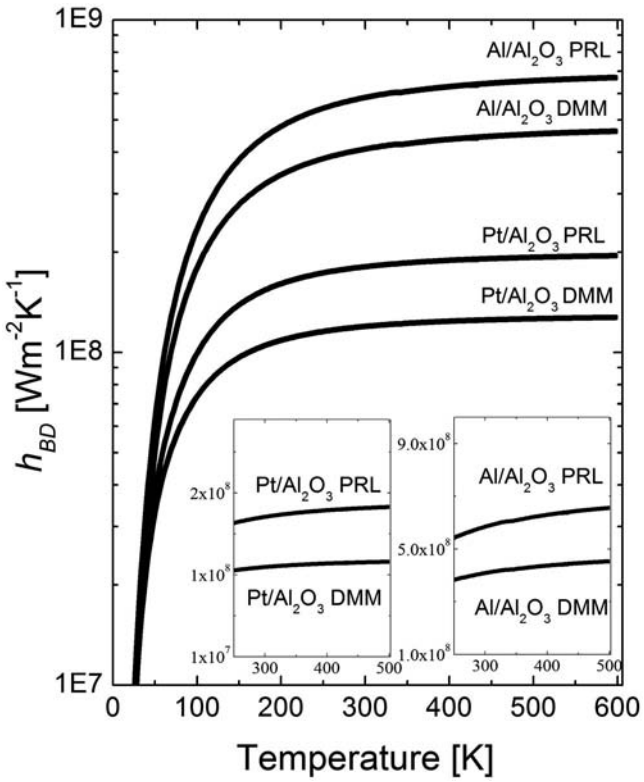


**Fig. 1 Thermal boundary conductance calculations of the $Al/Al_2O_3$ and $Pt/Al_2O_3$ interfaces using DMM and PRL. The models level off at higher temperatures due to the assumption of elastic scattering used in the calculations. The inset graphs show the DMM and PRL for the materials systems over only the temperature range used in this work.**

Another model for $h_{BD}$, the phonon radiation limit (PRL), provides a quick and simple determination of the maximum conductance for interfacial transport assuming complete elastic scattering [20]. Calculations of the PRL assume that phonons from Side 2 with frequencies below the cutoff frequency of Side 1 transmit completely to Side 1 [15]. The results of the DMM and PRL for $Al/Al_2O_3$ and $Pt/Al_2O_3$ interfaces are shown in Fig. 1 with parameters listed in Table 1. Since the PRL represents the upper limit of the elastic contribution to thermal transport, it will always predict a higher $h_{BD}$ than the DMM. Notice that the DMM and PRL predict a constant $h_{BD}$ at temperatures approaching $\theta_D$ in each material. The insets of Fig. 1 show a close-up of the DMM and PRL calculations for the two material systems over the temperature range used in this study.

In an attempt to investigate the underpredictive trends in $h_{BD}$ of the DMM and PRL, several computational and experimental efforts have been undertaken. In 1993, Stoner and Maris reported $h_{BD}$ at a range of acoustically mismatched interfaces from 50 K to 300 K [15,21]. As expected from the DMM, the measured $h_{BD}$ decreased with an increase in sample mismatch and the change in $h_{BD}$ decreased with temperature. In the sample with the greatest mismatch, Pb/diamond (Table 1), values of $h_{BD}$ were measured that exceeded the DMM prediction by over an order of magnitude, however, the measured $h_{BD}$ remained fairly constant over the temperature range investigated, which does not agree with the $T^3$ trend of the DMM at low temperatures. This measurement also significantly exceeded the prediction of the PRL. One possible explanation offered for this relatively large $h_{BD}$ was the occurrence of inelastic scattering—i.e., one or more phonons of frequency $\omega_1$ on Side 1 were emitting one or more phonons of frequency $\omega_2$ on Side 2—thereby offering more channels for transport than the DMM and PRL account for, leading to an underestimate of $h_{BD}$ by the DMM and PRL. For the Pb/diamond case, a high frequency diamond phonon could scatter at the interface and emit several low frequency phonons on the Pb side.

Chen et al. recently used molecular dynamics (MD) simulations to show a linear increase in $h_{BD}$ across a Kr/Ar nanowire with an increase in temperature from 35 K to 55 K, which they ascribed to anharmonic processes [22]. Kosevich considered the role of inelastic scattering on the phonon transmission probability [23]. With a multiharmonic model, Kosevich was able to show that inelastic scattering makes a greater contribution to $h_{BD}$ than elastic scattering for interfaces with very different vibrational spectra; these calculations, however, were not material specific. Observation of inelastic scattering in specific material systems applicable in microelectronic systems has not been predicted theoretically or computationally, and has been shown experimentally by Lyeo and Cahill only at low temperatures ($T \leqslant T_{room}$) [24]. They observed an approximately linear increase in $h_{BD}$ over a temperature range of 80–300 K on carefully prepared Pb and Bi thin films on diamond substrates with a pump-probe thermoreflectance technique. Like Stoner and Maris, Lyeo and Cahill observed $h_{BD}$ that was several times higher than the PRL but with a linear increase with temperature matching the aforementioned simulation results that suggested that multiple-phonon processes (inelastic scattering) can play a significant role in interface thermal conductance.

The purpose of this study is to examine the temperature dependence of $h_{BD}$ at temperatures around and above $\theta_D$. This research examines the assumption of phonon elastic scattering through measurements of $h_{BD}$ at increased temperatures ($T > T_{room}$) on a range of interfaces comprised of materials with varying $\theta_D$. Previous MD simulations show evidence of what could be inelastic phonon scattering occurring at the interface due to increased temperature. Stevens et al. observed thermal transport across the interface of two fcc lattice systems with varying degrees of mass and lattice mismatch at temperatures in the classical limit [25].

In the classical limit (for real materials $T \gg \theta_D$), $h_{BD}$ calculated by either the DMM or PRL is independent of temperature. The only temperature dependent part of both models is in the distribution function, which at temperatures well above the Debye temperature becomes constant. Because these models do not assume any inelastic scattering, the transmission coefficient is independent of temperature at high temperatures. To check the tempera-

**Table 1 Pertinent parameters for DMM and PRL calculations [27,43–45]**

| Material | $\theta_D$ (K) | $\nu_l$ (m s$^{-1}$) | $\nu_t$ (m s$^{-1}$) | $\rho$ (kg m$^{-3}$) | $M$ (kg mol$^{-1}$) |
|---|---|---|---|---|---|
| Al | 428 | 6,240 | 3,040 | 2,700 | 0.027 |
| Cr | 630 | 6,980 | 4,100 | 7,190 | 0.052 |
| Pb | 105 | 2,350 | 970 | 11,590 | 0.207 |
| Pt | 240 | 4,174 | 1,750 | 21,620 | 0.195 |
| Diamond | 2,230 | 17,500 | 12,800 | 3,512 | 0.012 |
| $Al_2O_3$ | 1,043 | 10,890 | 6,450 | 3,970 | 0.102 |
| AlN | 1,150 | 11,120 | 6,267 | 3,255 | 0.02 |
| Si | 645 | 8,970 | 5,332 | 2,330 | 0.028 |

ture dependence of $h_{BD}$, Stevens et al. conducted several simulations at a range of temperatures [25]. The simulations were conducted on both highly and lightly mismatched interfaces with Debye temperature ratios of 0.2 and 0.5.

A strong linear relationship was observed in the results of the MD calculations and $h_{BD}$ varied by nearly a factor of 4 for both interfaces for the temperature range considered. The strong linear dependence indicated that there is some thermal transport mechanism that is dependent on temperature, which would lead to a larger transmission coefficient. The most likely explanation for this discrepancy is that the DMM and PRL account only for elastic scattering, while MDS accounts for both elastic and inelastic scattering at the interface. The linear temperature dependence indicates a scattering process that is proportional to phonon population, since the phonon population increases linearly with temperature at high temperatures. In the classical limit, at temperatures above the Debye temperature, it appears that inelastic scattering provides the major contribution to the energy transport across the interface, surpassing the contribution of the elastic scattering.

In an effort to experimentally verify the results of the MD calculations, in this paper, the trends in $h_{BD}$ predicted by both the DMM and PRL are compared to experimental data from film/substrate samples of Cr/Si, Al/$Al_2O_3$, Pt/$Al_2O_3$, and Pt/AlN over a temperature range of 293–500 K obtained using the transient thermoreflectance (TTR) technique [26]. By increasing the temperature to levels near and above the Debye temperatures of the metals in these samples, the majority of the film's phonon populations were excited. Assuming elastic scattering, a phonon from the film will scatter at the interface and emit a phonon with the same frequency into the substrate, and a continued increase in temperature above $\theta_D$ should not significantly affect $h_{BD}$ since the change in the phonon population in the film is constant. However, results show a continued increase in $h_{BD}$ above the film's $\theta_D$ indicating that the change in the substrate phonon population, which is changing at a much faster rate than that of the film in the low $\theta_D$ film/high $\theta_D$ substrate systems studied in this work, is affecting the $h_{BD}$ via inelastic scattering events: A high frequency phonon in the substrate is scattering at the interface and breaking down into several low frequency phonons in the film.

## Experimental Considerations

**Samples.** Since the goal of this study is to examine the ability of the DMM and PRL (with their elastic scattering assumptions) to predict $h_{BD}$ at high temperatures, materials systems were chosen to encompass different regimes in which the degree of temperature dependence of $h_{BD}$ as predicted by the DMM would vary. Four materials systems were considered ($\theta_D$ film, $\theta_D$ film/substrate ratio ($\xi$)) [27]: Cr/Si (630 K, 0.98), Al/$Al_2O_3$ (428 K, 0.41), Pt/$Al_2O_3$ (240 K, 0.23), and Pt/AlN (240 K, 0.21). These materials systems allow investigation in temperature regimes where various trends in $h_{BD}$ are predicted by DMM and PRL. For example, assuming elastic scattering, some increase in $h_{BD}$ is expected in the Al/$Al_2O_3$ samples over most of the temperature range in this study (293–500 K) because the phonon population in Al will increase until $T > \theta_{D\_Al}$. However, in Pt/$Al_2O_3$, where $\theta_{D\_Pt} < T_{room}$, the increase in $h_{BD}$ should be relatively negligible since the entire Pt phonon population is excited below room temperature. Any increase in $h_{BD}$ when $T > \theta_{D\_Pt}$ could be evidence of more high frequency $Al_2O_3$ phonons exciting from the elevated temperature, scattering at the interface, and breaking down into two or more lower frequency phonons emitted into the Pt film.

The Cr, Al, and Pt film thicknesses were 50 nm, 75 nm, and 50 nm, respectively, chosen ~50% larger than the electron mean free path in these metals to minimize ballistic electron scattering at the boundary and to ensure that the electrons and phonons in the film have completely equilibrated by the time they reach the interface [28]. These thicknesses were also necessary to ensure that viable $h_{BD}$ information can be obtained from the TTR data from our experimental setup [8]. The Cr was deposited on an *n*-type Ph doped (100) Si substrate; the Al and Pt films were deposited on factory polished $Al_2O_3$, and an additional Pt film was deposited on factory polished AlN. The metals were deposited on their respective substrates in a multisource, high vacuum thin-film sputter deposition system, a Supersystem III manufactured by the Kurt J. Lesker Company capable of pumping down to $10^{-7}$ Torr. All substrates were (ETM) spin cleaned with reagent alcohol (90.7% ethyl alcohol; 4.8% isopropyl alcohol; 4.5% methyl alcohol; 0.12% water), trichloroethylene, and methanol, and then subsequently baked for 5 min at 400 K to remove any residual water that may have formed at the substrate surface as a result of the spin clean. The substrates were subject to a 5 min, 100 W backsputter etch, prior to film deposition, in an effort to remove the majority of the native oxide layer and any additional contaminants.

**Experimental Setup.** The TTR data were taken with the pump-probe experimental setup depicted in Fig. 2. The primary output of the laser system emanates from a Coherent RegA 9000 amplifier operating at a 250 kHz repetition rate with about 4 $\mu$J/pulse and a 150 fs pulse width at 800 nm. The pulses were split at a 9:1 pump to probe ratio. The pump beam, modulated at 125 kHz, was focused down to a 100 $\mu$m radius spot size to achieve 10 J m$^{-2}$ fluence. The probe beam was focused to the middle of the pump beam to achieve a pump to probe fluence ratio of 10:1. The radii of the pump and probe beams were measured with a sweeping knife edge [29]. Although the low repetition rate of the RegA system and the "one shot on-one shot off" modulation rate of the pump beam ensure minimal residual heating between pump pulses, the phase of the signal must still be taken into account. Phase correction was performed by the procedures for signal phase adjustment outlined in the references [29].

For the longer scans analyzed in this study (~1400 ps pump-probe delay), alignment of the pump and probe spots can become an issue [8,30]. To avoid misalignment problems, the probe beam was collimated before the probe delay stage and profiled with a sweeping knife edge at all time delays. In this study, a pump to probe radius ratio of 10:1 was used, and the probe was aligned with the delay stage resulting in less than 1.5 $\mu$m and 4.0 $\mu$m drift along the horizontal and vertical axes perpendicular to the surface, respectively. These spot characteristics result in less than 1% error due to misalignment of the beams [29].

The samples were mounted to a 5 mm thick Al plate attached to a Minco 5419 silicon rubber resistive heater. The samples were mounted on the front of the Al plate with Molykote 44 high temperature vacuum grease to reduce thermal resistance and the sides and back of the aluminum plate/heater were insulated with high temperature millboard insulation. Holes were drilled 1 mm underneath the front surface of the Al plate in four locations surrounding the sample and the temperature of the sample was monitored with Omega Engineering TT-T-20 thermocouple wires with NMP-U-M thermocouple male connectors. For each desired temperature, the Al block was heated and held at constant temperature for ~2 h to ensure that the sample/Al block system equilibrated before TTR measurements were taken. Since the thermal resistance between the Al block and the sample is much less than the thermal resistance between the sample surface and the ambient, it was valid to assume that the Al block and sample were at close temperatures. After several measurements at a certain temperature, the heater was turned off and the system returned to room temperature. Room temperature measurements were again taken and these measurements were compared to ensure that the sample was not damaged as a result of the heating. The value of $h_{BD}$ was determined by fitting the TTR data to the thermal model discussed in the next section. Repeatable results were found at all temperatures. The data presented in this paper are the statistical averages of the data at each temperature. Five to seven data sets were taken

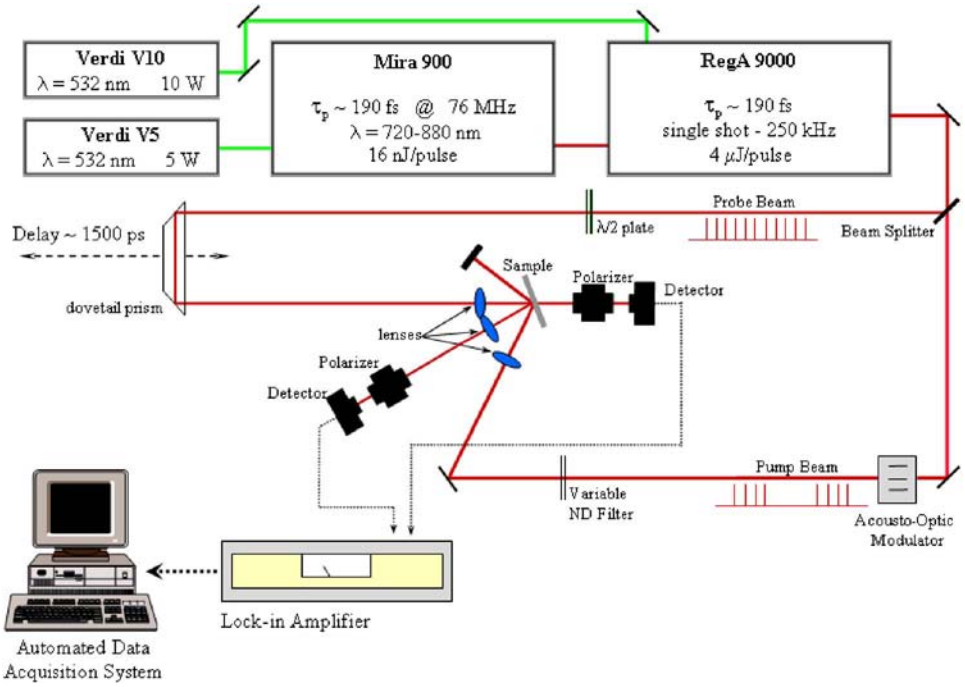


**Fig. 2 TTR setup**

at each temperature increment. A maximum deviation of 18% from the mean was calculated for the Cr/Si samples, and less than 10% was determined for the other systems.

**Thermal Model.** The TTR technique produces some excitation of the metal film followed by a cooling of the film due to the film's thermal connection to the substrate. To simplify data reduction, ideally the temperature response is influenced only by conductance across the interface and not by diffusion within the metal film. If the film is too thick or has a low thermal conductivity, however, then there will be two free parameters (film thermal conductivity $k_f$ and $h_{BD}$) when fitting experimental data to a thermal model. To avoid this situation, the Biot number, Bi, for the interface should be significantly less than 1 (typically less than 0.1) so that the film can be treated as a lumped thermal capacitance [31]. Therefore, the film thickness should be restricted to

$$\mathrm{Bi} = \frac{h_{BD} d}{k_f} < 0.1 \Rightarrow d < \frac{0.1 k_f}{h_{BD}} \tag{1}$$

where $d$ is the film thickness. A more detailed analysis of this assumption for each sample using values measured for $h_{BD}$ will be presented later.

Assuming the metal film can be treated as a lumped capacitance (i.e., Eq. (1) holds), the thermal model for the film and substrate system is

$$\rho d C_f \frac{dT_f(t)}{dt} = h_{BD}[T(0,t) - T_f(t)] \tag{2}$$

$$\frac{\partial T_s(x,t)}{\partial t} = \alpha_s \frac{\partial^2 T_s(x,t)}{\partial x^2} \tag{3}$$

where $T_f$ is the temperature of the film that is measured using the TTR technique, $T_s$ is the substrate temperature and is a function of time and space, and $\rho$, $C_f$, and $\alpha_s$ are the film density, film specific heat, and substrate diffusivity, respectively. Radiative and convective losses at the front of the film surface are negligible compared to a typical interface conductance of $10^6$–$10^8$ W m$^{-2}$ K$^{-1}$ and are therefore neglected. The temperatures in Eqs. (2) and (3) can be nondimensionalized by

$$\varphi_{f,s} = \frac{T_{f,s} - T_0}{T_f(0) - T_0} \tag{4}$$

where $T_0$ is the temperature of the film and substrate immediately before excitation and $T_f(0)$ is the temperature of the film immediately after excitation. Therefore, the thermal model can be expressed as

$$\frac{d\varphi_f(t)}{dt} = \frac{h_{BD}}{\rho d C_f}[\varphi_s(0,t) - \varphi_f(t)] \tag{5}$$

$$\frac{\partial \varphi_s(x,t)}{\partial t} = \alpha_s \frac{\partial^2 \varphi_s(x,t)}{\partial x^2} \tag{6}$$

subject to the following initial conditions:

$$\varphi_f(0) = 1 \tag{7}$$

$$\varphi_s(x,0) = 0 \tag{8}$$

and the following boundary conditions:

$$-k_s \frac{\partial \varphi_s(0,t)}{\partial x} = h_{BD}[\varphi_f(t) - \varphi_s(0,t)] \tag{9}$$

$$\frac{\partial \varphi_s(\infty,t)}{\partial x} = 0 \tag{10}$$

The semi-infinite assumption made in Eq. (10) is reasonable for the time scale of interest, ~1.5 ns. The thermal penetration depth for most substrates at this time scale is $(\alpha_s t)^{1/2} < 1$ $\mu$m, which is significantly smaller than the thickness of the substrates used in this study.

Equations (5) and (6) subject to Eqs. (7)–(10) were numerically solved using the Crank–Nicolson method, which has only a second order truncation error in both time and space. The thermal boundary conductance was determined by fitting the TTR data to the model using the material constants listed in Table 2. The models fit to Al/$Al_2O_3$ and Pt/$Al_2O_3$ TTR data taken at room and elevated temperatures are shown in Fig. 3. General assumptions and fitting sensitivity of this model are discussed in detail in the

**Table 2 Thermophysical properties used in determining $h_{BD}$ from Eqs. (5)–(10) (values listed are at room temperature ($T_{room}$=293 K). Note the film thermal conductivity is not needed for the lumped capacitance analysis, but is needed for thermal diffusion time approximations. Higher temperature values that were used can be found in the references [31,36,43–45]).**

| Material | $C_L$ (J m$^{-3}$ K$^{-1}$) | $k$ (W m$^{-1}$ K$^{-1}$) |
|---|---|---|
| Al | $2.44\times10^6$ | 237 |
| Cr | $3.3\times10^6$ | 93.7 |
| Pt | $2.83\times10^6$ | 73 |
| $Al_2O_3$ | $3.25\times10^6$ | 18 |
| AlN | $1.94\times10^6$ | 285 |
| Si | $1.66\times10^6$ | 148 |

references [8,15]. Note that the high temperature data, which have a higher $h_{BD}$ than the low temperature data, show a greater curvature in the exponential decay. In addition, note that the trends in the early part of the data do not match the trends predicted by the thermal model. This occurs in the first 30 ps after laser heating in the Al sample and 70 ps after laser heating in the Pt sample. This deviation is most likely due to thermal diffusion occurring in the film, which is not taken into account in the lumped capacitance thermal model. After this time, the primary source of energy transfer is thermal boundary conductance, and the model and the data agree well. The order of this diffusion time observed in the TTR data in Fig. 3 is in close agreement with diffusion time constants calculated in Table 3. Specifics of diffusion time constant calculations and further analysis are presented in a later section.

With the ultrashort laser pulses used in the TTR measurements, an electron-phonon nonequilibrium is induced in the early part of the TTR data. Using the two temperature model (TTM) to predict the electron-phonon thermalization time with the 10 J m$^{-2}$ incident fluence [32–34], the thermalization time in all the metal films is less than 5.0 ps. Therefore, it is expected that a fast transient spike in the early part of the TTR response due to the electron-phonon nonequilibrium would not affect determining $h_{BD}$ [35]. The result of this nonequilibrium period is a slight rise in lattice temperature due to hot electrons transferring energy to the lattice. Using the TTM with insulated boundary conditions, the predicted lattice temperature rise after electron-phonon equilibration and minimization in the spatial temperature gradient in the film is less than 10 K. Therefore, it should be noted that the actual temperatures of the interfaces could be slightly higher than the prescribed values in the experimental results due to lattice heating.

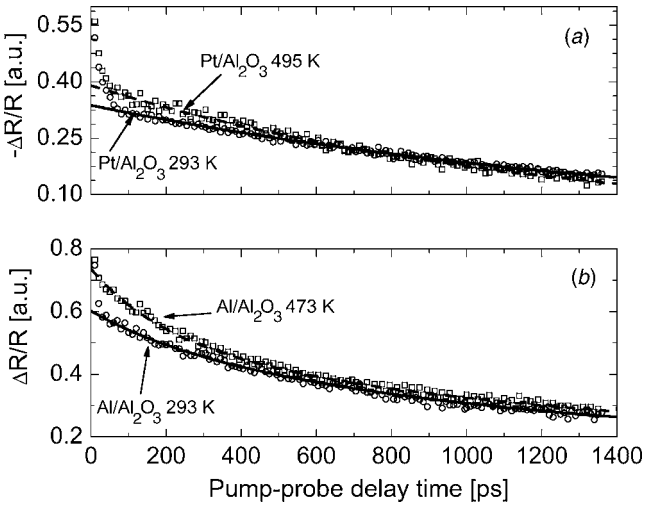


**Fig. 3 Thermal model (Eqs. (8)–(14)) fit to TTR data taken on (a) Pt/$Al_2O_3$ at 293 K and 495 K and (b) Al/$Al_2O_3$ at 293 K and 473 K. The thermal model is scaled to the TTR data at 200 ps for reasons that will be discussed later in this paper. The TTR data were phase fixed [29] and normalized at the peak reflectance to make clear the differences in the exponential cooling profiles at the different temperatures.**

**Table 3 Film thermal diffusion times**

| Material | $\tau_f$ at 293 K (ps) | $\tau_f$ at $T_{max}$ (ps) |
|---|---|---|
| Al | 56 | 62 |
| Cr | 86 | 101 |
| Pt | 97 | 102 |

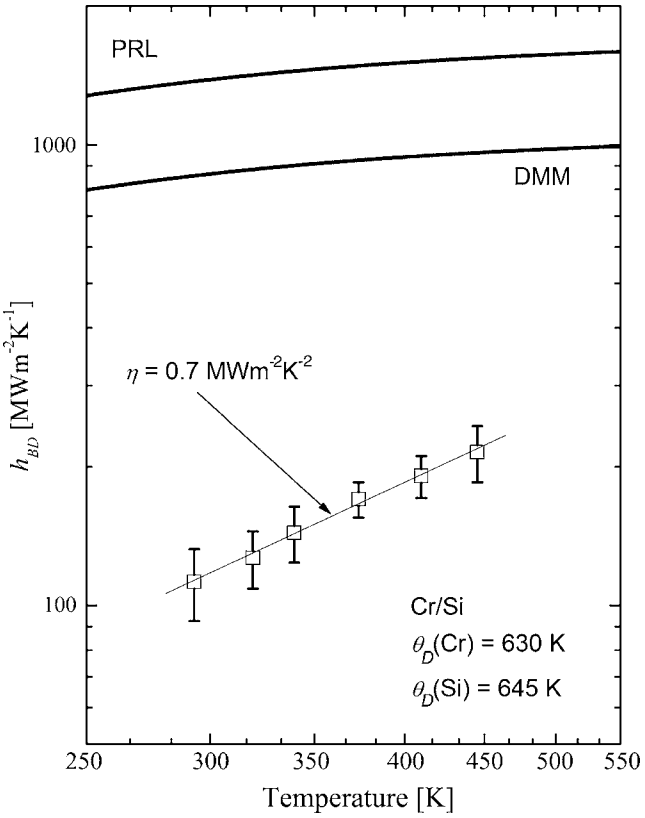


**Fig. 4 Thermal boundary conductance data across the Cr/Si interface over a range of temperatures. The data show a linear increase with temperature at a much greater rate than the DMM and PRL.**

## Experimental Results

The thermal boundary conductances measured from the TTR data are plotted against temperature for the four material systems studied in Figs. 4–7. The line fit to the data depicts the linearity of the relationship between temperature and $h_{BD}$ observed in the experiments. The slope of this line, $\eta$, is also presented in these figures along with the Debye temperatures of the materials. In addition, the calculations for the DMM and PRL in these systems are included in these graphs. Figure 4 presents $h_{BD}$ across the Cr/Si interface. In the Cr/Si system, a nearly linear increase of $h_{BD}$ is observed over the temperature range from 293 K to 460 K. Since the highest temperature investigated is less than the $\theta_D$ of both the film and substrate, an increase in $h_{BD}$ is expected. However, an 80% increase in $h_{BD}$ occurs over this range, where the DMM and PRL only predict a 15% nonlinear increase that decreases with increasing temperature. The linear temperature dependence may indicate a scattering process that is proportional to

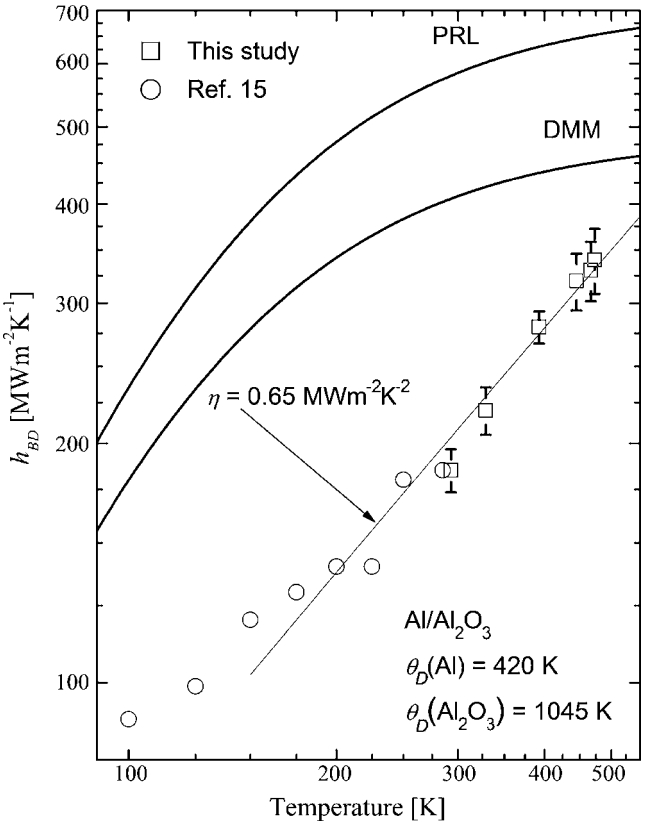


**Fig. 5 Thermal boundary conductance data across the $Al/Al_2O_3$ interface over a range of temperatures. This figure also includes data taken by Stoner and Maris (1993) at low temperatures [15]. The linear trend continues at temperatures higher than the Debye temperature of Al, indicating that inelastic phonon processes could be contributing to $h_{BD}$ at these elevated temperatures.**

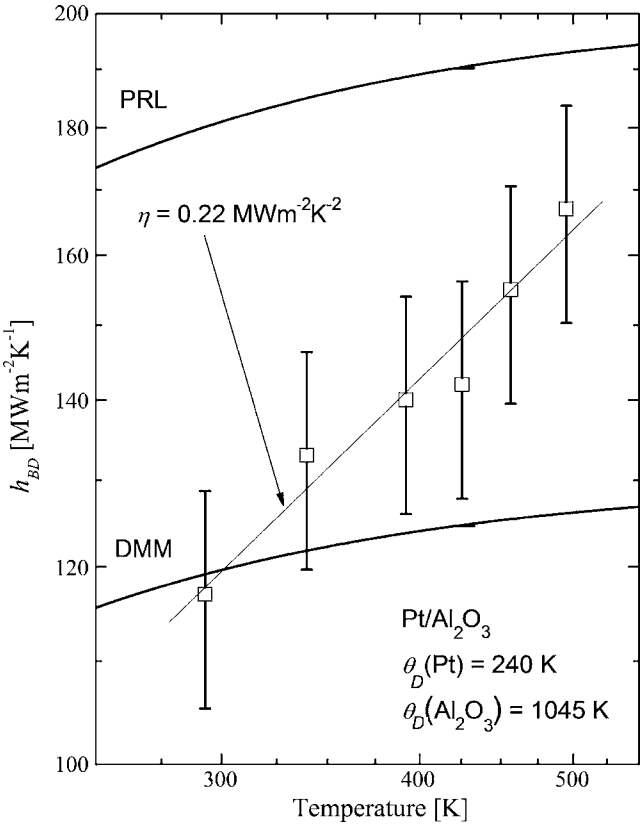


**Fig. 6 Thermal boundary conductance data across the $Pt/Al_2O_3$ interface over a range of temperatures. These temperatures are above the Debye temperature of Pt. According to theory, $h_{BD}$ should not change at temperatures above the Debye temperature of one of the materials assuming only elastic scattering. However, the continued linear increase in measured $h_{BD}$ indicates a contribution from inelastic processes.**

increased inelastic scattering events beyond the assumption of single elastic collisions. The change in phonon population with temperature close to and above the Debye temperature is constant, which leads to the temperature independent $h_{BD}$ predictions of the DMM and PRL. However, Cr and Si are very well acoustically matched samples and the deviation associated with measurement repeatability is the largest of any of the samples examined in this work. Although the linear trend with temperature suggests inelastic scattering, there are other transport mechanisms that could also explain the data, which will be discussed in the next section.

Since the change in phonon population is constant with temperatures above and around $\theta_D$, in highly mismatched systems, a continued linear increase of $h_{BD}$ is not expected when the temperature is driven higher than the lower $\theta_D$ of the film/substrate material system. With this in mind, Fig. 5 shows the measured $h_{BD}$ across the $Al/Al_2O_3$ interface. In addition to data measured in this study ($293\ K < T < 500\ K$), low temperature data from Stoner and Maris are included [15]. The linear fit included the data from this study and Stoner and Maris data from 150 K to room temperature. At 150 K, $h_{BD}$ appears to lose its $T^3$ dependence. Over the temperature range in this study, the experimental data increase by almost 100%, where the DMM only predicts a 10% increase. In addition, the data above the $\theta_D$ of Al continue to linearly increase over a 50 K temperature increase. The linear increase above $\theta_D$ of Al suggests that multiple-phonon processes may be occurring between single high frequency phonons in the $Al_2O_3$ and several low frequency phonons in Al. As the temperature was driven above $\theta_D$ of Al, the entire phonon population in Al was excited. However, the linear increase of $Al_2O_3$ phonon population continues and therefore, the increase in $h_{BD}$ above $\theta_D$ of Al suggests that $h_{BD}$ is dominated by inelastic scattering. The continued linear trend observed from the data from Stoner and Maris to the high temperature data even above $\theta_D$ of Al indicates that there is a smooth transition between regimes where $h_{BD}$ is dominated by elastic and inelastic scattering.

To examine the regime where inelastic scattering would dominate (i.e., temperatures above the Debye temperature of only one of the materials, so that the entire phonon population of one material is excited but not the other), the highly mismatched $Pt/Al_2O_3$ system was studied. Lyeo and Cahill studied this regime at low temperatures ($T < T_{room}$) with Pb and Bi on diamond [24]. The $Al/Al_2O_3$ system gives hints toward multiple-phonon processes with the data 50 K above $\theta_D$. However, due to the less than room temperature $\theta_D$ of Pt, the highly mismatched $Pt/Al_2O_3$ shows promising data that further support the findings of inelastic scattering processes in high temperature regimes. Figure 6 shows $h_{BD}$ versus temperature TTR results for $Pt/Al_2O_3$. The temperature of this interface was increased to over twice $\theta_D$ of Pt. Over the investigated temperature range, $h_{BD}$ almost doubles, which is a similar result to the MD calculations that model elastic and inelastic scattering [25].

Similar behavior was observed in the Pt/AlN system over the same temperature range, as seen in Fig. 7. A nearly linear increase in $h_{BD}$ is observed over the temperature range with values approaching the PRL at high temperatures. Aluminum nitride and sapphire have very similar Debye temperatures (Table 1) so similarities in $h_{BD}$ values and temperature trends are expected. The discrepancies in the measured $h_{BD}$ between these two samples

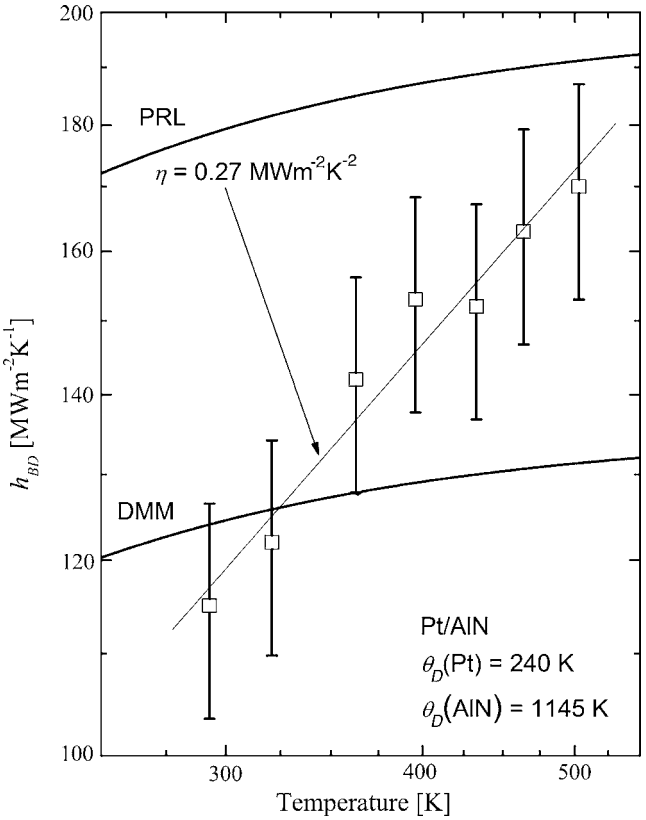


**Fig. 7 Thermal boundary conductance data across the Pt/AlN interface over a range of temperatures. A similar linear increase of $h_{BD}$ to the data in Fig. 7 is observed, presenting further evidence toward nonelastic phonon transport channels.**

could be due to differences in the physical properties of the boundary or slightly different densities of states not accounted for in the Debye model.

## Analysis

The thermal model used to determine $h_{BD}$ from the TTR data (Eqs. (5)–(10)) involves a lumped capacitance assumption in which minimal thermal diffusion is assumed through the film as compared to across the film/substrate interface. Therefore, this model must be scaled to the experimental data at times when the thermal gradient through the film is approximately zero. To estimate this scaling time, the film's thermal diffusion time is approximated from the Fourier number as $\tau_f = d^2/\alpha_f$ [36]. The thermal diffusion times for the films examined in this study are presented in Table 3. These values are calculated with the temperature dependent thermophysical properties of the corresponding bulk material. Since the thicknesses of the samples were chosen to be larger than the mean free path, minimal reduction in thermal conductivity is expected due to size effects [37]. However, to ensure that the model is fit to the data at times when the thermal gradient in the film is minimal, the thermal model was scaled to the TTR data 200 ps after the peak (as shown in Fig. 3), ensuring that even in the unlikely event of a reduction in $k_f$ due to film thickness or quality, the lumped capacitance model can still be correctly applied.

The thermal model is scaled at 200 ps and the thermal model is fit to the 1400 ps of TTR data to extract $h_{BD}$. In order to check that 1400 ps pump-probe delay is enough time to accurately determine $h_{BD}$ for these samples, the interfacial time constant is estimated as $\tau_{BD} = C_f d/h_{BD}$ [15]. Table 4 lists $\tau_{BD}$ for the samples examined in this study using $h_{BD}$ determined from the experiments. The interfacial time constant is less than the 1400 ps TTR scan time for all cases, although it is approaching 1400 ps in the Cr and Pt samples at 293 K. Since this calculation of $\tau_{BD}$ is based on bulk properties and is just an estimate, more $h_{BD}$ information could have been extracted from the TTR data with a longer probe delay. This could have lead to measured values of $h_{BD}$ being slightly off around room temperature. However, the room temperature Cr/Si data in this study agree well with previously reported values of $h_{BD}$ on a 50 nm Cr/Si sample subjected to the same deposition conditions as used here and using the same apparatus and same thermal model, but with the data scaled at an earlier time [17]. However, these data are slightly lower than that measured on a 30 nm Cr/Si sample [8]. This 30 nm Cr/Si sample was fabricated differently, however, and fabrication has been shown to cause deviation in $h_{BD}$ [17]. The thermal boundary conductances measured on Pt/$Al_2O_3$ and Pt/AlN are very close at room temperature (and at all temperatures, for that matter, as previously discussed). Even though $Al_2O_3$ and AlN have vastly different thermal properties, a similar $h_{BD}$ is expected due to the similar acoustic properties of these materials, giving more confidence in the resolution of $h_{BD}$ of these samples.

**Table 4 Interfacial time constants**

| Material | $\tau_{BD}$ at 293 K (ps) | $\tau_{BD}$ at $T_{max}$ (ps) |
|---|---|---|
| Cr/Si | 1342 | 850 |
| Al/$Al_2O_3$ | 924 | 546 |
| Pt/$Al_2O_3$ | 1179 | 884 |
| Pt/AlN | 1286 | 884 |

This brings up an important point about the thermal properties used in the model to extract $h_{BD}$ from the TTR data. In this study, bulk properties were used in the analysis. Of specific concern is a reduction in the substrate conductivity due to manufacturing conditions, which could lead to a transient rise in substrate temperature near the interface. When there is a negligible rise in $T_s$ near the interface, the thermal model is weakly dependent on the thermal conductivity of the substrate. However, this dependence increases if the rise in $T_s$ cannot be neglected, which could potentially be a problem in sapphire, which has a relatively low conductivity, leading to a nonexponential decay in the TTR data. The exponential decay in the Pt/$Al_2O_3$ data shown in Fig. 3 in addition to the similar values for $h_{BD}$ measured on the Pt/$Al_2O_3$ and Pt/AlN samples elucidates the suitability of the values for the thermal properties used in this study.

Although this study has focused on resolving inelastic scattering processes, other scattering phenomena could be participating in $h_{BD}$ that could influence these results. This is apparent by comparing the predictions of the DMM and PRL to the measured values of $h_{BD}$; at any given temperature in this study, the DMM and PRL calculations vary by an order of magnitude between the samples while the measured data are all within a factor of 2 of each other. In acoustically well matched material systems, such as Cr and Si, the DMM has been shown to overpredict experimental data when electron-phonon scattering processes occurring near the interface are not taken into account [38]. This scattering process would cause $h_{BD}$ to begin approaching a constant value at lower temperatures. Although this scattering process could explain the overestimation of the $h_{BD}$ by the DMM and PRL for the Cr/Si interface in this study, the linear increase in $h_{BD}$ with temperature observed in Fig. 4 would result from inelastic scattering.

Disorder and mixing around the interface of two materials could lead to multiple-phonon scattering events, which could also influence $h_{BD}$ measurements. These multiple scattering events increase in occurrence with a decrease in phonon mean free path (increase in temperature) [18,19]. Depending on the type of scattering event, different changes in $h_{BD}$ are expected. Multiple elastic scattering events increase $h_{BD}$ in acoustically mismatched

samples but decrease $h_{BD}$ in acoustically matched samples [12]. Assuming an increase in these scattering events with temperature, the Cr/Si $h_{BD}$ would suffer a reduction, while the data in Fig. 4 show an increase, strengthening the conclusion of inelastic scattering. In more heavily mismatched samples (Al/$Al_2O_3$, Pt/$Al_2O_3$, Pt/AlN), these multiple elastic scattering events could be contributing in part to the increase in $h_{BD}$ observed over the temperature range. However, MD simulations show this same linear trend at perfect interfaces, which has been attributed to inelastic scattering [25], further supporting the observation of inelastic scattering participating in $h_{BD}$ at high temperatures ($T > \theta_D$).

The experimental data in this study are compared to the DMM and PRL models, which were calculated assuming a Debye density of states. The Debye density of states provides a quick and simple calculation of the DMM and PRL; however, several studies have shown that using a more realistic density of states could significantly change the resulting calculations [39–42]. Recent calculations by Reddy et al. of metal films on semiconductor substrates use the Born von–Karmen model (BKM) to calculate an exact phonon dispersion in the DMM [41]. The more accurate density of states predicted a higher density at lower frequencies and a lower density at higher frequencies as compared to the Debye calculations. This resulted in higher values for the DMM at low temperatures and lower values for the DMM at higher temperatures (i.e., temperatures of interest in this study). With this in mind, the DMM and PRL calculations would decrease from the current results presented in Figs. 4–7. The trend in these calculations (i.e., change in $h_{BD}$ with temperature becomes negligible at temperatures approaching $\theta_D$) also changes with the BKM calculation [41]. With this more realistic density of states, the change in $h_{BD}$ with temperature becomes negligible at much lower temperatures. Applying this conceptual shift to the DMM and PRL data results in an even more drastic difference between the experimental data and the trends in the models assuming only elastic phonon collisions presented in Figs. 4–7. This indicates that inelastic scattering events participating in $h_{BD}$ at higher temperatures are being observed in the experimental data.

The slopes of the linear fit of $h_{BD}$ versus temperature exhibit an interesting trait among the different samples. The slopes of the linear trends ($\eta$) as a function of film/substrate Debye temperature ratio ($\xi$) are shown in Fig. 8 for the Pt data from this study, the Pb/diamond and Bi/diamond data from Lyeo and Cahill [24], and the Au/diamond data from Stoner and Maris [15]. The linear fit to these data is also shown in this figure ($\eta = (1.10\ \mathrm{MW\ m^{-2}\ K^{-2}})\xi$). These specific film/substrate systems are of interest because the majority of the thermal boundary conductances determined in these studies were measured at temperatures above the Debye temperature of the film; therefore, the slopes are representative of the influence of inelastic scattering on $h_{BD}$. Only the Au/diamond data above 150 K were used for the linear fit to ensure that the reported $\eta$ for Au/diamond can accurately represent the influence of multiple-phonon processes. The data show an increasing $\eta$ with increasing $\xi$, indicating that inelastic processes participating in $h_{BD}$ become more temperature dependent with an increase in acoustic similarity between materials. In samples with greater mismatch (smaller $\xi$), there exist substrate phonons with much higher frequencies than film phonons, which would have to break down several times to emit phonons with frequencies available in the film's population into the film. However, when the materials become acoustically similar (larger $\xi$), the decomposition cascade of the substrate phonons is much less severe. Figure 8 indicates that as the film and substrate increase in acoustic similarity, phonon decomposition could be happening more readily. This begins to elucidate the role of inelastic phonon scattering in thermal boundary conductance.

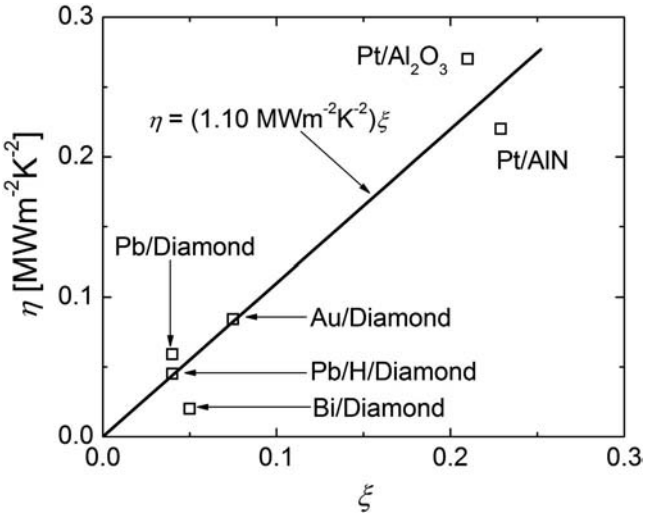


**Fig. 8 The slopes of the linear trends ($\eta$) as a function of film/substrate Debye temperature ratio ($\xi$) are shown for the Pt data from this study, the Pb/diamond and Bi/diamond data from Lyeo and Cahill [24], and the Au/diamond data from Stoner and Maris [15]. The linear trends were determined from $h_{BD}$ data measured above the various samples' Debye temperatures to make sure that these slopes represented regimes where inelastic scattering was contributing to $h_{BD}$. The linear fit to these points is depicted by the solid line. It is apparent that the two materials become acoustically similar (increasing $\xi$), and inelastic scattering becomes increasingly temperature dependent.**

## Conclusions

Traditional models for $h_{BD}$ (DMM and PRL) predict thermal boundary conductance at low temperatures ($T \ll T_{room}$, $\theta_D$) relatively well, but at temperatures closer to device operating temperatures these models fail to account for inelastic phonon scattering processes, which can contribute to interface conductance. Previous MD calculations showed strong evidence of inelastic phonon scattering at interfaces at elevated temperatures [25]. To test the effect of these inelastic processes, TTR experiments were performed at elevated temperatures ($T > T_{room}$). The TTR experiments measured the $h_{BD}$ at elevated temperatures on different samples with varying acoustic mismatch. At the temperatures in this study, $h_{BD}$ is assumed to be relatively constant by traditional models considering only elastic scattering. At temperatures around and above the Debye temperature of the metal films, the thermal boundary conductance was shown to increase linearly with temperature, similar to previous MD calculations that take into account inelastic phonon scattering, indicating that multiple-phonon processes are contributing to interfacial transport at high temperatures.

## Acknowledgment

The authors would like to thank Rich Salaway, Jennifer Simmons, Thomas Randolph, Jessica Sheehan, and Dr. Mike Klopf for their helpful insight and discussions. This work was funded by the National Science Foundation (CTS-0536744). P.E.H. is greatly appreciative for financial support from the National Science Foundation through the Graduate Research Fellowship Program.

## Nomenclature

Bi = Biot number
$C$ = heat capacity, J m$^{-3}$ K$^{-1}$
$d$ = film thickness, m
$h$ = thermal conductance, W m$^{-2}$ K$^{-1}$
$k$ = thermal conductivity, W m$^{-1}$ K$^{-1}$
$k_B$ = Boltzmann's constant, J K$^{-1}$
$M$ = atomic weight, kg mol$^{-1}$
$q$ = heat flux, W m$^{-2}$
$T$ = temperature, K

### Greek Symbols

$\alpha$ = thermal diffusivity, m$^2$ s$^{-1}$
$\eta$ = slope of linear fit to $h_{BD}$ temperature data, W m$^{-2}$ K$^{-2}$
$\theta_D$ = Debye temperature, K
$\nu$ = acoustic phonon velocity, m s$^{-1}$
$\rho$ = mass density, kg m$^{-3}$
$\tau$ = diffusion time, s
$\xi$ = ratio of film Debye temperature to substrate Debye temperature
$\varphi$ = nondimensionalized temperature

### Subscripts

BD = boundary
$f$ = film
$L$ = lattice
$l$ = longitudinal branch
$s$ = substrate
$t$ = transverse branch
0 = initial

## References


[1] Cahill, D. G., Ford, W. K., Goodson, K. E., Mahan, G. D., Majumdar, A., Maris, H. J., Merlin, R., and Phillpot, S. R., 2003, "Nanoscale Thermal Transport," J. Appl. Phys., **93**, pp. 793–818.
[2] Da Silva, L. W., and Kaviany, M., 2004, "Micro-Thermoelectric Cooler: Interfacial Effects on Thermal and Electrical Transport," Int. J. Heat Mass Transfer, **47**, pp. 2417–2435.
[3] Mahan, G. D., and Woods, L. M., 1998, "Multilayer Thermionic Refrigeration," Phys. Rev. Lett., **80**, pp. 4016–4019.
[4] Phelan, P. E., Song, Y., Nakabeppu, O., Ito, K., Hijikata, K., Ohmori, T., and Torikoshi, K., 1994, "Film/Substrate Thermal Boundary Resistance for an Er–Ba–Cu–O High-Tc Thin Film," ASME J. Heat Transfer, **116**, pp. 1038–1041.
[5] Phelan, P. E., 1998, "Application of Diffuse Mismatch Theory to the Prediction of Thermal Boundary Resistance in Thin-Film High-Tc Superconductors," ASME J. Heat Transfer, **120**, pp. 37–43.
[6] Chen, G., Tien, C. L., Wu, X., and Smith, J. S., 1994, "Thermal Diffusivity Measurement of GaAs/AlGaAs Thin-Film Structures," ASME J. Heat Transfer, **116**, pp. 325–331.
[7] Kim, E.-K., Kwun, S.-I., Lee, S.-M., Seo, H., and Yoon, J.-G., 2000, "Thermal Boundary Resistance at $Ge_2Sb_2Te_5/ZnS:SiO_2$ Interface," Appl. Phys. Lett., **76**, pp. 3864–3866.
[8] Stevens, R. J., Smith, A. N., and Norris, P. M., 2005, "Measurement of Thermal Boundary Conductance of a Series of Metal-Dielectric Interfaces by the Transient Thermoreflectance Technique," ASME J. Heat Transfer, **127**, pp. 315–322.
[9] Swartz, E. T., and Pohl, R. O., 1987, "Thermal Resistances at Interfaces," Appl. Phys. Lett., **51**, pp. 2200–2202.
[10] Cheeke, J. D. N., Ettinger, H., and Hebral, B., 1976, "Analysis of Heat Transfer Between Solids at Low Temperatures," Can. J. Phys., **54**, pp. 1749–1771.
[11] Little, W. A., 1959, "The Transport of Heat Between Dissimilar Solids at Low Temperatures," Can. J. Phys., **37**, pp. 334–349.
[12] Swartz, E. T., and Pohl, R. O., 1989, "Thermal Boundary Resistance," Rev. Mod. Phys., **61**, pp. 605–668.
[13] Cahill, D. G., Bullen, A., and Lee, S.-M., 2000, "Interface Thermal Conductance and the Thermal Conductivity of Multilayer Thin Films," High Temp. - High Press., **32**, pp. 135–142.
[14] Costescu, R. M., Wall, M. A., and Cahill, D. G., 2003, "Thermal Conductance of Epitaxial Interfaces," Phys. Rev. B, **67**, p. 054302.
[15] Stoner, R. J., and Maris, H. J., 1993, "Kapitza Conductance and Heat Flow Between Solids at Temperatures from 50 to 300 K," Phys. Rev. B, **48**, pp. 16373–16387.
[16] Hopkins, P. E., Salaway, R. N., Stevens, R. J., and Norris, P. M., 2006, "Dependence of Thermal Boundary Conductance on Interfacial Mixing at the Chromium-Silicon Interface," *IMECE2006*, Chicago, p. 15288.
[17] Hopkins, P. E., and Norris, P. M., 2006, "Thermal Boundary Conductance Response to a Change in Cr/Si Interfacial Properties," Appl. Phys. Lett., **89**, p. 131909.
[18] Beechem, T., and Graham, S., 2006, "Estimating the Effects of Interface Disorder on the Thermal Boundary Resistance Using a Virtual Crystal Approximation," *Proceedings of the 2006 ASME International Mechanical Engineering Congress*, Anaheim, CA, Paper No. IMECE2006–14161.
[19] Beechem, T. E., Graham, S., Hopkins, P. E., and Norris, P. M., 2007, "The Role of Interface Disorder on Thermal Boundary Conductance Using a Virtual Crystal Approach," Appl. Phys. Lett., **90**, p. 054104.
[20] Snyder, N. S., 1970, "Heat Transport Through Helium II: Kapitza Conductance," Cryogenics, **10**, pp. 89–95.
[21] The term "acoustic mismatch" describes two materials that have significantly different acoustic velocities; the degree of the acoustic mismatch can be easily determined by comparing the materials' Debye temperatures, $\theta_D$.
[22] Chen, Y., Li, D., Yang, J., Wu, Y., Lukes, J., and Majumdar, A., 2004, "Molecular Dynamics Study of the Lattice Thermal Conductivity of Kr/Ar Superlattice Nanowires," Physica B, **349**, pp. 270–280.
[23] Kosevich, Y. A., 1995, "Fluctuation Subharmonic and Multiharmonic Phonon Transmission and Kapitza Conductance Between Crystals With Very Different Vibrational Spectra," Phys. Rev. B, **52**, pp. 1017–1024.
[24] Lyeo, H.-K., and Cahill, D. G., 2006, "Thermal Conductance of Interfaces Between Highly Dissimilar Materials," Phys. Rev. B, **73**, p. 144301.
[25] Stevens, R. J., Zhigilei, L. V., and Norris, P. M., 2007, "Effects of Temperature and Disorder on Thermal Boundary Conductance at Solid-Solid Interfaces: Nonequilbrium Molecular Dynamics Simulations," Int. J. Heat Mass Transfer, **50**, pp. 3977–3989.
[26] Norris, P. M., Caffrey, A. P., Stevens, R. J., Klopf, J. M., Mcleskey, J. T., and Smith, A. N., 2003, "Femtosecond Pump-Probe Nondestructive Examination of Materials," Rev. Sci. Instrum., **74**, pp. 400–406.
[27] Kittel, C., 1996, *Introduction to Solid State Physics*, Wiley, New York.
[28] Hohlfeld, J., Wellershoff, S.-S., Gudde, J., Conrad, U., Jahnke, V., and Matthias, E., 2000, "Electron and Lattice Dynamics Following Optical Excitation of Metals," Chem. Phys., **251**, pp. 237–258.
[29] Stevens, R. J., Smith, A. N., and Norris, P. M., 2006, "Signal Analysis and Characterization of Experimental Setup for the Transient Thermoreflectance Technique," Rev. Sci. Instrum., **77**, p. 084901.
[30] Capinski, W. S., and Maris, H. J., 1996, "Improved Apparatus for Picosecond Pump-and-Probe Optical Measurements," Rev. Sci. Instrum., **67**, pp. 2720–2726.
[31] Ozisik, M. N., 1993, *Heat Conduction*, Wiley, New York.
[32] Anisimov, S. I., Kapeliovich, B. L., and Perel'man, T. L., 1974, "Electron Emission From Metal Surfaces Exposed to Ultrashort Laser Pulses," Sov. Phys. JETP, **39**, pp. 375–377.
[33] Qiu, T. Q., and Tien, C. L., 1992, "Heat Transfer Mechanisms During Short-Pulse Laser Heating on Metals," HTD (Am. Soc. Mech. Eng.), **196**, pp. 41–49.
[34] Smith, A. N., Hostetler, J. L., and Norris, P. M., 1999, "Nonequilibrium Heating in Metal Films: An Analytical and Numerical Analysis," Numer. Heat Transfer, Part A, **35**, pp. 859–873.
[35] Smith, A. N., Hostetler, J. L., and Norris, P. M., 2000, "Thermal Boundary Resistance Measurements Using a Transient Thermoreflectance Technique," Microscale Thermophys. Eng., **4**, pp. 51–60.
[36] Incropera, F., and Dewitt, D. P., 1996, *Fundamentals of Heat and Mass Transfer*, Wiley, New York.
[37] Tien, C. L., Armaly, B. F., and Jagannathan, P. S., 1969, "Thermal Conductivity of Thin Metallic Films and Wires at Cryogenic Temperatures," *Thermal Conductivity VIII*, Plenum, New York.
[38] Majumdar, A., and Reddy, P., 2004, "Role of Electron-Phonon Coupling in Thermal Conductance of Metal-Nonmetal Interfaces," Appl. Phys. Lett., **84**, pp. 4768–4770.
[39] Daly, B. C., Maris, H. J., Imamura, K., and Tamura, S., 2002, "Molecular Dynamics Calculation of the Thermal Conductivity of Superlattices," Phys. Rev. B, **66**, p. 024301.
[40] Young, D. A., and Maris, H. J., 1989, "Lattice-Dynamical Calculation of the Kapitza Resistance Between Fcc Lattices," Phys. Rev. B, **40**, pp. 3685–3693.
[41] Reddy, P., Castelino, K., and Majumdar, A., 2005, "Diffuse Mismatch Model of Thermal Boundary Conductance Using Exact Phonon Dispersion," Appl. Phys. Lett., **87**, p. 211908.
[42] Stevens, R. J., Norris, P. M., and Zhigilei, L. V., 2004, "Molecular-Dynamics Study of Thermal Boundary Resistance: Evidence of Strong Inelastic Scattering Transport Channels," *IMECE2004*, p. 60334.
[43] Levinshtein, M. E., Rumyantsev, S. L., and Shur, M. S., 2001, *Properties of Advanced Semiconductor Materials: GaN, AlN, InN, BN, SiC, SiGe*, Wiley-Interscience, New York.
[44] Fugate, R. Q., and Swenson, C. A., 1969, "Specific Heat of $Al_2O_3$ From 2 to 25 K," J. Appl. Phys., **40**, pp. 3034–3036.
[45] Gray, D. E., 1972, *American Institute of Physics Handbook*, McGraw-Hill, New York.

# Thermal Transport in a Microchannel Exhibiting Ultrahydrophobic Microribs Maintained at Constant Temperature

**D. Maynes**

**B. W. Webb**

**J. Davies**

Department of Mechanical Engineering,
Brigham Young University,
Provo, UT 84602-4201

*This paper presents numerical results exploring the periodically repeating laminar flow thermal transport in a parallel-plate microchannel with ultrahydrophobic walls maintained at constant temperature. The walls considered here exhibit alternating microribs and cavities positioned perpendicular to the flow direction. Results describing the thermally periodically repeating dynamics far from the inlet of the channel have been obtained over a range of laminar flow Reynolds numbers and relative microrib/cavity module lengths and depths in the laminar flow regime. Previously, it has been shown that significant reductions in the overall frictional pressure drop can be achieved relative to the classical smooth channel laminar flow. The present predictions reveal that the overall thermal transport is also reduced as the relative size of the cavity region is increased. The overall Nusselt number behavior is presented and discussed in conjunction with the frictional pressure drop behavior for the parameter range explored. The following conclusions can be made regarding thermal transport for a constant temperature channel exhibiting ultrahydrophobic surfaces: (1) Increases in the relative cavity length yield decreases in the Nusselt number, (2) increasing the relative rib/cavity module length yields a decrease in the Nusselt number, and (3) decreases in the Reynolds number result in smaller values of the Nusselt number.* [DOI: 10.1115/1.2789715]

*Keywords: ultrahydrophobic, microscale, convection, microribs, nonwetting*

## Introduction

As fluid flow components shrink in physical size, classical theory indicates that the pressures required to drive a given flow increase substantially, often to extreme levels. The motivation for exploring methods to decrease the required pumping power in microfluidic applications is thus considerable. The physics of transport at these physical scales has been the subject of significant recent attention. The hydrodynamics of fluid flow in microchannels has been explored, and a sampling of the growing body of related literature may be found in Refs. [1–6]. One technique proposed recently for reducing the frictional resistance to the liquid flow in microchannels is the addition of microribs and cavities on the channel walls [7–13]. If the rib/cavity surfaces are treated with an ultrahydrophobic coating and the cavity size is small enough, the flowing liquid will wet only the top surfaces of the ribs. A meniscus forms above the cavity, provided the pressure is not too great. The free surface meniscus separates the liquid flowing in the microchannel from the vapor trapped in the cavities. Because the liquid wets only the rib surfaces, the contact area between the channel walls and the flowing liquid is reduced. Microfabrication techniques now exist that permit the manufacture of such patterned surfaces. Several recent investigations report on the wetting characteristics of discrete liquid droplets on micropatterned superhydrophobic surfaces [14–19].

Several previous investigations have explored experimentally the potential advantage of patterned ultrahydrophobic microchannels to reduce frictional pressure drop. These include Ou et al. [7,8], Maynes et al. [9], and Davies et al. [13]. Analytical/numerical approaches to the problem have also appeared, including work by Davies et al. [13], Philip [20], Lauga and Stone [21], Cottin-Bizonne et al. [22], and Benzi et al. [23]. To date, the focus of prior work has been on understanding the hydrodynamics of patterned microchannels. A single recent study reports on an approximate analytical model of the thermal transport in parallel-plate channels subject to an imposed hydrodynamic slip at the wall and a constant imposed wall temperature in the slip region [24]. To the authors' knowledge, there has been no investigation of the combined momentum and heat transport in such channels wherein the microrib and cavity regions are coupled thermally and hydrodynamically. Such is the focus of this paper.

The fundamental thermal transport dynamics for liquids flowing through microengineered channels is expected to differ significantly from classical viscous boundary layer flow. Consider the near-wall region of a channel wall that exhibits microrib structures separated by vapor-filled cavities, as illustrated in Fig. 1. Liquid is flowing over the top of the wall and perpendicular to the ribs at a uniform core velocity. At the liquid/rib interfaces, classical convective heat transport prevails due to boundary layer growth and evolution. If continuum behavior prevails, the liquid velocity at the wall will vanish to satisfy the no-slip condition and the fluid temperature will match the rib temperature. At the liquid-vapor interface, the liquid will no longer be in contact with a solid surface and the liquid velocity at the vapor-liquid interface need not be zero. A thermal convection cell will exist in the vapor cavity, driven by the induced motion at the interface. The convection cell constitutes thermal resistance to heat transfer between the flowing liquid and the wall, which forms the cavity. At the second rib, a subsequent thermal boundary layer begins to grow inside of

Contributed by the Heat Transfer Division of ASME for publication in the JOURNAL OF HEAT TRANSFER. Manuscript received September 12, 2006; final manuscript received May 15, 2007; published online February 4, 2008. Review conducted by Yogendra Joshi.

  

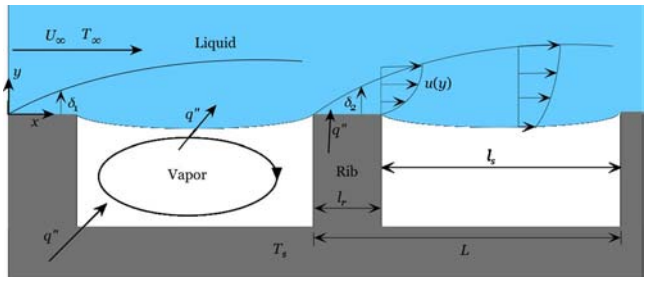


**Fig. 1 Schematic of the near-wall and cavity regions for liquid flow over an ultrahydrophobic surface exhibiting microrib structures and bulk flow perpendicular to the ribs [13]**

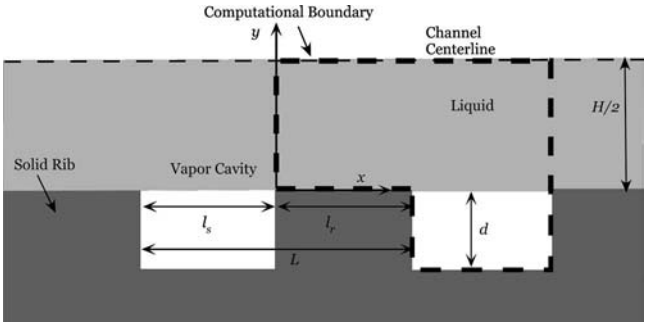


**Fig. 2 Schematic of the computational domain encompassing a rib/cavity module. Flow direction is from left to right [13].**

the first and the wall shear stress will again decrease along the solid rib in the streamwise direction, although the initial value of the stress will not be as high as for the preceding rib. This behavior will repeat in the streamwise direction, and at some point downstream from the channel inlet, a periodically thermally fully developed state may be established. At this point, the flow will exhibit periodic variations in the $x$ direction across repeating streamwise modules (of length $L$) consisting of a single rib and cavity. Coupling of the convective dynamics of the vapor cavity region with the liquid flow above the cavity requires matching the velocity, shear stress, temperature, and heat flux at the liquid/vapor interface.

Numerical results exploring the periodically repeating thermal transport in a parallel-plate microchannel with ultrahydrophobic walls maintained at constant wall temperature are presented. The numerical approach is based on the solution of the classical Navier–Stokes and energy equations and thus assumes that continuum behavior prevails. In reality, the liquid/vapor interface shape is dependent on the local balance between the surface tension force and the pressure differential across the interface. In this study, the liquid/vapor interface (meniscus) in the cavity regions was treated as ideal (flat) in the numerical analysis, and the liquid flow in the microchannel core and the vapor flow within the cavity are coupled at the interface hydrodynamically through the velocity and shear stress matching and thermally through temperature and heat flux matching. The influences of the channel Reynolds number $\mathrm{Re}=\rho\bar{u}D_h/\mu$, relative depth of the microribs, $Z_c=d/l_s$, relative cavity length, $F_s=l_s/L$, and relative width of the microrib/cavity module, $L/D_h$, are all quantified numerically. In the parameters above, $d$ is the cavity depth, $l_s$ is the cavity width, $L$ is the total length of a single microrib/cavity module, and $D_h$ is the channel hydraulic diameter, $2H$, where $H$ is the spacing between the channel walls.

## Methodology

Consider laminar flow of an incompressible Newtonian fluid in the absence of viscous dissipation effects. The coupled equations of mass, momentum, and energy assuming constant fluid properties are given as

$$\frac{\partial u}{\partial x}+\frac{\partial v}{\partial y}=0 \tag{1}$$

$$\rho u\frac{\partial u}{\partial x}+\rho v\frac{\partial u}{\partial y}=-\frac{\partial P}{\partial x}+\mu\left(\frac{\partial^2 u}{\partial x^2}+\frac{\partial^2 u}{\partial y^2}\right) \tag{2}$$

$$\rho u\frac{\partial v}{\partial x}+\rho v\frac{\partial v}{\partial y}=-\frac{\partial P}{\partial y}+\mu\left(\frac{\partial^2 v}{\partial x^2}+\frac{\partial^2 v}{\partial y^2}\right) \tag{3}$$

$$\rho c_p u\frac{\partial T}{\partial x}+\rho c_p v\frac{\partial T}{\partial y}=k\left(\frac{\partial^2 T}{\partial x^2}+\frac{\partial^2 T}{\partial y^2}\right) \tag{4}$$

In these governing equations, $u$ is the streamwise ($x$) velocity, $v$ is the wall-normal ($y$) velocity, $P$ is the static pressure, $T$ is the temperature, $\mu$ is the fluid viscosity, $\rho$ is the fluid density, $c_p$ is the fluid specific heat, and $k$ is the fluid thermal conductivity. The thermophysical and transport properties $\mu$, $k$, $c_p$, $\sigma$, and $\rho$ were assumed to remain constant for all scenarios considered. Consequently, buoyancy and thermocapillary influences were not considered in this study. The qualitative effects of thermocapillarity are discussed later. Equations (1)–(4) were solved for the domain illustrated schematically in Fig. 2. The figure indicates a repeating module consisting of one rib and cavity section of the two-dimensional channel. The shape of the meniscus at the cavity interface was assumed to be perfectly flat. In reality, the interface will not be flat but will exhibit curvature dependent on the local pressure differential between the liquid and vapor phases. This pressure differential is a function of the relative volume of the cavity and the local static pressure. Because the static pressure will decrease in the streamwise direction, the curvature at the interfaces will also vary in the streamwise direction. Thus, a flat interface is an idealization and represents only one of the infinite possible curvatures. It will be shown in results that will be presented later that the total transport through the interface region is at least two orders of magnitude smaller than the transport from the solid rib to the liquid. Consequently, the shape of the meniscus exerts only a secondary influence on the overall thermal transport. For the scenarios considered here, the capillary number $\mathrm{Ca}=\bar{u}\mu/\sigma$ ranged from $5\times10^{-4}$ at $\mathrm{Re}=4$ to 0.28 at $\mathrm{Re}=2000$. Consequently, since Ca is small, it is not expected that the interface will be deformed by the flow, except at the highest Re explored where some modest deformation may exist [25]. The vapor cavity is of length $l_s$, and the microrib length where the no-slip condition exists is of length $l_r$. The classical Navier–Stokes equations are employed here since the core flow is a liquid. As a consequence, the liquid Knudsen number will be small for all scenarios, and continuum behavior in the bulk flow will prevail. It is acknowledged that in the cavity regions, noncontinuum behavior is possible.

The boundary conditions were specified as symmetry at the channel centerline, $y=H/2$, and no-slip and constant wall temperature at the microrib surface, $y=0$ and $0\leqslant x\leqslant l_r$. The conditions at the upstream and downstream edges parallel to the $y$ axis were specified to be periodic, indicating that $u$, $v$, $\partial u/\partial y$, $\partial v/\partial y$, $\partial u/\partial x$, and $\partial v/\partial x$ were set to be equal at corresponding locations along these two vertical faces. At the immiscible liquid-vapor interface $y=0$ and $l_r\leqslant x\leqslant l_s+l_r$, the solutions were coupled by matching local velocities and shear stresses, and temperature and heat flux at the interface. The liquid properties were specified as those of water at standard temperature and pressure. Likewise, the vapor fluid properties were specified to be air at standard condi-

tions. The walls of the cavity region were specified as no-slip, impermeable, and constant wall temperature at the same value as the microrib surfaces.

Equations (1)–(4) are nonlinear and are dependent on the Reynolds and Prandtl numbers for a given $l_s$, $l_r$, $d$, and $H$. The governing equations were therefore solved numerically using the control volume approach [26], with the commercial CFD code FLUENT™ (Fluent, Inc., Hanover, NH). The domain was discretized and the governing equations were integrated around each computational cell. This results in a set of nominally linear algebraic equations in the unknown dependent variables. For the final grid-independent solutions reported here, the coupled liquid domain and cavity vapor recirculation computations were very time consuming and therefore first-order upwind differencing was used for the advective terms. The SIMPLE algorithm was employed to treat the pressure-velocity coupling. The accuracy of the first-order simulations was confirmed rigorously, as discussed in detail in a section to follow.

The periodicity in streamwise boundaries was ensured computationally by coupling the domain inlet boundary with the domain exit boundary such that the cells on these surfaces become computational neighbors. This guarantees continuity of both dependent variables (velocity, suitably normalized temperature, and pressure) and their gradients at the periodic boundaries. The periodicity condition provides that the velocity distribution within the computational domain defined in Fig. 2 repeats from module to module, such that the $u$ and $v$ velocity distributions are identical within each module, $u(\vec{s})=u(\vec{s}+L)=u(\vec{s}+2L)=\cdots$ and $v(\vec{s})=v(\vec{s}+L)=\cdots$. Here again, $L$ is the microrib/cavity module length. Although the pressure itself is not periodic, the pressure drop between modules is periodic such that the pressure drop from module to module is constant as given by $\Delta P=P(\vec{s})-P(\vec{s}+L)=P(\vec{s}+L)-P(\vec{s}+2L)=\cdots$. The pressure gradient driving the flow may thus be represented as the sum of a gradient of a linearly varying component and the gradient of a module-periodic component, $\nabla P=\psi+\nabla P(\vec{s})$. Thus, $\psi$ is the linearly varying component of pressure and $P(\vec{s})$ is the periodic pressure whose nonlinear distribution repeats from module to module. Computationally, either the module-to-module pressure drop $\psi$ or the total mass flow rate through the microchannel may be imposed. In this study, the mass flow rate in the microchannel was specified for each simulation, and $\psi$ was determined iteratively by updating its value through the course of the iterations. Corrections to the value of $\psi$ were made during the iterations based on the difference between the actual and the desired mass flow rate.

The absolute fluid temperature $T$ is not periodic from module to module, since heat transfer from the heated walls to the fluid results in a monotonic rise in fluid mean temperature. However, if one normalizes the temperature following the classical approach as [27] $\theta=(T_s-T)/(T_s-T_m)$, where $T_s$ and $T_m$ are the wall surface and fluid mean temperature, respectively, the normalized temperature is found to repeat from module to module in a fashion similar to the velocities, $\theta(\vec{s})=\theta(\vec{s}+L)=\theta(\vec{s}+2L)=\cdots$. Thus, the thermally periodically repeating condition indicates that $\theta$ and $\partial\theta/\partial x$ are equal at corresponding locations along these upstream and downstream faces of the computational domain.

Extremely high velocity and pressure gradients were anticipated in the domain, particularly along the microrib surface and near its edges where abrupt acceleration and deceleration regions associated with the transition between no-slip and reduced-shear regions exist. Thus, great care was taken to ensure that the solutions were grid independent. To achieve this, the following procedure was adopted. A relatively coarse grid was first deployed (typically 15,000–20,000 nodes) and the global iterations were taken to convergence. The adaptive grid utility of FLUENT was then employed to refine the computational mesh on the interior of the domain, and the solution was again iterated to convergence. The adaptive grid refinement utility adds nodes locally in the computational domain based on a user-selectable upper limit on the value of the gradient of the dependent variables. This adaptive interior-grid refinement procedure was followed two or three times until the overall flow and thermal behavior ceased to change appreciably. The boundary refinement tool in the adaptive grid refinement utility of FLUENT was then employed near the liquid-vapor interface and along the wall surfaces. The interior and boundary grid refinement procedure necessitated a grid refinement exercise for each set of problem parameters (Re, $l_s$, $l_r$, $d$, and $H$), and thus resulted in a different computational mesh for each simulation. The process of successively refining the grid was repeated until the solution ceased to change appreciably. Although the resulting grid was different for each set of problem parameters, the grid-independent hydrodynamic/thermal solutions achieved were typically on final grid distributions of 600,000 nodes. This grid produced changes in overall module heat transfer and module-to-module pressure drop less than 0.1% and 0.05%, respectively, relative to coarser grid simulations. The solution procedure required several hundred thousand iterations over 10–15 days of computation time for each simulation.

As noted previously, the impact of a higher-order numerical approximation on the predicted results was assessed. Simulations using second-order upwind differencing were performed for a few selected cases using the refined grid described previously. At conditions where modeling inaccuracies in the cavity recirculation zone associated with lower-order numerical differencing are expected to be among the worst (highest Reynolds number and largest relative cavity width), the maximum difference in predicted local shear stress along the liquid-vapor interface between the second-order and first-order upwind predictions was 3.3%, while the difference in total shear (area integration of shear stress along the liquid-vapor interface) was 1.3%. The total heat transfer through the liquid-vapor interface differed by less than 0.3% between the first-order and second-order upwind simulations. Further, as will be shown in the results reported hereafter, the total thermal transport through the liquid-vapor interface is nominally two orders of magnitude smaller than the transport from the solid rib to the liquid. Consequently, the impact of the lower-order numerical approximation employed is negligible.

A user-defined function was developed in FLUENT, following standard practice, to specify the hydrodynamic and thermal boundary conditions at the liquid-vapor interface above the cavity [28]. As required by the governing physics, the user-defined function forces a match of local velocity and shear stress, and temperature and heat flux in the two phases at the liquid-vapor interface, subject to the different viscosities and thermal conductivities in the liquid and vapor regions above and below the interface, respectively. At convergence, the velocity and temperature field within the liquid and vapor domains is that which satisfies both the conservation equations and the interface conditions in the liquid and vapor domains.

Several important nondimensional parameters exist for the varying scenarios of interest, these being the relative microrib/cavity module length, $L/D_h$, the relative cavity length, $F_s=l_s/L$, the Reynolds number $\mathrm{Re}=\rho\bar{u}D_h/\mu$, and the relative cavity depth, $Z_c=d/l_s$. $L/D_h$ and $F_s$ were varied in the ranges 0.05–2.5 and 0–98%, respectively. Re was varied from 4 to 2000 and $Z_c$ was varied from 0.1 to 4. The above parameter ranges are representative of realistic microfluidic conditions.

## Results and Discussion

The detailed hydrodynamic characteristics of the patterned microchannel have been presented and explored elsewhere [13]. Although the results here correspond to the classical constant wall temperature treatment, in general, the behavior for a constant heat flux condition should be qualitatively similar. Shown in Fig. 3 are illustrative examples of the nondimensional temperature field for two scenarios: $\mathrm{Re}=4$ and $F_s=0.5$ and $\mathrm{Re}=1000$ and $F_s=0.98$. The relative module length, $L/D_h$, was 0.25 and the relative cavity

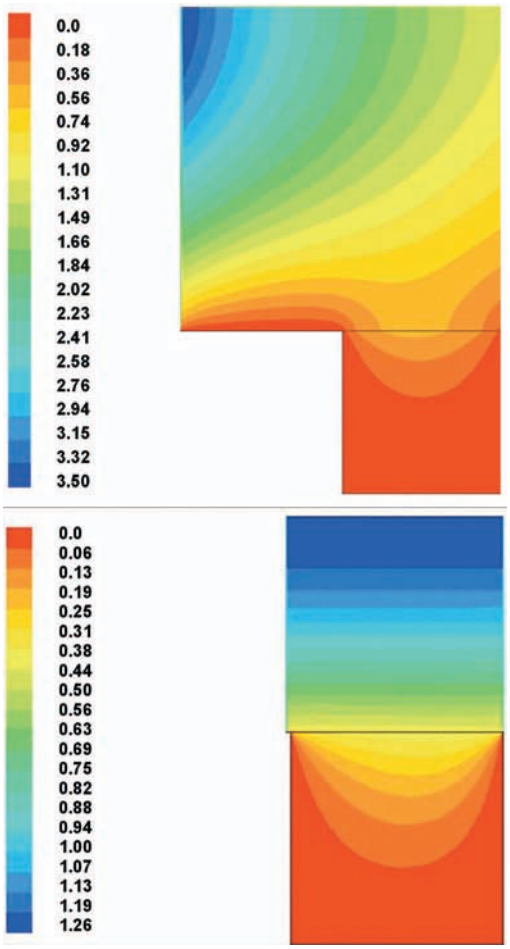


**Fig. 3 Contours of the nondimensional temperature $(T_s - T)/(T_s - T_{mo})$ in two channels where $L/D_h$=0.25, $Z_c$=1 for both channels. For the top contour plot, $F_s$=0.5 and Re=4, and for the bottom contour plot, $F_s$=0.98 and Re=1000.**

depth was $Z_c$=1.0 for both scenarios. The nondimensional temperature in these contour plots is defined as $(T_s-T)/(T_s-T_{mo})$, where $T_s$ is the constant wall surface temperature, $T$ is the local temperature, and $T_{mo}$ is the fluid mixed-mean temperature at the outlet of the repeating module. The contour plots show that the maximum nondimensional temperature in the domain is greater for the lower Reynolds number case. At the interface, the temperatures in the liquid and vapor phases are locally matched (continuous). The temperature gradient is much greater in the vapor phase, however, due to the large difference in thermal conductivity and the requirement of equal heat flux locally in the two phases. There exists much greater temperature variation in the axial direction for the lower Reynolds number case. For all scenarios, very low temperature gradients exist along the walls of the air cavity.

Profiles of the dimensionless temperature, $\theta=(T_s-T)/(T_s-T_m)$, are shown in Fig. 4 as a function of wall-normal position, $y^*=2y/H$. Here, the dimensionless temperature is normalized in the classical manner where $T_m$ is the local mixed-mean temperature in the liquid. Profiles are shown in the figure for two values of the relative cavity length, $F_s$=0.5 and 0.98, and at two axial locations, $x/L$=0 and 0.9. The relative module length was 0.25 and the relative cavity depth was $Z_c$=2 for all scenarios. The result for the classical parallel-plate channel is also shown. The $x/L$=0 location corresponds to the leading edge of the microrib and the $x/L$=0.9 position is therefore just upstream of the rib above the vapor cavity. At $x/L$=0 and at $y^*$=0, $\theta$ vanishes since the liquid temperature equals the solid rib temperature at the rib surface. At

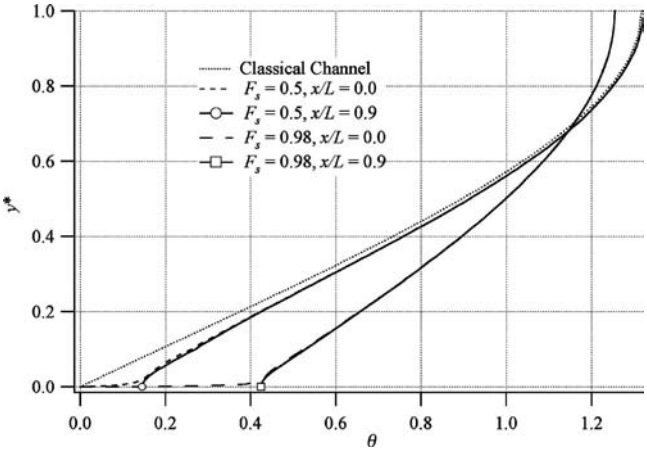


**Fig. 4 Profiles of the nondimensional temperature $\theta$ at two axial positions ($x/L$=0 and 0.9) for $F_s$=0.5 and 0.98 with Re =1000, $L/D_h$=0.25, and $Z_c$=2**

$x/L$=0.9 and $y^*$=0, however, $\theta$ does not vanish but reaches values of nominally 0.15 and 0.42 for the $F_s$=0.5 and 0.98 cases, respectively. Thus, above the vapor cavity, the nondimensional fluid temperature exhibits an apparent jump above the imposed rib surface temperature, caused by the existence of the vapor region where the prevailing shear stress drops significantly. The data show that above the rib ($x/L$=0), the wall-normal temperature gradient is much greater than what exists for the classical parallel-plate channel scenario. This behavior exists due to (1) increased fluid velocity above the rib resulting from the apparent slip above the cavity, (2) a reduction in the thermal energy transferred to the liquid in the cavity region preceding the rib, and (3) redevelopment of the thermal boundary layer. The temperature gradient at the wall is greater for the $F_s$=0.98 scenario since the relative cavity length is nearly twice as long. Above the cavity region, the wall-normal temperature gradient at the liquid-vapor interface approaches zero due to the large difference in thermal conductivity between the liquid and vapor phases. Far from the rib and liquid/cavity interface, the nondimensional temperature for the $F_s$=0.5 case is nearly the same as for the classical channel, whereas for $F_s$=0.98, the magnitude of $\theta$ is smaller.

Figure 5 illustrates the influence of the Reynolds number on the local normalized temperature profiles. Results for two Reynolds numbers are shown (Re=4 and 1000) where $F_s$=0.98, $L/D_h$

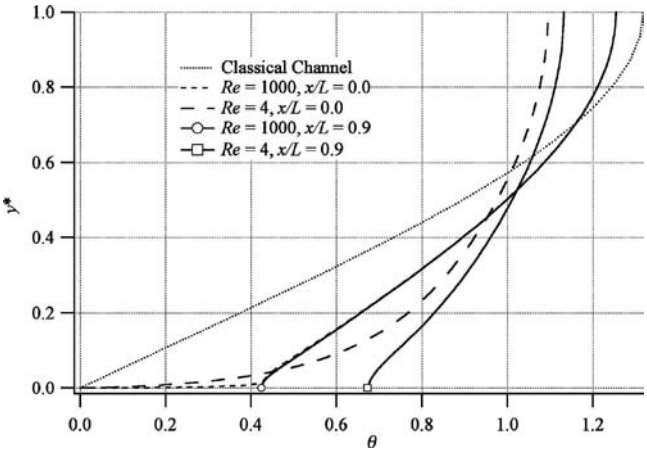


**Fig. 5 Profiles of the nondimensional temperature $\theta$ at $x/L$ =0 and 0.9 for two Reynolds numbers Re=4 and 1000, with $F_s$ =0.98, $L/D_h$=0.25, and $Z_c$=2**

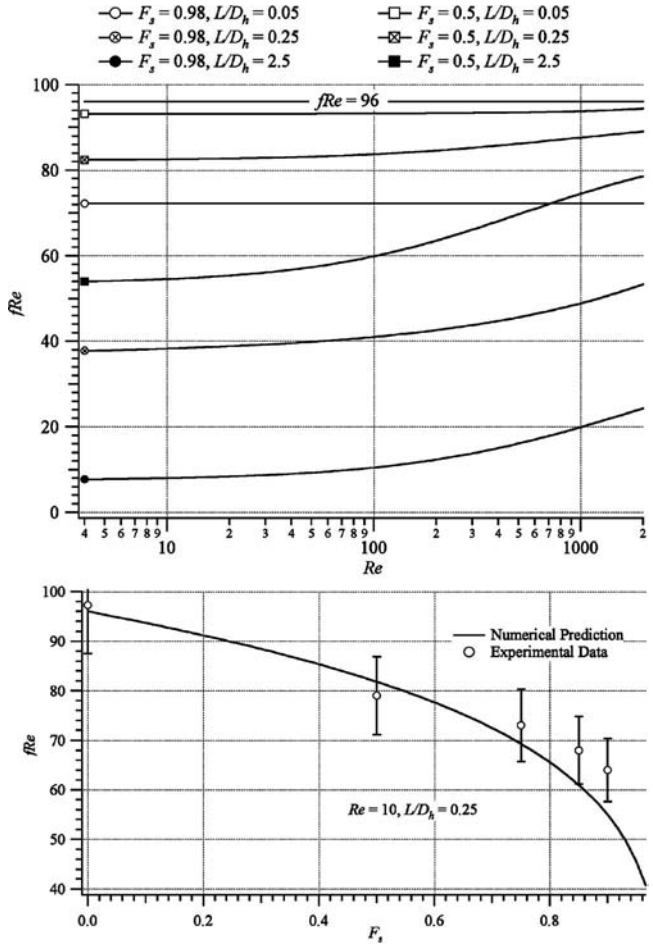


**Fig. 6 Variation of the average friction-factor Reynolds product number with Reynolds number for relative cavity lengths of $F_s$=0.5 and 0.98, relative microrib/cavity module lengths of $L/D_h$=0.05, 0.25, and 2.5, and $Z_c$=2 (top panel) and comparison between experimental measurement and predicted values of *f*Re as a function of the relative cavity length, $F_s$, at $L/D_h$ =0.25 and Re=10 (bottom panel) [13]**

=0.25, and $Z_c$=2 for all profiles. The results show that above the rib ($x/L$=0), the temperature gradient is greater for Re=1000 than for the Re=4 case. Also, above the cavity region ($x/L$=0.9), the magnitude of $\theta$ at $y^*$=0 increases for decreasing values of Re. In general, it can be observed from both Figs. 4 and 5 that the local temperature profiles exhibit the most radical departure from the classical behavior at low values of the Reynolds number and at large values of the relative cavity length. Indeed, as Re increases, the influence of the cavity region on the global flow field and thermal transport diminishes. This results from the fact that as Re increases, the time scale associated with streamwise advection becomes much smaller than that associated with diffusion. Consequently, the boundary layers formed on the microrib surfaces persist further downstream, with less change in the velocity and temperature profiles at higher Reynolds number. Thus, the cavity region is less effective at interrupting the thermal and hydrodynamic boundary layers at high Re. This will be corroborated in the Nusselt number results to follow.

Detailed discussion of the effect of the ultrahydrophobic ribs on the flow structure and frictional pressure drop was presented in Ref. [13]. The top panel of Fig. 6 presents the dependence of the friction-factor Reynolds number product, *f*Re, on Reynolds number, replotted from the data of Ref. [13]. This information is reproduced here since the momentum and heat transfer behavior are similar, and because relative effects are explored later. These predictions are for $F_s$=0.5 and 0.98, $Z_c$=2, and three values of $L/D_h$ ranging from 0.05 to 2.5. By way of reference, the classical solution yields the benchmark value *f*Re=96 (shown in the figure) for laminar flow in a parallel-plate channel in the absence of microribs and apparent fluid slip. Figure 6 illustrates reductions in *f*Re relative to the classical value for all $F_s$ and $L/D_h$. *f*Re is reduced as the relative module length increases, as the relative cavity length increases, and as the Reynolds number is decreased. The reductions in *f*Re can be significant; at Re=4, $F_s$=0.98, and $L/D_h$=2.5, the value of *f*Re is reduced to just 15% of the classical value, suggesting that dramatic decreases in frictional pressure drop would be possible for these conditions. As was observed in the temperature profiles shown in Figs. 4 and 5, the influence of the air cavity on the frictional resistance diminishes as Re increases. In general, the *f*Re value tends toward the classical behavior as Re increases, regardless of magnitudes of the relative cavity length and relative module length. Also shown in the bottom panel of Fig. 6 is a comparison of experimental measurement of *f*Re as a function of the relative cavity width, $F_s$, at Re=10 and $L/D_h$=0.25. As is evident by the data, good agreement exists between the trends in the experimental and predicted results, although the experimental data tend to exhibit values of *f*Re that are greater than the values derived from the numerical model.

The module-averaged Nusselt number is defined as

$$\mathrm{Nu} = \frac{\bar{h}D_h}{k} = \frac{q' D_h}{kL\Delta T_{lm}} \tag{5}$$

where $\Delta T_{lm}=(T_{mo}-T_{mi})/\ln[(T_s-T_{mo})/(T_s-T_{mi})]$ following the classical approach for a constant wall temperature condition [26], $q'$ is the total module heat transfer per unit channel width, and $T_{mi}$ is the liquid mixed-mean temperature at the repeating module inlet. $\bar{h}$ represents the convection coefficient spatially averaged over the entire rib-cavity module length, and is defined as $\bar{h}=q'/L\Delta T_{lm}$. The total module heat transfer per unit channel width $q'$ is determined from the liquid mean temperature rise across the module from the energy balance $q'=\dot{m}' c_p(T_{mo}-T_{mi})$, where $\dot{m}'$ is the channel mass flow rate per unit channel width. The length on which a Nusselt number is based is somewhat arbitrary; here, it is based on the hydraulic diameter defined as $D_h=2H$ and not on the ratio of flow cross section to perimeter wetted by the liquid, because there is thermal transport through the vapor cavity into the liquid. Further, such a definition enables direct comparison and evaluations between surfaces exhibiting different relative cavity lengths and comparisons with the classical channel results.

The predicted module-averaged Nusselt number dependence on Reynolds number, corresponding to the configurations whose *f*Re data are shown in the top panel of Fig. 6, is shown in Fig. 7. As expected, the average Nusselt number data exhibit trends very similar to those seen in the *f*Re predictions. The classical value of the Nusselt number for a parallel-plate channel with isothermal walls is 7.54 [26], which serves as the upper limit for parallel-plate channels with $F_s \to 0$. The figure shows that the Nusselt number increases with increasing Reynolds number. For the parameters investigated here, Nu asymptotes to the classical value of 7.54 for the lower relative cavity length ($F_s$=0.5), again due to the diminishing ability of the air cavity to disrupt the thermal and hydrodynamic boundary layers at higher Re. Nu is much lower than the classical value of 7.54 for the higher relative cavity length, and might be expected to experience transition to turbulence before reaching the asymptote. The figure also reveals that the module-averaged Nusselt number decreases as the relative module length $L/D_h$ increases. The reduction in Nusselt number relative to the classical value can be quite significant, with Nu dropping to approximately one-tenth the classical parallel-plate channel value in the worst case ($F_s$=0.98, $L/D_h$=2.5, and Re=4).

The dependence of the module-averaged Nusselt number on relative cavity length is illustrated in Fig. 8 for Re=1000, $Z_c$=2,

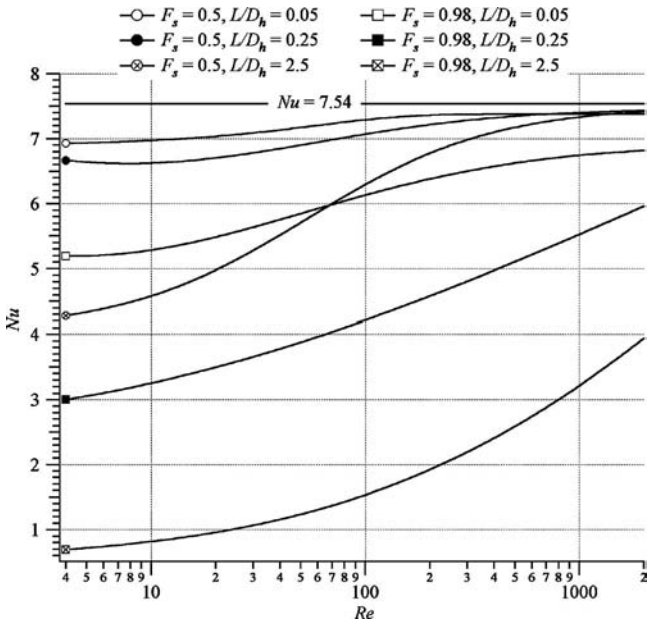


**Fig. 7 Variation of the average channel Nusselt number with Reynolds number for relative cavity lengths of $F_s$=0.5 and 0.98, relative microrib/cavity module lengths of $L/D_h$=0.25 and 2.5, and $Z_c$=2**

and values of $L/D_h$ ranging from 0.05 to 2.5. As expected, the figure shows that at low relative cavity length, the Nusselt number asymptotes to the value of 7.54 corresponding to laminar convective transport in a parallel-plate channel at constant wall temperature. There appears to be diminishing effect of relative cavity length on the average Nusselt number below $F_s \approx 0.5$. As $F_s$ approaches unity, there is a dramatic drop in the average Nusselt number due to the shrinking microrib surface area exposed to the flowing liquid. As was observed previously in Fig. 7, the Nusselt number decreases as the relative module length increases. Finally, detailed results presented elsewhere show that the value of the Nusselt number is insensitive to the relative cavity depth for $Z_c > 0.5$ [29].

Figure 9 shows the local heat flux to the liquid along the rib surface and the liquid-vapor interface as a function of normalized streamwise coordinate $x/L$. The predicted local flux, $q''$, has been normalized by the local heat flux that would exist in a thermally

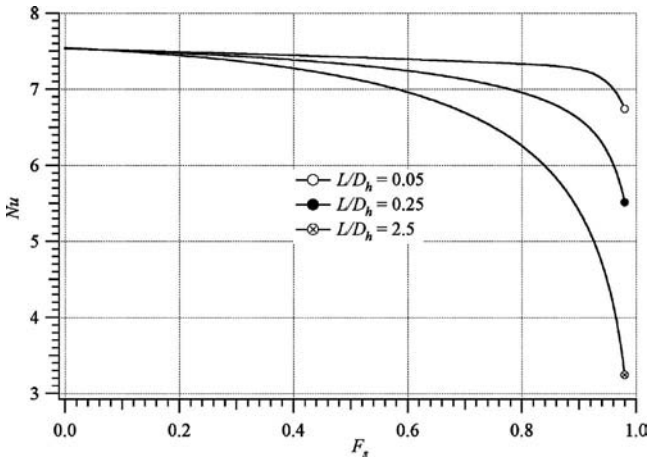


**Fig. 8 Variation of the average channel Nusselt number with relative cavity length at Re=1000 for relative microrib/cavity module lengths of $L/D_h$=0.05, 0.25, and 2.5, and $Z_c$=2**

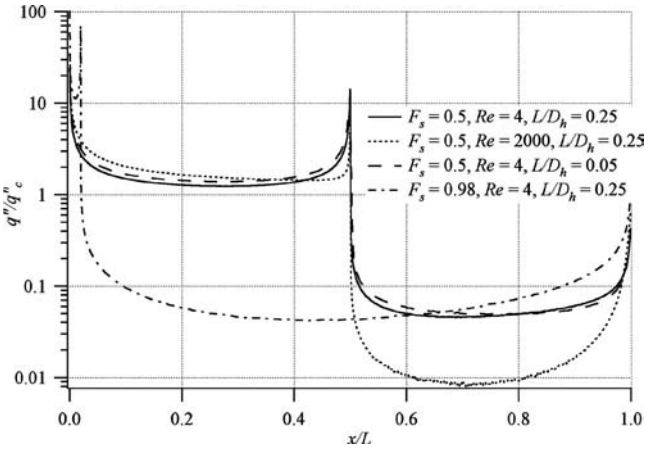


**Fig. 9 Relative heat flux, $q''/q''_c$, as a function of $x/L$ for several scenarios all at $Z_c$=2**

fully developed parallel-plate channel maintained at constant wall temperature, $q''_c$ (which falls exponentially with streamwise distance). Thus, magnitudes of the relative heat flux, $q''/q''_c$, greater than unity represent local enhancement relative to the classical fully developed scenario, while magnitudes less than unity represent a local reduction. Predictions are shown for four different scenarios chosen to illustrate the influence of Re, $L/D_h$, and $F_s$ on the local heat flux behavior. All scenarios reveal a steep decay in the relative heat flux with streamwise position from the leading edge of the microrib, associated with the growth of a new thermal boundary layer on each rib. Magnitudes of $q''/q''_c$ as high as 100 are observed at the leading edge of the rib, and $q''/q''_c > 1$ across the entire rib surface. Following the decay in $q''/q''_c$ along the rib, there exists an increase near the trailing edge of the rib. This behavior is manifest due to the local fluid acceleration in the transition between the rib and following cavity. A similar rise in local shear stress has been observed at this locale [13]. Along the liquid-vapor interface, the local heat flux is significantly below that observed along the rib. The increase in the relative heat flux observed as the flow approaches the leading edge of the downstream microrib ($x/L$=1) is consistent with the steeper temperature gradients illustrated in the thermal contour plots of Fig. 3.

Figure 9 reveals that marked differences in the local heat flux distribution exist as Re, $F_s$, and $L/D_h$ are varied. For example, at $F_s$ (0.98), the relative heat flux on the rib is approximately one order of magnitude greater than for the $F_s$=0 scenario, albeit confined to the much smaller microrib. For higher Reynolds number, the local heat flux on the microrib (for the same $F_s$ and $L/D_h$) is greater, presumably due to a thinner thermal boundary layer along the microrib. Further, the relative heat flux appears to exhibit a somewhat steeper decay with streamwise position at higher Re. Interestingly, the relative heat flux at the liquid-vapor interface is lower for increasing Re. This is consistent with previous observations that the impact of the cavity region on the heat transport is reduced at higher Re. In general, the results show that the thermal transport through the interface is several orders of magnitude smaller than the transport from the solid rib to the liquid, and consequently the interface shape exerts only a secondary influence. Lastly, all other parameters remaining unchanged, the impact of $L/D_h$ on the relative heat flux appears to be quite modest over the range of parameters explored.

It has been shown that the presence of ultrahydrophobic microribs decreases both the frictional pressure drop and the overall heat transfer in channels. It begs the question as to whether the decrease in $f$Re is more significant than the decrease in Nu. The parameter $\phi = \mathrm{Nu}/f\mathrm{Re}$ is proposed here as a measure of the combined hydrodynamic and thermal effect of the ultrahydrophobic

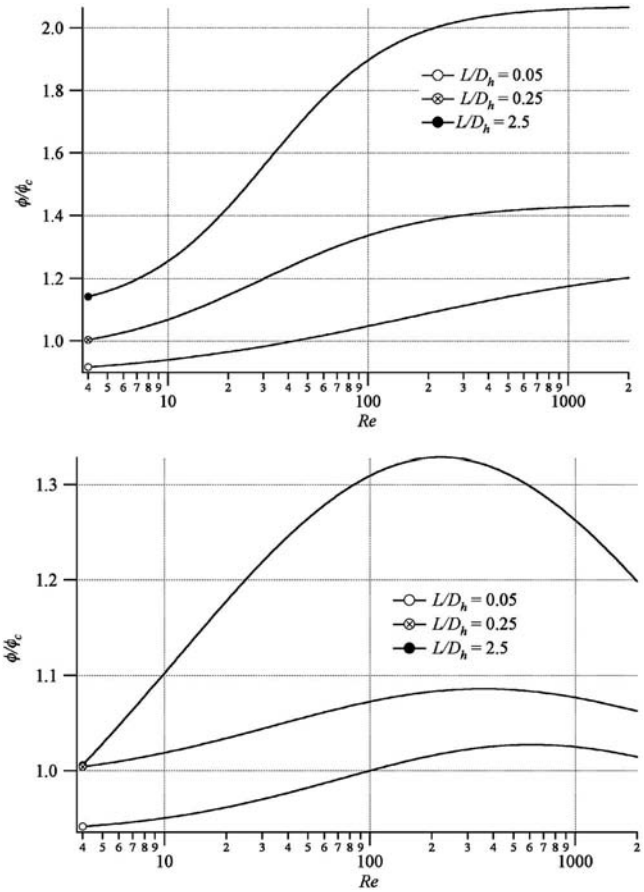


**Fig. 10 Variation of $\phi/\phi_c$ with Re for relative cavity lengths of $F_s$=0.98 (top) and $F_s$=0.5 (bottom) for relative microrib/cavity module lengths of $L/D_h$=0.05, 0.25, and 2.5, and $Z_c$=2**

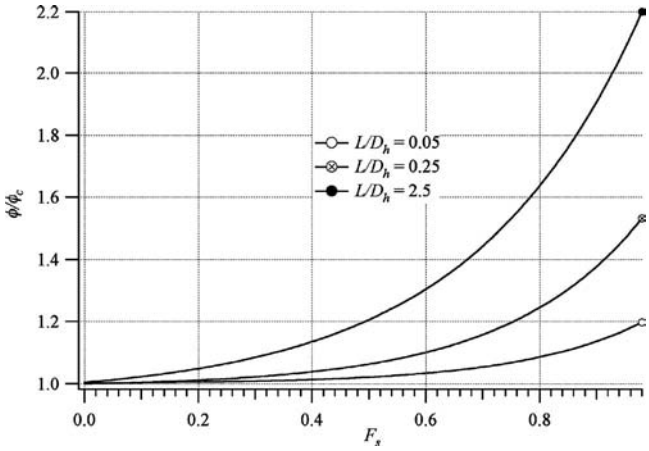


**Fig. 11 Variation of $\phi/\phi_c$ with relative cavity length at Re =1000 for relative microrib/cavity module lengths of $L/D_h$ =0.05, 0.25, and 2.5, and $Z_c$=2**

microribs. Higher $\phi$ is desired indicating increased heat transfer and/or decreased frictional resistance for a particular configuration. For the limiting case of the parallel-plate channel, the classical value $\phi_c=(\mathrm{Nu}/f\mathrm{Re})_c=7.54/96$. The ratio $\phi/\phi_c$ may be viewed as a composite measure of both reduction in frictional pressure drop and average heat transfer relative to the smooth channel. Values of $\phi/\phi_c>1$ indicate relative advantage in the pumping power versus heat transfer compromise. Figure 10 plots $\phi/\phi_c$ as a function of Reynolds number for relative cavity lengths of $F_s$=0.98 and $F_s$=0.5 at relative module lengths of $L/D_h$ =0.05, 0.25, and 2.5, and $Z_c$=2.0. For $F_s$=0.98, as the Reynolds number increases so also does the ratio $\phi/\phi_c$. In the extreme of low Re and small $L/D_h$, the ratio drops below unity, suggesting that the addition of ultrahydrophobic microribs results in a thermal-hydraulic disadvantage for these conditions. For $L/D_h$ =0.05, $\phi/\phi_c$ exceeds unity only for Reynolds numbers above 50. As Re and $L/D_h$ increase, the ratio $\phi/\phi_c$ also increases for all geometric parameters explored. At the highest Reynolds number and relative module length investigated, $\phi/\phi_c$ reaches its maximum value of approximately 2. The $\phi/\phi_c$ behavior for $F_s$=0.5 exhibits an interesting characteristic. Although the ratio increases with Reynolds number as with $F_s$=0.98, $\phi/\phi_c$ reaches a maximum at a Reynolds number that depends on $L/D_h$. The ratio then drops with further increases in Reynolds number. The local maximum suggests that an optimal thermal/hydraulic condition exists.

The influence of the slip fraction on the ratio $\phi/\phi_c$ is shown in Fig. 11 for three values of $L/D_h$ at a Reynolds number of Re =1000. The results confirm the previous observation that the flow and heat transfer approach classical behavior as $F_s\to 0$. At this value of the Reynolds number, the ratio $\phi/\phi_c$ is greater than unity for all values of the relative cavity length $F_s$. However, practical benefits perhaps can only be realized for relative cavity lengths greater than $F_s\approx 0.7-0.8$. As $F_s$ approaches unity, the ratio $\phi/\phi_c$ increases for all $L/D_h$ with greater benefit observed at larger values of the relative module length.

Because surface tension is a dominant factor in maintaining the liquid-vapor interface and temperature variations may exist along the interface, the question of whether Marangoni convection influences the overall thermal transport is now addressed. The induced convective velocity due to thermocapillarity has been shown to scale as $u_{\mathrm{Mar}}\sim\sigma_T\Delta T/\mu$ [25]. Such an induced velocity is in the direction of decreasing temperature (i.e., toward the middle of the liquid-vapor interface). Here $\sigma_T=\partial\sigma/\partial T$ and describes the dependence of the liquid surface tension on temperature and $\Delta T$ is the driving temperature potential along the liquid-vapor interface. The ratio of the induced Marangoni velocity to the forced average liquid velocity in the channel may thus be expressed as $u_{\mathrm{Mar}}/\bar{u}\sim \mathrm{Ma}/\mathrm{Pe}$, where Ma is the Marangoni number, $\mathrm{Ma}=\sigma_T\Delta T l_s/\mu\alpha$, and Pe is the Peclet number, Pe=RePr. The ratio $u_{\mathrm{Mar}}/\bar{u}$ will be the greatest at the lowest Re explored (Re =4) and for large values of the cavity length, $l_s$. Realistically, the cavity length must be smaller than nominally $l_s\approx 20$ $\mu$m if the interface is to be maintained. The above expressions yield $u_{\mathrm{Mar}}/\bar{u}\sim C\Delta T/\mathrm{Re}$, where $C$ is a constant of $O(1)$. The temperature difference $\Delta T$ exhibits dependence on the geometric parameters and on the Reynolds number. In general, as Re increases, the temperature difference will decrease. Clearly, at high Re, the influence of Marangoni induced velocities will be completely negligible. At lower values of Re, however, Marangoni convection may be important, dependent on the magnitude of the temperature variation along the interface between two adjacent ribs.

## Conclusions

Numerical predictions exploring the periodically repeating laminar flow thermal transport in a parallel-plate microchannel with ultrahydrophobic walls maintained at constant temperature have been presented. The ultrahydrophobic walls considered here exhibit alternating microribs and cavities positioned perpendicular to the flow direction. The analysis considered the idealized scenario where the liquid-vapor interface is flat. Results describing the thermally periodically repeating dynamics far from the inlet of the channel have been obtained over a range of flow Reynolds numbers and relative microrib/cavity module lengths and depths in the laminar flow regime. Previously, it has been shown that significant reductions in the overall frictional pressure drop can be achieved relative to the classical smooth channel laminar flow.

The present predictions reveal that the overall thermal transport is also reduced as the relative size of the cavity region is increased. The overall Nusselt number behavior was presented and discussed in conjunction with the frictional pressure drop behavior for the parameter range explored. In summary, the following conclusions are made regarding thermal transport for a constant temperature channel exhibiting ultrahydrophobic surfaces: (1) Increases in the relative cavity length yield decreases in the Nusselt number, (2) increasing the relative rib/cavity module length yields a decrease in the Nusselt number, and (3) decreases in the Reynolds number result in smaller values of the Nusselt number. However, the ratio of the Nusselt number to the friction-factor product is observed to increase over the classical value over a large range of the parameters investigated.

## Nomenclature

$c_p$ = fluid specific heat
Ca = capillary number ($\mathrm{Ca}=\bar{u}\mu/\sigma$)
$d$ = vapor cavity depth
$D_h$ = channel hydraulic diameter ($2H$)
$F_s$ = relative cavity length ($l_s/L$)
$\bar{h}$ = module-averaged convection coefficient
$H$ = channel gap width between microengineered walls
$k$ = thermal conductivity
$l_s$ = cavity length
$l_r$ = microrib length or region of no-slip interface
$L$ = microrib/cavity module length ($l_s+l_r$)
$\dot{m}'$ = mass flow rate per unit channel width
Ma = Marangoni number ($\sigma_T \Delta T l_s/\mu\alpha$)
Nu = Nusselt number ($\bar{h}D_h/k$)
$P$ = fluid pressure
Pr = Prandtl number ($\nu/\alpha$)
Pe = Peclet number (RePr)
$q'$ = total module heat transfer per unit channel width
Re = Reynolds number ($\rho\bar{u}D_h/\mu$)
$T$ = fluid temperature
$T_s$ = channel wall surface temperature
$T_m$ = fluid mean temperature
$T_{mi}$ = fluid mean temperature at the inlet of the module
$T_{mo}$ = fluid mean temperature at the exit of the module
$\Delta T_{\mathrm{lm}}$ = log-mean temperature difference
$u$ = streamwise fluid velocity
$\bar{u}$ = average fluid velocity
$v$ = wall-normal fluid velocity
$x$ = streamwise coordinate
$y$ = wall-normal coordinate
$Z_c$ = relative vapor cavity depth $d/l_s$

### Greek Symbols

$\alpha$ = thermal diffusivity
$\delta$ = boundary layer thickness
$\mu$ = fluid viscosity
$\phi$ = ratio of Nusselt number to friction-factor Reynolds number product ($\mathrm{Nu}/f\mathrm{Re}$)
$\rho$ = fluid density
$\sigma$ = liquid surface tension
$\theta$ = normalized temperature
$\psi$ = linear portion of the pressure gradient

## References


[1] Hetsroni, G., Mosyak, A., Pogrebnyak, E., and Yarin, L. P., 2005, "Fluid Flow in Micro-Channels," Int. J. Heat Mass Transfer, **48**, pp. 1982–1998.
[2] Thompson, B. R., Maynes, D., and Webb, B. W., 2005, "Characterization of the Re-Entrant Developing Flow in a Microtube Using MTV," ASME J. Fluids Eng., **127**, pp. 1003–1012.
[3] Baviere, R., Ayela, F., Le Person, S., and Favre-Marinet, M., 2005, "Experimental Characterization of Water Flow Through Smooth Rectangular Microchannels," Phys. Fluids, **17**, p. 098105.
[4] Sharp, K. V., and Adrian, R. J., 2004, "Transition From Laminar to Turbulent Flow in Liquid Filled Microtubes," Exp. Fluids, **36**, pp. 741–747.
[5] Rands, C., Webb, B. W., and Maynes, D., 2006, "Characterization of Transition to Turbulence in Microchannels," Int. J. Heat Mass Transfer, **49**, pp. 2924–2930.
[6] Judy, J., Maynes, D., and Webb, B. W., 2002, "Characterization of Frictional Pressure Drop for Liquid Flows Through Microchannels," Int. J. Heat Mass Transfer, **45**, pp. 3477–3489.
[7] Ou, J., Perot, B., and Rothstein, J. P., 2004, "Laminar Drag Reduction in Microchannels Using Ultrahydrophobic Surfaces," Phys. Fluids, **16**, pp. 4635–4643.
[8] Ou, J., and Rothstein, J. P., 2005, "Direct Velocity Measurements of the Flow Past Drag-Reducing Ultra-Hydrophobic Surfaces," Phys. Fluids, **17**, p. 103606.
[9] Maynes, D., Jeffs, K., Woolford, B., and Webb, B. W., 2005, "Laminar Flow in a Microchannel With Hydrophobic Surface Patterned Microribs Oriented Parallel to the Flow Direction," Phys. Fluids **19**, p. 093603.
[10] Gogte, S., Vorobieff, P., Truesdell, R., Mammoli, A., van Swol, F., Shah, P., and Brinker, C. J., 2005, "Effective Slip on Textured Superhydrophobic Surfaces," Phys. Fluids, **17**, p. 051701.
[11] Watanabe, K., Takayama, T., Ogata, S., and Isozaki, S., 2003, "Flow Between Two Coaxial Rotating Cylinders With a Highly Water-Repellent Wall," AIChE J., **49**, pp. 1956–1963.
[12] Watanabe, K., Udagawa, Y., and Udagawa, H., 1999, "Drag Reduction of Newtonian Fluid in a Circular Pipe With a Highly Water-Repellent Wall," J. Fluid Mech., **381**, pp. 225–238.
[13] Davies, J., Maynes, D., Webb, B. W., and Woolford, B., 2006, "Laminar Flow in a Microchannel With Super-Hydrophobic Walls Exhibiting Transverse Ribs," Phys. Fluids, **18**, p. 087110.
[14] Oner, D., and McCarthy, T. J., 2000, "Ultrahydrophobic Surfaces: Effects of Topography Length Scales on Wettability," Langmuir, **16**, pp. 7777–7782.
[15] Torkkeli, A., Saarilahti, J., Haara, A., Harma, H., Soukka, T., and Tolonen, P., 2001, "Electrostatic Transportation of Water Droplets on Superhydrophobic Surfaces," *Proceedings of the IEEE MEMS 2001 Conference*, pp. 475–478.
[16] Kim, J., and Kim, C.-J., "Nanostructured Surfaces for Dramatic Reduction of Flow Resistance in Droplet-Based Microfluidics," *Proceedings of the IEEE MEMS 2002 Conference*, Las Vegas, NV, pp. 479–482.
[17] Chen, W., Fadeev, A. Y., Hsieh, M. C., Oner, D., Youngblood, J., and McCarthy, J. T., 1999, "Ultrahydrophobic and Ultralyophobic Surfaces: Some Comments and Examples," Langmuir, **15**, pp. 3395–3399.
[18] Youngblood, J. P., and McCarthy, T. J., 1999, "Ultrahydrophobic Polymer Surfaces Prepared by Simultaneous Ablation of Polypropylene and Sputtering of Poly(terafluoroethylene) Using Radio Frequency Plasma," Macromolecules, **32**, pp. 6800–6806.
[19] Bico, J., Thiele, U., and Quere, D., 2002, "Wetting of Textured Surfaces," Colloids Surf., A, **206**, pp. 41–46.
[20] Philip, J. R., 1972, "Flows Satisfying Mixed No-Slip and No-Shear Conditions," Z. Angew. Math. Phys., **23**, pp. 353–371.
[21] Lauga, E., and Stone, H., 2001, "Effective Slip in Pressure-Driven Stokes Flow," J. Fluid Mech., **489**, pp. 55–77.
[22] Cottin-Bizonne, C., Barentin, C., Charlaix, E., Bocquet, L., and Barrat, J.-L., 2004, "Dynamics of Simple Liquids at Heterogeneous Surfaces: Molecular-Dynamics Simulations and Hydrodynamic Description," Eur. Phys. J. E, **15**, pp. 472–438.
[23] Benzi, R., Biferale, L., Sbragaglia, M., Succi, S., and Toschi, F., 2006, "Mesoscopic Modeling of Heterogeneous Boundary Conditions for Microchannel Flows," J. Fluid Mech., **548**, pp. 257–280.
[24] Enright, R., Eason, C., Dalton, T., Hodes, M., Salamon, T., Kolodner, P., and Krupenkin, T., 2006, "Friction Factors and Nusselt Numbers in Microchannels With Superhydrophobic Walls," ASME Paper No. ICNMM2006-96134.
[25] Panton, R. L., 2005, *Incompressible Flow*, 3rd ed., Wiley, New York.
[26] Patankar, S. V., 1980, *Numerical Heat Transfer*, Hemisphere, New York.
[27] Incropera, F. P., and Dewitt, D. P., 2002, *Fundamentals of Heat and Mass Transfer*, 5th ed., Wiley, New York.
[28] Fluent 6.2 Users Guide, Fluent Inc., Jan. 4, 2005.
[29] Davies, J., 2006, "Analysis of Viscous Drag Reduction and Thermal Transport Effects for Microengineered Ultrahydrophobic Surfaces," MS thesis, Brigham Young University, Provo, UT.

# Study on Micropump Using Boiling Bubbles

**Yasuo Koizumi**
e-mail: koizumiy@cc.kogakuin.ac.jp

**Hiroyasu Ohtake**
e-mail: at10988@ns.kogakuin.ac.jp

Department of Mechanical Engineering,
Kogakuin University,
2665-1, Nakano-machi, Hachioji-shi,
Tokyo 192-0015, Japan

*A micropump was developed using boiling and condensation in a microchannel. The length and hydraulic diameter of the semi-half-circle cross-section microchannel having two open tanks at both ends were* 26 mm *and* 0.465 mm*, respectively. A* $0.5 \times 0.5$ mm$^2$ *electrically heated patch was located at the offset location from the center between both ends of the microchannel, at a distance of* 8.5 mm *from one end and at a distance of* 17 mm *from the other end. The microchannel and the two open tanks were filled with distilled water. The heating patch was heated periodically to cause cyclic formation of a boiling bubble and its condensation. By this procedure, flow from the short side (*8.5 mm *side) to the long side was created. The flow rate increased as the heating rate was increased. The obtained maximum average flow velocity and flow rate were* 10.4 mm/s *and* 2.16 mm$^3$/s*, respectively. The velocity of an interface between the bubble and the liquid plug during the condensing period was much faster than that during the boiling period. During the condensing period, the velocity of the interface at the short channel side (*8.5 mm *side) was faster than that at the long channel side (*17 mm *side). The equation of motion of liquid in the flow channel was solved in order to calculate the travel of liquid in the flow channel. The predicted velocities agreed well with the experimental results. The velocity differences between the short side and the long side, as well as those between the boiling period and the condensing period, were expressed well by the calculation. Liquid began to move from the stationary condition during both the boiling and the condensing periods. The liquid in the inlet side (short side) moved faster than that in the outlet side (long side) during the condensing period because the inertia in the short side was lower than that in the long side. Since the condensation was much faster than boiling, this effect was more prominent during the condensing period. By iterating these procedures, the net flow from the short side to the long side was created.* [DOI: 10.1115/1.2787027]

*Keywords: micro-pump, boiling bubbles, bubble condensation, periodical heating*

## Introduction

Micromachine technology has been investigated extensively in recent decades because this technology appears promising for achieving advanced applications in mechanical engineering. Further progress is required in order to incorporate new developments in micromachine technology research into technologically advanced machines. Physics on the microscale, such as thermal hydraulics, material characteristics, and mechanical dynamics, must therefore be elucidated.

When the size of the flow channel is scaled down, the ratio of the surface area to the volume increases, and the frictional pressure loss increases drastically. Thus, a normal pumping system will no longer work in microscale systems. Various methods for moving fluids in microsystems have been proposed. For example, Jun and Kim [1] demonstrated the movement of bubbles in a $2 \times 10$ $\mu$m$^2$ rectangular channel some years ago. Electric heaters were located along the flow channel, and these heaters were heated sequentially to generate thermal bubbles in a sequential manner. The bubble in the upstream side functioned as a check valve while a new bubble was forming in the downstream side and expanding downstream. This sequential nonsymmetric expansion of bubbles produced unidirectional flow. The attained flow velocity was 200 $\mu$m/s.

Prosperetti et al. [2] heated salt water in a microchannel and generated bubbles periodically at an offset location from the center position of the flow channel. The generated bubbles moved away from the closest flow channel end and then condensed, disappearing around the midpoint of the flow channel. They demonstrated that the periodic growth and collapse of bubbles in the microchannel had a net pumping effect.

Matsumoto et al. [3] made use of the dependency of fluid viscosity on temperature to generate flow in a microchannel. The volume of the midpoint of the flow channel was cyclically expanded and contracted by a piezoactuator. Heaters were placed at the entrance and the exit positions of the flow channel. When the volume of the midpoint of the flow channel was shrunk, the entrance heater was not heated and the exit heater was heated. Thus, the fluid viscosity at the entrance was high and that at the exit was low. As a result, a flow to the exit was formed. Then, when the volume of the midpoint of the flow channel was expanded, the entrance heater was heated and the exit heater was not heated. The fluid viscosity at the entrance was lower than that at the exit. As a result, a flow from the entrance was induced. By iterating these procedures, a net flow from the entrance to the exit was created.

Yang [4] proposed a method of moving fluid by using a bubble that expanded and condensed synchronously with heating and unheating. A bubble expanding and condensing room had an expanding diffuser at one end and a contracting diffuser at the other end. By utilizing the difference of the flow resistance between the expanding and the contracting diffusers, one-directional flow was developed.

Okuyama et al. [5] introduced nucleate boiling into the microchannel and confirmed that a pumping head was created. When the wettablility of liquid is high, boiling that starts at one location

Contributed by the Heat Transfer Division of ASME for publication in the JOURNAL OF HEAT TRANSFER. Manuscript received August 7, 2006; final manuscript received May 12, 2007; published online February 15, 2008. Review conducted by Satish G. Kandlikar. Paper presented at the Fourth International Conference on Nanochannels, Microchannels and Minichannels (ICNMM2006), Limerick, Ireland, June 19–21, 2006.

  

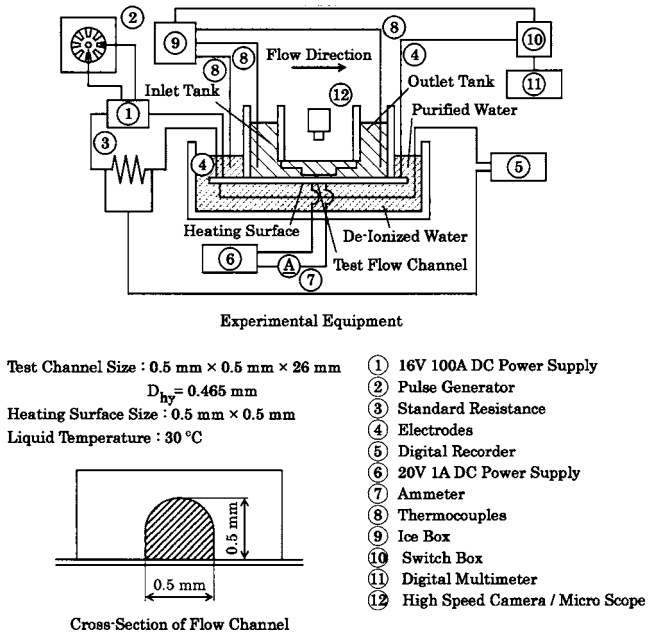


**Fig. 1 Experimental apparatus**

spreads propagatively. By inducing this propagative boiling in a flow channel, they succeeded in moving fluid in one direction.

Koizumi et al. [6] created a circulation flow in a microflow circuit by forming a back-and-forth flow at a *T* junction that was connected to the flow circuit. They created the back-and-forth flow by inducing bubble nucleation and condensation in a solid tank.

A pumping system that makes use of boiling does not have any mechanical moving parts. Thus, the system is quite simple and reliable. These are important criteria for micromechanical systems.

Until the boiling bubble pump is realized, a number of phenomena must be investigated, including boiling phenomena in the microchannel, fluid flow, heating, and cooling. As one of these tasks, the micropumping system using boiling bubbles has been reported [7], in which a single bubble was formed and condensed periodically in a microchannel to move liquid unidirectionally. In the present paper, additional experimental data and analytical results are presented, focusing on the bubbling phenomena and the flow characteristics.

## Experimental Apparatus and Procedures

The experimental apparatus used in the present study is shown schematically in Fig. 1. The apparatus is composed of a test microflow channel that is oriented horizontally, reservoirs at both ends of the test channel, an electric power supply system, and instruments. Distilled water is used as the test fluid in experiments. The test channel and the reservoirs are initially filled with water. Two reservoirs are connected by a pipe in order to eliminate any pressure difference between the two reservoirs. The entire system of a test apparatus is immersed in a distilled water bath. The temperature of water in the bath is controlled at a constant temperature of 30°C during the experiments.

A 26-mm-long groove was formed on a transparent Plexiglas plate. The groove was created as follows. A Plexiglas plate was cut slightly longer than 26 mm. A 0.5 mm diameter nichrome wire was sandwiched between the Plexiglas plate and a glass plate. The nichrome wire was then heated by electricity. The surface of the Plexiglas was melted by the heated nichrome wire. As a result, a groove was created on the Plexiglas plate surface. The crosssection of the groove is presented in Fig. 1. The surface of the plate was polished flatly to eliminate the swollen part of the groove edges because of melting. The length of the plate was also adjusted to 26 mm by polishing both ends. The exact cross-sectional area was determined by taking a close-up photograph and measuring the size of the groove on the photograph.

A Plexiglas plate that had a 26-mm-long groove was placed on a printed circuit board such that the grooved surface was facing downward. A 0.5 mm diameter semi-half-circle cross-section flow channel was formed between the Plexiglas plate and the printed circuit board. This flow channel was the test microchannel, the length of which was 26 mm. Both ends of the flow channel were abruptly opened to the reservoirs, and the reservoirs were open to the atmosphere. The part of the copper surface of the printed circuit board that faced the test flow channel was etched, except for a width of 0.5 mm at a distance of 8.5 mm from one end (herein referred to as the left end or the inlet), and at a distance of 17 mm from the other end (referred to as the right end or the outlet), and a width of 1 mm at a distance of 22 mm from the left end. The 0.5 mm unetched copper part and the 1 mm unetched copper part were electrically isolated. In the present paper, the 0.5 mm unetched copper part is referred to as the test heating surface, and the 1 mm unetched copper part is referred to as the fluid temperature measuring section. The thickness of the printed copper layer was 35 $\mu$m. The electric resistance of each unetched copper part in the test flow channel was calibrated prior to the experiment in order to obtain the relationship between electric resistance and temperature.

Electrodes were soldered to the copper surface. A low-voltage dc was supplied for the test heating surface via the electrodes. The electric power that was supplied for the test heating surface was derived from the supplied dc and the voltage across the test heating surface. The temperature of the test heating surface was determined by referring to the relationship between the temperature and the electric resistance of the copper on the board.

Other electrodes were also soldered onto a copper surface that was isolated from the heating part in order to measure fluid temperature. A dc of 0.5 A was supplied for the fluid temperature measurement section via these electrodes. The electric resistance of the fluid temperature measurement section was obtained from the voltage between the electrodes and the supplied dc. The temperature of the copper at the fluid temperature measurement section was then derived by referring to the calibrated relationship between temperature and electric resistance. In the present experiments, it was assumed that the obtained temperature was the temperature of the fluid in the test microchannel. Chromel-alumel thermocouples were used to measure the fluid temperature in the reservoirs and the water bath. A flow state in the test flow channel was observed from the top through the Plexiglas wall and was recorded using a charge-coupled device (CCD) and a high-speed video camera equipped with a microscopic lens.

In the experiments, the test heating surface was heated periodically by supplying a dc in rectangular waves, as shown in Fig. 2. The test conditions of the frequency of the rectangular waves, i.e., the heating and the nonheating period in 1 cycle, are tabulated in Table 1 together with other parameters.

The heating rate, i.e., the rectangular wave height of the dc that was supplied for the test heat transfer surface, was increased stepwise. Boiling started at a certain heating rate. By synchronization with the rectangular waves of heating and nonheating, the bubble formation and condensation continued iteratively, as shown in Fig. 2. The heating rate was further increased stepwise until the specified value was reached. The flow state was then recorded on the video recorder. Blue or red ink was mixed instantaneously into the left (inlet) tank, and the time interval between the ink mixing and ink flowing out to the right (outlet) tank was then measured. The average flow velocity in the microflow channel during that period was determined from this time interval and the channel length.

The dc and the voltage that was supplied for the test heating surface were stored in a digital recorder. The dc and the voltage for fluid temperature measurement in the flow path and thermo-

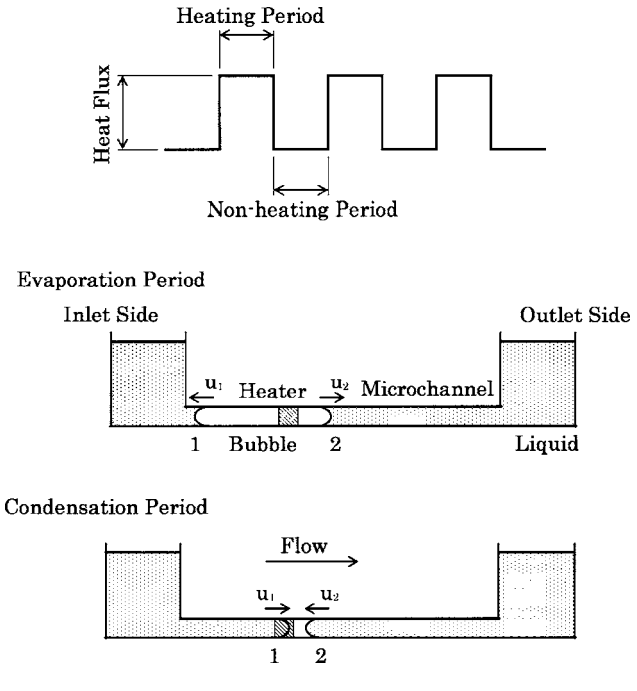


**Fig. 2 Test procedure**

couple outputs were measured with a digital multimeter. The instruments, including the CCD and the high-speed video camera, were conventional and reliable. The uncertainties were thus small.

## Experimental Results

Excess heating resulted in burnout of the test heating surface. Thus, the test condition was limited by the burnout.

When bubbling occurred and ink was mixed in the right reservoir, the ink never flowed out to the left reservoir. Only when ink was mixed in the left reservoir did the ink flow into the other (right) reservoir. The flow direction in the present experiments was always from left to right, as shown in Fig. 2.

The flowout of the ink to the other (right) reservoir was also confirmed not to be the result of diffusion. When the heating patch was not heated and the state in the flow channel and both reservoirs was stagnant, ink was mixed in the left reservoir. The ink never flowed out to the right reservoir, even after 1 h.

The photograph in Fig. 3 depicts the state in which blue ink that was mixed in the left (inlet) tank has just started to flow into the right (outlet) tank.

The average flow velocities measured in the present experiments are plotted with respect to the heat flux in Fig. 4. The test conditions in the figure are heating at 5 Hz (0.1 s heating followed by 0.1 s nonheating) and a water bath temperature of 30°C. The double circle symbols indicate the standard cases of a channel length of 26 mm and a heating patch offset of 4.0 mm. The solid circle symbols indicate an offset of 8.0 mm. The open circle symbols indicate a channel length of 50 mm. Although the data plots are scattered slightly, the flow velocity increases with the increase

**Table 1 Experimental conditions**

| Experimental parameter | Condition |
|---|---|
| Heat flux | 1.1–3.5 MW/m$^2$ |
| Nonheating period | 0.1–0.5 s |
| Heating frequency | 1.67–5 Hz |
| Heating period | 0.1–0.35 s |
| Heating surface offset | 4 mm, 8 mm |
| Channel length | 26 mm, 50 mm |

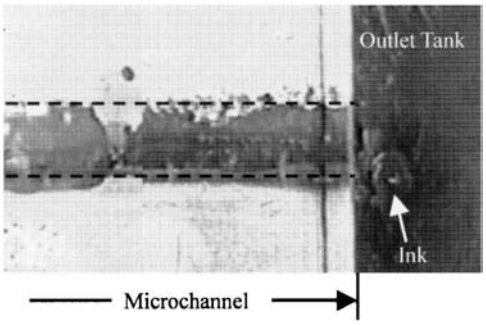


**Fig. 3 Flowout from the microchannel**

in the heat flux during the heating period. The flow velocities of the 4.0 mm offset cases are larger than those of the 8.0 mm offset cases. The velocity depends upon the heating-spot offset length, which implies that the offset length appears to have an optimum value. The offset ratios of the offset length to the flow path length are the same for the 26 mm channel length/ 8 mm offset case and the 50 mm channel length/15.4 mm offset case. The differences in flow velocities for these cases are slight. The flow velocity does not appear to be affected by the flow path length. A decrease in the heating cycle resulted in a decrease in the flow velocity, although this is not indicted in the figure.

A bubble grew during the heating period, and when the nonheating period was initiated, the bubble began to shrink and eventually disappeared due to condensation. The relationship between the heat flux and the maximum bubble length is shown in Fig. 5. The test conditions for the case in the figure were the same as those in Fig. 4. The maximum bubble length that is presented in the figure is the average value of ten successive bubbles. The maximum bubble length appears to become longer with an in-

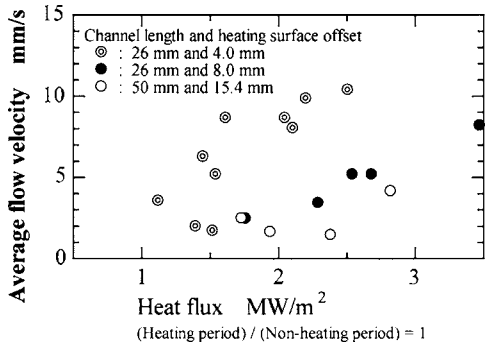


**Fig. 4 Relationship between average flow velocity and heat flux**

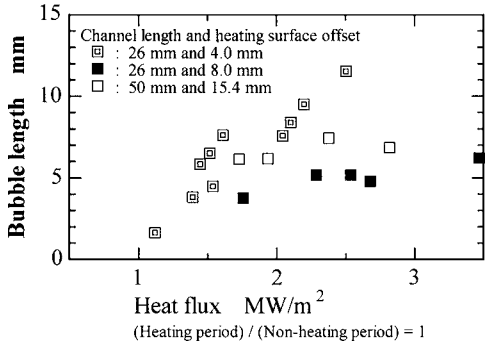


**Fig. 5 Relationship between maximum bubble length and heat flux**

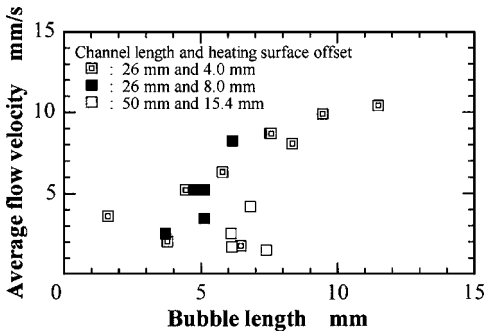


**Fig. 6 Relationship between average flow velocity and bubble length**

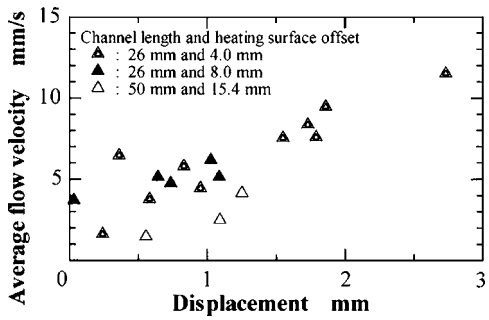


**Fig. 8 Relationship between average flow velocity and bubble disappearing point displacement**

crease in the heat flux. When the heat flux is lower than $\sim 2\ \mathrm{MW/m^2}$, the differences in the bubble length are slight among the three cases of 26 mm channel length/4.0 mm offset, 26 mm channel length/8.0 mm offset, and 50 mm channel length/15.4 mm offset. However, in the high heat flux region, the bubble length is the longest for the 26 mm channel length/4.0 mm offset case, followed by the 26 mm channel length/8.0 mm offset case, and the 50 mm channel length/15.4 mm offset case in that order. As shown in Fig. 4, the flow velocity depends on the channel length/offset quantity condition. Thus, the fluid temperature in the flow path might depend on the flow rate and differ among three cases. However, the differences in the measured temperature of fluid in the flow path were slight among the three cases, a few °C at the most, and were close to the water bath temperature of 30 °C. The magnitude of this temperature difference cannot explain the bubble length difference, and the reason for this difference remains unclear.

The relationship between the bubble length and the average flow velocity is shown in Fig. 6. The test conditions are the same as those in Figs. 4 and 5. Although the data plots are scattered slightly, a general trend is observed in that the flow velocity becomes fast as the bubble length becomes long. A group of the 50 mm channel length/15.4 mm offset case plots deviates slightly from the other data plots, as will be described later herein.

Figure 7 shows the relationship between the heat flux and the shift length (displacement) from the center of the heating spot to the final bubble disappearance point. The final bubble disappearance point was always in the right side (outlet side) from the heating surface. The test conditions are the same as those in Figs. 4 and 5. Although the data plots of the 50 mm channel length/15.4 mm offset case show a somewhat unusual trend, the shift length clearly increases with an increase in the heat flux. The displacements in the 26 mm channel length/4 mm offset case are larger than those in the other cases.

The average flow velocities are plotted with respect to the displacements in Fig. 8. The test conditions are the same as those in Figs. 4–6. The flow velocity increases with an increase in the heat flux. All of the data plots appear to remain in a band relating the displacement and the average flow velocity, irrespective of the test conditions. When the results of the 50 mm channel length/15.4 mm offset case are plotted in Fig. 8, the unusual trend observed in Fig. 6 seems to disappear.

Figures 4–8 indicate that as the heating rate is increased, the bubble length becomes longer, the displacement becomes larger, and the flow velocity becomes faster.

From this shift length (displacement), the water volume that is carried toward the right during one heating-condensing cycle can be calculated. The time-averaged volume flow rate can be obtained from this volume. In Fig. 9, the calculated volume flow rates are compared with the volume flow rates that were derived from the average velocities measured by mixing ink in the left reservoir. Since the data of all test conditions are presented in the figure, only test parameter ranges are presented, so as to avoid complexity. The agreement between these data is good.

The velocities of the bubble interface are presented in Fig. 10. The test conditions of the case were as follows: 26 mm channel length/4 mm offset, heat flux $2.12\ \mathrm{MW/m^2}$, and heating frequency 5 Hz (0.1 s heating and 0.1 s nonheating). The bubble interface position was derived from pictures that were captured using a high-speed video camera at a frame rate of 500 frames/s. The interface velocity was calculated from the interface traveling distance between frames and the time interval (0.002 s) between the frames. Thus, the plots in Fig. 10 are at intervals of 0.002 s. In

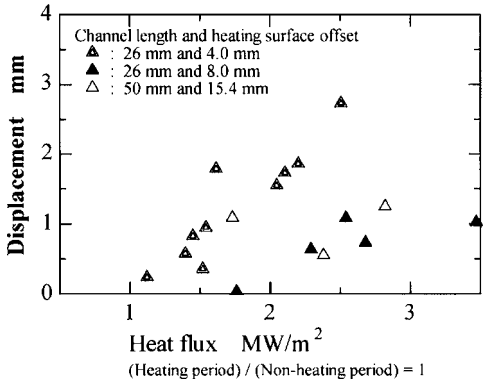


**Fig. 7 Relationship between bubble disappearing point displacement and heat flux**

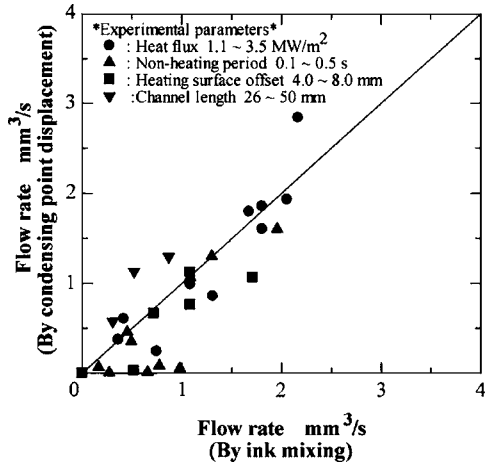


**Fig. 9 Flow rate in the microchannel**

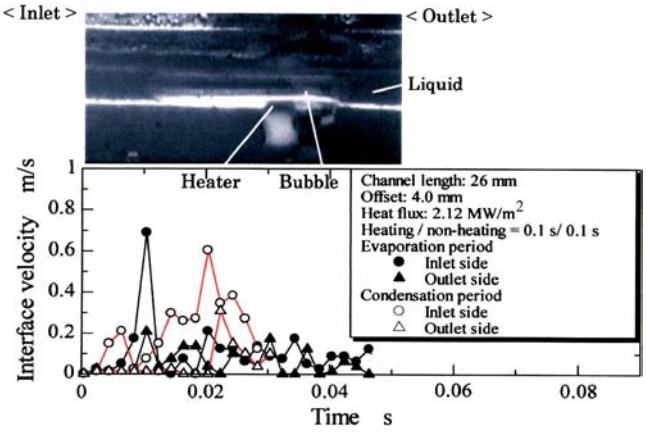


**Fig. 10 Bubble interface velocity**

the evaporation mode, time=0 indicates the frame time just before the frame that the bubble interface was captured first. The final plots correspond to the cessation of expansion. In the condensation mode, time=0 indicates the initiation of condensation. The final plots correspond to the disappearance of the bubble.

In Fig. 10, the evaporating period and the condensing period are shorter than durations of the heating and the nonheating of 0.1 s, respectively. In order to initiate boiling, a certain amount of dead time is required in order to heat up the fluid to superheat temperature. Thus, the evaporating period became shorter than the heating duration. In the condensing period, the condensation was so quick that the bubble disappeared before the nonheating period ceased.

First, we note that the condensing period is considerably shorter than the evaporating period in Fig. 10. During the boiling period, the velocity of the inlet side is slightly faster than that of the outlet side, and the difference is not so large. During the condensing period, the velocity of the inlet side is much faster than that of the outlet side. Another item of note is that the velocity of the inlet side during the condensing period is faster than that during the boiling period. The difference of the outlet side velocities between the boiling period and the condensing period is small.

The maximum time-averaged flow velocity and the maximum flow rate that were obtained in the present experiments were 10.4 mm/s and 2.16 $mm^3/s$, respectively, under the following conditions: 26 mm channel length/4 mm offset, heat flux 2.52 $MW/m^2$, and heating frequency 5 Hz (0.1 s heating and 0.1 s nonheating).

## Analysis

Experimental observation proves that the velocity of an interface during a condensing period is faster than that during an evaporating period. It is also shown that the velocity of the inlet side is faster than that of the outlet side during the condensing period. It appears that the longer the bubble grows, the faster the flow velocity is. These relationships are thought to be related to the flow formation in the test microchannel.

The boiling speed is not so fast that the bubble interfaces of the inlet and outlet sides are able to move toward the inlet and the outlet sides, respectively, depending on the flow resistance on the flow path wall. The condensing speed is so fast that the movement of the water plug in the flow path may be affected by inertia. The lower mass inertia in the inlet side may result in faster movement than that of the outlet side. The horizontal cross section of the reservoir at both ends of the test flow channel is $25\times45$ $mm^2$. The water level height in the reservoir was approximately 40 mm in the experiments. Thus, the fluid volume in the reservoir was approximately 45,000 $mm^3$. This volume is so large compared with the flow rate in the test flow channel (2.16 $mm^3/s$ at most) that the movement of fluid in the reservoir can be neglected.

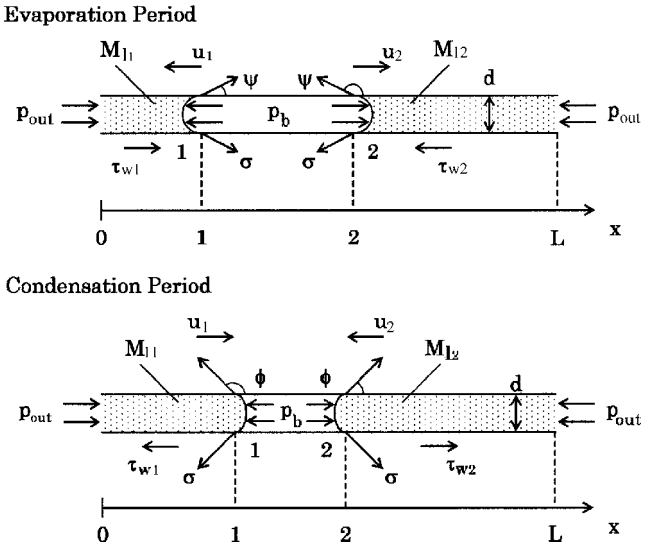


**Fig. 11 Analytical model**

When the motion of the fluid in the flow channel is examined, it is sufficient to consider only the inertia in the flow channel. As discussed in Fig. 5, the bubble expands more to the left side than to the right side. This situation is depicted in Fig. 2. Therefore, the water plug inertia in the left side of the flow path may be said to be smaller than that in the right side.

**Analytical Model.** The flow states in the test microchannel during the boiling and condensation period of a bubble are illustrated in Fig. 11. The water mass that is vaporized at the heat transfer patch during the heating period of 1 cycle of evaporation and the condensation is negligible compared with the total mass in the flow channel. Thus, the equation of motion of liquid in the test flow channel is expressed following Newton's law for the inlet and the outlet sides, as follows:

$$\frac{d(M_l u)}{dt} = \tau_w \pi D_{\text{hy}} \left( \pm \int_0^t u dt + x_0 \right) + \left\{ p_{\text{out}} - p_b + \varsigma \frac{\rho u^2}{2} \right\} A + \pi D_{\text{hy}} \sigma \cos\theta \quad (1)$$

where $x_0$ is the initial position, + for the inlet side, − for the outlet side, $D_{\text{hy}}$ is the hydraulic diameter, $L$ is the length of the flow channel, $M_l$ is the liquid mass, $p_b$ is the pressure in the bubble, $p_{\text{out}}$ is the pressure in the reservoirs, $u$ is the velocity of the interface between the bubble and the liquid (i.e., the velocity of the liquid in the flow channel), $t$ is the duration time from the initiation of movement, and $x$ is the distance from the left end of the flow channel. The symbol $\rho$ is the density, $\varsigma$ is the form loss coefficient at the end of the flow channel, $\sigma$ is the surface tension, $\tau_w$ is the wall shear stress, and $\theta$ is the contact angle. Subscripts 1 and 2 indicate the inlet and the outlet sides, respectively, in Fig. 11.

In Eq. (1), the left-hand side expresses the inertia term. The first term on the right-hand side is the wall friction term, the second term is the pressure term, and the third term is the surface tension term between the water plug and the bubble. Here, it is assumed that the wall at the bubble is dry. As shown in Fig. 10, the movement of the interface was intermittent. This may be realized as follows. In the evaporation mode, when the contact angle at the wall between the water plug and the bubble decreased to below the receding contact angle, the interface is caused to move. The pressure in the bubble is then released, and the contact angle becomes larger than the receding contact angle. The movement of the interface becomes slow or stops, and the pressure in the bubble is again elevated. The contact angle then decreases below

the receding contact angle, and the same cycle is iterated. The process in the condensing period is similar to that in the evaporating period. If the wall at the bubble is wet, i.e., the bubble is covered with a thin liquid film, the interface movement might be smoother.

When the interface position from the left end of the flow path is $x$, the interface velocity of the inlet side is

$$u_1 = \frac{dx_1}{dt} \tag{2}$$

and the interface velocity of the outlet side is

$$u_2 = \frac{dx_2}{dt} \tag{3}$$

where subscripts 1 and 2 indicate the inlet and the outlet sides, respectively.

The mass of the water plug in the inlet side is expressed as

$$M_{l1} = \frac{\pi}{4} D_{\mathrm{hy}}^2 x_1 \tag{4}$$

and the mass of the water plug in the outlet side is given as

$$M_{l2} = \frac{\pi}{4} D_{\mathrm{hy}}^2 (L - x_2) \tag{5}$$

Although it is not certain that the relationship between the frictional loss coefficient $\lambda$ and the flow velocity for a conventional size pipe can be applied to a microsize pipe, such as the test flow channel in the present experiment, it has been suggested by Ohtaki et al. [8] that the relation for the conventional size can be applicable down to a diameter of 0.12 mm. In the present experimental range, the Reynolds number for the average velocity in the test flow path was in the range of from 1 to 12. Thus, the wall shear stress was estimated using the conventional relation of the pipe friction factor for a laminar flow

$$\lambda = 64/\mathrm{Re} \tag{6}$$

where Re is the Reynolds number.

Ohtaki et al. [8] also reported results for the form loss coefficients of contraction and expansion. It has been suggested that the form loss coefficients depend upon the Reynolds number. However, no decisive results have been reported. Thus, the traditional values were used in the present analyses:

$$\varsigma = 0.5 \quad \text{for inflow into the test flow channel (contraction)} \tag{7}$$

$$\varsigma = 1.0 \quad \text{for outflow from the test flow channel (expansion)} \tag{8}$$

For the contact angle $\theta$, the receding contact angle $\psi$ and the advancing contact angle $\varphi$ of water [9]

$$\psi = 30^\circ \tag{9}$$

$$\varphi = 120^\circ \tag{10}$$

were used for the boiling and the condensation period, respectively, in the calculation.

The pressure $p_b$ in the bubble was calculated using the equation of state:

$$p_b V_b = M_b R T \tag{11}$$

where $M_b$ is the vapor mass in the bubble, $R$ is the gas constant of vapor, $T$ is the temperature, and $V_b$ is the volume of the bubble.

In the evaporation mode, the mass in the bubble can be expressed as

$$M_b = \frac{q_e S t}{h_{fg} + c_l \Delta T} \tag{12}$$

where $c_l$ is the specific heat of water, $h_{fg}$ is the latent heat of water, $q_e$ is the surface heat flux of the heating patch, $S$ is the surface area of the heating patch, and $t$ is the duration time from the initiation of boiling. The subcooling of water in the flow path is $\Delta T$. In Eq. (12), for simplicity, the dead time required to superheat water before the initiation of boiling is neglected. The subcooling was assumed to be constant at 70°C. As mentioned in Fig. 4, the temperature of water in the flow path was approximately 30°C during the experiment.

The volume $V$ of the bubble is related to the interface movement to the left side and to the right side as

$$V_b = \left( \int_0^t u_2 dt - \int_0^t u_1 dt \right) A \tag{13}$$

Thus, combining Eqs. (11)–(13), the pressure in the bubble during the boiling period is expressed as follows:

$$p_b = \frac{q_e S t R T}{(h_{fg} + c_l \Delta T) \left( \int_0^t u_2 dt - \int_0^t u_1 dt \right) A} \tag{14}$$

Similarly, in the condensation mode, the mass in the bubble is

$$M_b = M_{b0} - \frac{2 q_{cb} A t + \int_0^t \pi D_{\mathrm{hy}} q_{\mathrm{cw}} (x_2 - x_1) dt}{h_{fg}} \tag{15}$$

where $M_{b0}$ is the bubble mass at the initiation of condensation, $q_{cb}$ is the condensation heat flux at the interface between the water plug and the bubble, $q_{\mathrm{cw}}$ is the condensation heat flux at the flow channel wall, and $t$ is the duration time from the initiation of the condensation. It is difficult to determine the condensation heat fluxes $q_{cb}$ and $q_{\mathrm{cw}}$. Thus, in order to avoid complexity, Eq. (15) is simplified to

$$M_b = M_{b0} - \frac{q_{cr} S t}{h_{fg}} \tag{16}$$

In Eq. (16), $q_{cr}$ is the equivalent condensation heat flux that is converted based on the heating patch surface area.

The volume $V$ of the bubble is expressed as follows:

$$V_b = V_0 - \left( \int_0^t u_2 dt - \int_0^t u_1 dt \right) A \tag{17}$$

where $V_0$ is the bubble volume at the initiation of condensation.

Finally, the pressure in the bubble during the condensing period is expressed using Eqs. (11), (15), and (17), as follows:

$$p_b = \left( M_{b0} - \frac{q_{cr} S t}{h_{fg}} \right) \left[ \frac{R T}{V_0 - \left( \int_0^t u_1 dt - \int_0^t u_2 dt \right) A} \right] \tag{18}$$

By solving Eq. (1) with Eqs. (2)–(10) and (14) for the inlet side and the outlet side simultaneously, the bubble interface velocities $u_1$ and $u_2$ and the positions $x_1$ and $x_2$, at the inlet and the outlet sides during the evaporating period can be calculated. In addition, by solving Eq. (1) with Eqs. (2)–(10) and (18), for the inlet side and for the outlet side simultaneously, the bubble interface velocities $u_1$ and $u_2$ and the positions $x_1$ and $x_2$ at the inlet and outlet sides during the condensing period can be calculated.

In the calculation, bubble formation was initiated at $t=0$ and at the center of the heating patch. The evaporation duration time was adopted from the experimental result. After the calculation for the evaporation was completed, the calculation for the condensation was performed. The initial positions of the bubble interface in the

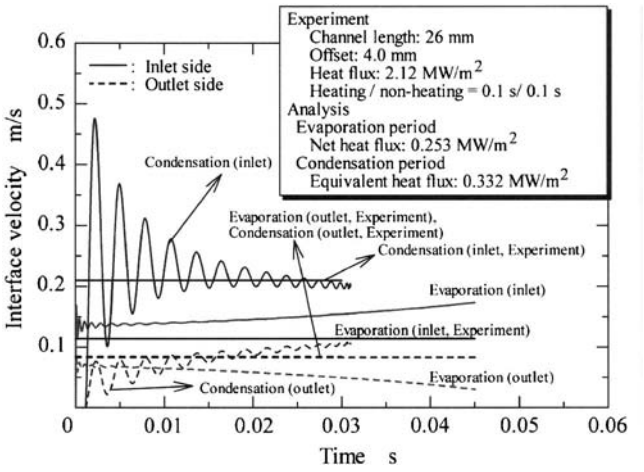


**Fig. 12 Predicted interface velocity**

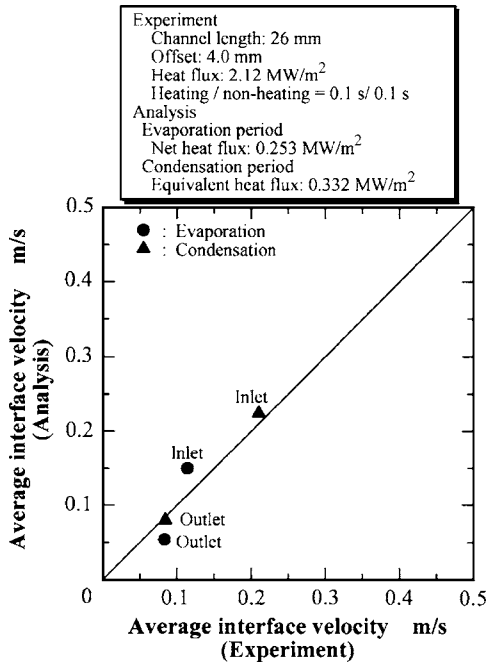


**Fig. 13 Comparison of predicted and measured interface velocities**

inlet and outlet sides for the condensation process were the final positions of the bubble in the evaporation process calculation. The Runge–Kutta–Gill method was used to solve Eq. (1) numerically.

**Comparison of Predicted and Experimental Results.** In solving Eq. (1), consideration of heat loss is critical. Heat loss is not included in Eq. (1). The test flow channel was immersed in a water bath of temperature 30°C in the experiments. The measured temperature of fluid in the flow path was approximately 30°C in all experiments. This indicated that there was considerable heat loss to the water bath. The proposed system includes the evaporation and condensation process. The condensation is caused by heat removal. The heat removal is caused by heat loss. The heat loss is considered to be necessary in the proposed pumping system.

In order to determine the net heat input during the evaporating period and net condensation heat flux during the condensing period, Eq. (1) was solved parametrically by changing $q_e$ in Eq. (14) and $q_{cr}$ in Eq. (18). The conditions under which the calculations were performed are as follows: channel length, 26 mm; heating patch offset, 4.0 mm; heating frequency, 5 Hz (0.1 s of heating followed by 0.1 s of nonheating); and water bath temperature, 30°C. The nominal heat flux during the evaporating period was 2.10 MW/m$^2$. When the measured net bubble growing time was given and the heat flux during the evaporating period was set at 0.253 MW/m$^2$, the calculated bubble length was very close to the measured length. Then, for the calculation of the following condensing period, when the calculated bubble length (equal to the measured maximum bubble length) was given at the condensation initiation and the equivalent condensation heat flux that was reduced based on the heating patch area was set at 0.332 MW/m$^2$, the measured net bubble shrinking time was very similar to the measured time. The net heat input during the evaporation and the net heat removal during the condensation in the calculations were 0.00285 J and 0.00257 J, respectively. These values were quite similar.

The calculated interface velocities are presented in Fig. 12. In the figure, the measured average velocities are also included for comparison. In the evaporating period, time=0 is the calculation starting time and the bubble appearance time in the experiment. The end of the evaporating period is the ceasing of the calculation and the end of the bubble growth in the experiment. In the condensing period, time=0 is the initiation of bubble shrinking. The end of the condensation is the bubble disappearance in both the calculation and the experiment.

In Fig. 12, all velocities are expressed as positive values. The predicted velocities are oscillatory. The measured velocities were also oscillatory, as shown in Fig. 10. From these predicted results, the average velocities during the evaporation and the condensing period can be obtained.

These average velocities are compared with the measured results in Fig. 13. The predicted average velocities agree well with the measured average velocities. During the evaporating period, the interface velocity at the inlet side is slightly faster than that at the outlet side in both the calculation and the experiments. During the condensing period, the interface velocity at the inlet side is considerably faster than that at the outlet side in both the calculation and the experiments. The interface velocity difference during the condensing period is mainly attributed to the inertia difference between the inlet (shorter) side and the outlet (longer) side. The analysis proves that the interface velocity difference between the inlet side and the outlet side during the condensing period created a pump effect.

In the calculation, a single value was given for the contact angle; the receding contact angle of 30 deg during the boiling period and the advancing contact angle of 120 deg during the condensing period. In reality, during the boiling period, for example, when the pressure in the bubble increased and the contact angle reached the receding contact angle, bubble-liquid interface movement was initiated. Once the interface moved, the excess pressure was relieved and the contact angle recovered to become larger than the receding contact angle. Thus, the interface ceased to move. Then, the pressure in the bubble recovered again and the above-described process was iterated, as shown in Fig. 10. If this contact angle variation is allowed in the calculation, more realistic results may be obtained. Further examination is required.

The final consideration is the pump efficiency. When it is assumed that the fluid flows at the measured average velocity and the flow path is filled with water during the entire time, the work done by the fluid is calculated as the sum of the work of the wall friction, the inlet and outlet form loss, and the surface tension. The pump efficiency was calculated as the ratio of the fluid work to the net heat input to the flow channel. The value was on the order of $10^{-5}$, which is quite low. Most of the heat that was supplied to the heating surface dissipated into the surroundings, i.e., the water bath. This might be the reason why the pump efficiency was quite low.

## Conclusions

By making use of boiling and condensation in a microchannel, a micropump was developed. The length and the hydraulic diameter of the semi-half-circle cross-section microchannel were 26 mm and 0.465 mm, respectively. The flow channel was filled with distilled water. A channel wall was heated locally over a length of 0.5 mm at a distance of 8.5 mm from one end and a distance of 17 mm from the other end. Heating was periodic. The following conclusions were obtained:

(1) As the heating rate was increased, one large bubble was formed synchronously with the heating of the patch. The bubble then condensed and disappeared during the next nonheating period. While this bubble formation and condensation were continued periodically, the flow from the short side (8.5 mm side) to the long side was maintained. The flow rate increased as the heating rate was increased. The maximum average flow velocity and the maximum flow rate that was obtained in the present experiments were 10.4 mm/s and 2.16 $mm^3/s$, respectively.
(2) The velocity of the interface between the bubble and the liquid during the condensing period was much faster than that during the boiling period. During the condensing period, the velocity of the interface at the short side (8.5 mm side) was faster than that at the long side (17 mm side). The flow occurrence in the flow channel was attributed to these velocity differences.
(3) The equation of motion of the liquid in the flow channel was solved to calculate the travel of liquid in the flow channel. The predicted liquid velocities of the short side and the long side during the boiling and the condensing period agreed well with the experimental results. The velocity difference between the short side and the long side, and also between the boiling period and the condensing period, were expressed well by the calculation. The pumping mechanism could be explained in the following manner. The liquid in the inlet side (short side) moves faster than that in the outlet side (long side) during the condensing period because the inertia in the short side is lower than that in the long side. Since the condensation was much faster than the boiling, this effect was more prominent during the condensing period. This faster movement of the short side liquid, compared to long side liquid, resulted in the formation of a net flow from the short side to the long side.

## Acknowledgment

The authors would like to thank Mr. N. Shimoju, a graduate student of Kogakuin University, for conducting the experiments and performing the calculations.

## Nomenclature

$A$ = cross-sectional area of microchannel ($m^2$)
$c$ = specific heat (J/kg K)
$D_{hy}$ = hydraulic diameter (m)
$h_{fg}$ = latent heat (J/kg K)
$L$ = length of microchannel (m)
$M$ = mass (kg)
$p$ = pressure (Pa)
$R$ = gas constant (J/kg K)
Re = Reynolds number=$uD_{hy}/\nu$
$q$ = heat flux ($W/m^2$)
$S$ = heating patch surface area ($m^2$)
$T$ = temperature (K)
$t$ = time (s)
$u$ = velocity of the interface of bubble (m/s)
$V$ = volume ($m^3$)
$x$ = axial position in the flow channel (m)

### Greek Symbols

$\Delta T$ = liquid subcooling (K)
$\zeta$ = form loss coefficient
$\theta$ = contact angle (deg)
$\lambda$ = pipe friction factor
$\nu$ = kinematic viscosity ($m^2/s$)
$\rho$ = density of liquid ($kg/m^3$)
$\sigma$ = surface tension (N/m)
$\tau_w$ = wall shear stress (Pa)
$\varphi$ = advancing contact angle (deg)
$\psi$ = receding contact angle (deg)

### Subscripts

0 = initial state
1 = inlet side of microchannel
2 = outlet side of microchannel
$b$ = bubble
$c$ = condensation
$e$ = evaporation
$l$ = liquid
out = reservoir
$r$ = reduced value to heating patch surface area
$w$ = wall

## References

[1] Jun, T. K., and Kim, C. J., 1998, "Valveless Pumping Using Traversing Vapor Bubble in Microchannels," J. Appl. Phys., **83**(11), pp. 5658–5664.
[2] Prosperetti, A., Yuan, H., and Yin, Z., 2001, "A Bubble-Based Micropump," *Proceedings of FEDSM'01*, pp. 889–894.
[3] Matsumoto, S., Klein, A., Schroth, A., and Maeda, R., 1997, "Micropump Based on Temperature Dependence of Liquid Viscosity," *Proceedings of SPIE, Smart Electronics and MEMS*, Vol. 3242, pp. 364–371.
[4] Yang, W. J., 2001, "Personal Viewpoint of Heat Transfer," Therm. Sci. Eng., **9**(4), pp. 3–8.
[5] Okuyama, K., Irikura, A., Takehara, R., Kin, S., and Iida, Y., 2001, "Micropump Using Boiling Propagation Phenomena," *Proceedings of 2001 JSME Annual Conference*, Vol. 5, pp. 193–194.
[6] Koizumi, Y., Ohtake, H., and Tabuchi, N., 2004, "Flow Formation in Micro-Size Fluid Flow Circuit," *Proceedings of ASME IMECE2004, Microelectromechanical Systems*, CD-ROM, Paper No. IMECE2004-59782.
[7] Koizumi, Y., Ohtake, H., and Shimojyu, N., 2003, "Study on Micro-Pump Using Bubbling in Micro-Channel," *Proceedings of the International Symposium on Micro-Mechanical Engineering 2003*, JSME Thermal Engineering Division, pp. 177–182.
[8] Ohtaki, H., Ohtake, H., and Koizumi, Y., 2006, "Frictional Pressure Drops of Gas-Liquid Two-Phase Flow in Minichannels," *Proceedings of Second International Symposium on Micro and Nano Technology*, pp. 121—124.
[9] Koizumi, Y., Ohtake, H., and Ueda, T., 1999, "A Study on the Minimum Wetting Rate of Isothermal Films Flowing Down on Outer Surface of Vertical Pipes," *Proceedings of Fifth ASME/JSME Joint Thermal Engineering Conference*, CD-ROM, Paper No. AJTE99-6426.

# Effective Thermal Diffusivity of Porous Media in the Wall Vicinity

**H. Sakamoto**
Mem. ASME
e-mail: sakamoto@ce.jp.nec.com

**F. A. Kulacki**
Fellow ASME
e-mail: kulacki@me.umn.edu

Thermodynamics and Heat Transfer Laboratory,
Department of Mechanical Engineering,
University of Minnesota,
Minneapolis, MN 55455

*Transient heat transfer from an impulsively heated vertical constant heat flux plate embedded in a stationary saturated porous medium is studied experimentally and analytically to determine near-wall thermal diffusivity. The effective diffusivity is shown to depend on the properties of the constituent materials and the near-wall particle morphology. For porous media comprising randomly stacked spheres, the near-wall region is characterized by fewer particle contacts with the wall than in the bulk medium, and this difference is the source of larger thermal diffusivity in the context of volume-averaged values, which apply to the bulk property far from the wall. For combinations of different spherical solids and interstitial fluids, which give a range of fluid:solid conductivity ratio from 0.5 to 2400, early-time transient temperature profiles can be predicted using the thermal conductivity of the interstitial fluid. A conjugate heat transfer analysis accurately predicts the time the conductive front takes to travel through the impermeable wall and quantifies the effect of conduction along the wall on the local and overall Nusselt numbers. The present results raise the possibility of reinterpretation of much of the porous media heat transfer experiments in the literature.* [DOI: 10.1115/1.2787022]

*Keywords: thermal diffusivity, porous medium, natural convection*

## Introduction

Thermal conductivity defined by Fourier's law is sometimes expanded to include convective effects. In such cases, the *effective* thermal conductivity is used as a predictor of the combined effects of conduction and convection without regard to the extent of each mode of heat transfer. While this approach is convenient, the artificial property is so specific to the set of conditions under which a value is obtained that it is only valid for, say, a narrow range of temperature and a given geometry of either the heat transfer domain or surface.

It was perhaps after Fourier and Biot that conductive and convective heat transfers recognized as separate modes of heat transfer [1]. When Newton developed his law of cooling, he probably did not realize that conduction within a solid body has an impact on the overall heat transfer. It took Fourier a letter from Biot to distinguish between the two modes and to begin to approach conduction as a boundary-value problem for which he became famous [2]. The inclusion of convective effects in the effective thermal conductivity is the usual practice in heat transfer in a saturated porous medium despite the critical role that the relative magnitudes of the two modes have on the overall heat transfer rate. The two modes of heat transfer influence each other at the most fundamental level by imposing temperature fields in the solid and fluid phases and by a complex interaction between them.

There have been a number of studies of effective conductivity of porous media when convective effects are either absent or minimal [3,4]. The term effective is used in the present study to mean only values obtained under these conditions so as to exclude the effects of convection. The term *stagnant thermal conductivity* is also used in this sense. Figure 1 summarizes some of the known experimental results for the effective thermal conductivity of saturated porous media comprising packed spherical particles with a saturating interstitial fluid [5–12]. These data have been obtained under stable temperature gradients, e.g., heating from above, to either prevent or minimize buoyant convection. This method, aiming to obtain bulk effective conductivity, raises two issues arising from the nonuniformity in composition near the heating surface. Because particles are aligned against the wall, the void fraction is locally very large, which makes the thermal conductivity very different from its bulk value. This difference is important near the heated surface, e.g., an embedded vertical wall, where local thermophysical properties play a dominant role in energy transport. Also, not all particles closest to the surface are strictly in contact with it, and thus the morphology of the particle matrix can contribute as well. This effect can be pronounced when the conductivity and thermal diffusivity of the two phases are very different.

The present study demonstrates a new method to measure the effective thermal diffusivity of a porous medium in the vicinity of a heated surface. The effective diffusivity is based on the effective conductivity and volumetric heat capacity in the wall region. The value obtained via this approach is more suitable when examining energy transport that occurs predominantly in the near-wall region, e.g., in free convection on a heated vertical surface. Further, the thermal diffusivity for this region should be used in determining a Rayleigh number rather than the bulk value that is representative of a location more than several particle diameters away from the wall.

## Analysis

Consider a heated vertical surface initially in an isothermal saturated porous medium. With a constant heat flux at the wall, one-dimensional transient heating of a semi-infinite domain ($y>0, t>0$) describes heat transfer. The governing equation is

$$\frac{\partial T_m}{\partial t} = \alpha_w \frac{\partial^2 T_m}{\partial y^2} \tag{1}$$

where $\alpha_w$ is the thermal diffusivity in the near-wall region $(\rho C)_m / k_m$. While diffusivity is not strictly constant in the near-wall region, a single representative value is of interest so that it can be used to analyze conduction, steady state convection, and the effects of the near-wall property variation, e.g., in the case of strongly temperature dependent thermophysical properties. Further, a finite thickness of the wall, which is necessary in experiments, presents a conjugate transient conduction problem for both constant wall heat flux and constant wall temperature boundary conditions. The heat transfer rate depends on the diffusivity of the

Contributed by the Heat Transfer Division of ASME for publication in the JOURNAL OF HEAT TRANSFER. Manuscript received June 8, 2006; final manuscript received May 1, 2007; published online February 4, 2008. Review conducted by Jose L. Lage. Paper presented at the 2005 ASME International Mechanical Engineering Congress (IMECE2005), Orlando, FL, November 5–11, 2005.

  

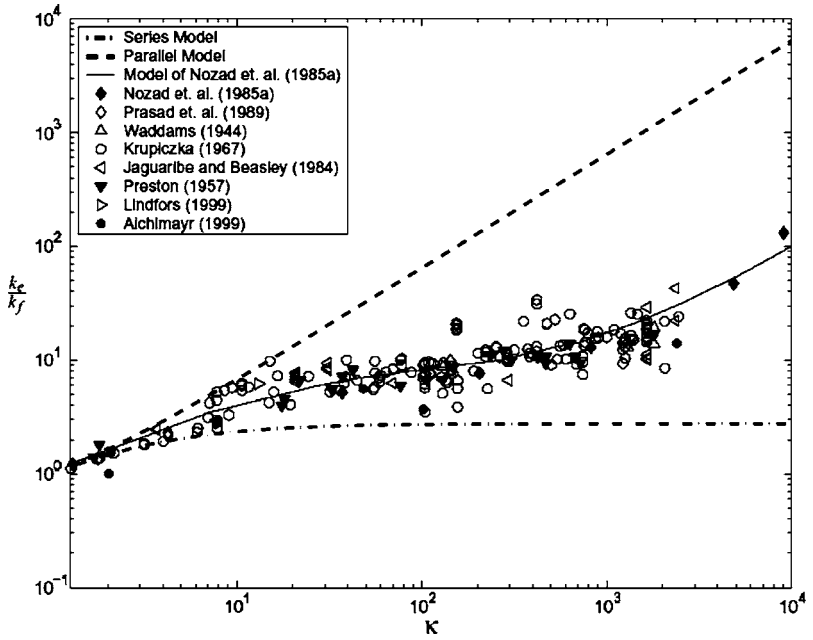


**Fig. 1 Summary of experimental investigations for stagnant thermal conductivity of porous media consisting of various bead materials and fluids [5–12]**

wall as well, but the problem remains one dimensional.

The analytical solution to Eq. (1) is

$$T_m(y,t) - T_i = \frac{2q''_w(\alpha_m t/\pi)^{1/2}}{k_m}\exp\left(\frac{-y^2}{4\alpha_m t}\right) - \frac{q''_w y}{k_m}\,\mathrm{erfc}\left(\frac{y}{2\sqrt{\alpha_m t}}\right) \tag{2}$$

and the wall temperature is

$$T_w(t) - T_i = 2q''_w\left[\frac{t}{\pi(\rho c)_m k_m}\right]^{1/2} \tag{3}$$

The application of this solution to the present case raises two difficulties. First, a heater producing the heat flux requires an impermeable wall with a finite thickness to provide a physical boundary for the medium. Second, the heat transfer rate to the medium does not equal the power input to the heater, and it is not constant during the initial conduction regime ($t=0^+$). However, this problem can be readily solved numerically, and this is how near-wall diffusivities are deduced in the present study.

Finite difference simulations are run first using only fluid properties, i.e., no porous matrix present, and the resulting temperature profile at the wall is compared to that obtained from experiment as a validation of the simulation. Then, experiments are conducted with the porous medium present. The corresponding simulation whose sole unknown now is the diffusivity of the porous medium is run iteratively to match the temperature profile obtained in experiments while changing the diffusivity values. Figure 2 shows the computational domain of the problem and the boundary conditions. The brass plate that serves as the solid boundary in the experiments has a prescribed heat flux, $q''_w$, on one side and an interface with the saturating fluid on the other. The porous medium is designed to model a semi-infinite domain by making the domain deep enough (at least ten times the plate thickness) and the far-end boundary adiabatic. The adiabatic condition allows the temperature to rise if the temperature front reaches the boundary, in which case the domain is extended and the calculation is repeated. Based on data availability, thermophysical properties are evaluated at 300 K for water (the fluid phase in the experiments) and 293 K for brass and are assumed constant. The finite difference method used for the simulation employs a forward in time, space centered scheme, and has accuracies of first order in time and second order in space. Forty-one grid points are allocated within the 3.2 mm wall, and this mesh size is used for both the fluid and the porous medium cases for computational consistency. Time steps of 25 $\mu$s and 50 $\mu$s are used for water and air, respectively, to keep the simulation stable. The numerical results are discussed with the experimental results below.

## Apparatus

The apparatus is designed for steady state experiments whose results have been reported earlier [13,14]. Figure 3 shows the apparatus comprising a thick, nearly adiabatic plastic cylinder ($350\times200$ mm$^2$ inside diameter (i.d.)) with the constant heat flux plate mounted inside near the centerline at the bottom. The heated plate is a symmetric laminate (230 mm high$\times$175 mm wide) with alloy 260 brass surface plates, each 3.2 mm thick, and two identical thin foil heaters on the center plane. These heaters have

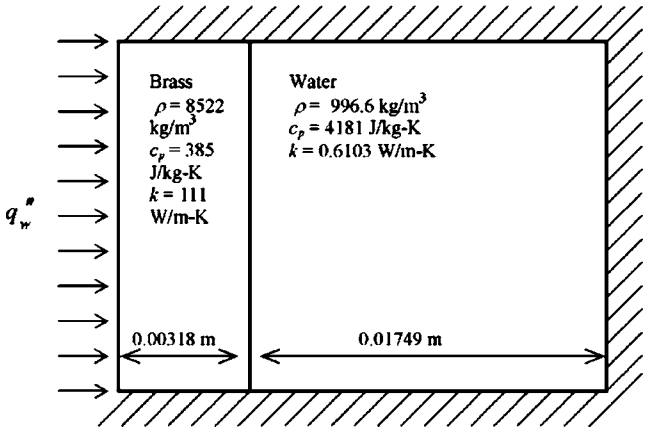


**Fig. 2 Computational domain for one-dimensional conjugate conduction analysis (not drawn to scale). Similar domains are used to simulate for porous media with appropriate properties and domain size.**

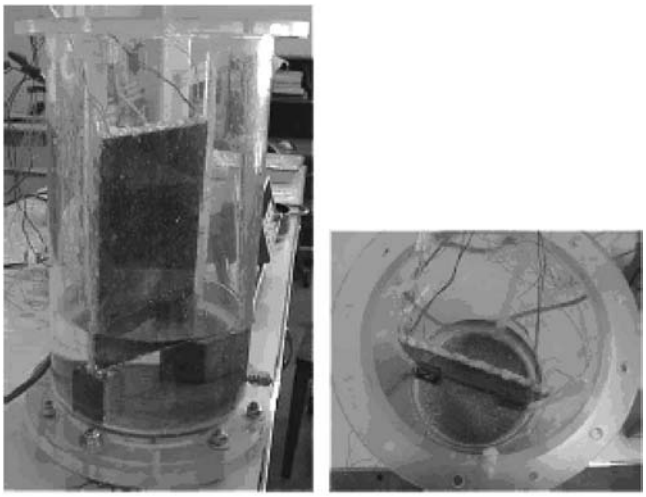


**Fig. 3 Experimental apparatus with heated plate assembly: (*a*) side view and (*b*) top view**

heating elements 3.2 mm wide etched in a serpentine fashion with a 3.2 mm gap between adjacent elements. The thermal conductivity and diffusivity of the plate material are 111 W/m K and $3.41\times10^{4}$ m$^2$/s at 293 K [15]. The overall thickness of a heater is approximately 0.32 mm, approximately a tenth of the plate thickness, and its heat capacity therefore is negligibly small [13]. The brass plate to which the heater is glued has a thickness that is the same as the width of the heating element to produce a nearly uniform heat flux to the porous medium while minimizing longitudinal conduction. The plates and foil heaters are fully bonded, and the assembly is sealed on its edges.

The location of the heated plate at the center cross section of the cylinder produces minimal effects on the two dimensionality of the boundary layer as it develops along the plate surface. With pure water as the working fluid, the boundary layer thickness is estimated to be $<1$ mm at steady state, and there is enough room in the cylinder for a boundary layer thickness larger by an order of magnitude in the saturated porous medium.

Wall temperatures are measured along the centerline of the plate at nine equidistant locations beginning near the leading edge, which is located 50 mm above the bottom of the cylinder. Wall thermocouples are plotted with high thermal conductivity cement in 1.6 mm diameter holes drilled to within 100 $\mu$m of the surface of the plate. The number of thermocouple locations is chosen to optimize spatial resolution, address machining requirements, and allow for accurate tracking of the time variation of wall temperature, which is limited by a data rate of 55 s$^{-1}$. For the transient experiments of the present study, one dimensionality is assumed to hold until the temperature measurements diverge at the several locations by 0.1 K. Thermocouples throughout the apparatus are 36 AWG type E with sensitivity of 80 $\mu$V/K. The calibration standard is a mercury in-glass thermometer with a resolution of $\pm0.1$ K and with a NIST-traceable calibration supplied by the manufacturer. To obtain the best possible precision in the present study, calibration curves are developed and used for each of the thermocouples between 298 K and 328 K [13].

Randomly stacked spheres of glass, steel, and polyethylene comprise the several porous matrices in the present study. Table 1 shows the relatively uniform distributions of bead diameters, and Table 2 summarizes key thermophysical properties. Water and air are used for the interstitial fluid, and the combination of these fluids and solids produces saturated porous media with $\kappa=1$ (glass water), 25 (glass air), 100 (steel water), and 2400 (steel air).

The bulk porosity is determined by measuring the volume of water that can be contained in the fully packed cylinder, and some uncertainty is expected owing to effects of the impermeable surface. Along the container wall, the vertical plate and its support structure create a surface along which the spheres are aligned with local values of porosity approaching 1.0. Generally, the high-porosity region near a solid surface in a situation like this extends more than a few particle diameters away from the surface [19]. Calculation shows that local porosity can be as low as 0.09 at one-half a bead diameter from the wall, which is much lower than the bulk value of 0.36–0.40 observed in the present study. Local porosity is calculated based on the area occupied by spherical beads at a given distance away from the wall and the area made by the centers of neighboring spheres. The neighboring spheres are assumed to arrange themselves in either a triangular fashion or a square fashion in which four spheres are involved (Fig. 4). These arrangements, respectively, give a near-wall porosity variation up to one-half diameter, i.e., $y=R$, of,

$$\phi_{\text{tri}} = 1 - \frac{\pi}{2\sqrt{3}}\left(2 - \frac{y}{R}\right)\frac{y}{R} \tag{4}$$

$$\phi_{\text{sq}}(y) = 1 - \frac{\pi}{2}\left(1 - \frac{y}{2R}\right)\frac{y}{R} \tag{5}$$

**Table 1 Solid phase materials and statistical variation in diameter of spherical particles**

| Material (bulk $\phi$) | Avg. diameter (mm) | Std. dev. (mm) | $N$ |
|---|---|---|---|
| Steel | 6.00 | 0.00 | 10 |
| (0.4) | 14.00 | 0.00 | 10 |
| Glass | 1.47 | 0.11 | 14 |
| (0.38) | 6.01 | 0.06 | 10 |
| Polyethylene (0.40) | 25.4 | 0 | 10 |

**Table 2 Thermophysical properties of materials for the porous medium**

| Material (source) | Thermophysical property |
|---|---|
| Chrome steel (1.34% Cr) AISI 52100 [15] | $\rho=7865$ kg/m$^3$<br>$C=4600$ J/kg K<br>$k=61$ W/m K<br>$\alpha=1.69\times10^{-5}$ m$^2$/s |
| Soda silicate glass [16] | $\rho=2500$ kg/m$^3$<br>$C=988.2$ J/kg K<br>$k=0.64$ W/m K<br>$\alpha=2.79\times10^{-7}$ m$^2$/s |
| High density polyethylene [12] | $\rho=958$ kg/m$^3$<br>$C=2100$ J/kg K<br>$k=0.329$ W/m K<br>$\alpha=1.57\times10^{-7}$ m$^2$/s |
| Water (300 K, 1 atm) [17] | $\rho=996.6$ kg/m$^3$<br>$C=4180.6$ J/kg K<br>$k=0.6103$ W/m K<br>$\alpha=1.46\times10^{-7}$ m$^2$/s |
| Air (293 K, 1 atm) [18] | $\rho=1.164$ kg/m$^3$<br>$C=1012$ J/kg K<br>$k=0.0251$ W/m K<br>$\alpha=2.13\times10^{-5}$ m$^2$/s |

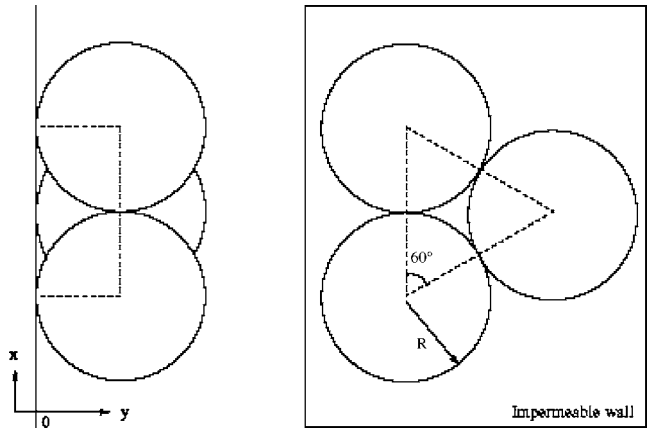


**Fig. 4 First-layer spheres in a triangular arrangement for model of local porosity dependence on distance from the wall as presented in Eq. (4)**

In the present experiments, the spherical particles are often observed to self-organize themselves against brass plate in triangular arrangements. While a square arrangement is rarely observed, the first-layer beads are, in some locations, recessed into the medium, creating locally high-porosity regions that extend approximately one bead diameter away from the wall. Therefore, the average near-wall porosity variation is expected to be greater than the profile suggested by the triangular arrangement, and may be close to that of the square arrangement in some locations (Fig. 5).

## Results

Figure 6 shows typical longitudinal temperature profiles on the plate from the start of heating to essentially steady state. This data set corresponds to a porous medium comprising six mm diameter glass beads and water, with a wall heat flux of 5160 $W/m^2$. Note that the initial rise in temperature is the same for all locations up to the time when boundary layer flow is initiated. It follows that the initial temperature rise will thus yield the effective thermal diffusivity in the near-wall region. The effective diffusivity for this region is not only useful for estimating the heat conduction rate but also is most appropriate when steady convection is of interest. In the latter case, the bulk value of diffusivity is quite different from that near the wall.

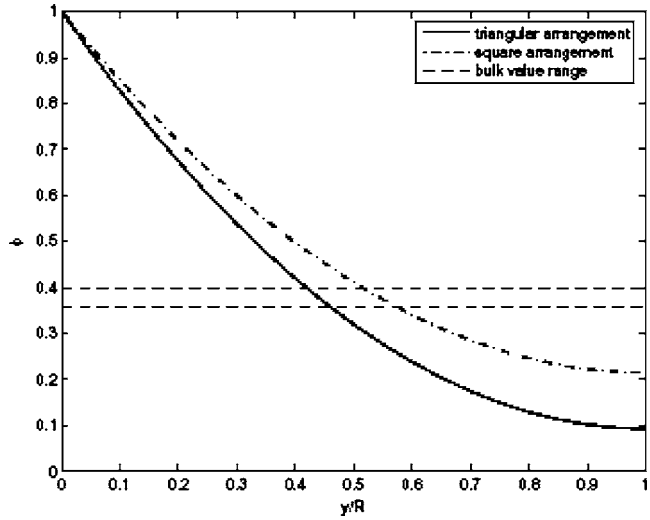


**Fig. 5 Near-wall porosity profile compared with bulk value obtained from experiments**

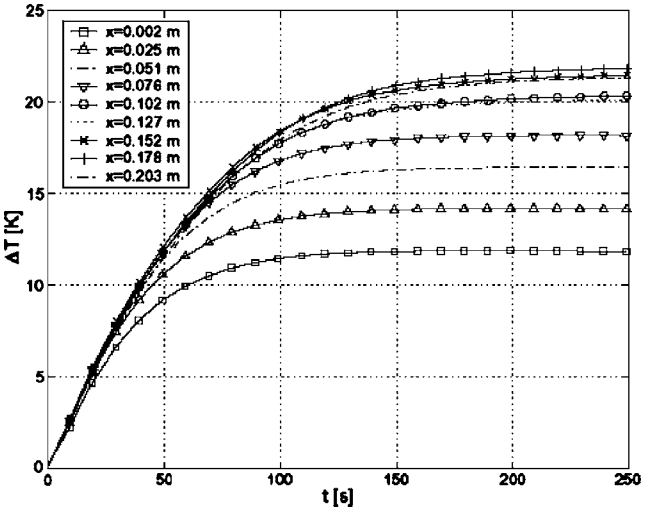


**Fig. 6 Wall temperature profile for a porous medium with 6 mm diameter glass spheres and water with an applied heat flux of 5160 $W/m^2$**

Transient wall temperatures with a water medium (no porous solid present) show how the present technique is used to measure near-wall thermal diffusivity. Figures 7(*a*) and 7(*b*) compare the resulting temperature trends at the wall as a function of time from both experiments and numerical simulations. The simulations using a thermal diffusivity of $1.46\times10^{-7}$ $m^2/s$ agree with the experiments. As shown in the figures, the wall thermocouples take a fraction of a second to respond to the heat input because they are located on the water side of the brass plate, and the heater is on the back, 3.2 mm removed. The measured temperatures exhibit small or negligible difference between longitudinal locations for a given time, indicating that the fluid remains in the conductive regime. In the high flux case (Fig. 7(*a*)), the temperature at the leading edge deviates from the remaining measurements along the plate. Heat conduction in the negative $x$ direction near the leading edge is considered to be the primary cause for this deviation.

Figure 8 shows early-time transient behavior of wall temperatures from both the experiment and the conjugate conduction solution for $q''_w=184$ $W/m^2$ with air as the working fluid and no porous solid present. The initial temperature rise is approximately 0.014 K/s (~1 K/70 s), and the simulation agrees very well with the experiment up to about 500 s after the heater is activated. After 500 s, effects of convection begin to be significant, with the plate remaining relatively uniform in temperature.

In the experiments with the water-glass medium, the particles are soda silicate glass with a thermal conductivity of 0.64 W/m K ($\kappa\approx1$). Bead diameters of 6.0 mm and 1.5 mm are used to address the effect of near-wall porosity variation, and the thermal diffusivity is $2.79\times10^{-7}$ $m^2/s$ for the glass, approximately twice that of water. Figure 9 compares wall temperature trends at $x=2.5$ cm, a distance away from the leading edge where longitudinal conduction is negligible, between pure water, 6 mm glass-water, and 1.5 mm glass-water media at heat fluxes of 5200 $W/m^2$, 5160 $W/m^2$, and 5360 $W/m^2$, respectively. The rate of temperature increase toward the beginning of heating shows agreement among all the cases plotted, and the higher thermal diffusivity of glass beads does not appear to affect the trend.

Figure 10 compares the steel-water cases at a similar heat flux as the glass-water medium for 6 mm steel-water (5160 $W/m^2$), 14 mm steel-water (5190 $W/m^2$), and water alone (5200 $W/m^2$). The initial slopes are very similar for the experimental observations and the conjugate simulation assuming pure conduction. The 6 mm steel-water medium results in a slightly different slope compared to the rest of the trends and is attributed to enhanced

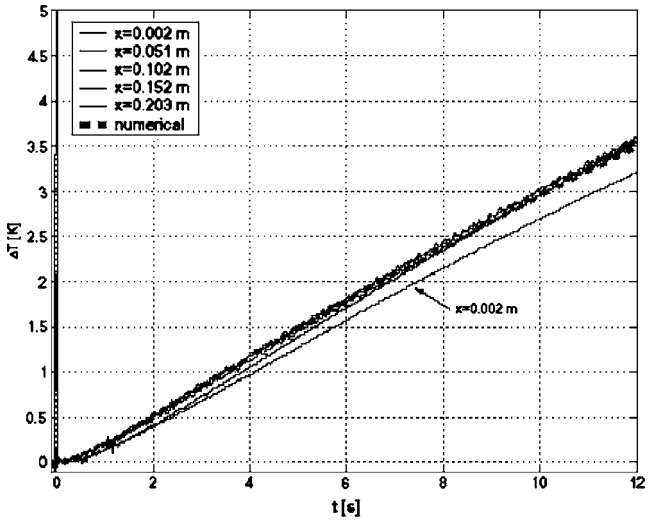


(*a*) High flux (5200 W/m$^2$) cases

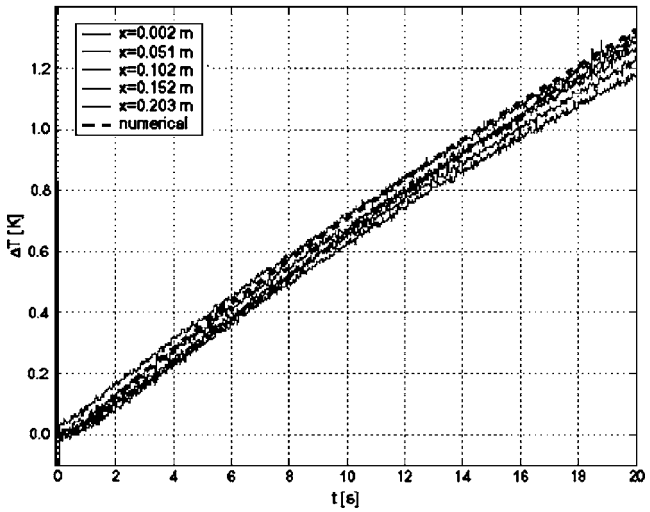


(*b*) Low flux (1250 W/m$^2$) cases

**Fig. 7 Comparison of experimental and computed temperature profiles for high (*a*) and low (*b*) applied wall heat fluxes**

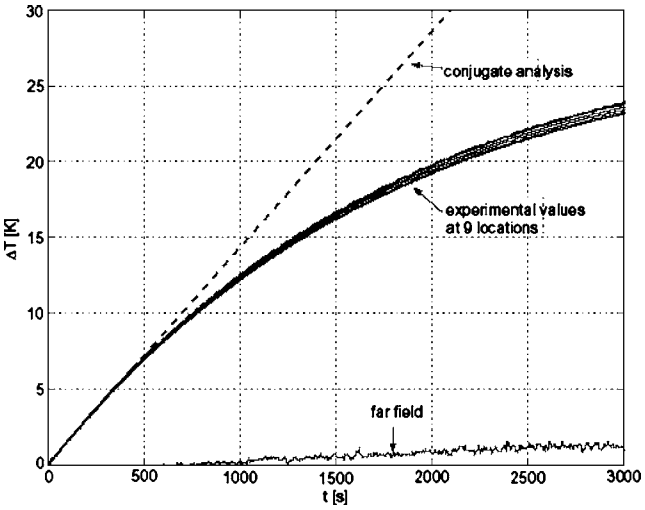


**Fig. 8 Temperature rise for air via measurement and simulation at all thermocouple locations**

near-wall diffusivity due to the presence of the steel beads. The chrome steel used in the present study has a value of thermal diffusivity ~116 times that of water. This case has a higher steady state temperature than that in pure water, indicating the combined effects of the flow-restricting morphology and the augmented conduction layer at the wall due to enhanced diffusivity, confirming the conventional knowledge that Nusselt number is inversely related to thermal diffusivity. While not within the scope of the present study, the two effects can possibly be separated by comparing the 6 mm steel case with the 6 mm glass case because they have presumably the same near-wall morphology.

Figure 11 compares results with air as the working fluid, and the conduction regime appears to be longer than that for water as the interstitial fluid. One reason for this result is the relatively lower applied heat flux so as to prevent overheating of the system. Another lies in the fact that air has a larger thermal diffusivity than does water, allowing more rapid propagation of the temperature front away from the plate. Unlike the water cases, the initial rates of temperature rise are very similar for different several solid-fluid combinations tested. This similarity shows that the thermal diffusivity of air dominates the trends in the conduction regime for the tested near-wall structures and the combinations of the thermal diffusivities of the constituents. With the transport properties of air being dominant, the penetration depth for the first 200 s can be estimated by $(\alpha\Delta t)^{1/2}$ as ~46 mm, and this value is greater than the diameter of the 1 in. polyethylene spheres, which is the largest bead size tested in the present study. Therefore, the near-wall thermal diffusivity of the porous medium with interstitial air may be estimated approximately by that of air.

Table 3 summarizes the initial temperature rise for several cases with water. The cases listed provide a closer examination of the effects of near-wall morphologies and diffusivity variations. Each medium, corresponding to a cell in the table, has two values obtained to show its response to different wall fluxes, which may or may not imply the same near-wall diffusivity because of the speed of the thermal penetration.

Table 4 lists the diffusivities that result from the simulations that match the observed derivatives. The values in parentheses are implied near-wall porosity assuming a parallel arrangement of constituent materials in the wall vicinity and one dimensionality. The effective diffusivity can then be expressed as

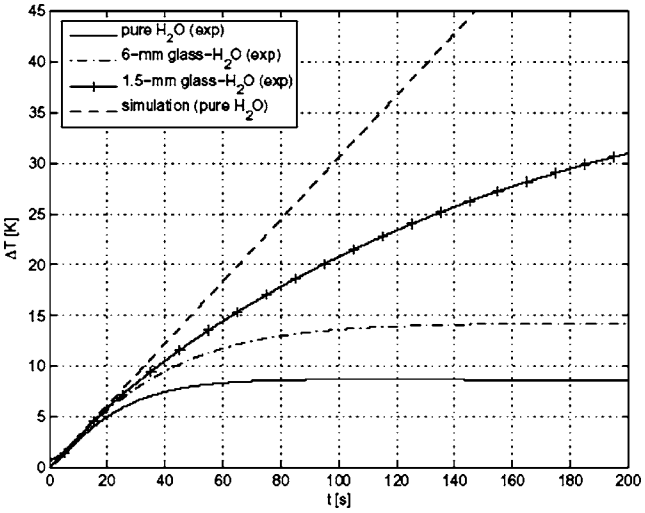


**Fig. 9 Transient temperature for the glass-water porous medium and water only measured at $x$=0.205 m and computed values**

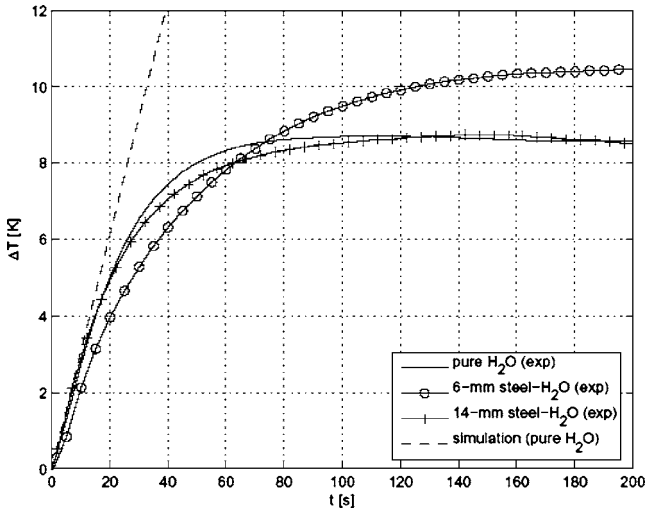


**Fig. 10 Transient temperature profiles at $x=0.025$ m for the glass-water and steel-water porous media and water alone. $q''_w \approx 5200$ W/m$^2$.**

$$\alpha_w = \phi_w \alpha_f + (1 - \phi_w)\alpha_s \tag{6}$$

This "parallel" conduction model is used to estimate near-wall porosity $\phi_w$ using the near-wall diffusivity $\alpha_w$ obtained from numerical simulation. Determining the validity of this model is outside the scope of the present study, and the effective stagnant conductivity for the bulk medium is known to deviate from that given by it (Fig. 1). However, this model provides an estimate of how much the diffusivity is shifted from that of the fluid as a result of particle-wall point contacts in the first-layer spheres.

The results obtained for the glass-water system at high heat flux are from a single simulation because of the similarity in their experimental observations. The implied low near-wall porosity is essentially the bulk value, which suggests that the penetration depth is so large for both cases that the difference in their near-wall morphologies does not play a significant role. However, the uncertainty in the near-wall porosity is relatively large because of the similar diffusivities between water and glass. This uncertainty obscures the diffusivity values obtained for different heat fluxes.

The same medium (glass-water) has different values at the lower flux of 1300 W/m$^2$. While the medium made of 1.5 mm diameter glass beads results in a near-wall porosity of 0.67, close

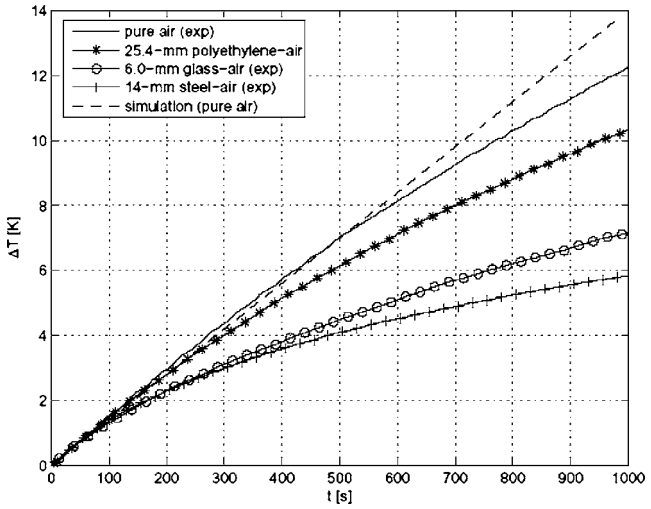


**Fig. 11 Transient temperature profiles at $x=0.025$ m for the glass-air and steel-air porous media and air alone. $q''_w \approx 184$ W/m$^2$.**

**Table 3 Measured values of $\partial T/\partial t$ (K/s) and $t_{max}$ (s) at which the derivative is estimated**

| Applied heat flux (W/m$^2$) | $d$ (mm) | 1.5 $\partial T/\partial t$ (K/s) | 1.5 $t_{max}$ (s) | 6.0 $\partial T/\partial t$ (K/s) | 6.0 $t_{max}$ (s) | 14.0 $\partial T/\partial t$ (K/s) | 14.0 $t_{max}$ (s) |
|---|---|---|---|---|---|---|---|
| 5200 | Glass-Water | 0.28 | 20 | 0.27 | 27 | — | — |
| 1300 | ($\kappa \sim 1$) | 0.046 | 130 | 0.050 | 66 | — | — |
| 5200 | Steel-water | — | — | 0.17 | 35 | 0.23 | 25 |
| 1300 | ($\kappa \sim 100$) | — | — | 0.013 | 400 | 0.038 | 60 |

to that of the high flux case, the medium with 6 mm diameter beads gives $\phi_w=0.97$, much greater than the bulk value. These results indicate that the relevant thermal penetration depth is relatively small compared to the spatial extent of the near-wall structure. The present study has avoided measurements inside the medium, and the temperature profiles remain unknown except along the wall. However, if the profiles were known, the apparent porosity (dependent on heat transfer) and a representative porosity based on the penetration depth could be compared.

The steel cases show similar trends of higher porosities with increasing bead diameter, but the values are greater in general than those for the glass cases, except for the 6 mm diameter beads at the low flux. For example, the cases with 14 mm diameter beads suggest a porosity of nearly 1.0 for both heat fluxes. This result is most likely caused by the large diameter of the beads, as well as a small number of point contacts between the beads and the wall due to the large diameter.

The trends for the 6 mm diameter bead cases appear opposite depending on the heat flux. The difference between the two media indicates the effect of the solid phase material and the resulting penetration speed as a function of heat flux. The glass-water system, on average, has a lower porosity than the steel-water system. This is an interesting result in that, with the high diffusivity of steel, the thermal penetration depth is expected to be larger with a steel-water medium. However, the present results suggest that the penetration depth may be larger for the glass-water system.

## Experimental Uncertainty

The uncertainty in determining the time derivative of temperature comes mainly from the difference between local and global derivatives. Global derivatives, determined using $t_{max}$ in Table 3, are used in both the experiments and the simulations. Local derivatives calculated in simulations are used to ensure similar behaviors of these derivatives, thereby similar temperature profiles. The differences arise from the fact that the temperature profiles are not perfectly linear, and they are treated as the main source of the uncertainties in the thermal diffusivity. Table 5 summarizes total experimental uncertainties in the thermal diffusivities presented in Table 4 for the glass-water and steel-water combinations. A complete uncertainty analysis is presented by Sakamoto [13].

**Table 4 Near-wall effective thermal diffusivity, $\alpha_w \times 10^7$ m$^2$/s, obtained from simulation**

| Heat flux (W/m$^2$) | $d$ (mm) | 1.5 $\alpha_w \times 10^7$ (m$^2$/s) | 1.5 $\phi_w$ | 6.0 $\alpha_w \times 10^7$ (m$^2$/s) | 6.0 $\phi_w$ | 14.0 $\alpha_w \times 10^7$ (m$^2$/s) | 14.0 $\phi_w$ |
|---|---|---|---|---|---|---|---|
| 5200 | Glass water | $2.2 \pm 0.5$ | 0.44 | $2.2 \pm 0.3$ | 0.44 | | |
| 1300 | ($\alpha_s/\alpha_f \sim 1.9$) | $1.9 \pm 0.4$ | 0.67 | $1.5 \pm 0.1$ | 0.97 | | |
| 5200 | Steel water | | | $7.2 \pm 2.6$ | 0.97 | $2.3 \pm 0.8$ | 1 |
| 1300 | ($\alpha_s/\alpha_f \sim 120$) | | | $20 \pm 7$ | 0.89 | $7.3 \pm 2.5$ | 0.97 |

**Table 5 Experimental uncertainty, $\delta\alpha_w$ ($m^2/s$), in measured thermal diffusivities**

| Applied heat flux ($W/m^2$) | $d$ (mm) | 1.5 | 6.0 | 14.0 |
|---|---|---|---|---|
| 5200 | Glass water | $\pm 0.5\times10^{-7}$ | $\pm 0.3\times10^{-7}$ | — |
| 1300 | ($\kappa\sim1$) | $\pm 0.4\times10^{-7}$ | $\pm 0.1\times10^{-7}$ | — |
| 5200 | Steel water | — | $\pm 2.6\times10^{-7}$ | $\pm 0.8\times10^{-7}$ |
| 1300 | ($\kappa\sim100$) | — | $\pm 7.0\times10^{-7}$ | $\pm 2.5\times10^{-7}$ |

## Conclusion

The effective thermal diffusivity of a porous medium is shown to be a function of the properties of constituent materials and near-wall morphology. The results also suggest a possible role for the applied heat flux, which affects the thermal penetration depth and thereby the effective diffusivity. Analytical representations of near-wall porosity profiles show a large variation ($0.1<\phi<1.0$) within one-half a bead diameter from the wall, and the resulting thermal diffusivities suggest representative near-wall porosities within this variation. Numerical simulation of the one-dimensional conjugate conduction problem reproduces the wall-to-medium interface temperatures observed in experiments for the pure fluid cases (water and air). Iterative simulations deduce the effective thermal diffusivity on the basis of matching computed and measured wall temperature profiles. The resulting diffusivities along with representative porosities are reported in Table 4 as representative values for the wall vicinity. Representative porosities have been calculated using a simple parallel model, Eq. (6), to relate the high porosities to the thermophysical property. It should be recalled that effective bulk conductivity generally does not follow the parallel conductance model shown as the upper limit in Fig. 1.

Near-wall thermal diffusivities obtained in the present work nevertheless suggest that values are altered toward that of the interstitial fluid. The fact that the spherical beads used in the experiments are aligned against the impermeable wall to create locally high-porosity supports this observation. Furthermore, for a medium made with stacked spheres, this region is accompanied by a reduced number of particle-to-particle contacts and a limited number of contacts between the wall and the solid material. Both geometrical factors will introduce larger near-wall thermal diffusivity in the context of volume-averaged values.

Thermal diffusivities are a key property in convective heat transfer. Whether forced or free, the heat transfer coefficient increases with decreasing thermal diffusivity. The higher the thermal diffusivity, the thicker the thermal boundary layer and a smaller temperature gradient exists at the wall. This phenomenon occurs only in the wall vicinity, and the properties used to characterize it must represent this region. In related research, it has been shown that the Nusselt number can be correlated with Rayleigh number for free convection from a bounding surface in a porous medium [13,14] but that the data do not collapse to a single line on logarithmic coordinates. This behavior is partly due to the misrepresentation of the region using the bulk value for diffusivity. Thus, to correctly characterize boundary layer flow and heat transfer, the thermophysical properties, specifically the thermal conductivity and diffusivity, must be representative of the region in which the phenomenon takes place.

## Nomenclature

$C$ = heat capacity, J/kg K
$d$ = particle diameter, m
$k$ = thermal conductivity, W/m K
$N$ = number of trials
$q''_w$ = wall heat flux, $W/m^2$
$R$ = particle radius, m
$T$ = temperature, K
$t$ = time, s
$x$ = longitudinal location, m
$y$ = transverse location, m

### Greek

$\alpha$ = thermal diffusivity, $m^2/s$
$\delta$ = experimental uncertainty
$\kappa$ = ratio of thermal conductivities, $k_s/k_f$
$\rho$ = density, $kg/m^3$
$\phi$ = porosity

### Subscripts

0 = reference
$\infty$ = far field
$e$ = effective value
$f$ = fluid
$i$ = initial
$m$ = porous medium with stagnant fluid
$s$ = solid
sq = square arrangement, Eq. (5)
tri = triangular arrangement, Eq. (4)
$w$ = wall-medium interface or wall vicinity of medium

## References


[1] Fourier, J. B. J., 1822, *Théorie Analytique de la Chaleur*, Firmin Didot, Paris.
[2] Grattan-Guinness, I., and Ravetz, J. R., 1972, *Joseph Fourier, 1768–1830: A Survey of His Life and Work, Based on a Critical Edition of His Monograph on the Propagation of Heat, Presented to the Institut de France in 1807*, MIT Press, Cambridge.
[3] Aichlmayr, H. T., and Kulacki, F. A., 2006, "On the Effective Thermal Conductivity of Saturated Porous Media," ASME J. Heat Transfer, **128**, pp. 1217–1220.
[4] Aichlmayr, H. T., and Kulacki, F. A., 2006, "The Effective Thermal Conductivity of Saturated Porous Media," Adv. Heat Transfer, **39**, pp. 377–460.
[5] Aichlmayr, H. T., and Kulacki, F. A., 2006, "A Transient Technique for Measuring the Effective Thermal Conductivity of Saturated Porous Media With a Constant Boundary Heat Flux," ASME J. Heat Transfer, **128**, pp. 1217–1220.
[6] Nozad, I., Carbonell, R. G., and Whitaker, S., 1985, "Heat Conduction in Multiphase Systems-I." Chem. Eng. Sci., **40**(5), pp. 843–855.
[7] Prasad, V., Kladias, N., Bandyopadhaya, A., and Tian, Q., 1989, "Evaluation of Correlations for Stagnant Thermal Conductivity of Liquid-Saturated Porous Beds of Spheres," Int. J. Heat Mass Transfer, **32**, pp. 1793–1796.
[8] Waddams, L., 1944, "The Flow of Heat Through Granular Material," J. Soc. Chem. Ind., London, **63**, pp. 337–340.
[9] Krupiczka, B., 1967, "Analysis of Thermal Conductivity in Granular Materials," Int. Chem. Eng., **7**, pp. 122–144.
[10] Jaguaribe, E. F., and Beasley, D. E., 1984, "Modeling of the Effective Thermal Conductivity and Diffusivity of a Packed Bed With Stagnant Fluid," Int. J. Heat Mass Transfer, **27**, pp. 399–407.
[11] Preston, F. W., 1957, "Mechanism of Heat Transfer in Unconsolidated Porous Media at Low Flow Rates," Ph.D. thesis, The Pennsylvania State University, State College, Minneapolis.
[12] Lindfors, J., 1999. "Boundary Layer Effects on the Stagnant Effective Thermal Conductivity of a Saturated Porous Medium," thesis, University of Minnesota, Minneapolis.
[13] Sakamoto, H., 2005, "Buoyancy-Driven Flow in Fluid Saturated Porous Media Near a Bounding Surface," Ph.D. thesis, University of Minnesota, Minneapolis.
[14] Sakamoto, H., and Kulacki, F. A., 2007, "Buoyancy-Driven Flow in Saturated Porous Media," ASME J. Heat Transfer, **129**, pp. 727–734; also *Proceedings of the 2005 National Heat Transfer Conference*, American Society of Mechanical Engineering, New York, Paper No. HT2005-72435.
[15] Eckert, E. R. G., and Drake, R. M., 1971, *Analysis of Heat and Mass Transfer*, McGraw-Hill, New York.
[16] Bansal, N. P., and Doremus, R. H., 1986, *Handbook of Glass Properties*, Academic, Orlando.
[17] Lemmon, E., McLinden, M., and Friend, D., 2003, "Thermophysical Properties of Fluid Systems: Water," *NIST Chemistry WebBook, NIST Standard Reference Database No. 69*, Linstrom, P., and Mallard W., eds., National Institute of Standards and Technology, Gaithersburg, (http://webbook.nist.gov).
[18] Kreith, F., and Bohn, M., 1993, *Principles of Heat Transfer*, 5th ed., West, St. Paul.
[19] Kaviany, M., 1995, *Principles of Heat Transfer in Porous Media*, 2nd ed., Springer-Verlag, New York.

# Thermophysical Properties of Biporous Heat Pipe Evaporators

**Tadej Semenic**

**Ying-Yu Lin**

**Ivan Catton**
e-mail: catton@ucla.edu

Department of Mechanical
and Aerospace Engineering,
University of California, Los Angeles,
420 Westwood Plaza,
Los Angeles, CA 90095-1597

*Thirty biporous slugs with 3 different cluster diameters and 5 different particle diameters (15 combinations with 2 repetitions) and 12 monoporous slugs with 6 different particle diameters were sintered from spherical copper powder, and thermophysical properties were measured. The neck size ratio for all the particles was approximately 0.4. The porosity of monoporous samples was found to be independent of particle diameter and was equal to 0.28, and the porosity of biporous samples was found to be independent of cluster and particle diameters, and was equal to 0.64. The liquid permeability and maximum capillary pressure of small pores were found to be a linear function of the particle diameter. Similarly, vapor permeability was found to be a linear function of the cluster diameter. The thermal conductivity of monoporous samples was measured to be* $142 \pm 3$ *W/m K at* $42 \pm 2$ *°C, and it was independent of particle diameter. The thermal conductivity of biporous samples was found to be a function of cluster to particle diameter ratio.* [DOI: 10.1115/1.2790020]

*Keywords: thermophysical properties of biporous wicks, porosity, liquid permeability, vapor permeability, capillary pressure, thermal conductivity of biporous wicks*

## Introduction

High heat flux heat pipe evaporators require working fluids with high latent heat of vaporization and high surface tension and wicks with high thermal conductivity, high liquid permeability, and small effective capillary radius. Conventional homogenous wicks (monoporous wicks) with small pores may have a small characteristic capillary radius and a high effective thermal conductivity, but have low liquid permeability. At high heat fluxes, the working fluid in even small pores starts to nucleate, and due to a fine pore structure the formed vapor cannot leave the evaporator and vapor pockets start to form and to prevent rewetting of the evaporator.

Konev et al. [1], North et al. [2], Cao et al. [3], and Semenic and Catton [4] used wicks with two characteristic pore sizes (biporous wicks), which were able to remove much more heat at the same superheat than monoporous wicks. The two pore sizes of biporous wicks yield improved performance through increased capillary pressure and vapor permeability. North et al. [2] argued that enhanced performance of biporous wicks is also due to an enhanced area available for thin film evaporation.

There are two types of biporous wicks: the first type is made of clusters of small particles, and the second type is made of large rough particles with small pores on the surface. Figure 1 shows a scanning electron microscope (SEM) photograph of the first kind of the biporous wicks used in our study (cluster size of 586 $\mu$m and powder size of 74 $\mu$m or abbreviated 586/74).

Several small pores are seen between the copper particles for liquid transport, and large pores are seen between the clusters for vapor transport. An optimal biporous evaporator is able to reach a very high heat flux at low superheat. Such an evaporator would have an optimal combination of particle diameter, particle-to-particle bonding area, cluster diameter, evaporator thickness, and evaporator radius.

Small particles result in small pores between the particles and large capillary pressure, but small liquid permeability. There certainly exist an optimal particle diameter where both capillary pressure and liquid permeability reach an optimum. The optimal particle-to-particle bonding area is achieved when pores between particles are large enough for enhanced liquid transport but small enough, on the other hand, to form a sintered compact with still acceptable fragile toughness. Optimal cluster diameter is small enough to have many cluster-to-cluster contacts for an enhanced transport of liquid and heat, and is large enough to have high vapor permeability. Also, large clusters result in increased vapor formation at the heat pipe wall-wick interface, which is not desired. The optimal evaporator thickness is achieved when both the mass flow rate of the liquid through the clusters and the vapor permeability reach an optimum. The evaporator radius is also a very important parameter because a larger radius will require that the fluid be pumped further if the center is to remain wet. We can see that all five parameters are related to each other, making optimization of heat transfer in biporous media a very difficult task.

This work relates thermophysical properties of the biporous wicks to the geometry of the media given with particle and cluster diameters. Fifteen combinations of three cluster diameters and five particle diameters were sintered into cylindrical slugs, and six more cylindrical slugs with different particle diameter ranges were sintered, and porosity, liquid permeability, capillary pressure, vapor permeability, and thermal conductivity were measured. For each combination of particle and cluster diameters were sintered two slugs having only different packings. Slugs sintered only from particles are referred to as monoporous slugs and slugs sintered from clusters as biporous slugs.

The objective of this work is to develop correlations that relate thermophysical properties of monoporous and biporous media to particle/cluster diameters. These correlations could, in the future, be used in optimization models that relate thermophysical properties of the biporous wicks to critical heat fluxes of biporous heat pipe evaporators.

## Method

The samples tested in this work were made by Advanced Cooling Technologies, Inc. Raw spherical copper powder produced by high-pressure water atomization was sieved into the fractions: 32–45 $\mu$m, 53–63 $\mu$m, 63–75 $\mu$m, 63–90 $\mu$m, 75–90 $\mu$m, and 90–106 $\mu$m. A particle size analyzer (LS13 330 from Beckman Coulter) was used to obtain particle size distributions. Figure 2 shows the particle size distributions for six different samples of

Contributed by the Heat Transfer Division of ASME for publication in the JOURNAL OF HEAT TRANSFER. Manuscript received January 10, 2006; final manuscript received July 4, 2007; published online February 4, 2008. Review conducted by Jamal Seyed-Yagoobi. Paper presented at the 2005 ASME Heat Transfer Summer Conference (HT2005), San Francisco, CA, July 15–22, 2005.

  

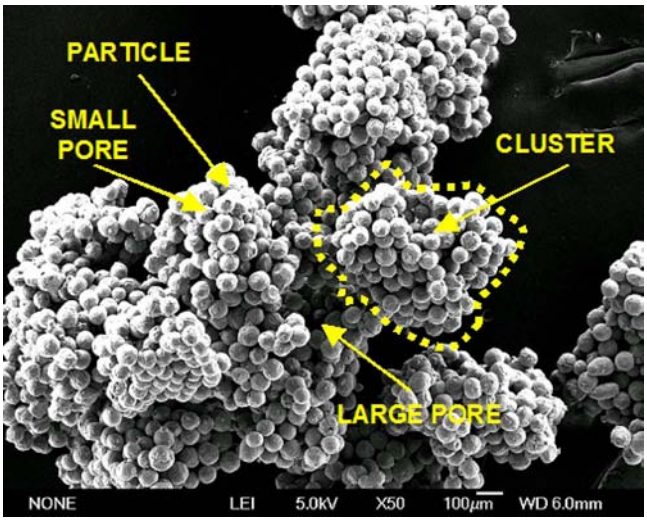


**Fig. 1 SEM photograph of a 586/74 biporous evaporator (magnification of 50 times)**

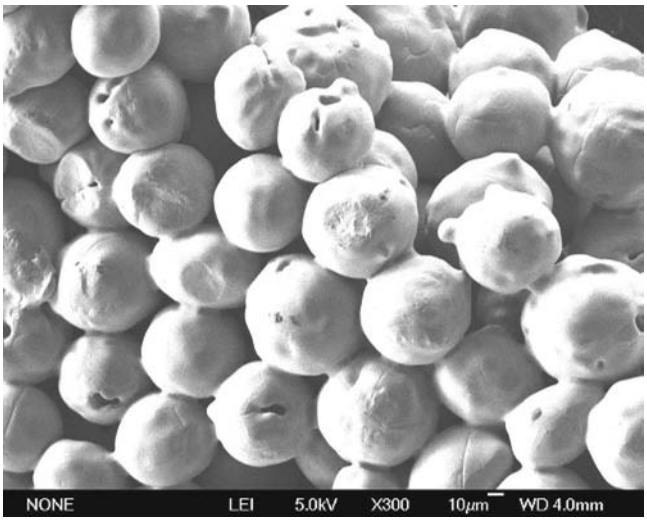


**Fig. 3 SEM of the 63–90 $\mu$m sintered matrix**

the same powder lot with the particle diameter range of 75–90 $\mu$m. The samples were dispersed in ethanol, and the sample obscurations were from 8 to 12. We can see that the distributions are only a function of the obscuration. The benefit of the particle analyzer is that the complex index of refraction of the particles is irrelevant.

By assuming forward scattering and by assuming that larger particles diffract the monochromatic laser light at smaller angles and that the wavelength of the laser light is much smaller than the particle diameter (Frauenhoffer diffraction), the particle diameters are calculated from

$$d = \frac{1.22\lambda}{\sin\theta} \tag{1}$$

Once particle size distributions for different samples of the powders were known, the distribution means were calculated from

$$d = \frac{\sum_{i=1}^{N} f_i d_i}{\sum_{i=1}^{N} f_i} \tag{2}$$

where $f_i$ is the volume fraction (%) at the particle size $d_i$ ($\mu$m). Particles with known size distributions were filled into sintering mandrels and sintered in the mixture of 5% hydrogen and 95% nitrogen. Sintering temperatures and times were obtained experimentally by using SEM of the random pieces of sintered matrices. From the theory of sintering, it is known that the pore size, smoothness, and interconnectivity of the pores strongly depend on particle diameter and variance, material properties, temperature, and sintering time. With proper sintering, optimal bonding between particles is achieved and results in many small size, fully connected pores, with acceptable compact hardness and strength. Since we are dealing with particles with a size distribution, sintering diagrams can only be used as guidance. Furthermore, some materials such as copper do not sinter by a single independent mechanism. Consequently, inclusion of multiple effects adds to the errors in calculations, and the overall sintering rate has to be determined experimentally. Sintering parameters were selected in a way to get a neck size ratio of approximately 0.4.

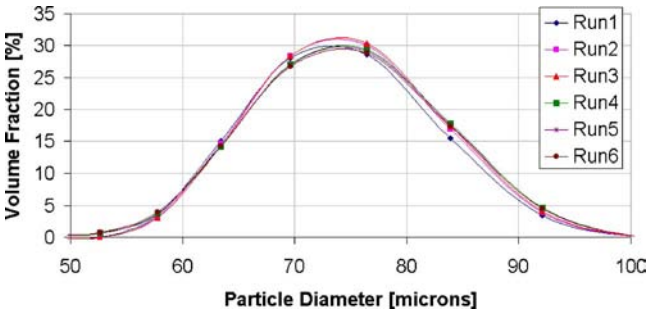


**Fig. 2 Particle size distribution for the 75–90 $\mu$m particle range**

A neck size ratio is defined as a neck dimension divided by the particle diameter. Necks are welds or bonds between particles. Figure 3 shows a SEM photograph of properly bonded particles. By assuming uniform spheres initially in the point contact, the neck growth by a single mechanism can be represented by a generalized equation (German [5]),

$$\left(\frac{X}{R}\right)^n = \frac{Bt}{R^m} \tag{3}$$

where $X$ is the neck radius, $R$ is the particle radius, $t$ is isothermal sintering time, and $B$ is a collection of material and geometric constants. The exponent $n$ is the mechanism characteristic exponent and $m$ is a constant that depends on the particle diameter. From Eq. (3), we can see that smaller particles require shorter sintering time; therefore, it is desirable to have a narrow particle size range in a way to keep the neck size ratio constant.

Sintered compacts with different characteristic particle diameters were then ground and sifted into fractions of 250–355 $\mu$m, 500–710 $\mu$m, and 710–1000 $\mu$m. The size distributions of the clusters were measured with the particle analyzer, and the distribution means were calculated for

$$D = \frac{\sum_{i=1}^{N} f_i D_i}{\sum_{i=1}^{N} f_i} \tag{4}$$

where $f_i(\%)$ is the volume fraction at the cluster diameter $D_i$ ($\mu$m). Different fractions of these produced clusters were then sintered for the second time into biporous slugs. Slugs (12 monoporous and 30 biporous) with diameter of 13 mm and length of

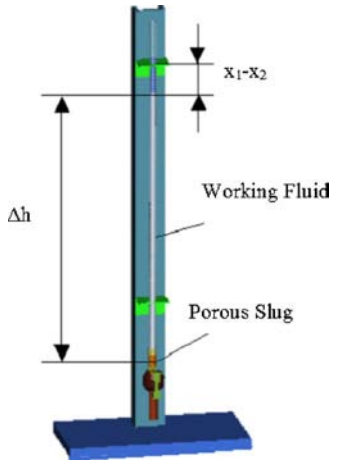


**Fig. 4 Permeability apparatus**

25 mm were sintered into 15 combinations of cluster and particles sizes for thermophysical property measurements.

**Porosity.** Porosity is the fraction of the total volume that is void. For samples with complex shapes, the porosity can be measured by optical metallography and a point counting technique (Underwood [6]) or by a liquid injection method. For samples with known geometry, the porosity can be simply obtained by measuring the weight and dimensions of the samples. This method is called the density method (Scheidegger [7]) and was used in our work. The diameter and length of each slug were measured with a caliper and the mass with a precise laboratory scale from Denver Instrument Company (accuracy of $\pm 0.15$ mg at 25 g). The porosity $\varepsilon$ of the samples with mass $m_s$, length $L$, and diameter $D$ was calculated using the following equation:

$$\varepsilon = 1 - \frac{m_s/(\pi D^2 L/4)}{\rho_{\mathrm{Cu}}} \tag{5}$$

where $\rho_{\mathrm{Cu}}$ is the density of pure copper and is equal to 8933 kg/m$^3$ (Mills [8]).

**Liquid Permeability.** Liquid permeability of biporous wicks is very difficult to measure because the working fluid is transported through a complex network of clusters with a size distribution and is a strong function of packing and cluster-to-cluster contacts. Furthermore, at low heat fluxes, a large portion of the liquid is transported over the rough surface of the clusters. We decided to measure liquid permeability of a single cluster. Instead of evaluating properties for the single cluster with random shapes and sizes, the measurements were performed on monoporous slugs. Permeability $K$ for a flow through a packed bed of spheres with diameter $d$ and porosity $\varepsilon$ can be calculated with the Blake–Kozeny equation (Luikov [9]),

$$K = \frac{d^2 \varepsilon^3}{150(1-\varepsilon)^2} \tag{6}$$

Since our samples are not uniform spheres connected at a point contact, we expect some deviation from permeability predicted by Eq. (6). The apparatus used to measure the permeability of our samples is shown in Fig. 4.

The porous sample was placed inside a tightly fitted latex tube and tied with several thin metal lock wires to prevent bypass flow. The sample was flushed with distilled water underhigh pressure for about 15 min, placed at the end of the glass tube of the apparatus, and left overnight to fully saturate. Different liquid levels inside the glass tube result in a pressure difference across the porous sample. By monitoring the rate of the liquid level drop, the velocity of the liquid was calculated. Knowing the fluid velocity, the pressure difference, the porous sample length $L$, the fluid viscosity $\mu$, and the fluid density $\rho$, the permeability $K$ was calculated using Darcy's law,

$$K = -\frac{\mu}{\nabla p} \underline{v} = -\frac{\mu}{\rho g \Delta h / L}\left(\frac{x_1 - x_2}{\Delta t}\right) \tag{7}$$

where $\Delta h$ is the height of the liquid column, and $x_1$ and $x_2$ are liquid levels at times zero and $\Delta t$. The working fluid for the monoporous samples was distilled water at room temperature. Each sample was measured three times. Each permeability measurement was an average of 15 permeability readings.

**Vapor Permeability.** Yu and Cheng [10] reported a model to predict the permeability of biporous media,

$$K = \frac{\pi}{128}\frac{L_0^{1-D_T}}{A}\frac{D_f}{3 + D_T - D_f}\bar{\lambda}_{\max}^{3+D_T} \tag{8}$$

$$A = \frac{1}{2}\pi R^2\left(\frac{1-\varepsilon_m}{1-\varepsilon_b}\right) \tag{9}$$

$$L_o = 2R + \Delta L = 2\left(1 + \sqrt{\frac{2\pi}{\sqrt{3}}\frac{1-\varepsilon_m}{1-\varepsilon_b}} - 2\right) \tag{10}$$

$$\bar{\lambda}_{\max} = \frac{\lambda_{\max} + \Delta L}{2} \tag{11}$$

$$\lambda_{\max} = R\sqrt{2\left(\frac{1-\varepsilon_m}{1-\varepsilon_b} - 1\right)} \tag{12}$$

where $\varepsilon_m$ and $\varepsilon_b$ are porosities of monoporous and biporous media, respectively, $R$ is the average cluster radius, $D_f$ is the pore fractal dimension, and $D_T$ is the tortuosity fractal dimension. Both fractal dimensions can be obtained from micrographs of biporous media. Chen et al. [11] reported that the permeability of biporous medium is almost the same as the permeability of monoporous medium when the macropore diameter of the biporous medium is the same as the pore diameter of the monoporous medium.

It is very difficult to obtain both fracture dimensions and also to precisely measure pore diameters of biporous medium and find the monoporous medium with an equivalent pore diameter; therefore, we decided to measure the permeability of biporous slugs with the same method used for monoporous slugs, but with a different working fluid. The viscosity of distilled water is too small and results in high superficial velocities through the biporous slugs; therefore, we used silicone oils with kinematic viscosities of $3.5\times10^{-4}$ m$^2$/s, $10^{-4}$ m$^2$/s, and $2\times10^{-5}$ m$^2$/s as the working fluids. The silicone oil with the smallest viscosity was used for the smallest cluster size. Each sample was measured three times. Each permeability measurement was an average of 15 permeability measurements. Measurements were performed at room temperature.

**Capillary Pressure.** When meniscus is formed at the liquid-gas interface, the capillary pressure $p_c$ can be calculated with the Laplace and Young equation as

$$p_c = \sigma\left(\frac{1}{R_1} + \frac{1}{R_2}\right) \tag{13}$$

where $R_1$ and $R_2$ are the principal radii of curvature of the meniscus and $\sigma$ is the surface tension of the liquid. In particular, we are interested in finding the maximum value of $(1/R_1 + 1/R_2)$, and hence the maximum capillary pressure $p_{c,\max}$. For convenience, it is common practice to write Eq. (13) as (Chi [12])

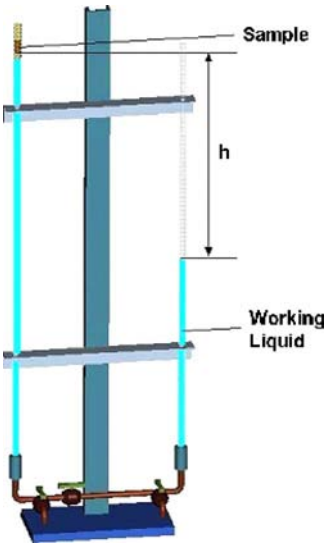


**Fig. 5 Capillarity apparatus**

$$p_{c,\max} = \frac{2\sigma}{r_c} \tag{14}$$

The effective capillary radius $r_c$ in Eq. (14) is defined such that $2/r_c$ is equal to the maximum possible value of $1/R_1+1/R_2$. For packed uniform spheres, the $r_c$ is equal to $0.21d_{\text{sphere}}$ (Chi [12]).

The maximum capillary pressure was measured for monoporous slugs with the apparatus shown in Fig. 5. A monoporous slug was placed into a tightly fitted latex tube, tied with several thin lock wires, placed on top of the left glass tube, and flushed with water under high pressure. The de-aeration process was repeated for about 15 min. When it was assumed that the sample was de-aerated, it was left for another 10 h to fully de-aerate. Capillary pressure for samples with only a very small amount of air trapped inside the pores was almost half of the fully de-aerated sample. Once the sample was ready, the liquid from the right side tube was gradually drained in 5 cm increments. If there was no change in liquid level on the right side at some liquid height $h$ for 10 h, another 5 cm of water was drained until the liquid column broke. Close to the breaking point, the increments were decreased to 2.5 cm. The liquid column broke when the maximum capillary forces developed at the water-air menisci of the sample were equal to the applied gravitational head.

For simplicity, let us assume that there are only two connected pores inside the slug (Fig. 6). The liquid column will break at the pore on the left within the red circle. We can see that the liquid column breaks at the most constricted part of the largest pore. At this particular location of the pore, it is assumed that the meniscus has the maximum value of $1/R_1+1/R_2$.

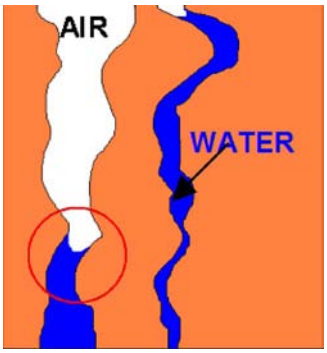


**Fig. 6 Measured pore diameter**

Capillary pressure was measured at room temperature. Partially saturated samples develop smaller capillary pressures than the maximum capillary pressure, and so capillary pressure changes with temperature since surface tension and wetting angle are both temperature dependent.

**Thermal Conductivity.** Carson et al. [13] divided porous materials based on heat conduction paths into two groups. The first group is referred to as *external porosity materials*, which are particulate-type materials in which a phase with a lower thermal conductivity (for instance, air) comprises the continuous phase with a higher thermal conductivity (for instance, copper particles), and the second type is referred to as *internal porosity materials*, which are materials such as foams, sponges, and honeycomb structures in which air, for instance, is dispersed within a continuous condensed phase. According to Carson et al. [13], the external porosity materials are bounded below by the Maxwell–Eucken 2 model (Hashin and Shtrikman [14]),

$$k_e = k_2 \frac{2k_2 + k_1 - 2(k_2 - k_1)(1-\varepsilon)}{2k_2 + k_1 + (k_2 - k_1)(1-\varepsilon)} \tag{15}$$

and at the upper bound by the effective medium theory (EMT) model (Landauer [15] and Kirkpatrick [16]),

$$k_e = 0.25\{(3\varepsilon - 1)k_2 + [3(1-\varepsilon) - 1]k_1 + \sqrt{[(3\varepsilon - 1)k_2 + (3(1-\varepsilon) - 1)k_1]^2 + 8k_1k_2}\} \tag{16}$$

where $\varepsilon$ is the porosity, $k_1$ is the thermal conductivity of copper, and $k_2$ is the thermal conductivity of air (in our case).

The internal porosity materials are bonded by the EMT model on the lower bound and by Maxwell–Eucken 1 model on the upper bound (Maxwell [17]),

$$k_e = k_1 \frac{2k_1 + k_2 - 2(k_1 - k_2)\varepsilon}{2k_1 + k_2 + (k_1 - k_2)\varepsilon} \tag{17}$$

Carson et al. [13] tested these bounds with experimental data from the literature for dry and loose sand, consolidated sand (sandstone), food gel, an aqueous alginate/saponin foam, a metallic foam, and a cellular ceramic. For all the cases, the experimental data lie within these bounds.

Tsotsas and Martin [18] found a good agreement between the thermal conductivity of packed beds of spheres predicted by Zehner [19] and Bauer models [20] and the experimental data. The Zehner [19] and Bauer [20] models take into account deformation between particles, thermal radiation, pressure dependence, particle flattening, particle shape, and size distribution of the particles. These models work well for cases where the particle deformation or neck dimensions and the optical shape factors are known.

Bauer [20] measured and calculated thermal conductivities of bidispersed mixtures of spherical particles of stellite (2.5 W/m K) at various porosities. The overall agreement between the model and the measured data was good.

Hsu et al. [21] developed a lumped-parameter model to determine the effective stagnant thermal conductivity of two-dimensional and three-dimensional monodispersed porous media with periodic structures. The model predicts the thermal conductivity of monoporous media if geometrical and contact scales of particles and ratios of thermal conductivities for both phases are known.

Chen et al. [11] calculated the thermal conductivity of a bidispersed porous medium by assuming that the medium in the microlevel (within the clusters) and the macrolevel (between the clusters) consists of spatially periodic porous cubes, both of which were modeled as three-dimensional touching cubes. The model can be used if geometric and contact lengths of the clusters are known. They found a good agreement between experimental data and their model.

Yu and Cheng [22] developed a two-fractal thermal conductiv-

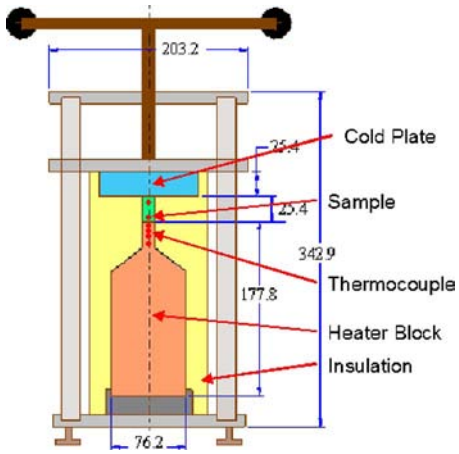


**Fig. 7 Thermal conductivity apparatus**

ity model based on the fractal characteristics of the microstructure of bidispersed porous media and on the electrical analogy technique. The proposed models are a function of tortuosity fractal dimension, area fractal dimension, porosity, ratios of the areas, length scales, and contact lengths. For given monoporous and biporous porosities and length scales, one can get ratios of contact length scales for clusters and particles, but the problem arises in estimating nontouching areas of the clusters and maximum capillary diameters.

We decided to measure the thermal conductivity of monoporous and biporous samples experimentally and to test them with the bounds of Carson et al. [13]. It is expected that the results will be bounded with Maxwell–Eucken 2 and EMT models. Samples for thermal conductivity were sintered at the same conditions as the samples for permeability and capillary pressure measurements and had two 1 mm diameter, 65 mm deep holes for thermocouples. The holes were 20 mm apart.

The thermal conductivity apparatus (Fig. 7) consisted of an electrically ground copper block with cartridge heaters, a ring made of a high temperature resistant plastic to align the heater neck and the sample, the sample that is being tested, and the cooling plate. Four thermocouples were soldered in the copper neck of the heater to monitor the heat flux into the sample. Water at a constant temperature of 20°C and a constant flow rate was circulated through the cold plate. The cold plate was mounted on an aluminum plate and connected via an axial bearing to a threaded rod with a dial, which allowed control of the applied torque. The aluminum cold plate had two brass bushings for a smooth movement of the plate on the two stainless steel precision ground rods. The top, middle, and bottom plates were made of 13 mm thick aluminum. The heater block was placed on a Teflon base. The heater and the sample were insulated with an amorphous silica blanket. The apparatus was calibrated with three materials of known thermal conductivity: AISI 304 stainless steel, brass, and 101 OFE copper. Thermal conductivities for the three materials were taken from Mills [8].

Two calibrated thermocouples with average junction diameters of 0.97 mm were glued with high temperature epoxy inside two 1 mm diameter, 20 mm apart, and 65 mm deep holes. On both faces of the samples were placed thin layers of SAF-T-EZE copper antiseize to reduce the contact resistance. Figure 8 shows the measured values of thermal conductivity versus the reported ones (Mills [8]). Six independent runs were made for each sample. We can see that the measured values were about 4% lower than the reported ones. The difference between measured and reported values was due to heat losses, possible displacement of thermocouples, and interface resistance. Instead of trying to estimate every single bias uncertainty, we used the three standard samples to calibrate the apparatus,

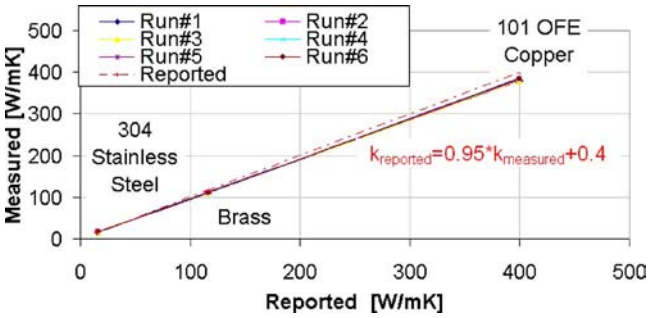


**Fig. 8 Thermal conductivity apparatus calibration curve**

$$k_{\text{actual}} = 0.95k_{\text{measured}} + 0.4 \tag{18}$$

Equation (18) was used to correct measured thermal conductivities of porous samples. To account for the interface resistance, three independent runs for each sample were made, and between individual runs the samples were permutated so that the top face of run 1 became the bottom face of run 2. For all bulk samples and monoporous samples, the same pressure between the cold plate and the heater was applied. For the biporous samples, the applied pressure was about half of the pressure of the monoporous samples due to low compact hardness of the biporous samples. Also, all biporous slugs were covered with high temperature resistant, low thermal conductivity epoxy to increase the strength of the samples. Thermal conductivity was calculated with the following equation:

$$k_{\text{sample}} = \frac{[-k\,\nabla\,T]_{\text{heater}}}{[-\nabla T]_{\text{sample}}} = \left[k_{\text{Cu}}\left(\frac{dT}{dx}\right)\right]\frac{\Delta x_{\text{sample}}}{\Delta T_{\text{sample}}} \tag{19}$$

where $k_{\text{sample}}$ is identical to $k_{\text{measured}}$ in Eq. (18). The gradient $(dT/dx)$ at the heater neck was obtained from a linear regression on four temperature readings. The uncertainty in measuring heat flux was not computed since the thermocouples were soldered in the heater neck, the insulation around the heater was always the same, and the apparatus was calibrated with the three standard samples. Temperatures were recorded with the Omega 931 acrosystem and LABTECH NOTEBOOKPRO VERSION 12.1 software. Fifty temperature readings were averaged for each steady state. Temperature was assumed to be steady when it did not rise to more than 0.5°C in 15 min. Temperature recordings started 30 min after changing the sample. The samples reached a steady state in 10 min. The average standard deviation in temperature for 50 temperature readings was 0.2°C.

## Results and Discussion

Particle size distributions for all particles were obtained with a laser diffraction particle size analyzer. Three independent samples of powders from each lot were evaluated separately. Samples of about 50 particles were also observed under the optical microscope, and the particle diameters were measured. The particle size distributions with the averages of sieve sizes and the averages obtained with the optical microscope are plotted in Fig. 9.

The solid line shows the distribution obtained with the particle analyzer, the triangles the average of the sieve sizes, and the circles the averages of the 50 particle diameters obtained with the optical microscope. Diameters measured with the optical microscope and diameters based on the average sieve size were scaled to bring them closer to the results of the particle analyzer. We can see that the agreement is very good for small particle sizes.

Figure 10 shows cluster size distributions (solid line) and averages of the two sieves (circles). Cluster diameters were not measured with the optical microscope due to the random shapes of clusters (see Fig. 1). Tables 1 and 2 compare average particle (cluster) diameters obtained with different methods. The last two columns give skewness and kurtosis of the distributions. Skew-

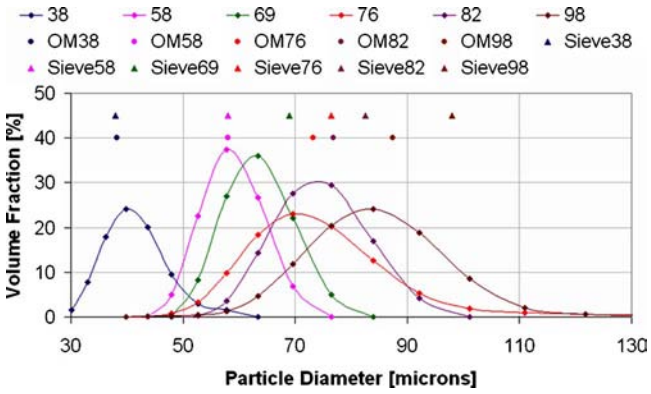


**Fig. 9 Particle size distributions**

ness is a measure of a degree of asymmetry of a distribution, and it is positive for right skewed distributions and negative for left skewed distributions. The skewness of a normal distribution is zero. Kurtosis is a parameter that describes the degree of peakedness of a distribution. Distribution with large tails is leptokurtic (positive kurtosis) and distribution with small tails is platykurtic (negative kurtosis). The kurtosis of normal distribution is zero. From Tables 1 and 2, we can see that all distributions are slightly right skewed and platykurtic. Only the distribution for the 302 $\mu$m average cluster size is leptokurtic.

Knowing the average of the two sieve sizes and the corresponding mean of the distribution computed with Eq. (2), both averages can be related by (see Fig. 11)

$$d_{\text{particle\_analyzer}} = 0.7 d_{\text{sieve}} + 15.6 \tag{20}$$

Similarly, for clusters we found

$$D_{\text{particle\_analyzer}} = 1.06 D_{\text{sieve}} - 30.64 \tag{21}$$

Particle and cluster diameters are in microns. We see that there exists a linear relationship between the two averages. It is beneficial to relate measured thermophysical properties to the actual distributions of the particles (clusters) as measured with the particle analyzer. The distributions for particles and clusters were represented with the distribution means.

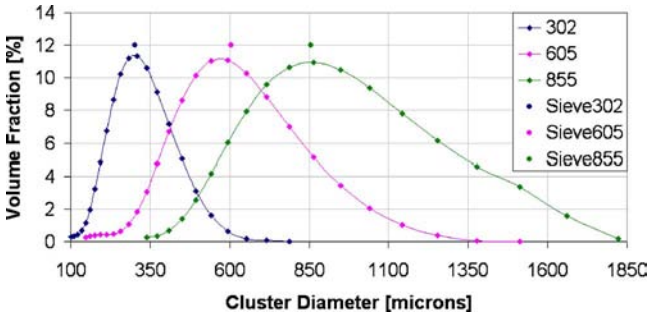


**Fig. 10 Cluster size distributions**

**Table 2 Average cluster diameters**

| Particle range [$\mu$m] | Average sieve size [$\mu$m] | Particle analyzer [$\mu$m] | Skewness | Kurtosis |
|---|---|---|---|---|
| 250–355 | 302 | 302 | 1.31 | 0.20 |
| 500–710 | 605 | 586 | 0.94 | −0.68 |
| 710–1000 | 855 | 892 | 1.22 | −0.06 |
| Normal | / | / | 0 | 0 |

Figure 12 shows results for the porosity of monoporous and biporous slugs. We can see that porosity does not depend on particle diameter and also not on cluster diameter.

Capillary pressure and liquid permeability tests showed that the sample with a particle size of 41 $\mu$m does not have through pores; therefore, it was not included in the correlations for liquid permeability and capillary pressure nor in computing the average porosity of monoporous samples. The average porosity of monoporous samples is $0.277 \pm 0.005$ and that of biporous samples is $0.642 \pm 0.01$. All particles are spherical and the clusters are made with the same procedure; therefore, it is expected that the porosity will not depend on cluster or particle diameters.

Figure 13 shows a comparison between measured capillary pressure and capillary pressure computed with Eq. (14) with $r_c$ equal to $0.21 d_{\text{sphere}}$. Figure 14 gives results for liquid permeability of the same monoporous samples. We can see that in both cases, results for the 74 $\mu$m particle diameter are consistent and also different from the rest of the results. To understand what is behind this anomaly, the samples would have to be analyzed with X-ray tomography. Also, the liquid permeability tests were performed on four samples with a 74 $\mu$m particle size, and all results were consistent. Since at this point we do not know what caused the difference, we decided to eliminate the results for the samples with the particle size of 74 $\mu$m.

By eliminating results for the 74 $\mu$m particle diameter, the linear regression on measured capillary pressure is

$$p_{c,\max} = -0.202 d + 27.806 \tag{22}$$

where $p_{c,\max}$ is the maximum capillary pressure in kPa and $d$ is the particle diameter in microns. The agreement of a property $x$ is defined as

$$\text{agreement} = \left| \frac{x_{\text{measured}} - x_{\text{correlated}}}{x_{\text{measured}}} \right| 100\% \tag{23}$$

The average agreement between measured values and correlation (Eq. (22)) is 5%, while the average agreement between measured values and those obtained with the spherical approximation is 24%.

Figure 14 gives the results for the liquid permeability of monoporous samples. Again, by eliminating results for the 74 $\mu$m particle size, the linear regression of the measured liquid permeability yields

**Table 1 Average particle diameters obtained with different methods**

| Particle range [$\mu$m] | Average sieve size [$\mu$m] | Particle analyzer [$\mu$m] | Optical microscope [$\mu$m] | Skewness | Kurtosis |
|---|---|---|---|---|---|
| 32–45 | 38.5 | 41 | 38 | 0.59 | −1.37 |
| 53–63 | 58 | 58 | 58 | 0.63 | −1.30 |
| 63–75 | 69 | 63 | / | 0.54 | −1.49 |
| 63–90 | 76.5 | 72 | 73 | 1.09 | −0.34 |
| 75–90 | 82.5 | 74 | 77 | 1.04 | −0.49 |
| 90–106 | 98 | 83 | 87 | 1.21 | −0.02 |
| Normal | / | / | / | 0 | 0 |

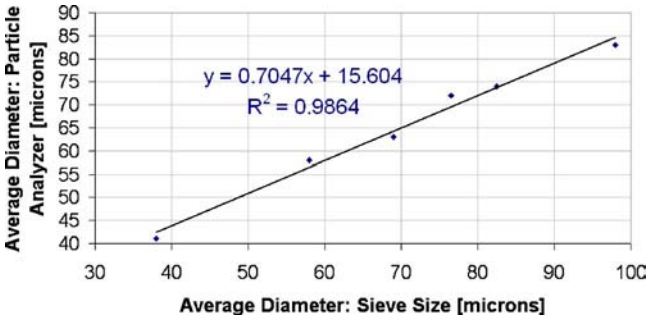


Fig. 11 Average particle diameters

$$K_{\text{liquid}} = 0.0388d - 0.8309 \quad (24)$$

The average agreement of the correlation (Eq. (24)) with the measured data is 4%, while average agreement of the Blake–Kozeny equation (Eq. (6)) with the measured data is 29%. From results for capillary pressure and liquid permeability, we see that as the particle diameter decreases, the liquid permeability decreases, but the capillary pressure increases.

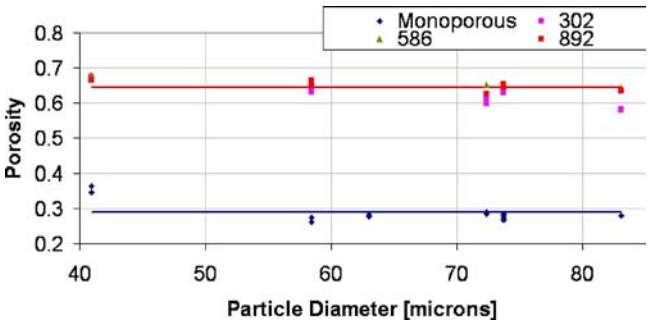


Fig. 12 Porosity

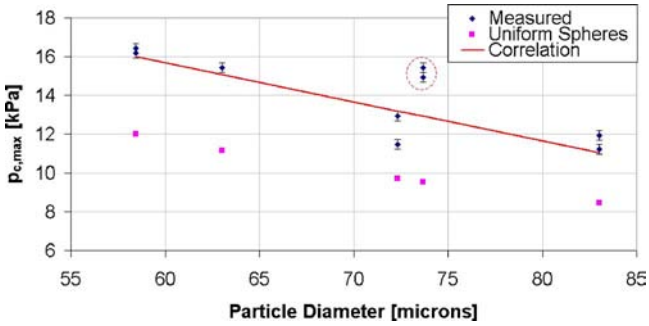


Fig. 13 Maximum capillary pressure

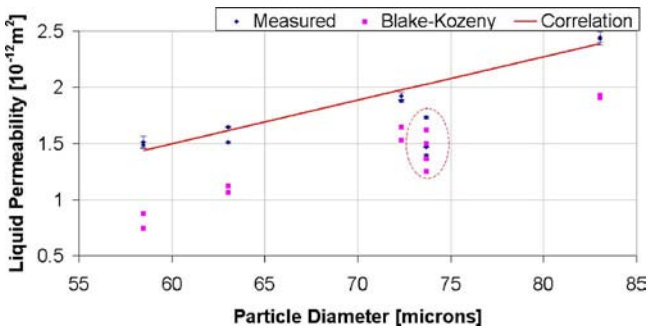


Fig. 14 Liquid permeability

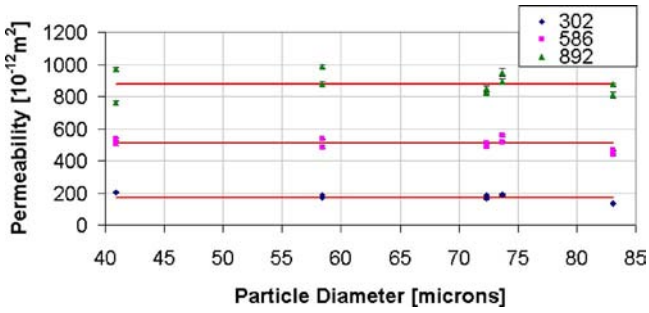


Fig. 15 Vapor permeability

Figure 15 shows the results for vapor permeability as a function of particle diameter for different cluster diameters. We can see that vapor permeability is only a function of cluster diameter; therefore, we can relate the average vapor permeability to the average cluster diameter as

$$K_{\text{vapor}} = 1.18D - 190.1 \quad (25)$$

The average agreement of the correlation given by Eq. (25) with the measured data is 8%.

Figure 16 shows results for the measured thermal conductivity of the monoporous samples and the computed thermal conductivity using the Maxwell–Eucken 1 model, which is the model suggested in many heat pipe books (see Chi [12] or Faghri [23]). We can see that the thermal conductivity of monoporous samples does not depend on particle diameter and also that the Maxwell–Eucken 1 model overpredicts the thermal conductivity by as much as 75%.

The average thermal conductivity of the monoporous samples is $142 \pm 3$ W/m K when measured at an average temperature of $42 \pm 2$°C. Figure 17 shows results for the thermal conductivity of the biporous samples. The average temperature of the biporous samples was $85 \pm 5$°C. Uncertainty intervals in Figs. 16 and 17 represent the variations of the three measured values from the mean.

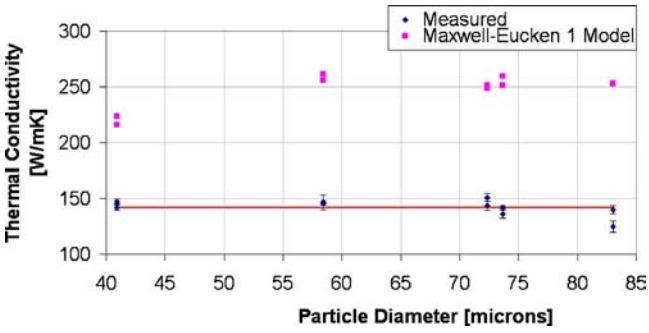


Fig. 16 Thermal conductivity of monoporous samples

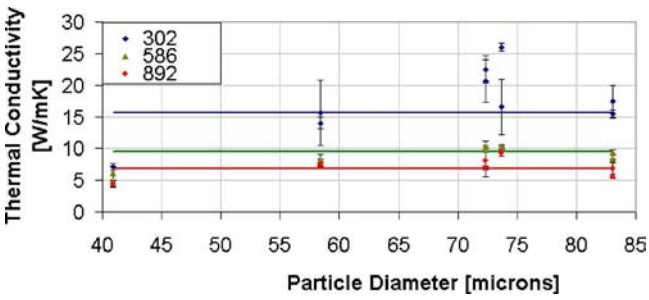


Fig. 17 Thermal conductivity of biporous samples

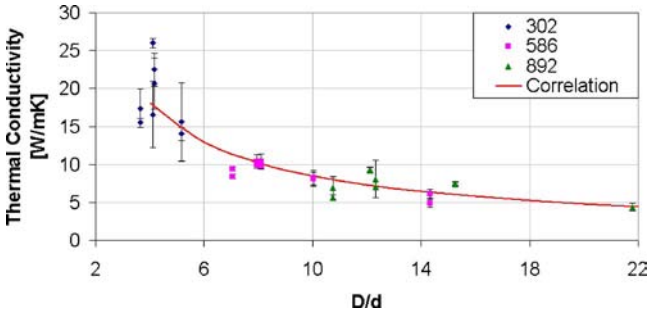


**Fig. 18 Thermal conductivity as a function of cluster to particle ratio**

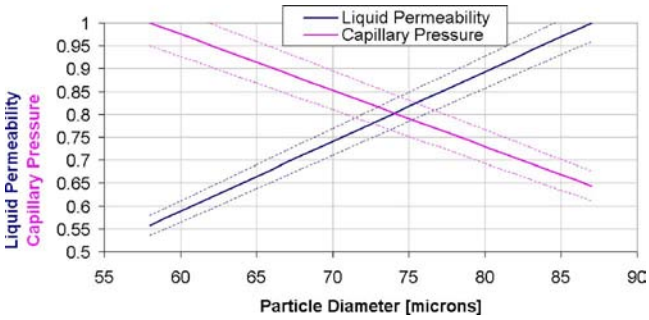


**Fig. 20 Normalized capillary pressure and liquid permeability**

The results given in Fig. 17 were replotted as thermal conductivity as a function of cluster to particle diameter ratio $D/d$ (Fig. 18). We can see that the thermal conductivity of biporous samples is a function of cluster to particle ratio,

$$k_e = 56.54\left(\frac{d}{D}\right)^{0.823} \tag{26}$$

The average agreement of Eq. (26) with measured data is 14%. Following the suggestion of Carson et al. [13], we can normalize the measured thermal conductivities and plot them as a function of porosity (Fig. 19).

It can be seen that almost all measurements lie within the bounds for external porosity materials. Two points for thermal conductivity of monoporous samples that differ from the rest of the points are for the samples with a particle diameter of 41 $\mu$m. It was also found that sintering temperatures that are too high result in increased porosity but that the thermal conductivity of the sample does not change.

Correlations for capillary pressure and liquid permeability are valid for particles with diameters of 58–87 $\mu$m, and correlations for vapor permeability and thermal conductivity of biporous samples are valid for cluster diameters of 302–892 $\mu$m. We can normalize Eqs. (22) and (24) so that the maximum value of the capillary pressure and the liquid permeability is equal to 1. By plotting them on the same graph (Fig. 20), we can clearly see that as particle diameter increases, liquid permeability increases, but maximum capillary pressure decreases.

Similarly, we can normalize Eqs. (25) and (26) with $d$ equal to 74 $\mu$m and plot them on the same graph (Fig. 21). We can clearly see that as cluster diameter increases, vapor permeability increases, but the thermal conductivity of the media decreases. A similar trend as for thermal conductivity versus cluster diameter is expected if we would plot the theoretical mass flow rate of liquid pumped through the clusters as a function of cluster diameter. Smaller clusters have more cluster-to-cluster contacts per unit volume available for the liquid transport.

## Uncertainty Analysis

There is a naturally present randomness due to random shapes and random packing of clusters. To account for this randomness, a statistically large enough number of samples had to be measured. Porosity for biporous slugs was computed by averaging the porosity of 30 biporous slugs: vapor permeabilities were computed by averaging permeabilities of 10 slugs with the same cluster size. Each vapor permeability value was an average of 45 measurements. A correlation for the thermal conductivity of biporous slugs was obtained by using results for 28 biporous slugs. The thermal conductivity of each slug was measured three times.

Assuming a normal population, we can obtain the population mean $\mu$, a best approximation of the true value $a_{\text{true}}$, using the following relationship:

$$\mu = \bar{a} \pm t_{\nu,\%} S_{\bar{a}} \tag{27}$$

where $\bar{a}$ is the mean of a sample with sample size $N$, calculated using

$$\bar{a} = \frac{1}{N}\sum_{i=1}^{N} a_i \tag{28}$$

Here, $S_a$ is the standard deviation of the sample mean obtained from

$$S_{\bar{a}} = \frac{S_a}{\sqrt{N}} = \frac{1}{\sqrt{N}}\left[\frac{1}{N-1}\sum_{i=1}^{N}(a_i - \bar{a})^2\right]^{1/2} \tag{29}$$

where $t_{\nu,\%}$ is the student $t$-distribution variable. The quantity $S_a$ in Eq. (29) is the sample standard deviation. The variable $t_{\nu,\%}$ depends on the degrees of freedom, $\nu=(N-1)$, and the confidence level, %. $t_{95}$ values for different degrees of freedom are tabulated in the literature, for example, Mills and Chang [24].

We can also define relative uncertainty $r$ as

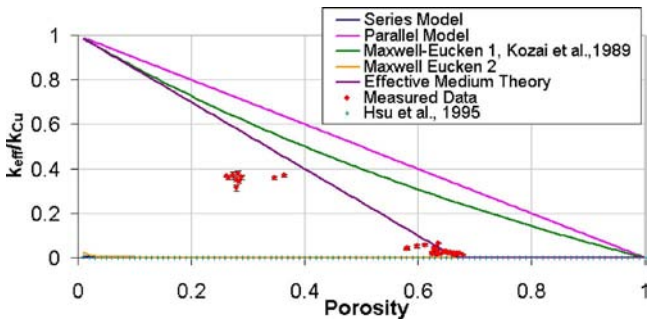


**Fig. 19 Comparison between different models and measured thermal conductivity**

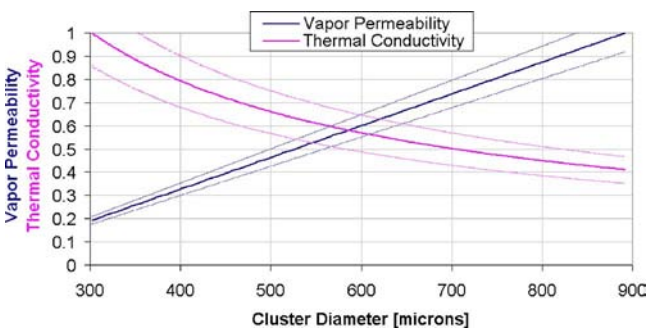


**Fig. 21 Normalized vapor permeability and thermal conductivity**

$$r = \frac{t_{\nu,\%} S_{\bar{a}}}{\bar{a}} 100\% \tag{30}$$

**Particle and Cluster Diameters.** The particle size analyzer is expected to measure large particles less accurately because the diffraction angle for large particles is smaller. Average particle diameters measured with the optical microscope were, on average, 3% bigger than those measured with the particle analyzer. The agreement between average particle (cluster) diameters measured with the particle analyzer and predicted with Eqs. (20) and (21) is also 3%.

**Porosity.** Precision uncertainty in measuring porosity could come from the offset of the laboratory scale. The scale was calibrated before each measurement, which made precision uncertainty much smaller than bias uncertainties in measuring the length and diameter of the slugs. The relative uncertainty in measuring the porosity of monoporous samples is 1.7%, and the relative uncertainty in measuring the porosity of biporous samples is 1.5%.

**Permeability.** The average uncertainty in measuring liquid permeability is 1.7%, and the liquid permeability correlation agrees with measurements within 4%. The average uncertainty in measuring vapor permeability is 1.4%, and the correlation for vapor permeability agrees with measured data within 8%. Each sample was tested three times. Possible differences of the results among the three runs were due to bypass flow and not fully saturated samples.

**Capillary Pressure.** The average relative uncertainty in measuring capillary pressure is 2%, and the capillary pressure correlation agrees with measured data within 5%. The uncertainty in measuring capillary pressure came from the resolution of capillary pressure readings, which were 2.5 cm of water or 125 Pa. If the sample was not completely de-aerated, the capillary pressure readings were incorrect and the measurement had to be repeated.

**Thermal Conductivity.** The average relative uncertainty in measuring the thermal conductivity of monoporous samples is 2.6%, and the average agreement between the average value (142 W/m K) and the measured values is 3.6%. The average relative uncertainty in measuring the thermal conductivity of biporous samples is 10.4%, and the average agreement between measured data and the predicted thermal conductivity with the correlation is 14.3%. The large relative uncertainties in measuring the thermal conductivity of biporous slugs came from interface resistance, which was due to rough surfaces of biporous slugs and to low applied pressure between the cooling plate and the heater. Also, a thin layer of the epoxy on the outside of the biporous slugs had some effect on the measurements.

## Concluding Remarks

Apparatuses for measuring permeability, capillary pressure, and thermal conductivity were built. Several monoporous and biporous wicks were made and tested. Particle and cluster size distributions were measured with an optical microscope and a laser diffraction particle size analyzer. Porosity was measured with the density method. Permeability was obtained by measuring the pressure and volume flow rate of unidirectional liquid flow through a porous sample. Capillary pressure was measured by a falling meniscus method. Thermal conductivity was measured with a steady state technique.

Correlations that relate thermophysical properties to the geometry of the biporous and monoporous media are developed. Correlations for liquid permeability and capillary pressure agree within 5%, and the correlation for vapor permeability agrees with measured data within 8%. The average thermal conductivity for monoporous media agrees with measurements within 3%, and the correlation for predicting thermal conductivity of biporous media agrees with measured data within 14%. The Blake–Kozeny equation underpredicts the permeability of monoporous samples. Maximum capillary pressure was found to be slightly higher than predicted by the spherical approximation. Measured thermal conductivities are bounded by the Maxwell–Eucken 2 model and the EMT model proposed by Carson et al. [13] for the external porosity materials. The correlations are ready to be used in optimization models that relate thermophysical properties to the critical heat flux of the biporous evaporators.

To the best of our knowledge, we believe that we are the first who based correlations for thermophysical properties of biporous media on distribution means of clusters and particles and not on the averages of the sieve sizes. This is the first work to measure thermal conductivities of biporous media for a wide range of particles and clusters and which compares measured thermal conductivities to thermal conductivities of materials with similar heat conduction pathways (Carson et al. [13]). In this work, the amount of oxide on the wicks was not measured, and correlations that were developed are only valid within the ranges of particle and cluster diameters that were tested.


## Acknowledgment

The authors would like to acknowledge the support of the U.S. Navy/Office of Naval Research and Dr. Mark Spector as program manager. The grant award number is N00014-04-1-0280. They would also like to thank Brenda Chang and Christian Diego Di Sanzo for help with the measurements.


## Nomenclature

$a_i$ = measured value of quantity
$B$ = a collection of material and geometric constants
$d$ = particle diameter ($\mu$m)
$D$ = cluster diameter ($\mu$m), slug diameter (mm)
$D_T$ = tortuosity fractal dimension
$D_f$ = pore fractal dimension
$f_i$ = volume fraction (%)
$h$ = height (mm)
$k_1$ = thermal conductivity of phase 1 (W/m K)
$k_2$ = thermal conductivity of phase 2 (W/m K)
$k_e$ = effective thermal conductivity (W/m K)
$K$ = permeability ($m^2$)
$L$ = length of the slug (mm)
$m$ = sintering constant that depends on diameter
$m_s$ = mass of the slug (g)
$n$ = sintering mechanism characteristic exponent
$N$ = number of measurements (points)
$p$ = pressure (kPa)
$r$ = relative uncertainty
$r_c$ = effective capillary radius ($\mu$m)
$R$ = particle radius ($\mu$m)
$R_1$, $R_2$ = principal radii of curvature of the meniscus (m)
$S_a$ = sample standard deviation
$S_a$ = standard deviation of the population mean
$v$ = velocity (m/s)
$t$ = time (s)
$t_{\nu,\%}$ = student $t$-distribution variable
$T$ = temperature (K)
$x$ = location (mm)
$X$ = neck radius
$\varepsilon$ = porosity
$\varepsilon_m$, $\varepsilon_b$ = porosity of monoporous and biporous media
$\lambda$ = wavelength of the laser light source ($\mu$m)
$\mu$ = population mean, viscosity (kg/ms)
$\rho$ = density ($kg/m^3$)
$\sigma$ = surface tension (N/m)

$\theta$ = diffraction angle

## References


[1] Konev, S. V., Polasek, F., and Horvat, L., 1987, "Investigation of Boiling in Capillary Structures," Heat Transfer-Sov. Res., **19**(1), pp. 14–17.

[2] North, M. T., Rosenfeld, J. H., and Shaubach, R. M., 1995, "Liquid Film Evaporation From Bidisperse Capillary Wicks in Heat Pipe Evaporators," *Proceedings of the ninth International Heat Pipe Conference*, Albuquerque, NM, May 1–5.

[3] Cao, X. L., Cheng, P., and Zhao, T. S., 2002, "Experimental Study of Evaporative Heat Transfer in Sintered Copper Bidispersed Wick Structures," J. Thermophys. Heat Transfer, **16**(4), pp. 547–552.

[4] Semenic, T., and Catton, I., 2006, "High Heat Flux Removal Using Biporous Heat Pipe Evaporators," ASME J. Heat Transfer, submitted, Paper No. HT-06-1468.

[5] German, R., 1984, *Powder Metallurgy Science*, Metal Powder Industries Federation, Princeton, NJ.

[6] Underwood, E. E., 1970, *Quantitative Stereology*, Addison-Wesley, Reading, MA.

[7] Scheidegger, E., 1963, *The Physics of Flow Through Porous Media*, University of Toronto Press, Toronto, ON, p. 10.

[8] Mills, A. F., 1999, *Heat Transfer*, 2nd ed., Prentice-Hall, Englewood Cliffs, NJ.

[9] Luikov, A. V., 1966, *Heat and Mass Transfer in Capillary-Porous Bodies*, Pergamon, London.

[10] Yu, B., and Cheng, P., 2002, "A Fractal Permeability Model for Bi-Dispersed Porous Media," Int. J. Heat Mass Transfer **45**, pp. 2983–2993.

[11] Chen, Z. Q., Cheng, P., and Zhao, T. S., 2000, "An Experimental Study of Two Phase Flow and Boiling Heat Transfer in Bidispersed Porous Channels," Int. Commun. Heat Mass Transfer, **27**(3), pp. 293–302.

[12] Chi, S. W., 1976, *Heat Pipe Theory and Practice*, Hemisphere, Washington, D.C., McGraw-Hill, New York..

[13] Carson, J. K., Lovatt, S. J., Tanner, D. J., and Cleland, A. C., 2005, "Thermal Conductivity Bounds for Isotropic Porous Materials," Int. J. Heat Mass Transfer, **48**, pp. 2150–2158.

[14] Hashin, Z., and Shtrikman, S., 1962, "A Variational Approach to the Theory of the Effective Magnetic Permeability of Multiphase Materials," J. Appl. Phys., **33**, pp. 3125–3131.

[15] Landauer, R., 1952, "The Electrical Resistance of Binary Metallic Mixtures," J. Appl. Phys., **23**, pp. 779–784.

[16] Kirkpatrick, S., 1973, "Percolation and Conduction," Rev. Mod. Phys., **45**, pp. 574–588.

[17] Maxwell, J., 1891, *A Treatise on Electricity and Magnetism*, 3rd ed., Clarendon, Oxford, Vol. 1..

[18] Tsotsas, E., and Martin, H., 1987, "Thermal Conductivity of Packed Beds: A Review," Chem. Eng. Process., **22**, pp. 19–37.

[19] Zehner, P., 1972, "Experimentelle und theoretische Bestimmung der effektiven Wärmeleitfähigkeit durchströmter Kugelschüttungen bei mässigen und hogen Temperatured," Ph.D. thesis, Karlsruhe.

[20] Bauer, R., 1976, "Effective Radiale Wärmeleitfähigkeit Gasdurchströmter Schüttungen Mit Partikeln Unterschiendlicher Form und Größenverteilung," Ph.D. thesis, Karlsruhe.

[21] Hsu, C. T., Cheng, P., and Wong, K. W., 1995, "A Lump-Parameter Model for Stagnant Thermal Conductivity of Spatially Periodic Porous Media," ASME J. Heat Transfer, **117**, pp. 264–269.

[22] Yu, B., and Cheng, P., 2002, "Fractal Models for Effective Thermal Conductivity of Bidispersed Porous Media," J. Thermophys. Heat Transfer, **16**(1), pp. 22–29.

[23] Faghri, A., 1995, *Heat Pipe Science and Technology*, Taylor & Francis, New York.

[24] Mills, A. F., and Chang, B. H., 2003, "Error Analysis of Experiments; A Manual for Engineering Students," unpublished.

# Heat-Transfer Enhancement by Chaotic Advection in the Eccentric Helical Annular Flow

**José P. B. Mota**

**António J. S. Rodrigo**

Requimte/CQFB,
Departamento de Química,
Faculdade de Ciências e Tecnologia,
Universidade Nova de Lisboa,
2829-516 Caparica, Portugal

**Estéban Saatdjian**
LEMTA,
2 Avenue de la Forêt de Haye,
BP 160,
54504 Vandœuvre Cédex, France

*Chaotic advection in the eccentric helical annular heat exchanger is investigated as a means to enhance its thermal efficiency. Chaotic streak lines are generated by steadily rotating one boundary while the other is counter-rotated with a time-periodic angular velocity. The effects of the eccentricity ratio and modulation frequency on the heat-transfer rate are analyzed by numerically solving the 3D convection-diffusion equation for a broad range of parameter values. For the frequency range over which chaotic advection can be effectively promoted, the efficiency of the heat exchanger is enhanced over that obtained for steady boundary rotation. Other tools, such as stretching field calculations and streak-line plots, applicable for dissipative dynamical systems, are implemented. These tools qualitatively confirm the quantitative heat-transfer results obtained.* [DOI: 10.1115/1.2787023]

*Keywords: eccentric helical annular flow, chaotic advection, heat transfer, mixing*

## Introduction

One major device used to heat highly viscous fluids is the annular heat exchanger. In this apparatus, fluid flows in the annular region between two cylinders. This configuration is especially effective for heating highly viscous, low thermal-conductivity fluids, because heat can be transferred into the fluid via both the inner and outer cylinders. Because of the high fluid viscosity, the flow is laminar in practically all cases; increasing the heat-transfer rate by turbulent eddies would lead to very high pressure drops.

For the case where the hydrodynamic and thermal balances can be decoupled, the heat-transfer rate for motionless boundaries has been calculated analytically for either isothermal or constant heat-flux boundary conditions [1]. Different geometrical configurations for this apparatus, such as eccentric cylinders and confocal elliptical cross sections, have also been analyzed in an attempt to obtain higher heat-transfer rates [2].

Much higher thermal efficiency can be achieved in this heat exchanger if chaotic advection is promoted. Chaotic advection implies that fluid particles follow chaotic trajectories (as in turbulent flow), even though the flow is laminar [3]. From an Eulerian viewpoint, the flow is periodic; however, in a Lagrangian reference frame, the flow is chaotic or periodic depending on the initial location of a given material point [4].

Chaotic advection can be promoted in the annular heat exchanger by either superposing a 2D cross-sectional flow, generated by boundary rotation, onto the axial flow, or by rendering the flow spatially periodic through insertion of internal mixing elements. In the former case, the geometry must be modified to create a cross-sectional flow topology with a vortex zone. To achieve this, the inner cylinder is moved into an eccentric position, thus separating the cross-sectional flow field into two or more independent zones. The resulting geometry is known as eccentric helical annular configuration. To obtain chaotic particle trajectories, at least one boundary must be rotated at a time-periodic angular velocity, while the other boundary turns at constant speed. In this paper, the boundaries turn in opposite directions.

In the first mixing experiments in an eccentric helical annular flow for an axial Reynolds number of about unity [5], the recorded photographs clearly demonstrate the existence of chaotic streak lines. The influence of the axial velocity on this flow was shown to be very important. We have recently [6–8] developed the mathematical basis necessary for the analysis of mixing and heat transfer in these flows. For one geometrical configuration, we have shown that chaotic advection in this flow works as a frequency-selective amplifier. When the outer cylinder is steadily rotated, there is a given frequency of the sinusoidal modulation of the inner-cylinder rotation that gives the highest heat-transfer rate. As in many fluid instability phenomena, very low or very high modulations of the angular velocity render the system stable.

The objective of the present work is to implement the above analysis for different geometrical configurations of the eccentric helical annular heat exchanger. In particular, the value of the eccentricity ratio and modulation frequency of the inner boundary leading to the highest heat-transfer efficiency are determined.

## Annular Flow Between Eccentric Rotating Cylinders

A sketch of the eccentric helical annular heat exchanger and of its cross-sectional geometry are shown in Fig. 1. Apart from the axial length $L$, two dimensionless parameters are required to define the geometry. They are the outer-to-inner radii ratio, $R_2/R_1$, and the eccentricity ratio, $\epsilon = e/(R_2 - R_1)$, where $e$ is the distance between the centers of the two cylinders.

The flow is assumed to be dominated by viscous forces and the physical properties of the fluid are considered constant. Under these assumptions, the 3D flow field can be determined analytically by solving the Stokes equations

$$\nabla P = \mu \nabla^2 \mathbf{V} \qquad \nabla \cdot \mathbf{V} = 0 \tag{1}$$

in an appropriate coordinate system. In this study, we use a bipolar coordinate system $[\alpha, \beta, z]$, which is defined by the following transformations from Cartesian coordinates $[x, y, z]$:

$$x = \frac{-a \sinh \alpha}{\cosh \alpha - \cos \beta} \qquad y = \frac{a \sin \beta}{\cosh \alpha - \cos \beta} \qquad z = z \tag{2}$$

The Lamé coefficients in the three directions are $(h, h, 1)$, where $h = a/(\cosh \alpha - \cos \beta)$.

For this 3D flow, the cross-sectional components ($V_\alpha$ and $V_\beta$) can be solved independently from $V_z$. The solution for the stream function, expressed as a function of the angular velocity at the rotating boundaries, is given in Ref. [9]. The axial velocity component, $V_z(\alpha, \beta)$, was obtained by Snyder and Goldstein [10] from the solution of

$$h^2 \frac{dP}{dz} = \mu \left( \frac{\partial^2 V_z}{\partial \alpha^2} + \frac{\partial^2 V_z}{\partial \beta^2} \right) \tag{3}$$

By superposing the cross-sectional and axial velocity solutions, the 3D flow field in the heat exchanger is completely defined.

Contributed by the Heat Transfer Division of ASME for publication in the JOURNAL OF HEAT TRANSFER. Manuscript received July 6, 2006; final manuscript received May 2, 2007; published online February 4, 2008. Review conducted by Chang Oh.

  

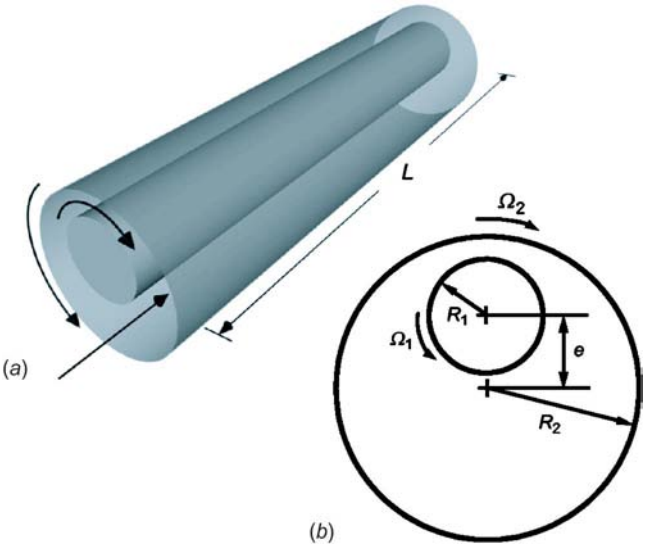


**Fig. 1 Sketch of (*a*) the eccentric helical annular heat exchanger and (*b*) its cross-sectional geometry**

In order to promote chaotic advection, at least one of the cylinders must turn at a time-varying angular velocity. In the present study, the two cylinders turn in opposite directions (counter-rotation), with the outer cylinder rotating at a constant angular velocity and the inner cylinder rotating at a time-periodic angular velocity. This velocity protocol can be expressed as

$$\Omega_1 = \bar{\Omega}_1(1 + \delta \sin \omega t) \quad \bar{\Omega}_1/\Omega_2 < 0 \tag{4}$$

where $\Omega_1$ and $\Omega_2$ are the angular velocities of the inner and outer cylinders, respectively, and $\delta$ and $\omega$ are the amplitude and frequency of the inner-cylinder modulation.

The analytical solution for the velocity field given above was obtained for steady cylinder rotation and, therefore, is not valid when the inner boundary rotates at a time-periodic angular speed. However, if the Strouhal number defined as $\mathrm{Sr}=\omega L/V_{\mathrm{ref}}$, where $V_{\mathrm{ref}}$ is a characteristic velocity (e.g., $\Omega_2 R_2$), is small, then it is valid to assume that the process is quasistatic and the analytical solution is that given at the instantaneous angular velocity ratio [10].

Previous work [11–14] on chaotic advection in the 2D flow between eccentric cylinders ($V_z=0$) showed that the amplitude must be chosen as large as possible, as long as Stokes flow conditions are maintained. In this way, the saddle point, which appears in the region of minimum gap, is displaced from the vicinity of one boundary to the vicinity of the other. For this reason, in the present work, $\delta$ is fixed at a large value ($\delta=0.9$), although there are no fixed points in the 3D flow under study.

As in Ref. [4], the following dimensionless control parameters are defined:

$$N_T = \frac{\Omega_2 \tau}{2\pi} \quad N_P = \frac{\omega \tau}{2\pi} \tag{5}$$

where $\tau=L/\langle V_z \rangle$ is the residence time of the fluid in the heat exchanger, $\langle V_z \rangle = F/A$ is the average axial velocity, $F$ is the flow rate, and $A=\pi(R_2^2-R_1^2)$ is the annular cross-sectional area. Both dimensionless control parameters have physical meaning: $N_T$ represents the number of turns that the outer cylinder makes over $\tau$ time units, whereas $N_P$ gives the number of modulation periods of the inner-cylinder angular velocity per average residence time.

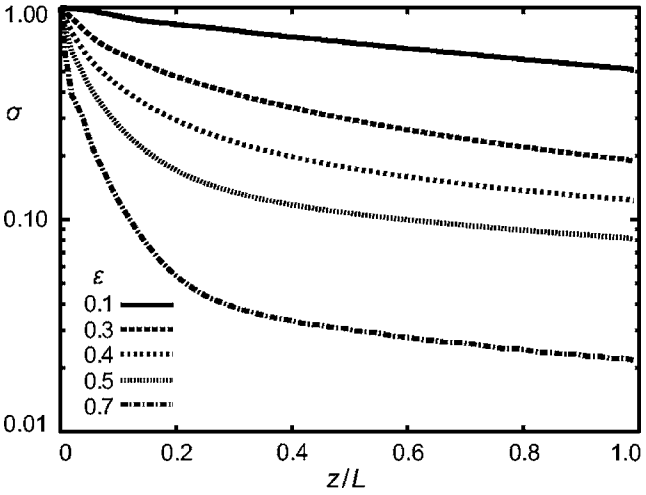


**Fig. 2 Axial $\sigma$ profile as a function of $\epsilon$ for steady boundary rotation**

## Heat-Transfer Analysis

To investigate the effect of geometry and inner-cylinder modulation protocol on the thermal efficiency of the heat exchanger, the following numerical experiment is implemented. The inner and outer boundaries are assumed adiabatic and fluid is continuously injected into the apparatus with an inlet temperature that is a linear function of the bipolar coordinate $\alpha$:

$$T(\alpha,\beta,0) = T_1 + \frac{T_2 - T_1}{\alpha_2 - \alpha_1}(\alpha - \alpha_1) \tag{6}$$

Note that this temperature distribution is the solution of the 2D steady-state heat conduction equation for the cross section of the heat exchanger with isothermal boundary conditions. It is evident that the best geometry and modulation protocol are those which give the most uniform outlet temperature distribution.

Uniformity of the cross-sectional temperature field is measured by its standard deviation, $\sigma'(z,t)$, defined as

$$[\sigma'(z,t)]^2 = \frac{1}{F}\int\int_A V_z(T - \langle T \rangle)^2 dA \tag{7}$$

where

$$\langle T \rangle(z,t) = \frac{1}{F}\int\int_A V_z T dA \tag{8}$$

is the cross-sectional average temperature. The influence of the chosen inlet temperature field can be largely eliminated if $\sigma'(z,t)$ is normalized with respect to its inlet value:

$$\sigma(z,t) = \sigma'(z,t)/\sigma'(0,t) \tag{9}$$

Because the velocity field is time periodic, the average of $\sigma(z,t)$ over a modulation period

$$\bar{\sigma}(z,t) = \frac{\omega}{2\pi}\int_t^{t+2\pi/\omega} \sigma(z,t) dt \tag{10}$$

becomes time invariant after a sufficiently long period of time. We denote by $\bar{\sigma}^{\infty}(z)$ the axial $\bar{\sigma}$ profile when this steady-periodic regime is established.

## Results and Discussion

We start by examining the influence of the eccentricity ratio on the performance of the eccentric annular heat exchanger for steady rotation of both boundaries. Figure 2 shows the axial $\sigma$

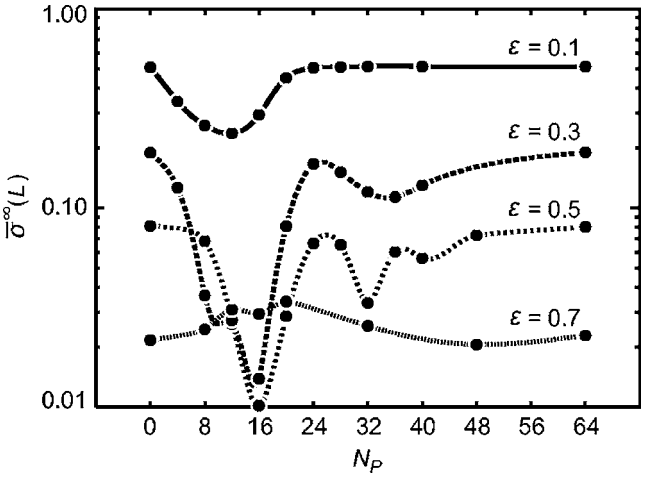


**Fig. 3 Exit value of $\bar{\sigma}^{\infty}(z)$ as a function of $N_P$ and $\epsilon$. Other parameters are $R_2/R_1=2$, $\bar{\Omega}_1/\Omega_2=-2$, and $N_T=30$.**

profile as a function of $\epsilon$. The other parameters are $R_2/R_1=2$, $\Omega_1/\Omega_2=-2$ (the inner cylinder counter-rotates at twice the angular velocity of the outer cylinder), and $N_T=30$. It is clear from the plotted results that a better performance is obtained when the cylinder centers are further apart, i.e., when $\epsilon$ is increased.

Let us now look at the effect of the inner-cylinder modulation on the performance of the heat exchanger. Figure 3 shows the exit value of $\bar{\sigma}^{\infty}(z)$ as a function of $N_P$ for different values of $\epsilon$. The other parameters are the same as those in Fig. 2. For values of $\epsilon$ equal to 0.1, 0.3, and 0.5, there is an optimum modulation frequency that minimizes the value of $\bar{\sigma}^{\infty}$. However, for $\epsilon=0.7$, the modulation of the inner-cylinder rotation leads to a performance decrease. The lowest value of $\bar{\sigma}^{\infty}$ is obtained for a moderate value of $\epsilon$ at the appropriate modulation frequency. This result is shown in Fig. 4, where the value of $\bar{\sigma}^{\infty}$ obtained at the optimum value of $N_P$ is plotted as a function of $\epsilon$. The best results are obtained for $\epsilon\approx 0.4$.

These results can be graphically and qualitatively confirmed in different ways using tools applicable for dissipative dynamical systems. In particular, the stretching field of a material point is an excellent indicator of the phenomena occurring in the heat exchanger. The stretching distribution provides a means of characterizing the distribution of mixing intensities within the flow.

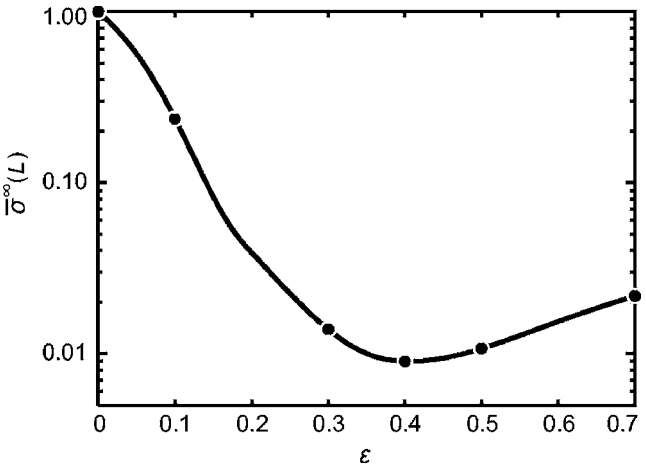


**Fig. 4 Minimum value of $\bar{\sigma}^{\infty}(z)$ at the optimal $N_P$ value as a function of $\epsilon$. Other parameters are the same as those in Fig. 3.**

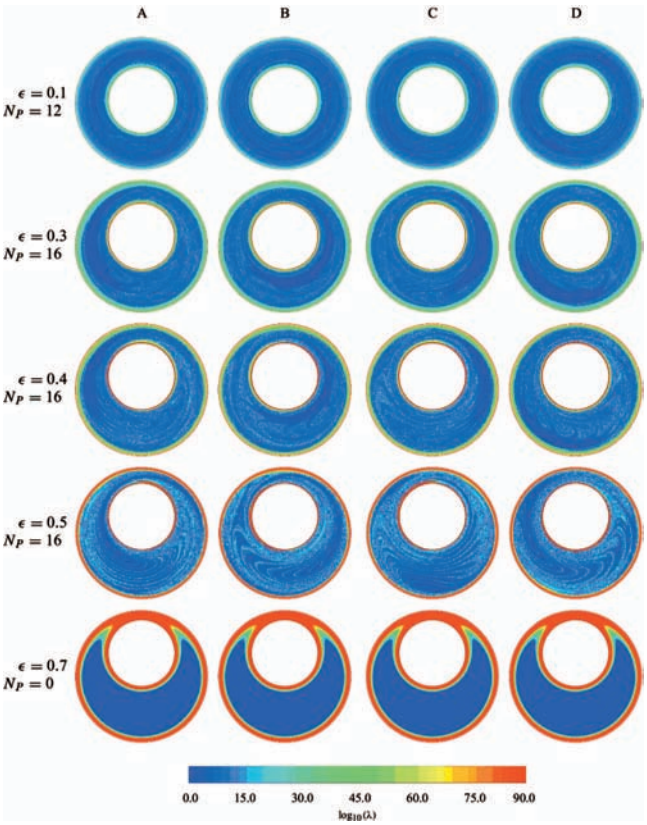


**Fig. 5 Logarithm of exit stretching distribution for the optimal $N_P$ value as a function of $\epsilon$. Other parameters are the same as those in Fig. 3.**

Points experiencing high and low stretching correspond to regions of good and poor micromixing, respectively. This tool was first introduced by Swanson and Ottino [14] for the journal bearing flow.

The stretching of a fluid element $\mathbf{l}$, associated with a particle initially located at $\mathbf{x}_0$, is monitored by integrating

$$\frac{d\mathbf{x}}{dt}=\mathbf{V}(\mathbf{x},t) \quad \frac{d\mathbf{l}}{dt}=(\nabla\mathbf{V})^T\cdot\mathbf{l} \tag{11}$$

The total accumulated stretching $\lambda$ experienced by the fluid element until it reaches the outlet of the heat exchanger is

$$\lambda=\|\mathbf{l}\|/\|\mathbf{l}_0\| \tag{12}$$

Calculations were performed with $N=2\times10^4$ particles covering uniformly the entire inlet cross section. Since the stretching increases exponentially, the logarithm of $\lambda$ is a more appropriate quantity to monitor. Figure 5 shows the exit distribution of $\log\lambda$ at the optimal $N_P$ value for each value of $\epsilon$. The contour plots in each column were obtained by feeding the particles at a particular instant of the modulation period: (a) at the beginning, (b) after one quarter of a period, (c) after half a period, and (d) after three quarters of a period. Although the contours were obtained at the optimal operating conditions for a given eccentricity value, one can see that only for moderate values of $\epsilon$ does $\log\lambda$ become uniformly distributed over the cross section.

Furthermore, it is for $\epsilon\approx0.4-0.5$ that the regions of very low stretching are minimized and, consequently, cold or hot spots are less likely to occur. This is demonstrated in Fig. 6, where the probability density function of $\log\lambda$

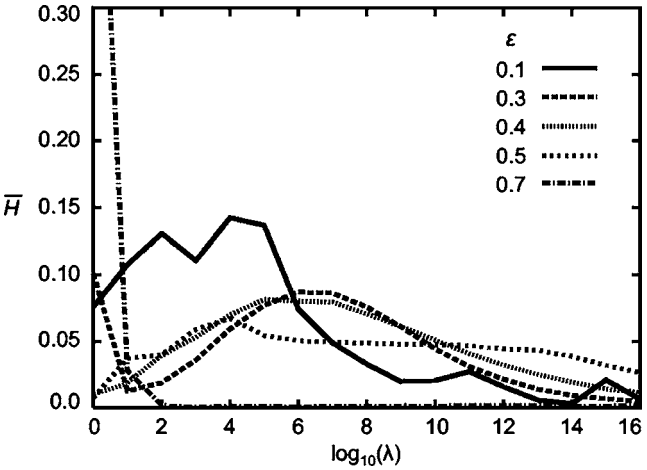


**Fig. 6 Probability density function, $H(\log \lambda)$, at the optimal $N_P$ value for different values of $\epsilon$. The plot is a close-up image of the low-stretching region. Other parameters are the same as those in Fig. 3.**

$$H(\log \lambda) = \frac{1}{N}\frac{dn(\log \lambda)}{d \log \lambda} \tag{13}$$

is plotted over the lower range of $\log \lambda$ at the optimal $N_P$ value for each eccentricity. In the above definition, $dn(\log \lambda)$ is the number of material points with accumulated stretching between $\log \lambda$ and $\log \lambda + d(\log \lambda)$.

Finally, Fig. 7 displays streak lines generated from the inlet of the heat exchanger for three different values of the modulation frequency. The geometrical configuration of the apparatus is the optimal one ($\epsilon$=0.4). The top figure, in which the streak lines are helical, was obtained for steady rotation of the inner cylinder. For the optimal $N_P$ value, the streak line is chaotic, as shown in the middle plot. Notice that even though the axial flow always moves forward, parts of the streak line go back since they wander into regions of low axial velocity, while other parts of the streak line bulge forward. However, when the modulation frequency is increased further, as in the bottom figure, the streak line is reorganized and becomes qualitatively very similar to that of the top figure. This phenomenon is very common in fluid instability theory, where it is known that instability occurs over a certain frequency range. For values outside that range, perturbations are damped and the system is stable.

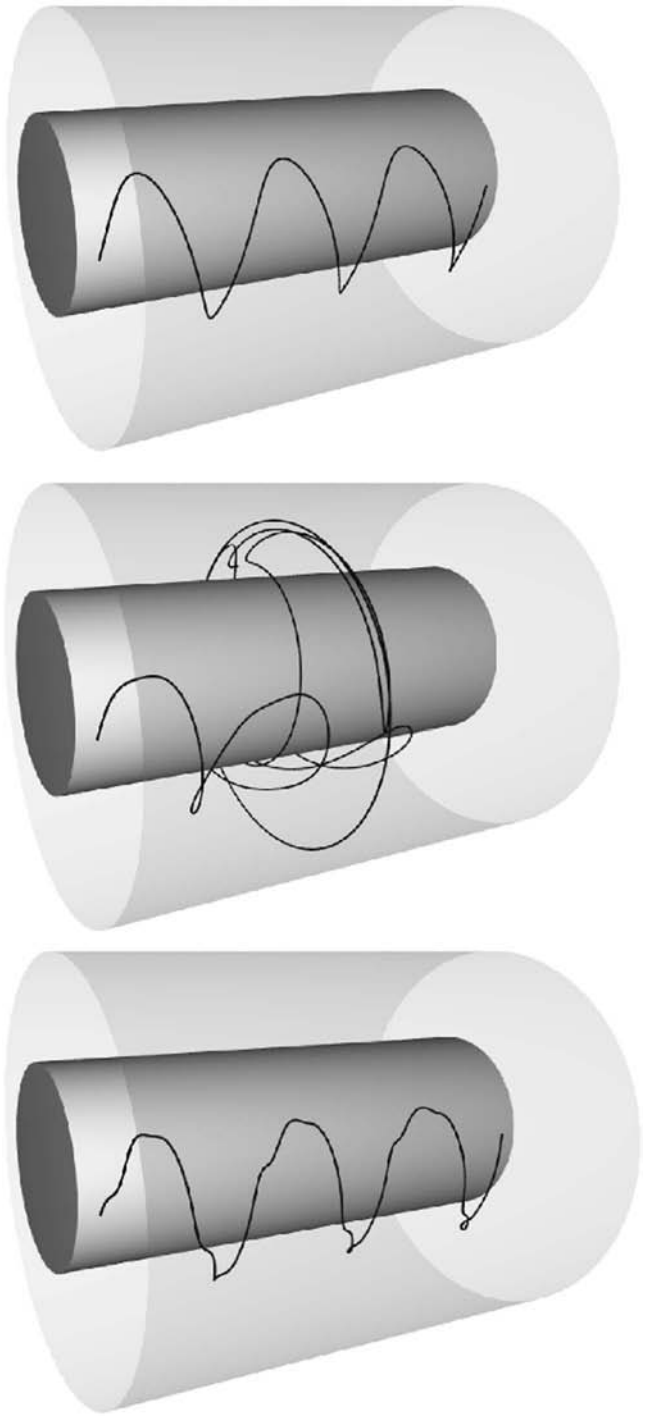

**Fig. 7 Streak lines generated for three different values of $N_P$. The operating parameters are $\epsilon$=0.4, $R_2/R_1$=2, $\bar{\Omega}_1/\Omega_2$=−2, and $N_T$=30; the $N_P$ values are, from top to bottom, 0, 16, and 64.**

## Conclusions

The convection-diffusion equation was solved numerically for 3D laminar flow in the eccentric helical annular heat exchanger. The outer cylinder turns at a constant velocity, while the inner-cylinder angular velocity varies time periodically in the opposite direction. If both cylinders turn at constant velocity, the largest thermal efficiency is obtained for highly eccentric configurations. If the inner-cylinder angular velocity is modulated at the appropriate frequency, the efficiency is shown to be better than that obtained without modulation. However, for this to occur, the geometrical configuration must be moderately eccentric, $\epsilon \approx 0.4-0.5$.

## Nomenclature

$H$ = probability density function
$L$ = axial length
$N_P$, $N_T$ = control parameters, Eq. (5)
$P$ = pressure
$R$ = cylinder radius
$T$ = temperature
$V$ = velocity component
$z$ = axial coordinate

### Greek Symbols

$\alpha, \beta$ = bipolar coordinates
$\delta$ = modulation amplitude
$\epsilon$ = eccentricity ratio
$\lambda$ = stretching of a material point
$\mu$ = fluid viscosity
$\sigma$ = standard deviation
$\omega$ = modulation frequency

$\Omega$ = angular velocity

**Subscripts**

1 = inner cylinder
2 = outer cylinder

## References


[1] Kays, W. M., 1968, *Convective Heat Transfer*, McGraw-Hill, New York.
[2] Shah, R. K., 1978, *Laminar Flow Forced Convection in Ducts*, Academic, New York.
[3] Aref, H., 2002, "The Development of Chaotic Advection," Phys. Fluids, **14**, pp. 1315–1325.
[4] Ottino, J. M., 1989, *The Kinematics of Mixing: Stretching, Chaos and Transport*, Cambridge University Press, Cambridge.
[5] Kusch, H. A., and Ottino, J. M., 1992, "Experiments on Mixing in Continuous Chaotic Flows," J. Fluid Mech., **236**, pp. 319–342.
[6] Rodrigo, A. J. S., Mota, J. P. B., Lefèvre, A., and Saatdjian, E., 2003, "On the Optimization of Mixing Protocol in a Certain Class of 3-D Stokes Flows," Phys. Fluids, **15**, pp. 1505–1515.
[7] Lefèvre, A., Leprévost, J. C., Mota, J. P. B., Rodrigo, A. J. S., and Saatdjian, E., 2003, "Chaotic Advection in a 3-D Stokes Flow," AIChE J., **29**, pp. 2749–2758.
[8] Rodrigo, A. J. S., Rodrigues, R. C. R., Formiga, N. F. C., Mota, J. P. B., and Saatdjian, E., 2006, "Mixing Enhancement by Frequency-Selective Chaotic Advection in a 3-D Time-Periodic Stokes Flow," Chem. Eng. Commun., **193**, pp. 743–753.
[9] Saatdjian, E., Midoux, N., and Andre, J. C., 1994, "On the Solution of Stokes Equations Between Confocal Ellipses," Phys. Fluids, **6**, pp. 3833–3846.
[10] Snyder, W. T., and Goldstein, G. A., 1965, "An Analysis of Fully Developed Laminar Flow in an Eccentric Annulus," AIChE J., **11**, pp. 762–767.
[11] Aref, H., and Balanchandar, A., 1986, "Chaotic Advection in a Stokes Flow," Phys. Fluids, **29**, pp. 3515–3521.
[12] Chaiken, J., Chevray, R., Tabor, M., and Tan, Q. M., 1986, "Experimental Study of Lagrangian Turbulence in a Stokes Flow," Proc. R. Soc. London, Ser. A, **408**, pp. 165–174.
[13] Kaper, T. J., and Wiggins, S., 1993, "An Analytical Study of Transport in Stokes Flows Exhibiting Large-Scale Chaos in the Eccentric Journal Bearing," J. Fluid Mech., **253**, pp. 211–243.
[14] Swanson, P. D., and Ottino, J. M., 1990, "A Comparative Computational and Experimental Study of Chaotic Mixing in Viscous Fluids," J. Fluid Mech., **213**, pp. 227–249.

# Analytical Solution for Heat Conduction Near an Encapsulated Sphere With Heat Generation

**Douglas L. Oliver**
Associate Professor
Mechanical Engineering,
University of Toledo,
Toledo, OH 43606

*Keywords: generation, conduction, sphere, analytic, transient*

## Introduction

The analytic study of heat conduction near spheres is a relatively mature science. Even so, there are still a number of analytic conduction solutions being published. For example, Atefi and Moghimi [1] recently presented a Fourier series solution for heat transfer near a hollow sphere.

Probably the most comprehensive collection of classic analytic solutions to heat conduction problems is found in the text by Carslaw and Jaeger [2]. One of the solutions in that text relates to the temperature profile about a spherical void where the surface of the void was exposed to a uniform heat flux (Eq. (4) of Section 9.10 of Ref. [2]).

One modification of the above classical solution is to consider an encapsulated sphere with a uniform volumetric heat generation rate, $\dot{q}$. If the temperature of the sphere is initially equal to that of the surrounding medium, and if the sphere has a negligible capacity for storing heat (e.g., $\rho c \approx 0$), then the temperature profile in the encapsulating medium is given by

$$\frac{k_2(T(r,\tau)-T_\infty)}{\dot{q}a^2} = \frac{1}{3r}\left[\operatorname{erfc}\left(\frac{r-1}{2\sqrt{\tau}}\right) - \exp(r-1+\tau)\operatorname{erfc}\left(\frac{r-1}{2\sqrt{\tau}}+\sqrt{\tau}\right)\right] \quad (1)$$

where $a$ is sphere radius, $k_2$ is the thermal conductivity of the surrounding medium, $r$ is the dimensionless radial coordinate, and $\tau$ is the dimensionless time.

The present work expands the classic solution given in Eq. (1) to include spheres with non-negligible heat capacities. This work proposes an analytic solution for transient conduction from a highly conductive sphere that is encapsulated in an infinite medium. The sphere is heated with a uniform rate of heat generation. This heat generation could be from electrical resistance heating, nuclear decay, or from an exothermic (or endothermic) chemical reaction. The transient heat transfer from the sphere is modeled as a function of the ratio of heat capacitance of the sphere to that of the surrounding material.

## Problem Statement

Consider a highly conductive sphere encapsulated in an infinite medium. The sphere is experiencing a uniform rate of heat generation. If the thermal conductivity of the sphere is much larger than the thermal conductivity of the surrounding material, then the temperature profile of the sphere will be nearly spatially uniform. That is, this solution assumes that

$$k_1/k_2 \gg 1$$

where $k$ is the thermal conductivity. The subscript 1 refers to the sphere and 2 refers to the surrounding material.

If the sphere is in good thermal contact with the surrounding material, then the (spatially uniform) temperature of the sphere will be the same as the temperature of the inner surface of the surrounding material.

Finally, the temperature profile is assumed to be a transient function of the radial coordinate. That is, the temperature profile is assumed to be independent of the tangential and azimuthal coordinates.

With the above assumptions, only the temperature in the surrounding material needs to be modeled. The dimensional diffusion equation for conduction in the surrounding material is

$$\frac{1}{\hat{r}^2}\frac{\partial}{\partial \hat{r}}\left(\hat{r}^2\frac{\partial T_2}{\partial \hat{r}}\right) = \frac{1}{\alpha_2}\frac{\partial T_2}{\partial t} \quad (2)$$

The initial and boundary conditions imposed on Eq. (2) are

$$T_1(t=0) = T_2(\hat{r}, t=0) = T_\infty$$

$$T_2(\hat{r}=a,t) = T_1(t)$$

$$\lim_{\hat{r}\to\infty} T_2 = T_\infty$$

where $T_\infty$ is the far-field temperature.

An energy balance on the sphere yields the following relation:

$$\left(\frac{4}{3}\pi a^3\right)\dot{q} + k_2(4\pi a^2)\left.\frac{\partial T_2}{\partial \hat{r}}\right|_{\hat{r}=a} = (\rho c)_1\left(\frac{4}{3}\pi a^3\right)\frac{dT_1}{dt} \quad (3)$$

where $a$ is the sphere radius, $\dot{q}$ is the volumetric rate of heat generation in the sphere, $\rho_1$ is the density of the sphere, and $c_1$ is the specific heat of the sphere.

## Problem Solution

The above equations may be made dimensionless with the following transformations:

$$r = \frac{\hat{r}}{a} \quad \tau = \frac{\alpha_2 t}{a^2} \quad \Theta_1(\tau) = \frac{k_2(T_1-T_\infty)}{\dot{q}a^2} \quad \Theta_2(r,\tau) = \frac{k_2(T_2-T_\infty)}{\dot{q}a^2}$$

Equation (2) in a dimensionless format is

$$\frac{1}{r^2}\frac{\partial}{\partial r}\left(r^2\frac{\partial \Theta_2}{\partial r}\right) = \frac{\partial \Theta_2}{\partial \tau} \quad (4)$$

The corresponding initial and boundary conditions are

$$\Theta_1(\tau=0) = \Theta_2(r, \tau=0) = 0$$

$$\Theta_1(\tau) = \Theta_2(r=1,\tau)$$

$$\lim_{r\to\infty} \Theta_2 = 0$$

Finally, Eq. (3) in dimensionless format is

$$1 + 3\left.\frac{\partial \Theta_2}{\partial r}\right|_{r=1} = C\frac{d\Theta_1}{d\tau} \quad (5)$$

where $C$ is the heat capacitance ratio defined by $C=(\rho c)_1/(\rho c)_2$.

Equation (4) may be solved using Laplace transforms with the following transformed variables: $x=r-1$ and $U(x,\tau)=r\Theta_2$. In terms of these variables, Eq. (4) is

$$\frac{\partial^2 U}{\partial x^2} = \frac{\partial U}{\partial \tau} \quad (6)$$

with initial and boundary conditions of

$$U(x, \tau=0) = 0$$

Contributed by the Heat Transfer Division of ASME for publication in the JOURNAL OF HEAT TRANSFER. Manuscript received October 24, 2006; final manuscript received May 17, 2007; published online February 4, 2008. Review conducted by Ramendra P. Roy.

  

$$U(x=0,\tau)=\Theta_1(\tau)$$

$$\lim_{x\to\infty} U < O(x^1) \tag{7}$$

Finally, Eq. (5) becomes

$$1+3\left.\frac{\partial U}{\partial x}\right|_{x=0}-3U(x=0,\tau)=C\left.\frac{\partial U}{\partial \tau}\right|_{x=0} \tag{8}$$

A solution to Eq. (6) may be obtained using Laplace transforms with $L[U(x,\tau)]=F(x,s)$. (See Chapter 7 of Ozisik [3] for an overview of Laplace transform methods as applied to heat conduction.) Substituting this into Eq. (6) with the initial condition yields

$$\frac{d^2F}{dx^2}=sF(x,s) \tag{9}$$

A general form of a solution to Eq. (9) is

$$F(x,s)=g(s)e^{-x\sqrt{s}}+h(s)e^{x\sqrt{s}}$$

The boundary condition imposed by Eq. (7) implies that $h(s)=0$ or

$$F(x,s)=g(s)e^{-x\sqrt{s}} \tag{10}$$

Substituting this into the Laplace transform of Eq. (8) yields

$$g(s)=\frac{1}{s(Cs+3\sqrt{s}+3)} \tag{11}$$

The temperature profile in the surrounding material is then

$$\Theta_2(r,\tau)=\frac{1}{r}L^{-1}\left[\frac{e^{-(r-1)\sqrt{s}}}{s(Cs+3\sqrt{s}+3)}\right] \tag{12}$$

While the dimensionless temperature of the sphere is

$$\Theta_1(\tau)=L^{-1}\left[\frac{1}{s(Cs+3\sqrt{s}+3)}\right]$$

Assuming that $C\neq 3/4$, Eq. (12) may be inverted using the sum of partial fractions. The corresponding value for $\Theta_2(x,\tau)$ is then

$$\begin{aligned}\Theta_2(x,\tau)=&\frac{1}{3r}\left[\operatorname{erfc}\left(\frac{r-1}{2\sqrt{\tau}}\right)\right]\quad(\text{for } C\neq 3/4)\\&+\frac{1}{r}\frac{2C(-3+\sqrt{9-12C})}{(18-12C)\sqrt{9-12C}-54+72C}\\&\times\exp[-R_a(r-1)+R_a^2\tau]\operatorname{erfc}\left(-R_a\sqrt{\tau}+\frac{r-1}{2\sqrt{\tau}}\right)\\&+\frac{1}{r}\frac{2C(3+\sqrt{9-12C})}{(18-12C)\sqrt{9-12C}+54-72C}\\&\times\exp[-R_b(r-1)+R_b^2\tau]\operatorname{erfc}\left(-R_b\sqrt{\tau}+\frac{r-1}{2\sqrt{\tau}}\right)\end{aligned} \tag{13}$$

where

$$R_a=\frac{-3+\sqrt{9-12C}}{2C}\quad\text{and}\quad R_b=\frac{-3-\sqrt{9-12C}}{2C}$$

There are at least two practical problems with the form of Eq. (13). First, as $\tau$ increases Eq. (13) becomes difficult to evaluate. Second, for values of $C>3/4$ the argument used for the complementary error function is complex. Both of these problems may be solved by using the complex Faddeeva function, $w(z)$ (see, for example, Eq. 7.1.3 of Abramowitz and Stegun, Ref. [4]):

$$w(z)=\exp(-z^2)\operatorname{erfc}(-iz) \tag{14}$$

To restate Eq. (14) in terms of the Faddeeva function, use the complex arguments:

$$z_a(\tau)=\left(-R_a\sqrt{\tau}+\frac{r-1}{2\sqrt{\tau}}\right)i\quad\text{and}\quad z_b(\tau)=\left(-R_b\sqrt{\tau}+\frac{r-1}{2\sqrt{\tau}}\right)i \tag{15}$$

Substitution of Eqs. (14) and (15) into Eq. (13) yields the dimensionless temperature in terms of the Faddeeva function:

$$\begin{aligned}\Theta_2(x,\tau)=&\frac{1}{3r}\left[\operatorname{erfc}\left(\frac{r-1}{2\sqrt{\tau}}\right)\right]\quad(\text{for } C\neq 3/4)\\&+\frac{1}{r}\frac{2C(-3+\sqrt{9-12C})}{(18-12C)\sqrt{9-12C}-54+72C}\\&\times\exp\left(\frac{-(r-1)^2}{4\tau}\right)w(z_a(\tau))\\&+\frac{1}{r}\frac{2C(3+\sqrt{9-12C})}{(18-12C)\sqrt{9-12C}+54-72C}\\&\times\exp\left(\frac{-(r-1)^2}{4\tau}\right)w(z_b(\tau))\end{aligned} \tag{16}$$

The software used to calculate the Faddeeva function was copied from Munoz [5]. This software was checked for accuracy against selected values of $w(z)$ using Table 7.9 of Ref. [4].

A short discussion is in order as to why Eq. (16) yields real values for $\Theta_2$. For $C<3/4$ both $z_a$ and $z_b$ are pure imaginary numbers. Inspection of Eq. (14) will reveal that if $z$ is a pure imaginary number, then $w(z)$ is a real number.

Conversely, for $C>3/4$ $z_b=-\bar{z}_a$ and

$$\frac{2C(-3+\sqrt{9-12C})}{(18-12C_r)\sqrt{9-12C}-54+72C}=\overline{\left(\frac{2C(3+\sqrt{9-12C})}{(18-12C_r)\sqrt{9-12C}+54-72C}\right)}$$

From Eq. (7.1.12) of Ref. [4], it may be shown that

$$w(-\overline{z_a(\tau)})=\overline{w(z_a(\tau))}$$

Hence, Eq. (16) may be shown to be the sum of a complex conjugate pair of numbers with

$$\begin{aligned}\Theta_2(x,\tau)=&\frac{1}{3r}\left[\operatorname{erfc}\left(\frac{r-1}{2\sqrt{\tau}}\right)\right]\quad(\text{for } C>3/4)+\frac{1}{r}\exp\left(\frac{-(r-1)^2}{4\tau}\right)\\&\times\left\{\frac{2C(-3+\sqrt{9-12C})}{(18-12C_r)\sqrt{9-12C}-54+72C}w(z_a(\tau))\right.\\&\left.+\overline{\left(\frac{2C(-3+\sqrt{9-12C})}{(18-12C_r)\sqrt{9-12C}-54+72C}w(z_a(\tau))\right)}\right\}\end{aligned} \tag{17}$$

Since the sum of a complex conjugate pair is a real number, it follows that Eq. (16) results in a real value for $\Theta_2$ when C $>3/4$.

## Results and Discussion

The implementation of Eq. (16) may be verified by comparing it with the simpler solutions for three limiting cases of $C=0$, as $C$ becomes large, and for steady-state.

*Special Case 1:* $C=0$. As discussed above, for the special case where $C=0$ the solution may be adapted from Eq. (4) of Section 9.10 of Ref. [2]:

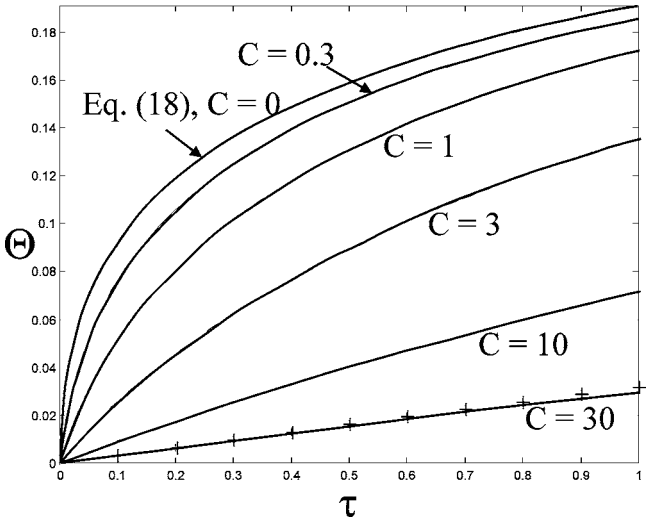


**Fig. 1 $\Theta_1(\tau)$ for several values of *C* at moderate times. The "+" symbol represents the predictions of Eq. (21) for *C*=30. (The steady-state value of Θ is 1/3.)**

$$\lim_{C\to 0}\Theta_2(r,\tau)=\frac{1}{3r}\,\mathrm{erfc}\left(\frac{r-1}{2\sqrt{\tau}}\right)-\frac{1}{3r}\exp(r-1+\tau)\mathrm{erfc}\left(\sqrt{\tau}+\frac{r-1}{2\sqrt{\tau}}\right) \tag{18}$$

The results of Eq. (16) are compared with the special case of $C=0$ on Fig. 1 at the sphere surface ($r=1$) and on Fig. 2 at a distance of one radius into the surrounding material ($r=2$). As is demonstrated in Figs. 1 and 2, for the limiting case of $C\to 0$, the predictions of Eq. (16) model well those of Eq. (18).

*Special Case 2: $C\to\infty$.* As *C* becomes very large, the surrounding material may be modeled as being in a quasisteady state. Under these circumstances, the temperature profile in the surrounding material may be approximated as

$$\lim_{C\to\infty}\Theta_2(r,\tau)\approx\frac{\Theta_1(\tau)}{r} \tag{19}$$

Substituting this relation into Eq. (5) yields the following ordinary differential equation in dimensionless form:

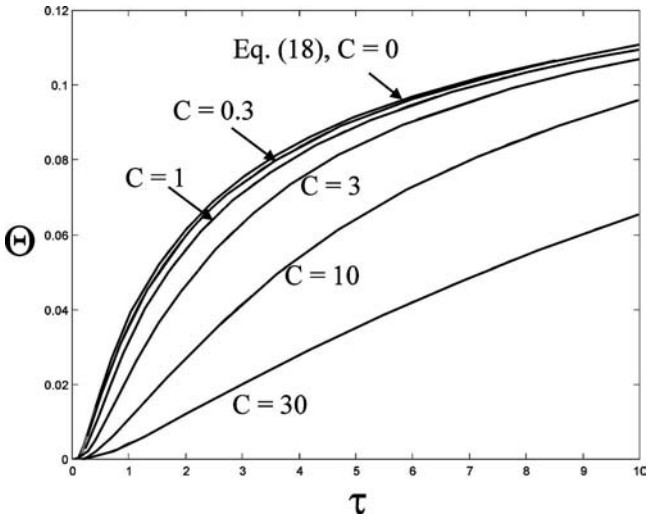


**Fig. 2 $\Theta_2(r,\tau)$ with $r=2$ for several values of *C*. (The steady-state value of Θ is 1/6.)**

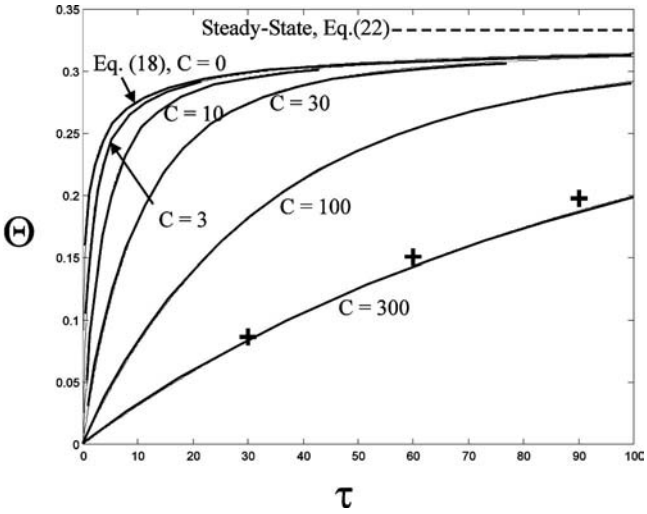


**Fig. 3 $\Theta_1(\tau)$ for several values of *C* at large times. The "+" symbol represents the predictions of Eq. (21) for *C*=300.**

$$1-3\Theta_1=C\frac{d\Theta_1}{d\tau} \tag{20}$$

The initial condition on Eq. (20) is $\Theta_1(\tau=0)=0$. The solution is then

$$\lim_{C\to\infty}\Theta_1(\tau)=\frac{1}{3}\left(1-\exp\left(-\frac{3\tau}{C}\right)\right). \tag{21}$$

The predictions of Eq. (16) are compared with those of Eq. (21) for $C=30$ on Fig. 1 and for $C=300$ on Fig. 3. Equation (21) is in reasonable agreement with Eq. (16) if $\tau$ is sufficiently low.

*Special Case 3: Steady State*. The steady-state solution may be readily shown to be

$$\lim_{\tau\to\infty}\Theta_2(r,\tau)=\frac{1}{3r} \tag{22}$$

Equation (22) should serve as an upper bound for the temperature profile. Note in Figs. 1 and 2 that for short times, the predicted temperature profile is well below those of Eq. (22). However, at very large times, the results of Eq. (16) slowly approach the steady-state value predicted by Eq. (22) as is illustrated in Fig. 3.

## Conclusion

The temperature profile near a highly conducting sphere enclosed in an infinite conducting medium has been analytically determined. This solution considers the effect of the heat capacitance ratio *C* as well as the dimensionless radial coordinate and time. This solution has been compared with solutions for three limiting cases.

## Nomenclature

$a$ = radius of the sphere
$c$ = specific heat
$C$ = heat capacitance ratio $C=\rho_1 c_1/\rho_2 c_2$
$k$ = thermal conductivity
$\dot{q}$ = heat generation rate ($W/m^3$)
$\hat{r}$ = dimensional radial coordinate
$r$ = $r=\hat{r}/a$
$R$ = see Eq. (13)
$s$ = parameter for Laplace transforms
$t$ = time
$T$ = temperature
$U$ = $r\Theta_2$

$w(z)$ = Faddeeva function, see Eq. (14)
$x$ = $r-1$

**Greek**

$\alpha$ = thermal diffusivity
$\rho$ = density
$\tau$ = dimensionless time, $\tau=\alpha_2 t/a^2$
$\Theta$ = $\Theta=k_2(T-T_\infty)/\dot{q}a^2$

**Subscripts**

1 = pertaining to the sphere
2 = surrounding material
$\infty$ = far-field value

## References


[1] Atefi, G., and Mahadi, M., 2006, "A Temperature Fourier Series Solution for a Hollow Sphere," ASME J. Heat Transfer, **128**(9), pp. 963–968.
[2] Carslaw, H. S., and Jaeger, J. C., 1959, *Conduction of Heat in Solids*, 2nd ed., Oxford, New York.
[3] Necati Ozisik, M., 1993, *Heat Conduction*, 2nd ed., Wiley-Interscience, New York.
[4] Abramowitz, M., and Stegun, I. A., 1964, *Handbook of Mathematical Functions*, National Bureau of Standards.
[5] Munoz, V., 2004, Octave-based function *faddeeva(z)*, Version 1.0, available at http://wiki.octave.org

# Simulation of Thermal Transport in Open-Cell Metal Foams: Effect of Periodic Unit-Cell Structure

**Shankar Krishnan**[1]

**Suresh V. Garimella**
e-mail: sureshg@ecn.purdue.edu

**Jayathi Y. Murthy**

Cooling Technologies Research Center,
School of Mechanical Engineering,
Purdue University,
West Lafayette, IN 47907-2088

*Direct simulation of thermal transport in open-cell metal foams is conducted using different periodic unit-cell geometries. The periodic unit-cell structures are constructed by assuming the pore space to be spherical and subtracting the pore space from a unit cube of the metal. Different types of packing arrangement for spheres are considered—body centered cubic, face centered cubic, and the A15 lattice (similar to a Weaire-Phelan unit cell)—which give rise to different foam structures. Effective thermal conductivity, pressure drop, and Nusselt number are computed by imposing periodic boundary conditions for aluminum foams saturated with air or water. The computed values compare well with existing experimental measurements and semiempirical models for porosities greater than 80%. The effect of different foam packing arrangements on the computed thermal and fluid flow characteristics is discussed. The capabilities and limitations of the present approach are identified.* [DOI: 10.1115/1.2789718]

## Introduction

Foams and other highly porous cellular solids have many interesting combinations of physical, mechanical, electrical, and thermal properties such as high stiffness, flow permeability, and thermal and electrical conductivity along with low specific weight. Many common materials are highly porous in nature. Examples of such highly porous natural materials include cork, wood, bones (trabecular and cancellous), and sponges [1–3]. Current state-of-the-art manufacturing methods allow foaming of polymers, most metals and their alloys, ceramics, and graphite. Among the available synthetic open porous materials, polymer foams have enjoyed widespread use in many industrial technologies [3]. Recently, open-cell metal foams have been attracting increased attention as multifunctional materials due to their versatility in absorbing sound and energy [2]. Open-cell foams have a random reticulated structure of open polyhedral cells connected by continuous metal ligaments. Due to their highly porous reticulated nature, open-cell foams with negative Poisson's ratio (termed auxetic foams) have been produced by Lakes [4] and by many others [5] from conventional positive Poisson's ratio materials. Depending on the porosity of the cellular materials, a wide range of applications is possible. Figure 1 shows the variation of the degree of openness of the foams and their corresponding application [3].

Open-cell foams have been proposed for many applications such as porous tissue engineering scaffolds [6,7], hydrogen storage technologies [8], thermal control of electronics, catalysis [9], solar energy storage [10], electrochemical cells [11], and others [2,12]. The present study is primarily concerned with thermal management applications. With increased heat dissipation requirements for microprocessors [13] and many other electronics systems, demand for the development of compact heat dissipation systems continues to increase. Open-cell materials, owing to their ability to integrate multiple functions, are very attractive as thermal management materials. Many previous investigators have proposed and analyzed metal foams for possible applications as heat exchangers [14–16], heat sinks [17,18], and heat pipe wicks.

Experimental measurements and numerical modeling to understand the overall, macroscopic thermal and fluid flow characteristics such as effective thermal conductivity, friction factor, and Nusselt number have been conducted by many previous investigators [15,19–21]. However, not many studies have attempted a detailed understanding at the pore scale. Some of the available literature on the microscopic approach to modeling foams is reviewed in Ref. [22]. Detailed modeling of pore-scale heat transfer is necessary for a number of reasons. Resolution of flow and heat transfer at the pore scale has been found to yield accurate predictions of effective thermal conductivity, pressure drop, and local heat transfer coefficient. Pore-scale models are also required to develop closure arguments for macroscopic models [17]. Furthermore, such models allow the investigation of flow and thermal dispersion effects.

The objective of this work is to extend to lower porosities the methodology described in our previous work on direct simulation of heat and fluid flow through open-cell foams [22]. In our previous work, we proposed a unit-cell body-centered cubic (bcc) geometry for representing open-cell foams. The detailed simulations on the foam unit cell were able to predict effective thermal conductivity, friction factor, and interstitial Nusselt number, which agreed with existing experimental measurements for $\varepsilon > 0.94$. The present work examines alternative unit-cell representations for foams and identifies those which best capture experimental data on friction factor, Nusselt number, and effective thermal conductivity as a function of porosity. In the next section, we describe the foam geometry creation followed by a brief discussion of our mathematical and computational methodology [22]. Subsequently, we discuss the predictions obtained, and provide conclusions and remarks on future work.

## Foam Geometry

In this work, we use the same methodology for geometry creation as discussed in Ref. [22]. The shape of the pore is assumed to be spherical and spheres of equal volume are arranged according to the following three lattice structures: (i) bcc, (ii) face-centered cubic (fcc), and (iii) A15 lattice, a geometry similar to Weaire-Phelan structure [23,24]. The periodic foam unit-cell geometry is obtained by subtracting the unit-cell cube from the spheres at the various lattice points, as shown in Fig. 2(*a*). The cross section of the foam ligaments is a set of convex triangles (Plateau borders), all of which meet at symmetric tetrahedral vertices [23]. It may be noted that there is a nonuniform distribution of metal mass along the length of the ligament with more mass accumulating at the vertices (nodes) resulting in a thinning at the center of the ligament as experimentally observed in foam samples by many authors (e.g., Ref. [25]). Figure 2(*b*) shows sample open-cell structures formed for three different lattice arrangements.

The distinguishing features of this approach are that (i) the geometry creation is simple, (ii) it captures many of the important features of real foams, and (iii) meshing of the geometry is easier compared to the approach adopted in Ref. [26] for computing pressure drop.

[1]Currently at Bell Labs Ireland, Dublin, Ireland.

Contributed by the Heat Transfer Division of ASME for publication in the JOURNAL OF HEAT TRANSFER. Manuscript received December 8, 2006; final manuscript received June 4, 2007; published February 6, 2008. Review conducted by Jamal Seyed-Yagoobi. Paper presented at the 2006 ASME International Mechanical Engineering Congress (IMECE2006), Chicago, IL, November 5–10, 2006.

  

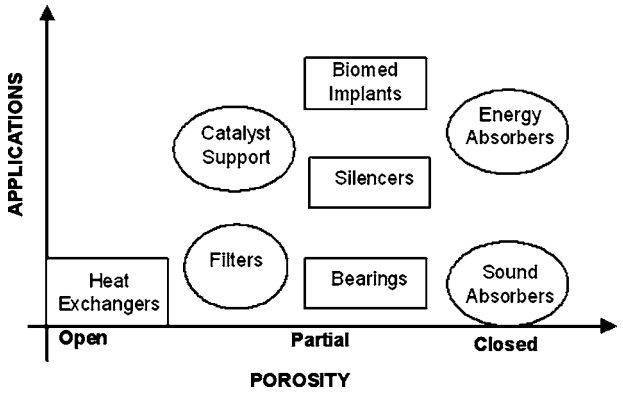


**Fig. 1 Applications of porous cellular materials classified by the type of cellular geometry (adapted from Ref. [3])**

## Mathematical Modeling

**Flow and Temperature Periodicity for Convective Flow and Heat Transfer Simulation.** We first consider the formulation employed for computing flow and heat transfer through the pores; the formulation for computing effective thermal conductivity of foam-fluid mixtures is given in a separate section. We consider a three-dimensional periodic module with a constant translational vector ($\mathbf{L}$) with respect to a flow direction ($x$ axis), as shown in Fig. 3. For periodic boundaries, according to Ref. [27], the velocity and the pressure at any position $\mathbf{r}$ can be written as

$$u_i(\mathbf{r}) = u_i(\mathbf{r}+\mathbf{L}) = u_i(\mathbf{r}+2\mathbf{L}) = \cdots$$

$$P(\mathbf{r}) - P(\mathbf{r}+\mathbf{L}) = P(\mathbf{r}+\mathbf{L}) - P(\mathbf{r}+2\mathbf{L}) = \cdots$$

It should be noted that there may be other periodic boundaries in the module, but there is *no net inflow* through any of these boundaries. For flow through periodic unit cells, the pressure gradient can be divided into two components: (a) periodic component, $\partial\hat{p}/\partial x_i$, and (b) a linearly varying component, $(\partial\bar{p}/\partial x_i)\mathbf{e}_L$, such that $\partial P/\partial x_i = (\partial\bar{p}/\partial x_i \mathbf{e}_{L,i}) + (\partial\hat{p}/\partial x_i)$, where, $e_{L,i}$ is the $i$th component of the unit vector in the direction $\mathbf{L}$.

A constant heat flux is imposed on the metal foam surfaces. For given heat-flux boundary conditions, the form of the temperature field becomes constant from module to module. Thus, the periodic condition for the temperature is given by

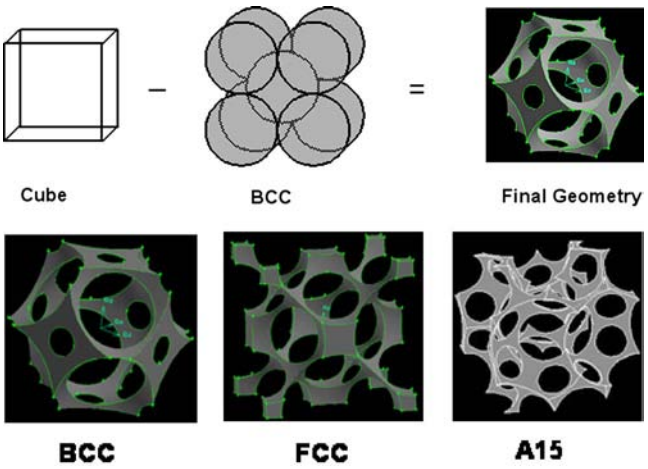


**Fig. 2 (*a*) Schematic representation of foam geometry creation and (*b*) sample images of foam geometry created for bcc, fcc, and A15 arrangements of spherical pores**

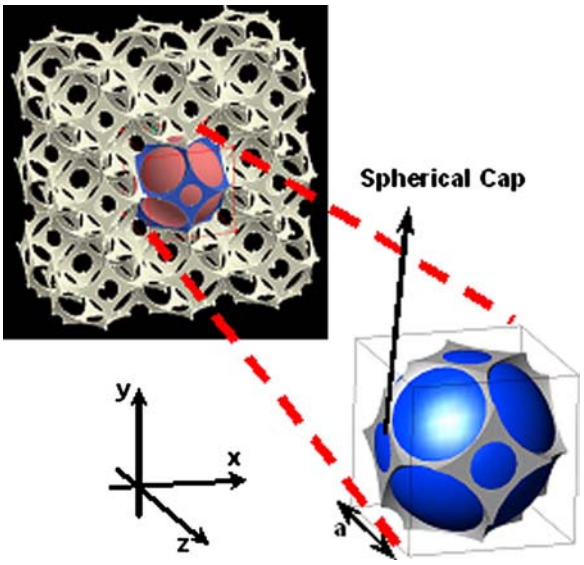


**Fig. 3 Schematic illustration of a periodic domain**

$$T(\mathbf{r}) - T_b(\mathbf{r}) = T(\mathbf{r}+\mathbf{L}) - T_b(\mathbf{r}+\mathbf{L}) = T(\mathbf{r}+2\mathbf{L}) - T_b(\mathbf{r}+2\mathbf{L}) = \cdots$$

Here, the bulk temperature $T_b$ is defined as

$$T_b = \frac{\int\int_A |u_i e_{L,i}| T dA}{\int\int_A |u_i e_{L,i}| dA}$$

where $A$ is the area of cross section.

**Governing Equations.** The governing flow and heat transfer equations for *laminar, periodic, fully developed, incompressible*, steady flow of a Newtonian fluid are [27,28]

$$\frac{\partial}{\partial x_i}(\rho u_i) = 0 \tag{1}$$

$$\frac{\partial}{\partial x_j}(\rho u_i u_j) = -\frac{\partial\hat{p}}{\partial x_i} + \frac{\partial}{\partial x_j}\left(\mu\frac{\partial u_i}{\partial x_j}\right)_i - \frac{\partial\bar{p}}{\partial x_i}e_{L,i} \tag{2}$$

$$\frac{\partial}{\partial x_i}(\rho u_i C_p T) = \frac{\partial}{\partial x_i}\left(k\frac{\partial T}{\partial x_i}\right) \tag{3}$$

The above equations are written assuming that the flow is thermally and hydrodynamically fully developed. Though the current study considers only the laminar flow condition, it can be extended to fully developed turbulent regimes. In Eq. (3), the terms involving $\partial^2/\partial x^2$ have been included to account for the large local streamwise gradients that may occur in periodically fully developed flows. The $\partial\bar{p}/\partial x_i$ term in Eq. (2) is assigned a priori, and controls the mass flow rate through the module, and hence, the pore Reynolds number. A no-slip boundary condition is imposed for the velocities on the bounding walls. As mentioned previously, a constant heat flux is specified for the energy equation on the foam surfaces. Details of the mathematical model are available in Refs. [22,27], while those on the numerical methods for periodic flow and heat transfer on unstructured meshes along with the implementation are outlined in Ref. [28].

The various periodic unit-cell geometries used in this work were created using the commercial software GAMBIT [29]. The geometry was discretized into three-dimensional finite volumes using hybrid (tetrahedral and hexahedral) elements in GAMBIT by specifying the minimum edge length. The finite volume mesh so

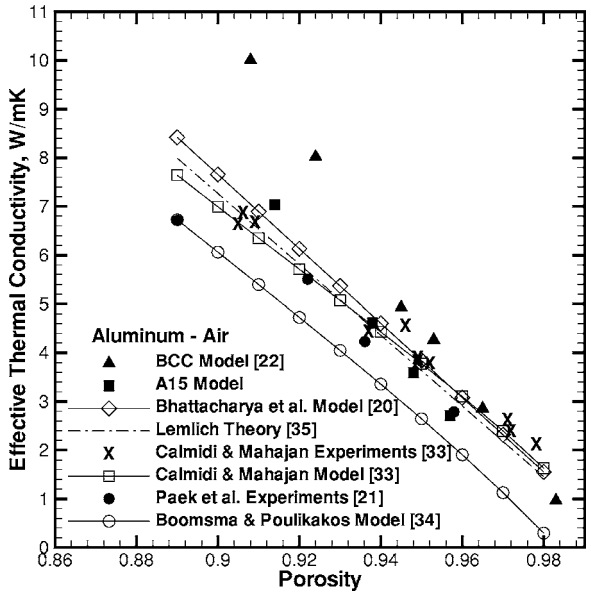


**Fig. 4 Predicted effective thermal conductivity of an aluminum foam-air system for a range of porosities. Also plotted are available semiempirical models and experimental measurements.**

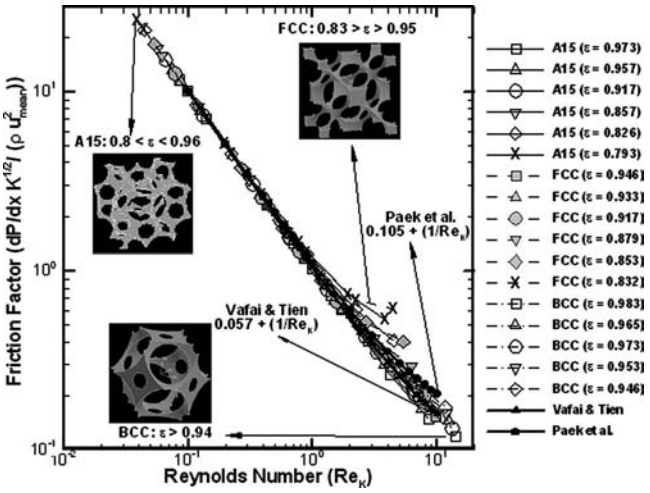


**Fig. 5 Predicted friction factor as a function of modified Reynolds number ($Re_K = Re_d(\sqrt{K/D})$). Results for the A15 lattice are plotted in red with symbols corresponding to the porosity range: $0.8 < \varepsilon < 0.96$. The fcc ($0.83 < \varepsilon < 0.95$) and bcc ($\varepsilon > 0.94$) [22] results are shown in green and blue, respectively. Also, experimental correlations from Refs. [21,36] are plotted.**

created was exported to the commercial code FLUENT [30] for flow and heat transfer simulations. A second-order upwind scheme was used for the convective calculations. A colocated pressure-velocity formulation in conjunction with the SIMPLE algorithm was used for obtaining the velocity fields, and the linearized systems of equations solved using an algebraic multigrid algorithm. Details of the numerical method may be found in Ref. [31]. The calculations were terminated when the (scaled) residual [30] had dropped below $10^{-6}$ for all governing equations.

Grid-independence tests were performed using the procedures detailed in Ref. [22]. The calculations reported in this paper were performed using approximately 200,000 finite volumes.

## Results and Discussion

**Effective Thermal Conductivity.** The numerical results for effective thermal conductivity for an aluminum-air system are considered first. The effective thermal conductivity is computed by numerically solving the conduction heat transfer through both the metal foam and the interstitial air on a single periodic module. A given heat-flux condition is not employed as above; instead, continuity of temperature and heat flux are employed as the interfacial conditions. Under the periodicity assumption, each module in the heat flow direction experiences an equal temperature drop. Computations are performed on a periodic module by imposing an arbitrary temperature drop $\Delta T$ across the periodic module along the heat flow direction, say, the $x$ axis. The resulting heat transfer rate at the periodic boundaries is used to obtain the effective thermal conductivity of the system using the relation

$$k_{\text{eff}} = \frac{-\int_{A_p} \mathbf{J} d\mathbf{A}}{(\Delta T A_p / \mathbf{L})} \tag{4}$$

where $\mathbf{J}$ is the diffusion flux vector at the periodic face, $d\mathbf{A}$ is the outward pointing elemental face area vector on the periodic face, and $A_p$ is the area of the periodic face. Calculations are performed using a modified version of the commercial code FLUENT [30]. Details of the mathematical model and numerical method are outlined in Refs. [22,32].

Figure 4 shows the calculated effective thermal conductivity for an aluminum foam-air system as a function of foam porosity. Also plotted in Fig. 4 are the predictions from the available semiempirical models, and experimental measurements from the literature [20,21,33,34]. The available experimental effective thermal conductivity measurements for foams cover a porosity range of $0.89 < \varepsilon < 0.98$. Paek et al. [21] and Calmidi and Mahajan [33] reported experimental uncertainties of 12% and 3.6% for the effective thermal conductivity measurements, respectively. It should be noted that the bcc and A15 models used in the present work do not employ any arbitrary parameters to match the experiments. Also plotted is the theoretical result from Lemlich's original work on electrical conductivity of liquid foams [35]. Using a direct analogy between Ohm's law and Fourier's law, we adopt his results for effective thermal conductivity of metal foams ($k_{\text{eff}} = k_s(1-\varepsilon)/3$). Details of the Lemlich theory and its implications are discussed in Ref. [22]. It can be inferred from Fig. 4 that both A15 and bcc models compare well with the existing literature for high porosities. The bcc model, as discussed in Ref. [22], deviates from experiments for porosities below 0.94 because the foam geometry ceases to be open celled, and there is an accumulation of metal mass at the nodes. The predictions of the A15 model match experiments for porosities $\varepsilon > 0.9$. However, there are no experimental data for porosities below 0.9, making validation difficult for high-density foams. In Fig. 4, the predictions from the fcc model are not plotted because the model underpredicted the experimental results by a factor of approximately 3.

**Pressure Drop and Nusselt Number.** We now consider predictions of the pressure drop and Nusselt number for the fcc and A15 lattice models. The predictions of the bcc model [22] are also plotted for comparison. As noted above, a constant heat-flux boundary condition is imposed on the ligament walls for all the cases considered. Hence, heat conduction through the foam ligaments is not modeled. Constant temperature boundary conditions may be alternatively employed on the foam walls; the predicted Nusselt numbers under those conditions would differ somewhat from those predicted with the constant flux conditions employed in this study [27].

Figure 5 shows the results for the friction factor calculated for an aluminum foam-air system from the numerical simulations based on the fcc and A15 modules. Also plotted are the experimental correlations from Refs. [21,36]. Paek et al. reported the repeatability error for the measurement of pressure drop to be 3%

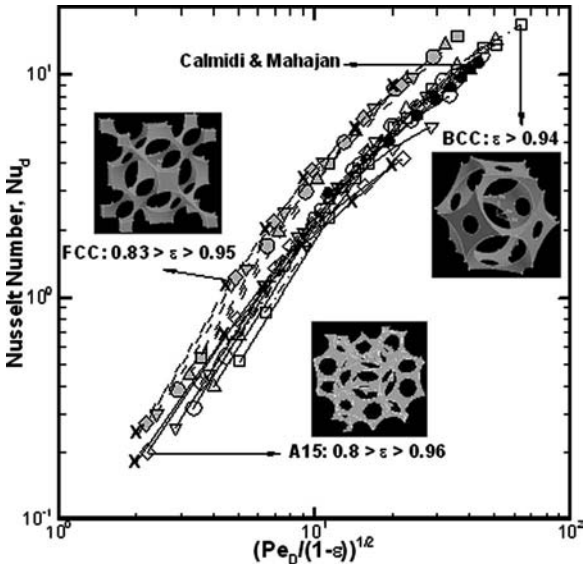


**Fig. 6 Predicted Nusselt number as a function of square root of Peclet number. Results for the A15 lattice are plotted in red with symbols corresponding to the porosity range: $0.8<\varepsilon<0.96$. The fcc ($0.83<\varepsilon<0.95$) and bcc ($\varepsilon>0.94$) [22] results are in green and blue, respectively. Please refer to Fig. 5 for the legend.**

for foam samples of porosity $0.89<\varepsilon<0.97$. The porosity range considered by Vafai and Tien was $0.94<\varepsilon<0.97$. Furthermore, results for a bcc model from our previous work [22] are also plotted in the figure. The permeability of the foam was calculated using the expression $K=-(\mu u_{\text{mean}})/(\partial\bar{p}/\partial x_i)$, where $u_{\text{mean}}$ was obtained for specified inlet mass flow rate in the Darcy regime ($\text{Re}<10$). The friction factor shown in Fig. 5 is defined as

$$f=\frac{(-\partial\bar{p}/\partial x_i)\sqrt{K}}{\rho u_{\text{mean}}^2} \tag{5}$$

The predicted friction factors from all the three models (bcc, fcc, and A15) compare well with the experimental correlations for porosities $\varepsilon>0.88$ and deviations for both the fcc and A15 are observed for porosities $<0.88$. It should be noted that the fcc model overpredicts the friction factor compared to the A15 model.

The Nusselt number for the foam was also calculated for the different cases considered and is defined as

$$\text{Nu}_D=\frac{hD}{k_f}=\frac{q''D}{k_f(\bar{T}_s-T_b)} \tag{6}$$

In the above equation $\bar{T}_s$ is the averaged temperature of the foam. In Fig. 6, the predicted local Nusselt number for the fcc and A15 lattices is plotted as a function of $(\text{Pe}_D/(1-\varepsilon))^{1/2}$, where the modified Peclet number ($\text{Pe}_D$) is $\text{Re}_d\text{Pr}$. This $x$-axis scale is obtained by balancing the convective and axial diffusive fluxes. It may be noted that predictions from the A15 model compare well with those from the bcc model for $\varepsilon>0.86$ and with experimental correlation from Calmidi and Mahajan [22,33]. Also, plotted are experimental correlation from Calmidi and Mahajan [33]. For lower porosities ($<0.86$), the local Nusselt number based on the permeability decreases due to the decrease in the permeability of the porous medium.

## Conclusions

This paper presents an approach for the modeling of open-cell foam geometries for porosities $\varepsilon>0.8$. The distinguishing feature of this approach is that no adjustable geometric parameters were used to match the experiments, unlike in previous published work. The fcc and A15 unit-cell models, along with the bcc model considered previously [22], are shown to predict friction factor and Nusselt number values, which are in good agreement with available experimental and semianalytical results.

The bcc and A15 models also predict thermal conductivity reasonably well. The predictions from the A15 model compared well with available range of experimental thermal conductivity measurements ($\varepsilon>0.89$) and bcc model predictions; the fcc model predictions for effective thermal conductivity showed greater deviations from the available measurements. Based on the results, there is a clear need for experimental results at foam porosities below 0.89. For convective flow calculations, the predicted friction factor and local Nusselt number from both fcc and A15 models compare well with our previous (bcc) model and with available experimental results for $\varepsilon>0.86$. The accuracy of the pressure drop and Nusselt number predictions depends on how well the unit-cell representation captures the surface-to-volume ratio of the real foam. On the other hand, the effective thermal conductivity depends strongly on capturing the ligament resistance correctly, and would require an accurate representation of the ligament cross-sectional area-to-length ratio. An evaluation of unit-cell models along these lines would benefit from the characterization of actual foams for a range of porosities and manufacturing techniques.

## Acknowledgment

Support for this work from industry members of the Cooling Technologies Research Center, a NSF Industry/University Cooperative Research Center (www.ecn.purdue.edu/CTRC), is gratefully acknowledged.

## Nomenclature

$a$ = edge length of the unit cell, m
$A$ = area, $\text{m}^2$
$C_p$ = specific heat capacity, $\text{J kg}^{-1}\text{ K}^{-1}$
$D$ = diameter of the pore, m
Da = Darcy number
$f$ = friction factor
$h$ = heat transfer coefficient, $\text{W m}^{-2}\text{ K}^{-1}$
$\mathbf{J}$ = diffusion flux vector, $\text{m}^2\text{ s}^{-1}$
$K$ = permeability, $\text{m}^2$
$k$ = thermal conductivity, $\text{W m}^{-1}\text{ K}^{-1}$
$L$ = length of the periodic module, m
Nu = Nusselt number
$q''$ = heat flux, $\text{W m}^{-2}$
Pr = Prandtl number
Pe = Peclet number
$R$ = radius of the pore, m
Re = Reynolds number
$s$ = center-to-center distance, m
$T$ = temperature, K
$t$ = time, s
$u,v,w$ = velocities along $x,y,z$ directions, $\text{m s}^{-1}$
$V$ = volume, $\text{m}^3$
$x,y,z$ = Cartesian coordinates

### Greek Symbols

$\alpha$ = thermal diffusivity, $\text{m}^2\text{ s}^{-1}$
$\varepsilon$ = porosity
$\mu$ = dynamic viscosity, $\text{kg m}^{-1}\text{ s}^{-1}$
$\rho$ = density, $\text{kg m}^{-3}$

### Superscript

- = average or mean

### Subscripts

$b$ = bulk
bc = body center

$D$ = Darcian
eff = effective
$f$ = fluid
in = inlet
int = intersection
$K$ = permeability
$s$ = solid
sa = surface area
sc = spherical cap

## References


[1] Gibson, L. J., and Ashby, M. F., 1999, *Cellular Solids: Structure and Properties*, Cambridge University Press, New York.
[2] Ashby, M. F., Evans, A., Fleck, N. A., Gibson, L. J., Hutchinson, J. W., and Wadley, H. J. G., 2000, *Metal Foams: A Design Guide*, Butterworth-Heinemann, Boston.
[3] Banhart, J., 2001, "Manufacture, Characterization and Application of Cellular Metals and Metal Foams," Prog. Mater. Sci., **46**, pp. 559–632.
[4] Lakes, R. S., 1987, "Foam Structures With a Negative Poisson's Ratio," Science, **235**, pp. 1038–1040.
[5] Chan, N., and Evans, K. E., 1997, "Fabrication Methods for Auxetic Foams," J. Mater. Chem., **32**, pp. 5945–5953.
[6] Preciado, J. A., Cohen, S., Skandakumaran, P., and Rubinsky, B., 2003, "Utilization of Directional Freezing for the Construction of Tissue Engineering Scaffolds," HTD (Am. Soc. Mech. Eng.), **374**, pp. 439–442.
[7] Freyman, T. M., Yannas, I. V., and Gibson, L. J., 2001, "Cellular Materials as Porous Scaffolds for Tissue Engineering," Prog. Mater. Sci., **46**, pp. 273–282.
[8] Heung, L. K., 2002, "Design of Metal Hydride Vessels for Processing Tritium," *Sixth International Conference on Tritium Science and Technology*, pp. 1–11.
[9] Peng, Y., and Richardson, J. T., 2004, "Properties of Ceramic Foam Catalyst Supports: One-Dimensional and Two-Dimensional Heat Transfer Correlations," Appl. Catal., A, **266**, pp. 235–244.
[10] Fend, T., Hoffschmidt, B., Pitz-Paal, R., Reutter, O., and Rietbrock, R., 2004, Energy, **29**, pp. 823–833.
[11] Montillet, A., Comiti, J., and Legrand, J., 1993, "Application of Metallic Foams in Electrochemical Reactors of Filter-Press Type Part I: Flow Characterization," J. Appl. Electrochem., **23**, pp. 1045–1050.
[12] Kamiuto, K., Andou, J., Miyanaga, T., and Taniyama, S., 2005, "Mist Transpiration Cooling System Using Open-Cellular Porous Materials," J. Thermophys. Heat Transfer, **19**, pp. 250–251.
[13] Krishnan, S., Garimella, S. V., Chrysler, G. M., and Mahajan, R. V., 2005, "Towards a Thermal Moore's Law," IEEE Trans. Adv. Packag., **30**, pp. 462–474.
[14] Ozmat, B., Leyda, B., and Benson, B., 2004, "Thermal Applications of Open-Cell Metal Foams," Mater. Manuf. Processes, **19**, pp. 839–862.
[15] Boomsma, K., Poulikakos, D., and Zwick, F., 2003, "Metal Foams as Compact High Performance Heat Exchangers," Mech. Mater., **35**, pp. 1161–1176.
[16] Klein, J., Gilchrist, G., Karanik, J., Arcas, N., Yurman, R., Whiteside, J., Shields, B., and Bartilucci, T., 2003, "Thermal Management of Airbourne Early Warning and Electronic Warfare Systems Using Foam Metal Fins," *International Electronic Packaging Technical Conference and Exhibition (IPACK'03)*, Paper No. IPACK2003-35187.
[17] Krishnan, S., Murthy, J. Y., and Garimella, S. V., 2004, "A Two-Temperature Model for the Analysis of Passive Thermal Control Systems," ASME J. Heat Transfer, **126**, pp. 628–637.
[18] Krishnan, S., Murthy, J. Y., and Garimella, S. V., 2005, "A Two-Temperature Model for Solid-Liquid Phase Change in Metal Foams," ASME J. Heat Transfer, **127**, pp. 995–1004.
[19] DuPlessis, P., Montillet, A., Comiti, J., and Legrand, J., 1994, "Pressure Drop Prediction for Flow Through High Porosity Metallic Foams," Chem. Eng. Sci., **49**, pp. 3545–3553.
[20] Bhattacharya, A., Calmidi, A. A., and Mahajan, R. L., 2002, "Thermophysical Properties of High Porosity Metal Foams," Int. J. Heat Mass Transfer, **45**, pp. 1017–1031.
[21] Paek, J. W., Kang, B. H., Kim, S. Y., and Hyun, J. M., 2000, "Effective Thermal Conductivity and Permeability of Aluminum Foam Materials," Int. J. Thermophys., **21**, pp. 453–464.
[22] Krishnan, S., Murthy, J. Y., and Garimella, S. V., 2006, "Direct Simulation of Transport in Open-Cell Metal Foam," ASME J. Heat Transfer, **128**, pp. 793–799.
[23] Phelan, R., Weaire, D., and Brakke, K., 1995, "Computation of Equilibrium Foam Structures Using the Surface Evolver," Exp. Math., **4**, pp. 181–192.
[24] Weaire, D., 2001, "A Philomorph Looks at Foam," *Proceedings of the American Philosophical Society*, Vol. 145, pp. 564–574.
[25] Dharmasena, K. P., and Wadley, H. N. G., 2002, "Electrical Conductivity of Open-Cell Metal Foams," J. Mater. Res., **17**, pp. 625–631.
[26] Boomsma, K., Poulikakos, D., and Ventikos, Y., 2003, "Simulations of Flow Through Open Cell Foams Using an Idealized Periodic Cell Structure," Int. J. Heat Fluid Flow, **24**, pp. 825–834.
[27] Patankar, S. V., Liu, C. H., and Sparrow, E. M., 1977, "Fully Developed Flow and Heat Transfer in Ducts Having Streamwise-Periodic Variations of Cross-Sectional Area," ASME J. Heat Transfer, **99**, pp. 180–186.
[28] Murthy, J. Y., and Mathur, S., 1997, "Periodic Flow and Heat Transfer Using Unstructured Meshes," Int. J. Numer. Methods Fluids, **25**, pp. 659–677.
[29] Fluent Inc., User's Guide for GAMBIT 2.0, 2002.
[30] Fluent Inc., User's Guide for FLUENT 6.0, 2002.
[31] Mathur, S. R., and Murthy, J. Y., 1997, "A Pressure-Based Method for Unstructured Meshes," Numer. Heat Transfer, Part B, **31**, pp. 195–216.
[32] Kumar, S., and Murthy, J. Y., 2005, "A Numerical Technique for Computing Effective Thermal Conductivity of Fluid-Particle Mixtures," Numer. Heat Transfer, Part B, **47**, pp. 555—572.
[33] Calmidi, V. V., and Mahajan, R. L., 1999, "The Effective Thermal Conductivity of High Porosity Fibrous Metal Foams," ASME J. Heat Transfer, **121**, pp. 466–471.
[34] Boomsma, K., and Poulikakos, D., 2001, "On the Effective Thermal Conductivity of a Three-Dimensionally Structured Fluid-Saturated Metal Foam," Int. J. Heat Mass Transfer, **44**, pp. 827–836.
[35] Lemlich, R., 1978, "A Theory for the Limiting Conductivity of Polyhedral Foam at Low Density," J. Colloid Interface Sci., **64**, pp. 107–110.
[36] Vafai, K., and Tien, C. L., 1982, "Boundary and Inertia Effects on Convective Mass Transfer in Porous Media," Int. J. Heat Mass Transfer, **25**, pp. 1183–1190.

# Rewetting Analysis of Hot Vertical Surfaces With Precursory Cooling by the Heat Balance Integral Method

**S. K. Sahu**
Graduate Student
e-mail: sksahu@mech.iitkgp.ernet.in

**P. K. Das**
Professor
e-mail: pkd@mech.iitkgp.ernet.in

**S. Bhattacharyya**
Professor
e-mail: souvik@mech.iitkgp.ernet.in

Department of Mechanical Engineering,
Indian Institute of Technology Kharagpur,
Kharagpur-721302, India

*The effect of precursory cooling on conduction-controlled rewetting of both slab and solid cylinder is analyzed by the heat balance integral method. A constant heat transfer coefficient is assumed in the wet region behind the wet front, while an exponentially decaying heat flux is assumed in the dry region ahead of the wet front. The physical problem is characterized by two dimensionless constants describing the extent of precursory cooling and three dimensionless numbers, namely, Peclet number, Biot number, and the nondimensional temperature. Results of the present solution are found to be in good agreement with other analytical solutions obtained through the Weiner–Hopf technique and the separation of variables as well as with the published experimental data for different coolants over a varied range of coolant flow rate. It is seen that precursory cooling increases the rewetting velocity particularly at higher flow rates. If it is neglected, the model grossly underpredicts the quench velocities.*
[DOI: 10.1115/1.2787021]

*Keywords: integral method, rewetting, quench front, precursory cooling, conduction controlled*

## 1 Introduction

When a hot surface is brought into contact with a liquid medium, often an intermediate vapor film forms between the solid and liquid and lowers the rate of heat transfer between them. The establishment of a solid liquid contact due to the collapse of vapor film during gradual cooling is known as rewetting. This phenomenon is of great importance in the cooling of reactor cores after a loss of coolant accident, cryogenic systems, metallurgical processes, etc. For the rewetting analysis, various one-dimensional and two-dimensional models have been developed to correlate experimental data at varied ranges of coolant flow rates. Conduction models based on a one-dimensional assumption have successfully correlated the experimental data at lower flow rates. However, the two-dimensional models that assume an adiabatic condition in the dry region ahead of the wet front have been partially successful in correlating the experimental data at higher flow rates. This is due to the fact that at higher flow rates, part of the coolant is sputtered away as droplets, which come into contact with surfaces and cause precooling of dry surface ahead of the wet front (Fig. 1). Consequently, the heat transfer from the hot surface takes place by convection and radiation to the surrounding droplet-vapor mixture and also due to direct impingement of small water droplets. This mode of cooling, termed as precursory cooling, is found to strongly influence rewetting velocity.

A large number of theoretical and experimental investigations [1–15] have been conducted on the rewetting of hot surfaces. In modeling the precursory cooling, either a constant coefficient for heat transfer [12–14] or a variable coefficient for heat transfer [1] or a variation of heat flux [7–9] ahead of the wet front has been considered. In the case of constant heat transfer, the highest heat flux from the wall occurs at the farthest location in the downstream direction of the quench front, which is physically unrealistic. However, if a variation of heat transfer ahead of the quench front is considered, the knowledge of the variation of temperature of the droplet-vapor mixture $T_a$ with distance is necessary. This is difficult to obtain in a real situation. In this context, the variable heat flux model is more convenient and is considered here. The analytical models [7–9] employ either a separation of variables method or the Weiner–Hopf technique to solve the conduction equation with precursory cooling. Recently, Sahu et al. [16] presented a comprehensive analysis of rewetting, employing the heat balance integral method (HBIM). Though precursory cooling was ignored, the model exhibited an excellent agreement with experimental data covering a wide range, particularly at low coolant flow rates. Encouraged by the success of this model, it is extended in the present work to include the effect of precursory cooling. Analysis has been done for two-dimensional planar and cylindrical geometries. The present results agree very well with the earlier analytical results and a exhibit good agreement with published experimental data.

## 2 Physical Model

Figure 1 schematically depicts the falling film rewetting of a two-dimensional slab or a rod of infinite length. The assumptions common in the conduction-controlled rewetting modeling are presented elsewhere [16]. Additionally, an exponentially decaying heat flux of the form $\bar{q}=(Q_0/N)\exp(-d\bar{x})$ is assumed ahead of the quench front. Suitable values of rewetting temperature, heat transfer coefficient, and solid length influenced by precursory cooling $d$ are kept constant a priori with an adjustable magnitude of precursory cooling ($N$) [1,7].

**2.1 Mathematical Formulation.** The conduction equation valid both for rectangular Cartesian and cylindrical polar coordinate systems (Fig. 1) can be written in a generalized form presented below,

$$\frac{1}{\bar{r}^n}\frac{\partial}{\partial \bar{r}}\left(\bar{r}^n\frac{\partial T}{\partial \bar{r}}\right)+\frac{\partial^2 T}{\partial \bar{x}^2}=\frac{\rho C}{K}\frac{\partial T}{\partial t} \quad 0<\bar{r}<b \quad -\infty<\bar{x}<\infty \quad t>0$$

$$n=\begin{cases}0 & \text{for a Cartesian geometry, with } \bar{r}\equiv\bar{y},\ b\equiv\delta\\ 1 & \text{for a cylindrical geometry}\end{cases} \tag{1}$$

The following normalized variables are defined:

$$x\equiv\frac{\bar{x}}{\delta} \quad r\equiv\frac{\bar{r}}{b} \quad a\equiv d\delta \quad \mathrm{Pe}\equiv\frac{\rho C u b}{K} \quad \mathrm{Bi}\equiv\frac{hb}{K}$$

$$\theta\equiv\frac{T-T_s}{T_0-T_s} \quad \theta_1\equiv\frac{T_w-T_0}{T_0-T_s} \tag{2}$$

Contributed by the Heat Transfer Division of ASME for publication in the JOURNAL OF HEAT TRANSFER. Manuscript received June 8, 2006; final manuscript received June 18, 2007; published online February 15, 2008. Review conducted by Chang Oh.

  

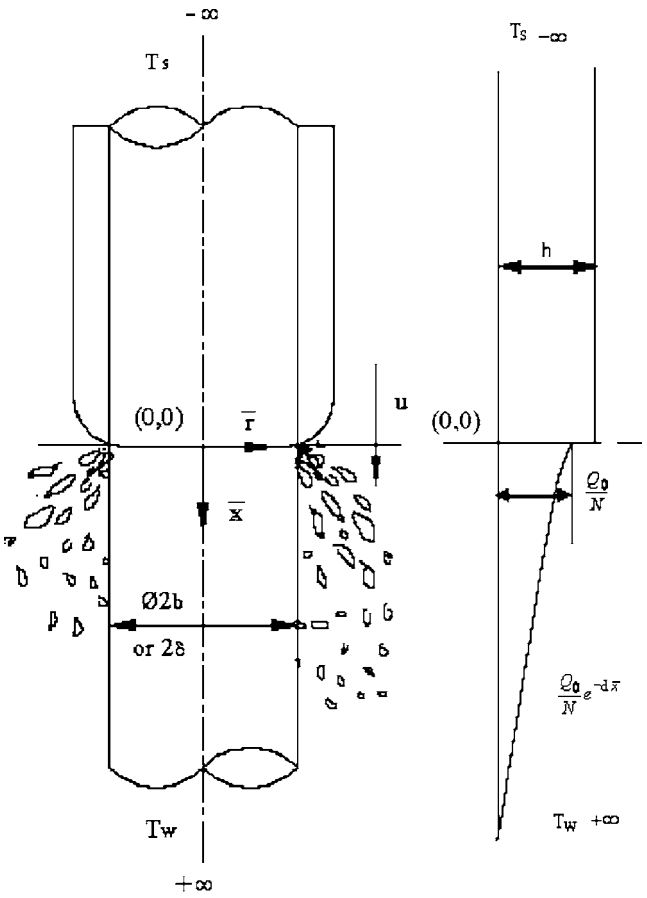


**Fig. 1 Schematic diagram of top flooding with precursory cooling of hot surfaces of a two-dimensional object**

Utilizing Eq. (2) and the quasi-steady-state assumption ($\partial T/\partial t = -u\partial T/\partial \bar{x}$), Eq. (1) yields

$$\frac{1}{r^n}(r^n\theta_r)_r + \theta_{xx} + \mathrm{Pe}\,\theta_x = 0 \tag{3}$$

subject to boundary conditions given by

$$\theta_r = \begin{cases} 0 & r=0 \quad (-\infty < x \leqslant 0) & (4a) \\ -\mathrm{Bi}\,\theta_i & r=1 & (4b) \\ 0 & r=0 \quad (0 \leqslant x < \infty) & (4c) \\ (-\mathrm{Bi}/N)\exp(-ax) & r=1 & (4d) \end{cases}$$

$$\theta = \begin{cases} 1 & r=1 \quad x=0 & (4e) \\ \theta_i & r=1 \quad (-\infty < x < +\infty) & (4f) \end{cases}$$

$$\theta = \begin{cases} 0 & x \to -\infty & (4g) \\ 1+\theta_1 & x \to +\infty & (4h) \end{cases}$$

**2.2 Solution Procedure.** Assuming a temperature profile in the transverse direction, the energy equation can be integrated as follows:

$$\int_0^1 \left[\frac{1}{r^n}(r^n\theta_r)_r + \theta_{xx} + \mathrm{Pe}\,\theta_x\right] r^n dr = 0 \tag{5}$$

and $\bar{\theta}$ can be defined as

$$\bar{\theta} = \int_0^1 \theta r^n dr \tag{6}$$

This gives a single ordinary differential equation valid for both wet and dry regions,

$$\bar{\theta}_{xx} = \mathrm{Pe}\,\bar{\theta}_x + (r^n\bar{\theta}_r)_{r=1} - (r^n\bar{\theta}_r)_{r=0} = 0 \quad (-\infty < x < +\infty) \tag{7}$$

At this juncture, we have selected a simple yet generalized temperature profile as a function of transverse coordinates containing three unknown parameters $\alpha$, $\beta$, and $\gamma$. The general solution of the problem for both Cartesian and cylindrical geometries based on this profile is as follows:

$$\theta = \alpha r^{-n} + \beta r + \gamma r^{(2-2n)} \tag{8}$$

Combining Eqs. (7) and (8) and employing boundary conditions given by Eqs. (4*a*)–(4*h*) yield

$$\theta(x) = \begin{cases} \exp\{0.5\mathrm{Pe}[(1+4M/\mathrm{Pe}^2)^{1/2}-1]x\} & (-\infty < x \leqslant 0) \\ 1+\theta_1[1-\exp(-\mathrm{Pe}x)] + \dfrac{\mathrm{Bi}}{3N}\dfrac{(Z_1-ja)}{ja}\exp(-\mathrm{Pe}x)[\exp(-jx)-1] & (0 \leqslant x < \infty) \end{cases} \tag{9}$$

Applying the continuity of heat flux at $x=0$ to Eq. (9), the following expression for the dimensionless wet front velocity is obtained:

$$\theta_1 = \frac{0.5}{\mathrm{Pe}}\left\{[(\mathrm{Pe}^2+4M)^{1/2}-\mathrm{Pe}] + \frac{Z_2\mathrm{Bi}}{Na} - \frac{2\mathrm{Bi}a}{3N} + \frac{2\mathrm{BiPe}}{3N}\right\} \tag{10}$$

where

$$j = a - \mathrm{Pe} \quad M = \mathrm{Bi}/(1+\mathrm{Bi}/3) \quad Z_2 = (2/3)Z_1$$

$$Z_1 = \begin{cases} 3 & \text{for a Cartesian geometry} \\ 6 & \text{for a cylindrical geometry} \end{cases} \tag{11}$$

## 3 Results and Discussion

The physical problem can be expressed by two dimensionless constants ($d$,$N$) and three dimensionless numbers (Pe, Bi, and $\theta_1$) irrespective of geometry (slab/cylinder). Previous researchers [1,7] also reported expressions involving these five parameters.

**Table 1 A comparison of the nondimensional temperature ($\theta_1$) obtained by HBIM and other analytical techniques for Bi=0.5 and $a$=0.005. SV: Separation of variables method, WH: Wiener–Hopf technique.**

| | | | | | | | |
|---|---|---|---|---|---|---|---|
| $N\rightarrow\infty$ | | | | | | | |
| Pe | 6.144 | 3.113 | 0.8777 | 0.5182 | 0.1305 | 0.0678 | 0.01402 |
| SV | 0.05 | 0.1 | 0.5 | 1 | 5 | 10 | 50 |
| WH | 0.05006 | 0.09997 | 0.5001 | 1 | 4.98 | 9.978 | 49.97 |
| HBIM | 0.011 | 0.042 | 0.398 | 0.89 | 4.541 | 9.169 | 46.197 |
| $N$=100 | | | | | | | |
| Pe | 27.16 | 13.33 | 2.64 | 1.375 | 0.3165 | 0.1645 | 0.03388 |
| SV | 0.05 | 0.1 | 0.5 | 1 | 5 | 10 | 50 |
| WH | 0.04999 | 0.09992 | 0.5001 | 1.001 | 5 | 9.949 | 49.94 |
| HBIM | 0.03907 | 0.07909 | 0.4385 | 0.91936 | 4.7957 | 9.5916 | 48.3468 |
| $N$=10 | | | | | | | |
| Pe | 296.3 | 122.6 | 21.26 | 10.45 | 2.069 | 1.042 | 0.2125 |
| SV | 0.05 | 0.1 | 0.5 | 1 | 5 | 10 | 50 |
| WH | 0.04941 | 0.0997 | 0.5003 | 1.001 | 5.005 | 10.01 | 49.99 |
| HBIM | 0.05042 | 0.09826 | 0.48798 | 0.9775 | 4.9416 | 9.9165 | 49.69 |
| $N$=1 | | | | | | | |
| Pe | | 4989 | 287.8 | 119.4 | 20.66 | 10.16 | 2.009 |
| SV | | 0.1 | 0.5 | 1 | 5 | 10 | 50 |
| WH | | 0.1001 | 0.5001 | 0.9979 | 5.007 | 10.01 | 50.05 |
| HBIM | | 0.1867 | 0.5141 | 1.0042 | 5.0079 | 10.0133 | 50.0394 |

However, different functional forms were obtained. The five-parameter relationship for small Peclet numbers obtained from a two-dimensional analysis [7] is expressed as

$$\mathrm{Pe} = F - A_1/F \tag{12}$$

where

$$F = f(\mathrm{Bi}, N, a, \theta_1) \quad A_1 = 3\mathrm{Bi}/(1+3\mathrm{Bi}) \tag{13}$$

To avoid repetition, elaborations are made for a two-dimensional slab geometry. It is interesting to note that the value of $A_1$ obtained by Dua and Tien [7] shown in Eq. (13) is exactly the same as $M$ (effective Biot number) defined in Eq. (11) of the present HBIM solution. In all the models [1,7–9], the parameter $N$ is defined as the magnitude of precursory cooling, which depends on the flow rate. When the coolant flow rate increases, the number of coolant droplets increases in the sputtering region. Consequently, the heat transfer from the hot surface increases, yielding a stronger precursory cooling. Therefore, $N$ decreases with increasing coolant mass flow rate. Previously, a correlation was proposed [7] with $N$ and flow rate as $N=(160/\Psi)+1$. It suggests that $N$ should tend to 1 for high flow rates. This trend is observed in the present solution as well. A comparison of nondimensional temperatures ($\theta_1$) predicted by the method of separation of variables [8], the Wiener–Hopf technique [9], and the HBIM for various Pe is shown in Table 1. Results obtained by HBIM are in good agreement with the reported analytical results for low values of both Pe and $N$.

In the literature, most of the top flooding experiments have been conducted for rods over a varied range of coolant flow rate. In most of the cases, water has been used as the coolant under atmospheric condition. In these experiments, a precise estimation of the heat transfer coefficient (Biot number) has not been mentioned. Various theoretical models have been developed for top flooding of slabs and rods with precursory cooling [1,7,15]. Most of the theoretical models consider an approximate Bi to solve conduction equations. In the present analysis, we are able to forward a unified five-parameter relationship for conduction-controlled rewetting with precursory cooling for two different geometries. In this model, Bi, nondimensional temperature $\theta_1$, and exponent in the decay of precursory cooling $d$ are kept constant a priori with an adjustable value of $N$ for comparison with the experimental results.

The present predictions are compared with the experimental data taken from various sources with different wall thicknesses, as shown in Figs. 2(*a*)–2(*c*). The experimental data are taken from a water–stainless steel pair, considering water as the coolant. It is observed that the value of $N$ and $d$ have been obtained with the knowledge of variation of heat flux in the dry region ahead of the quench front for a nitrogen-copper pair [4]. However, the detailed information on the variation of heat flux in the dry region ahead of the wet front for a water-stainless pair is not available in the literature. In the present prediction, the value of $d$ is taken as 0.05 $\mathrm{cm}^{-1}$ for comparing the experimental results in Figs. 2(*a*)–2(*c*). A similar value was adopted in earlier studies [1,7] as well. However, while comparing against experimental data (Fig. 3), for a nitrogen-copper pair, a $d$ of 0.079 $\mathrm{cm}^{-1}$ was employed by Dua and Tien [4]; a similar value is considered in the present study as well and the comparison is presented in Fig. 3. Previously, other researchers [1,7] have followed the same procedure to compare their model with the experimental data. It may be noted that the experimental data are from various sources and for different dry wall temperatures and wall thicknesses. They also cover a wide variation of coolant flow rate and coolant type. Nevertheless, the extremely good agreement between the HBIM prediction Eq. (10) and the data set establishes the strength of the method.

## 4 Conclusions

In the present investigation, HBIM has been applied to analyze the conduction-controlled rewetting with precursory cooling. A unified solution comprising a five-parameter relationship is obtained for two different geometries, namely, two-dimensional slab and rod. The predicted results show an excellent agreement with the previously reported experimental and analytical results. It is observed that the extent of precooling increases with increasing mass flow rates. At large mass flow rates, the wet front velocity is indeed high, and a one-dimensional analysis of precursory cooling becomes inadequate. A better agreement is obtained by adopting a

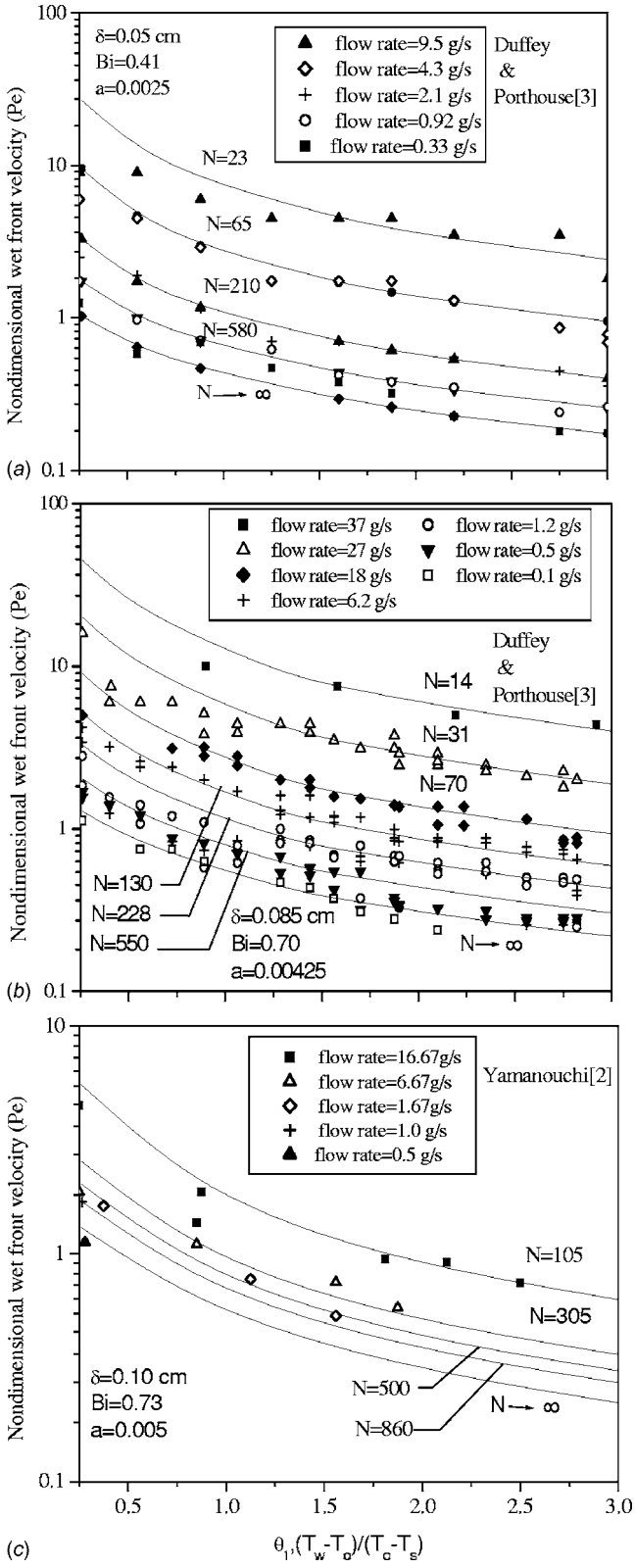


**Fig. 2 Comparison of predicted wet front velocity with experimental results of (*a*) Duffey and Porthouse [3] with wall thickness of 0.05 cm, (*b*) 0.085 cm, and (*c*) Yamanouchi [2] with wall thickness of 0.1 cm**

two-dimensional analysis. It is concluded that precursory cooling may strongly enhance the rewetting rate, while neglecting it leads to an underprediction of the rewetting velocity. The complexities

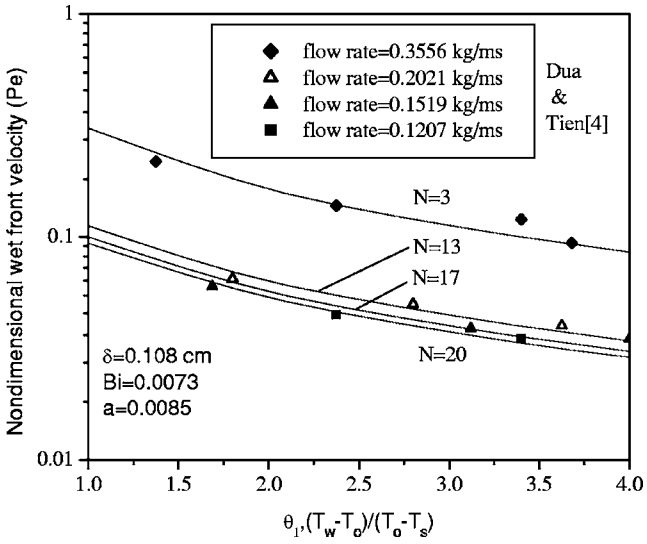


**Fig. 3 Comparison of predicted wet front velocity with experimental results of Dua and Tien [4] (wall thickness of 0.108 cm)**

of the heat transfer mechanism from the dry wall ahead of the wet front to the surrounding droplet-vapor can be successfully modeled by using HBIM.

## Nomenclature

$A_1$ = defined in Eq. (13)
$a$ = dimensionless exponent $d\delta$
$b$ = radius of cylinder
Bi = Biot number
$C$ = thermal capacitance, J/kg°C
$d$ = exponential power in Fig. 1
$F$ = defined in Eq. (13)
$h$ = heat transfer coefficient, $W/m^2°C$
$j$ = defined in Eq. (11)
$K$ = thermal conductivity, W/m°C
$M$ = effective Biot number defined in Eq. (11)
$N$ = magnitude of precursory cooling
$n$ = constant defined in text
Pe = Peclet number, defined in Eq. (2)
$Q_0$ = heat flux at the wet front, $h(T_0-T_s)$
$T$ = temperature, °C
$T_a$ = temperature of the droplet-vapor mixture
$T_0$ = rewetting or sputtering temperature, °C
$T_s$ = saturation temperature, °C
$T_w$ = initial temperature of the dry surface, °C
$t$ = time, s
$u$ = wet front velocity, m/s
$\bar{x},\bar{y},\bar{r}$ = length coordinates, m
$x,y,r$ = dimensionless length coordinates
$Z_1,Z_2$ = constant defined in Eq. (11)

### Greek Symbols

$\alpha,\beta,\gamma$ = constants defined in the text
$\delta$ = wall thickness, m
$\theta$ = nondimensional temperature defined in Eq. (2)
$\theta_1$ = nondimensional temperature parameter defined in Eq. (2)
$\bar{\theta}$ = nondimensional temperature integral defined in Eq. (6)
$\theta_i$ = nondimensional surface temperature
$\Psi$ = flow rate per unit perimeter g/cm s
$\rho$ = density, $kg/m^3$

### Subscripts

$x, r$ = derivatives with respect to $x$ and $r$, respectively.

## References


[1] Sun, K. H., Dix, G. E., and Tien, C. L., 1975, "Effect of Precursory Cooling on Falling-Film Rewetting," ASME J. Heat Transfer, **97**, pp. 360–365..

[2] Yamanouchi, A., 1968, "Effect of Core Spray Cooling in Transient State After Loss-of-Coolant Accident," J. Nucl. Sci. Technol., **5**, pp. 547–558.

[3] Duffey, R. B., and Porthouse, D. T. C., 1972, "Experiments on the Cooling of High Temperature Surfaces by Water Jets and Drops," *CREST Specialist Meeting on Emergency Core Cooling for Light Water Reactors*, Munich, Germany.

[4] Dua, S. S., and Tien, C., L., 1978, "An Experimental Investigation of Falling Film Rewetting," Int. J. Heat Mass Transfer, **5**, pp. 955–965.

[5] Duffey, R. B., and Porthouse, D. T. C., 1973, "The Physics of Rewetting in Water Reactor Emergency Core Cooling," Nucl. Eng. Des., **25**, pp. 379–394.

[6] Tien, C. L., and Yao, L. S., 1975, "Analysis of Conduction-Controlled Rewetting of a Vertical Surface," ASME J. Heat Transfer, **97**, pp. 161–165.

[7] Dua, S. S., and Tien, C. L., 1976, "Two Dimensional Analysis of Conduction-Controlled Rewetting With Precursory Cooling," ASME J. Heat Transfer, **98**, pp. 407–413.

[8] Olek, S., 1988, "The Effect of Precursory Cooling on Rewetting of Slab," Nucl. Eng. Des., **108**, pp. 323–330.

[9] Olek, S., 1990, "Wiener-Hopf Technique Solution to a Rewetting Model With Precursory Cooling," Nucl. Sci. Eng., **105**(3), pp. 271–277.

[10] Elias, E., and Yadigaroglu, G., 1977, "A General One-Dimensional Model for Conduction-Controlled Rewetting of Surface," Nucl. Eng. Des., **42**, pp. 185–186.

[11] Davidy, A., Elias, E., and Olek, S., 2001, "Quenching of Hot Oxidizing Surfaces," Nucl. Eng. Des., **204**, pp. 361–368.

[12] Sawan, M. E., and Temraz, H. M., 1981, "A Three Regions Semi-Analytical Rewetting Model," Nucl. Eng. Des., **64**, pp. 319–327.

[13] Hsu, C.-H., Chieng, C.-H., and Hua, T., 1983, "Two-Dimensional Analysis of Conduction-Controlled Rewetting with Internal Heat Generation," *Proceedings of International Conference on Numerical Methods in Engineering*, Montreal, Canada.

[14] Salcudean, M., and Bui, T. M., 1980, "Heat Transfer During the Rewetting of Hot Horizontal Channels," Nucl. Eng. Des., **59**, pp. 369–377.

[15] Olek, S., 1989, "Rewetting of a Solid Cylinder With Precursory Cooling," Appl. Sci. Res., **46**, pp. 347–364.

[16] Sahu, S. K., Das, P. K., and Bhattacharyya, S., 2006, "A Comprehensive Analysis of Conduction-Controlled Rewetting by the Heat Balance Integral Method," Int. J. Heat Mass Transfer, **49**, pp. 4978–4982.

# Discussion: "Effects of Various Parameters on Nanofluid Thermal Conductivity" (Jang, S. P., and Choi, S. D. S., 2007, ASME J. Heat Transfer, 129, pp. 617–623)

**C. Kleinstreuer**
e-mail: ck@eos.ncsu.edu

**Jie Li**

MAE Department,
NC State University,
Raleigh, NC 27695-7910

## Background Information

In a series of articles, Jang and Choi [1–3] listed and explained their effective thermal conductivity ($k_{\text{eff}}$) model for nanofluids. For example, in the 2004 article [1], they constructed a $k_{\text{eff}}$ correlation for dilute liquid suspensions interestingly, based on kinetic *gas* theory as well as nanosize boundary-layer theory, the Kapitza resistance, and nanoparticle-induced convection. Three mechanisms contributing to $k_{\text{eff}}$ were summed up, i.e., base-fluid and nanoparticle conductions as well as convection due to random motion of the liquid molecules. Thus, after an order-of-magnitude analysis, their effective thermal conductivity model of nanofluids reads

$$k_{\text{eff}} = k_f(1-\varphi) + k_{\text{nano}}\varphi + 3C_1\frac{d_f}{d_p}k_f \,\text{Re}_{d_p}^2 \,\text{Pr}\,\varphi \tag{1}$$

where $k_f$ is the thermal conductivity of the base fluid, $\varphi$ is the particle volume fraction, $k_{\text{nano}}=k_p\beta$ is the thermal conductivity of suspended nanoparticles involving the Kapitza resistance, $C_1=6\times10^6$ is a constant (never explained or justified), $d_f$ and $d_p$ are the diameters of the base-fluid molecules and nanoparticles, respectively, $\text{Re}_{d_p}$ is a "random" Reynolds number, and Pr is the Prandtl number. Specifically,

$$\text{Re}_{d_p} = \frac{\bar{C}_{\text{RM}}d_p}{\nu} \tag{2}$$

where $\bar{C}_{\text{RM}}$ is a random motion velocity and $\nu$ is the kinematic viscosity of the base fluid.

Jang and Choi [3] claimed that they were the first to propose Brownian motion induced nanoconvection as a key nanoscale mechanism governing the thermal behavior of nanofluids. However, they just added a random term to Eq. (1), actually quite small in magnitude for certain base liquids, although enhanced by the large factor 3 $C_1=18\times10^6$, while, independently, in the same year, Koo and Kleinstreuer [4] proposed their effective thermal conductivity model, based on *micromixing* induced by Brownian motion, followed by Prasher et al. [5] and others (see review by Jang and Choi [3]).

However, it should be noted that the validity of the different origins for the unusual thermal effect of nanofluids has been questioned (see Evans et al. [6] and Vladkov and Barrat [7], among others) as well as the actual $k_{\text{eff}}$ increase as reported in experimental papers (see Venerus et al. [8] and Putnam et al. [9], among others). Controversies arose from using different experimental techniques (e.g., transient hot wire versus optical methods) and from phenomenological models relying more on empirical correlations rather than sound physics and benchmark experimental data.

In 2006, Jang and Choi [2] changed the thermal conductivity correlation slightly to

$$k_{\text{eff}} = k_f(1-\varphi) + k_p\beta\varphi + 3C_1\frac{d_f}{d_p}k_f \,\text{Re}_{d_p}^2 \,\text{Pr} \tag{3}$$

where the volume fraction term $\varphi$ is now missing in the last term. Most recently, Jang and Choi [3] tried to explain more clearly the modeling terms they had proposed. Their present thermal conductivity model reads

$$k_{\text{eff}} = k_f(1-\varphi) + k_p\beta\varphi + 3C_1\frac{d_f}{d_p}k_f \,\text{Re}_{d_p}^2 \,\text{Pr}\,\varphi \tag{4}$$

## Parameter Analysis

In the 2006 article [2], the random motion velocity, which is used to define the Reynolds number (see Eq. (2)), was defined as

$$\bar{C}_{\text{RM}} = \frac{2D_0}{l_f} \tag{5a}$$

while in the 2007 article [3], the authors changed the random motion velocity to

$$\bar{C}_{\text{RM}} = \frac{D_0}{l_f} \tag{5b}$$

where $D_0=\kappa_b T/3\pi\mu d_p$ is the diffusion coefficient given by Einstein [10], and $l_f$ is the mean free path of the (liquid) base fluid. The mean free path of the base fluid is calculated from Kittel and Kroemer [11], which deals only with transport properties of ideal gases (see their Chap. 14):

$$l_f = \frac{3k_f}{\bar{c}\hat{C}_V} \tag{6a}$$

where $\bar{c}$ is the mean molecular velocity, and $\hat{C}_V$ is the heat capacity per unit volume. Although Eq. (6*a*) is certainly not applicable to liquids, the mean free path for (ideal) gases can also be written as

$$l_f = \frac{3k_f}{\rho c_v \bar{c}} \tag{6b}$$

with $c_v$ being the thermal capacity at constant volume, where $\rho c_v \equiv \hat{C}_V$.

## Model Comparisons

According to the parameters Jang and Choi [3] provided and the terms they explained, the effective thermal conductivities of CuO-water and $Al_2O_3$-water nanofluids were calculated and compared. Figures 1 and 2 provide comparisons of Jang and Choi's 2007 model [3] with the experimental data sets of Lee et al. [12] for CuO-water and $Al_2O_3$-water nanofluids, respectively. Two random motion velocities $\bar{C}_{\text{RM}}$ were compared, where the dashed line relates to Eq. (5*a*) while the solid line is based on Eq. (5*b*). Clearly, these comparisons do not match the results given by Jang and Choi [3] in their Fig. 2, unless new matching coefficients in the third term of Eq. (4) are applied. Specifically, the first two terms contribute very little, i.e., $\Sigma_{i=1}^2 \text{term}_i/k_f \approx 0.99$. Is the contribution of the particle's thermal conductivity really that small? Many researchers indicated that the higher thermal conductivity of the nanoparticles is a factor in enhancing the effective thermal conductivity (Hong et al. [13], Hwang et al. [14]). It has to be stressed that all the data comparisons are based on the thermal properties provided by Jang and Choi [3] in Table 1. However, thermal conductivity values found in the literature indicated

Contributed by the Heat Transfer Division of ASME for publication in the JOURNAL OF HEAT TRANSFER. Manuscript received July 1, 2007; final manuscript received September 24, 2007; published online February 6, 2008. Review conducted by Peter Vadasz.

  

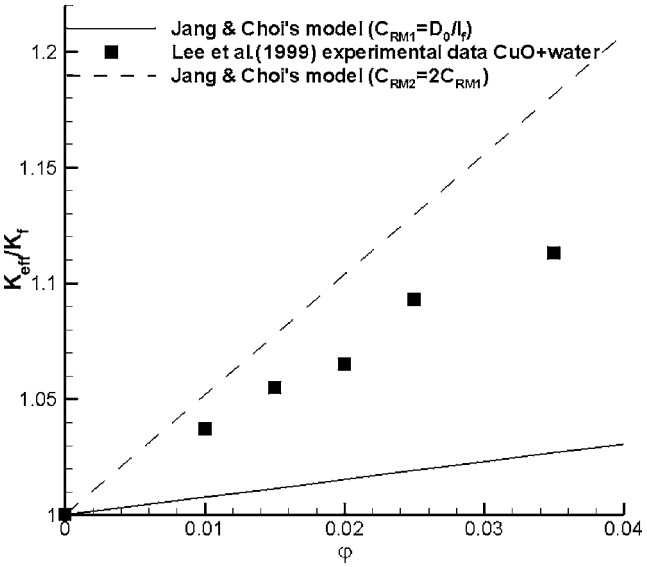


**Fig. 1 Comparison of the experimental data (Lee et al. [12]) for CuO-water nanofluids with Jang and Choi's [3] model for different random motion velocity definitions**

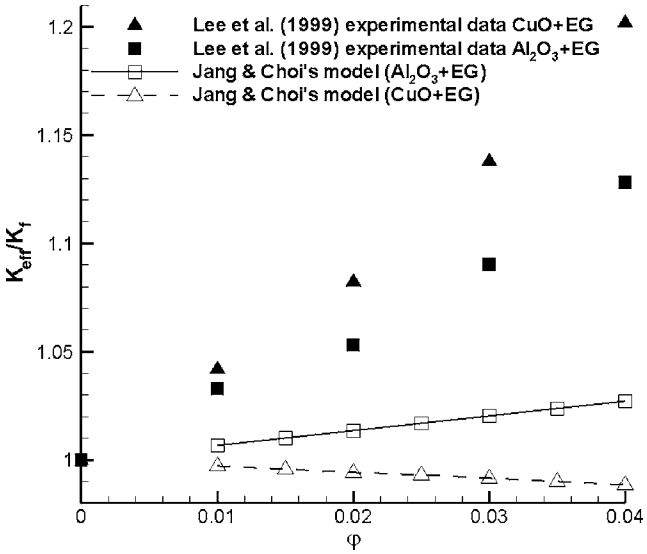


**Fig. 3 Comparison of the experimental data (Lee et al. [12]) for $Al_2O_3$-EG and CuO-EG nanofluids with Jang and Choi's [3] model**

32.9 W/m K for CuO (Wang et al. [15]) and, for $Al_2O_3$, a range of 18–35 W/m K depending on the purity, i.e., 94–99.5%.[1] When using the more reasonable particle thermal conductivity values in the model of Jang and Choi [3], only small differences were observed.

Now, in contrast to water, if the base fluid is changed to ethylene glycol (EG), the third term in Eq. (4) is suddenly of the order of $10^{-6}$, i.e., it does not contribute to the effective thermal conductivity when compared to the first two terms ($10^{-1}$ and $10^{-3}$). The nondimensionalized effective thermal conductivity of CuO-EG nanofluids is about 0.99 for all volume fraction cases, while for $Al_2O_3$-EG nanofluids, $k_{\text{eff}}/k_f$ is slightly higher at approximately 1.015. Both graphs are well below the experimental data of Lee et al. [12], as shown in Fig. 3. The larger EG viscosity provided a much smaller Reynolds number, which almost eliminates the third term.

For the experimental result of Das et al. [16], Jang and Choi [3] compared their model for $Al_2O_3$ particles with a volume fraction of 1% in their Fig. 7. Considering the temperature influence on the thermal characteristics of base fluid (water), Fig. 4 provides again an updated comparison. If we consider $\bar{C}_{\text{RM}}=2D_0/l_f$, indicated with the dashed curve, the model shows a good agreement in the lower temperature range; however, the model prediction fails when the temperature is higher than 40°C. Figure 5 shows the comparison of Jang and Choi's model with the experimental data of Das et al. [16] when the volume fraction is 4%. Clearly, their model does not match the experimental results well.

[1]http://www.accuratus.com/alumox.html

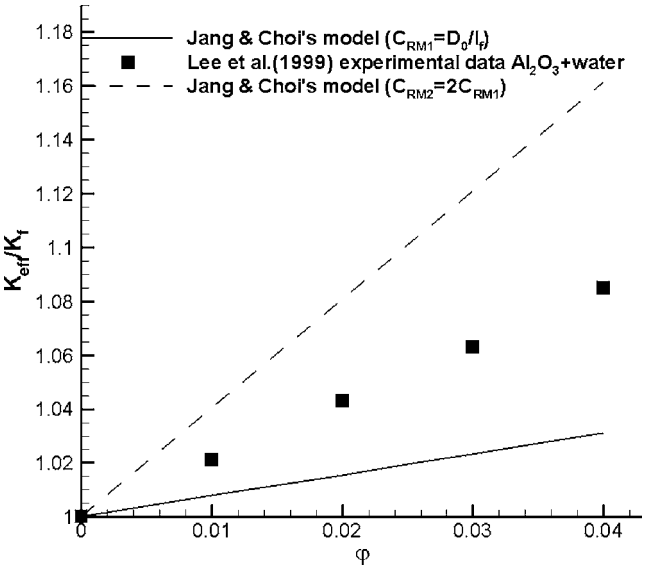


**Fig. 2 Comparison of the experimental data (Lee et al. [12]) for $Al_2O_3$-water nanofluids with Jang and Choi's [3] model for different random motion velocity definitions**

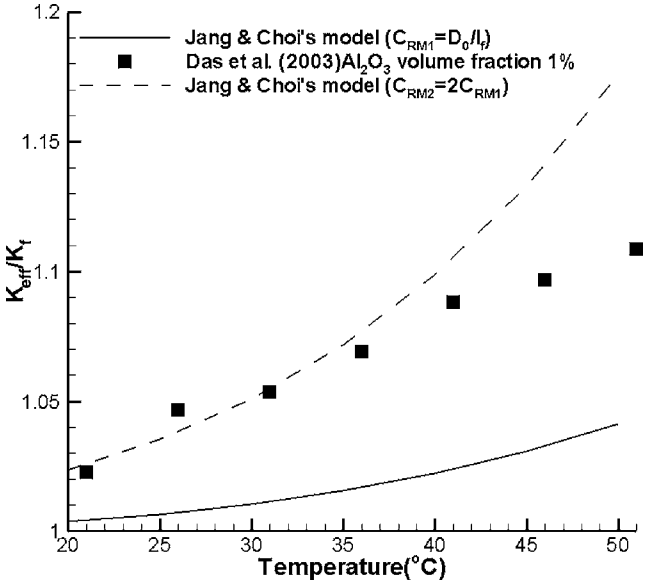


**Fig. 4 Comparison of the experimental data (Das et al. [16]) for 1% $Al_2O_3$-water nanofluids with Jang and Choi's [3] model for different random motion velocity definitions**

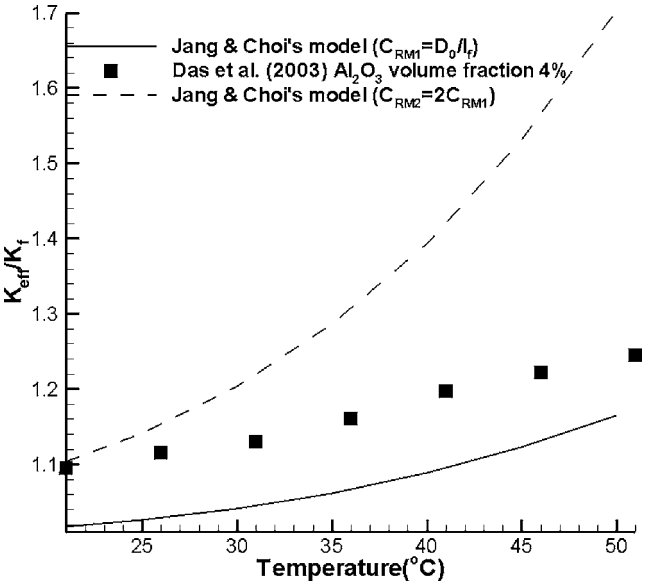


**Fig. 5 Comparison of the experimental data (Das et al. [16]) for 4% $Al_2O_3$-water nanofluids with Jang and Choi's [3] model for different random motion velocity definitions**

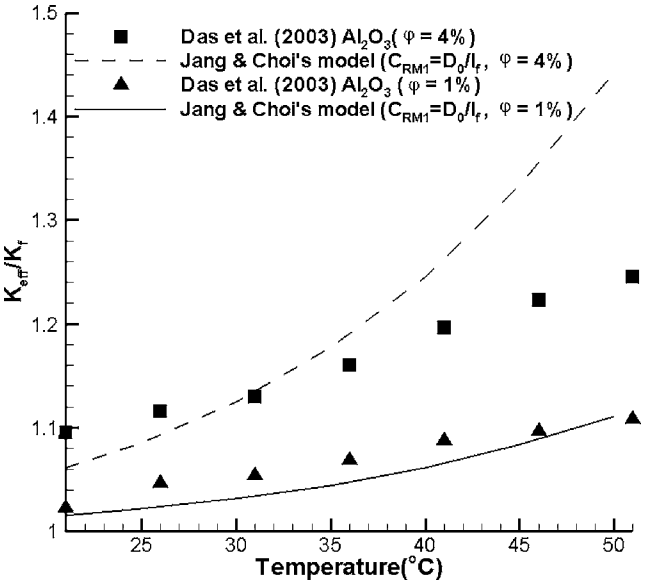


**Fig. 7 Comparison of the experimental data (Das et al. [16]) for 1% and 4% $Al_2O_3$-water nanofluids with Jang and Choi's [3] model (new proportionality constant and new particle diameters are applied)**

On June 14, 2007, Choi responded to the analysis presented so far. Specifically, he provided the following new information:

- Number-weighted diameters (24.4 nm for $Al_2O_3$ and 18.6 nm for CuO) were replaced with the area-weighted diameters (38.4 nm for $Al_2O_3$ and 23.6 nm for CuO),
- the random motion velocity $\bar{C}_{RM}=D_0/l_f$ was selected, and
- new proportionality constants, i.e., $C_1=7.2\times10^7$ for water and $C_1=3.2\times10^{11}$ for EG, were recommended.

Thus, employing the new information, Figs. 6 and 7 now replace Figs. 3–5, respectively. The Jang and Choi [3] model achieved a good match with the new numerical values for CuO-water nanofluids and $Al_2O_3$-water nanofluids (not shown). However, when using EG-based nanofluids, the model still cannot provide a good match even for the very large proportionality constant of $C_1=3.2\times10^{11}$ (see Fig. 6). When compared with the experimental data of Das et al. [16], as shown in Fig. 7 for a volume fraction of 1%, the model generates a decent data match, which is not the case when the volume fraction reaches 4%.

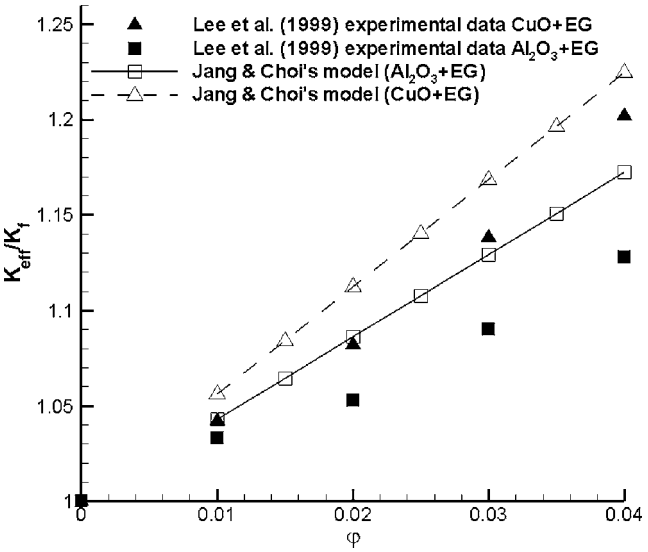


**Fig. 6 Comparison of the experimental data (Lee et al. [12]) for $Al_2O_3$-EG and CuO-EG nanofluids with Jang and Choi's [3] model (new proportionality constant and new particle diameters are applied)**

## References


[1] Jang, S. P., and Choi, S. U. S., 2004, "Role of Brownian Motion in the Enhanced Thermal Conductivity of Nanofluids," Appl. Phys. Lett., **84**, pp. 4316–4318.

[2] Jang, S. P., and Choi, S. U. S., 2006, "Cooling Performance of a Microchannel Heat Sink With Nanofluids," Appl. Therm. Eng., **26**, pp. 2457–2463.

[3] Jang, S. P., and Choi, S. U. S., 2007, "Effects of Various Parameters on Nanofluid Thermal Conductivity," ASME J. Heat Transfer, **129**, pp. 617–623.

[4] Koo, J., and Kleinstreuer, C., 2004, "A New Thermal Conductivity Model for Nanofluids," J. Nanopart. Res., **6**, pp. 577–588.

[5] Prasher, R. S., Bhattacharya, P., and Phelan, P. E., 2006, "Brownian Motion Based Convective Conductive Model for the Effective Thermal Conductivity of Nanofluids," ASME J. Heat Transfer, **128**, pp. 588–595.

[6] Evans, W., Fish, J., and Keblinski, P., 2006, "Role of Brownian Motion Hydrodynamics on Nanofluid Thermal Conductivity," Appl. Phys. Lett., **88**, pp. 093116.

[7] Vladkov, M., and Barrat, J. L., 2006, "Modeling Transient Absorption and Thermal Conductivity in a Simple Nanofluid," Nano Lett., **6**(6), pp. 1224–1228.

[8] Venerus, D. C., Kabadi, M. S., Lee, S., and Peres-Luna, V., 2006, "Study of Thermal Transport in Nanoparticle Suspensions Using Forced Rayleigh Scattering," J. Appl. Phys., **100**, pp. 094310.

[9] Putnam, S. A., Cahill, D. G., Braun, P. V., Ge, Z., and Shimmin, R. G., 2006, "Thermal Conductivity of Nanoparticle Suspensions," J. Appl. Phys., **99**, pp. 084308.

[10] Einstein, A., 1956, *Investigation on the Theory of Brownian Movement*, Dover, New York.

[11] Kittel, C., and Kroemer, H., 1980, *Thermal Physics*, Freeman, San Franciso.

[12] Lee, S., Choi, S. U. S., Li, S., and Eastman, J. A., 1999, "Measuring Thermal Conductivity of Fluids Containing Oxide Nanoparticles," ASME Trans. J. Heat Transfer, **121**(2), pp. 280–289.

[13] Hong, T., Yang, H., and Choi, C. J., 2005, "Study of the Enhanced Thermal Conductivity of Fe Nanofluids," J. Appl. Phys., **97**, p. 064311.

[14] Hwang, Y., Park, H. S., Lee, J. K., and Jung, W. H., 2006, "Thermal Conductivity and Lubrication Characteristics of Nanofluids," Curr. Appl. Phys., **6**, pp. 67–71.

[15] Wang, B., Zhou, L., Peng, X., and Zhang, X., 2003, "Enhancing the Effective Thermal Conductivity of Liquid With Dilute Suspensions of Nanoparticles," 15th Symposium on Thermophysical Properties.

[16] Das, S. K., Putra, N., Thiesen, P., and Roetzel, W., 2003, "Temperature Dependence of Thermal Conductivity Enhancement for Nanofluids," ASME J. Heat Transfer, **125**, pp. 567–574.

# Erratum: "Optimally Staggered Finned Circular and Elliptic Tubes in Turbulent Forced Convection" [Journal of Heat Transfer, 2007, 129(5), pp. 674–678]

**R. L. S. Mainardes, R. S. Matos, J. V. C. Vargas, and J. C. Ordonez**

The original paper reported a heat transfer gain of up to 80% of the optimized elliptical tubes arrangement with respect to the optimized circular one. In fact, the actual heat transfer gain found experimentally is up to 23% only. Therefore corrections are needed in the paper, as follows.

(1) Abstract: correct to "…A relative heat transfer gain of up to 23% ($Re_{2b}$=10,600)…" and "…A relative heat transfer gain of 23% is…."

(2) Section 4 Results and Discussion:

(i) Correct Eq. (10) to "$\tilde{q}_{*,mmm}=1299.5+0.47003\,Re_{2b}+0.000034064\,Re_{2b}^2$, $R=0.99053$"

(ii) Correct the 7th paragraph to: "In sum, a heat transfer gain of up to 23% was observed…."

(3) Section 5 Conclusions: correct the 2nd paragraph to "…The three-way optimized elliptic arrangement exhibits a heat transfer gain of up to 23% relative to…."

(4) Figures 3 and 4 need to be replaced by the following ones with the corrected results.

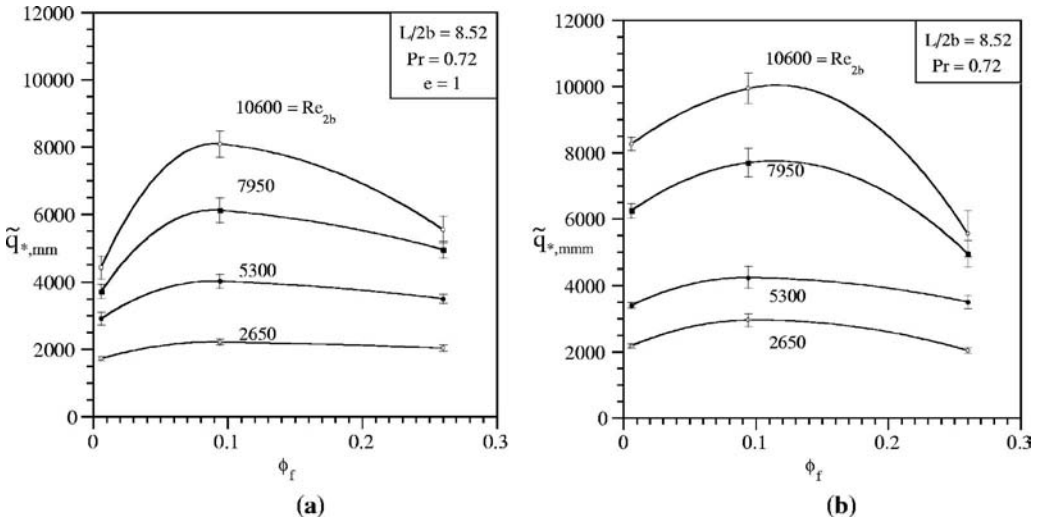


**Fig. 3 (*a*) Two-way optimization of finned circular arrangements with respect to tube-to-tube and fin-to-fin spacing and (*b*) three-way optimization of finned arrangements with respect to tube-to-tube spacing, eccentricity and fin-to-fin spacing**

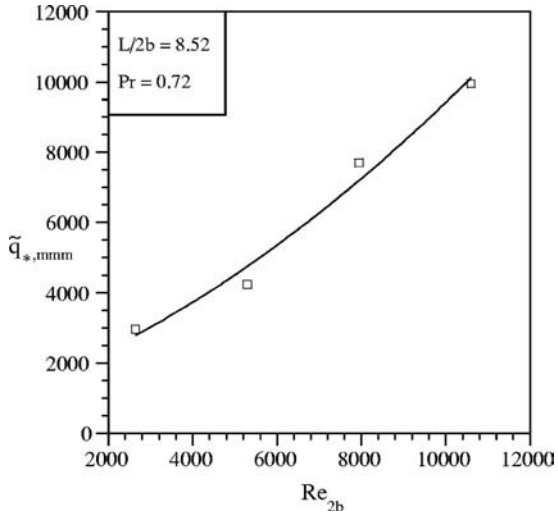


**Fig. 4 The three-way maximized dimensionless heat transfer rate with respect to $Re_{2b}$**

  